UNIVERSITY OF CALIFORNIA

Los Angeles

# The Early Lunar Magmatic and Impact Histories Recorded by Apollo Zircons

A dissertation in partial satisfaction of the

requirements for the Doctor of Philosophy

in Geochemistry

by

Carolyn Alicia Crow

2015

ABSTRACT OF THE DISSERTATION

The Early Lunar Magmatic and Impact Histories

Recorded by Apollo Zircons

by

Carolyn Alicia Crow

Doctor of Philosophy in Geochemistry

University of California, Los Angeles, 2015

Professor Kevin McKeegan, Chair

The nature of the early lunar magmatic and impact histories remains a fundamental, yet poorly understood area of planetary science. Lunar zircons are thought to have formed in enriched residual melts and their crystallization ages have thus been used to infer the timing of KREEP magmatism. However, models of the lunar magma ocean (LMO) solidification are inconsistent with the implied duration of KREEP magmas (4.4-3.9 Ga). Additionally, the proposed late heavy bombardment (LHB), or lunar cataclysm, during a similar era of lunar history has recently been called into question. The latter has implications beyond the Moon, because the lunar impact record is used to constrain dynamical models of solar system evolution and to calibrate ages of planetary surfaces. Investigating early lunar history requires samples older than the proposed cataclysm, which may also record signatures of magmatic crystallization and subsequent impact events. Lunar zircons are ideal for this study

for several reasons: first, the population of lunar zircons identified in Apollo sample thin sections all have $^{207}Pb$-$^{206}Pb$ crystallization ages older than the LHB, and second, zircons from both Earth and the Moon have been shown to retain textural and chemical evidence of impact shock events.

The research presented in this thesis consists of coordinated analyses of individual zircons recovered from Apollo 14, 15, and 17 samples aimed at investigating both facets of the early history of the Moon. An extensive U-Pb and $^{207}Pb$-$^{206}Pb$ age survey reveals that >90% of lunar zircons crystallized before ~4.1 or 4.2 Ga. The relative scarcity of textures commonly associated with Pb-loss and age disturbances in the studied zircon population indicates that these ages likely reflect igneous crystallization ages. This suggests a 200 – 300 Myr duration of KREEP magmatism, which is shorter than previous estimates based on the full range of lunar zircon ages, but is more consistent with the time scales for LMO solidification models.

Trace element analyses reveal that contributions from micron to sub-micron impact melt glass inclusions common in lunar zircons are significant sources of contamination. After filtering the data to remove analyses that contained these inclusions, the lunar zircons can be described by one Rare Earth Elements (REE) pattern that is characterized by a negative Eu anomaly and an absence of a positive Ce anomaly. This observation is contrary to previous reported results that did not account for contamination effects, and suggests that the lunar zircons formed in a reducing environment. Concentrations of titanium were measured to calculate crystallization temperatures. Using new estimates for oxide activities, we find that temperatures range between 958 ± 57° to 1321 ± 100°C. This range is bounded by the dry

granite solidus and zircon saturation temperatures for KREEP rich-samples, and do not require hydrous conditions as suggested by previous authors (who assumed equal oxide activities). The zircon trace element analyses reported herein therefore support the general understanding of the lunar environment as reducing and anhydrous.

We also present the first U-Pu-Xe age analyses of lunar zircons and compare them with terrestrial shocked zircons from the Vredefort impact structure in South Africa. The terrestrial zircons show no evidence of impact-associated Xe-loss, but do record a signature of a later local intrusive event. This suggests impact shock alone does not result in appreciable Xe-loss, however prolonged exposure to elevated temperatures can disturb U-Xe ages. Xe analyses of the lunar zircons reveal that some grains retain their fission Xe for >3.8 Ga, while others appear to have experienced significant Xe-loss within the last ~0.5 Gyr. Contributions from an isotopically heavy Xe component, most likely due to spallation from REE, allowed for only minimum degassing ages to be determined. Nonetheless, the high retentivity of Xe, and consequently old U-Xe ages, in some lunar zircon grains suggests that U-Pu-Xe dating is a promising method for investigating the early impact history of the Moon, and future analyses to constrain spallation Xe yields will allow for more precise degassing ages to be determined.

The dissertation of Carolyn Alicia Crow is approved.

Bradley Hansen

T. Mark Harrison

Kevin McKeegan, Committee Chair

University of California, Los Angeles

2015

I dedicate this thesis to my parents, Art and Julie, to my husband Paul, and to my brother Ian. Thank you for all your love and support during my graduate career, and for always encouraging me to follow my dreams.

## Table of Contents

**Table of Figures**

**Chapter 1**



**Chapter 2**



**Chapter 3**

**Chapter 4**

**Acknowledgements**

I would like to express gratitude to my advisor, Prof. Kevin McKeegan, for his guidance and motivation throughout my graduate career. Without his support and encouragement, I would not have cultivated the fruitful collaborations I have developed with researchers and institutions around the world. I would also like to thank my thesis committee: Prof. T. Mark Harrison, Prof. David Paige, Prof. Bradley Hansen, and Dr. Paul Warren. Their guidance has helped me become a better scientist. My decision to pursue a PhD was greatly influenced by my undergraduate advisor and mentor, Dr. Lucy McFadden, who introduced me to meteorites, which ultimately me to my study of Cosmochemistry and work with lunar samples. I thank her for helping me find this passion.

While conducting my thesis research, I also had the pleasure to collaborate with many extraordinary scientists. I would like to thank my fellow group members Dr. Beth Ann Bell, Dr. Matthew Wielicki, Patrick Boehnke, and Prof. Rita Economos for their assistance in SIMS laboratory analyses and endless discussions of zircons, the moon, and bolide impacts. I would also like to give special thanks to Patrick Boehnke for his assistance with statistical analyses and collaboration on diffusion experiments, which supported the Xe study in this thesis. My sincere thanks go to Dr. Sarah Crowther, Prof. Jamie Gilmour, and Mark Nottingham at the University of Manchester, who granted access to the RELAX facility and assisted with Xe data reduction and interpretation. I would also like to acknowledge and thank Prof. Desmond Moser and Ivan Barker at the University of Western Ontario for their collaboration on the shock microstructural survey. I am grateful for Dr. Benjamin Jacobsen, Dr. Peter Weber, and Dr. Ian Hutcheon at Lawrence Livermore National Laboratory for

collaborating to develop new zircon dating NanoSIMS techniques and characterizing the standard glass materials. I also thank Veronika Heber and Henner Busemann for characterizing our irradiated standard glasses at ETH Zurich.

I also take this opportunity to thank the JPL Division 4 ice hockey team for giving me the opportunity to make their team coed. I was honored to lead you as your assistant captain for the last two years. Go Rovers! I am also grateful for the staff of Copa Vida in Pasadena for their excellent coffee and for providing a wonderful environment where I wrote the vast majority of my thesis. I would like to thank my friends, who were the best support group a graduate student could ask for, and my family who were my constant cheerleaders and always reminded me not to take life too seriously. Finally, I would like to thank my husband Paul for his unwavering love and support during my entire graduate career. You inspire me to be a better scientist and to be authentically myself.

# Carolyn A. Crow

## Research Interests:

Investigating the magmatic and impact record of early solar system recorded in returned samples from the Moon, Mars, and other planetary bodies.

## Education:

**M.S.**, Geochemistry, University of California, Los Angeles (March 2012)
**B.S.,** Astronomy, University of Maryland (December 2008)

## Professional Experience:

Graduate Research Assistant, UCLA, 2011-Present
- Identified and pursued multi-faceted analytical study of lunar zircons with implications for the early magmatic and impact history of the Moon
- Developed technique for U-Pb dating by NanoSIMS at LLNL

Executive Secretary, NASA Review Panel, Sep 2013
Research Assistant, U. Maryland, Jan 2009 – August 2010
- Researched remote sensing of biosignatures using NASA EPOXI mission data, and published a first-author paper in the Astrophysical Journal
- Processed Hubble Space Telescope images for NASA EPOXI Mission

Undergraduate Research Assistant and Data Analyst, U. Maryland, Mar-Dec 2008

## Awards:

Meteoritical Society McKay Award (Best Student Oral Presentation) 2015
NASA Earth and Space Sciences Fellow 2012-Present
Meteoritical Society Wiley-Blackwell Award (Outstanding Student Oral Presentation) 2014
UCLA ESS Department Teaching Award 2012
Lunar and Planetary Institute Career Development Award 2012

## Teaching & Education Experience:

Teaching Assistant, UCLA, Fall 2010 [Earthquakes], Winter 2012 [Solar System and Planets – EPSS Departmental Teaching Award]
Student Member, NASA Dawn Mission Education and Public Outreach Team, 2009 – 2010
Teaching Assistant, U. Maryland, Fall 2008, Spring 2009 [Introduction to Astronomy]

## Publications:

**Crow, C. A.**, McKeegan, K. D. (2015). Lunar Zircon Survey: Early Lunar Magmatic and Impact History. *In Prep* for *Meteor. Planet. Sci.*

**Crow, C. A.**, Moser, D. E., McKeegan, K. D., Barker, I. (2015). Impact Shock Microstructures in Apollo 14 and 15 Zircons. *In Prep* for *Meteor. Planet. Sci.*

McFadden, L. A., Bastien, F. A., Mutchler, M., **Crow, C. A.,** Weir, H., Li, J.-Y., Hamilton, D. P. Search for Satellites of Vesta: Upper Limits on Their Size. (2012). *Icarus*, 220, 305-310.

**Crow, C. A.**, McFadden, L. A., Robinson, T., Meadows, V., Livengood, T. A., Hewagama, T., Barry, R. K., Deming, L. D., Lisse, C. M., Wellnitz, Dennis. (2011). Views from EPOXI: Colors in our Solar System as an Analog for Extrasolar Planets. *Astrophys. J.*, 729, 130.

## Most Recent Conference Oral Presentations:

**Crow, C. A.**, Jacobsen, B., McKeegan, K. D., Moser, D. E. (2015). Investigating Zircon Shock Microstructures with NanoSIMS. 46th Lunar and Planetary Science Conference. #2470

**Crow, C. A.**, McKeegan, K. D., Moser, D. E. (2015). Lunar Zircons: What's the Big Picture? Workshop: Early Solar System Impact Bombardment III. #3020

**Crow, C. A.**, Moser, D. E., McKeegan, K. D., Barker, I. (2014) Impact Shock Microstructures in Apollo 14 Zircons. 77th Meteoritical Society meeting. #5366 [Wiley-Blackwell Award]

**Crow, C. A**., McKeegan, K. D., Gilmour, J. D., Crowther, S. A., Taylor, D. J. (2013) Zircons as a Probe of Early Lunar History. 76th Meteoritical Society Meeting. #5083

**Crow, C. A**., McKeegan, K. D., Gilmour, J. D., Crowther, S. A., Taylor, D. J. (2012) Are Apollo Zircons Witness to a Lunar Cataclysm? 43rd Lunar and Planetary Science Conf. #1639

**Crow, C. A.**, McFadden, L. A., Robinson, T., Meadows, V., Livengood, T. A., Hewagama, T., Barry, R. K., Deming, L. D., Lisse, C. M. (2010) Views from EPOXI: Colors in our Solar System as an Analog for Extrasolar Planets. 42nd Meeting Division of Planetary Sciences, AAS. #52.06

## Chapter 1: Introduction

The return of lunar samples by NASA's Apollo missions between 1969 and 1972 has greatly contributed to our understanding of the Earth-Moon system. The ongoing study of these samples has led to better constraints on the formation, magmatic evolution, and impact history of the Moon, however many aspects of these remain to be well understood. To better contextualize the research reported in this thesis, which focuses on the first ~600 Myr after lunar formation, it is useful to review the current understanding of early lunar history.

### 1.1 Early Magmatic History of the Moon

The most favored view of lunar formation is by a giant impact between the proto-Earth and a Mars sized object, which resulted in a debris disk that coalesced to form the Moon (e.g. Hartmann and Davis, 1975; Boss and Peale, 1986; Canup and Asphaug, 2001). Hf-W model ages of Apollo samples and lunar meteorites suggest the timing of lunar formation occurred between 4.53 and 4.54 Ga (Lee et al., 1997; Yin et al., 2002; Jacobsen, 2005; Kleine et al., 2005; Touboul et al., 2009). The anorthositic crust of the Moon is most likely a cumulate float from a global magma ocean, which suggests the Moon was partially or totally molten after accretion (Binder, 1986; Solomon, 1986; Pritchard and Stevenson, 2000). Time scales for solidification of the lunar magma ocean (LMO) range between 10 Myr, using a simple two stage model involving both radiative and conductive cooling, and up to ~220 Myr, which requires tidal heating to sustain longer durations of magmatism (Meyer et al., 2010; Elkins-Tanton et al., 2011).

The first minerals to form in the fractionally crystallizing LMO would have been dense, Mg-rich olivine and pyroxene, which would have settled to the bottom of the LMO. When anorthosite saturation was reached, these cumulates would have floated to the top of the LMO to form the anorthositic crust (e.g. Shearer et al., 2006). Borg et al. (2015) reviewed the ages of crustal rocks and found that the most robust ages for these samples span between 4306 ± 6 and 4108 ± 40 Ma suggesting the lunar crust was formed during this interval. As the LMO continued to solidify, the crystallizing minerals would before increasingly enriched in Fe resulting in a density inversion in the LMO cumulate. A mantle overturn event resulting from this stability has been proposed based on solidification models and the existence of the Mg-suite lunar rocks, however the existence and timing of such an event is not known (Elkins Tanton et al., 2002; Shearer et al., 2006; Borg et al., 2015).

After >99% of the LMO has crystallized, the residual melts would have become increasingly enriched in incompatible elements and this residual melt has been termed KREEP due to its high abundance of K, rare earth elements (REEs), and P (Meyer and Hubbard, 1970; Meyer et al., 1971; Meyer, 1977; Warren and Wasson, 1979). Model ages place the separation of the KREEP source between 4389 ± 45 Ma (Sm-Nd of Mg-suite rocks and KREEP basalts) and 4478 ± 46 Ma (Lu-Hf of lunar zircons) ( Taylor et al., 2009b; Borg et al., 2015). This is the most likely source region for lunar zircons and as a result, their crystallization ages have therefore been used to suggest KREEP magmatism occurred between ~4.4 and 3.9 Ga (see references bellow). However, the 500 Myr duration of KREEP magmatism is inconsistent with the modeled timescales of LMO crystallization.

Later mare volcanism on the lunar near side occurred between ~ 4.2 and 2.5 Ga, and may have started even as far back at 4.35 Ga (Head, 1976; Taylor et al., 1983; Terada et al., 2007) (dark regions in Figure 1-1). Remote sensing data from Lunar Prospector revealed that the lunar near side is also enriched in Th and other heat producing elements in a region called the Procellarum KREEP Terrain (PKT) (Lawrence et al., 1999) (Figure 1-2). The spatial

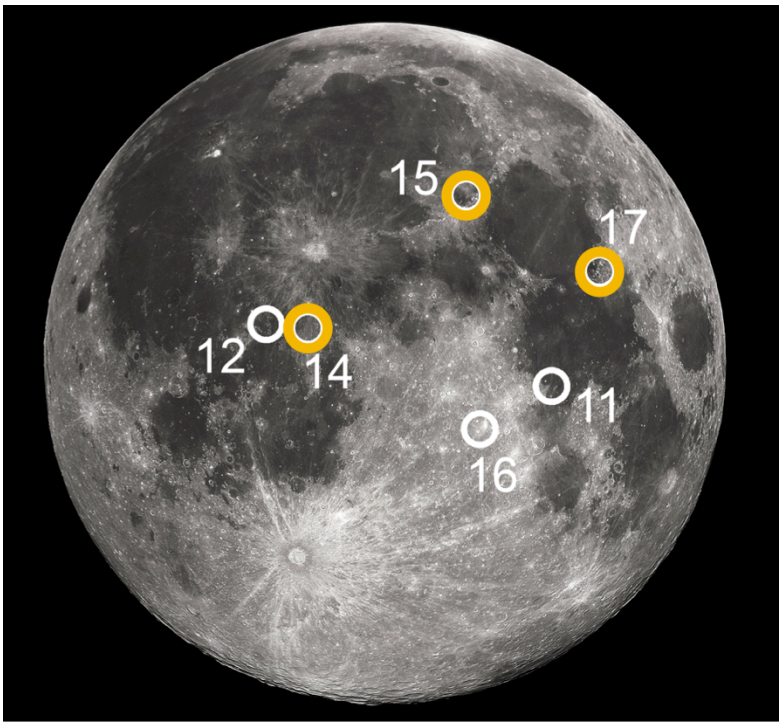


Figure 1-1: Image of the nearside of the Moon showing the location of the Apollo landing sites and the contrasting dark mare and bright highland regions. Image credit: NASA.

proximity of the lunar mare and the PKT suggests partial melting due to radioactive decay of elements such as U and Th is likely the mechanism that generated mare magmas (e.g. Wieczorek and Philips, 2000). The average model age for the mare basalt source region

reported by Borg et al. (2015) is 4354 ± 25 Ma, which they note is similar to the KREEP source model ages.

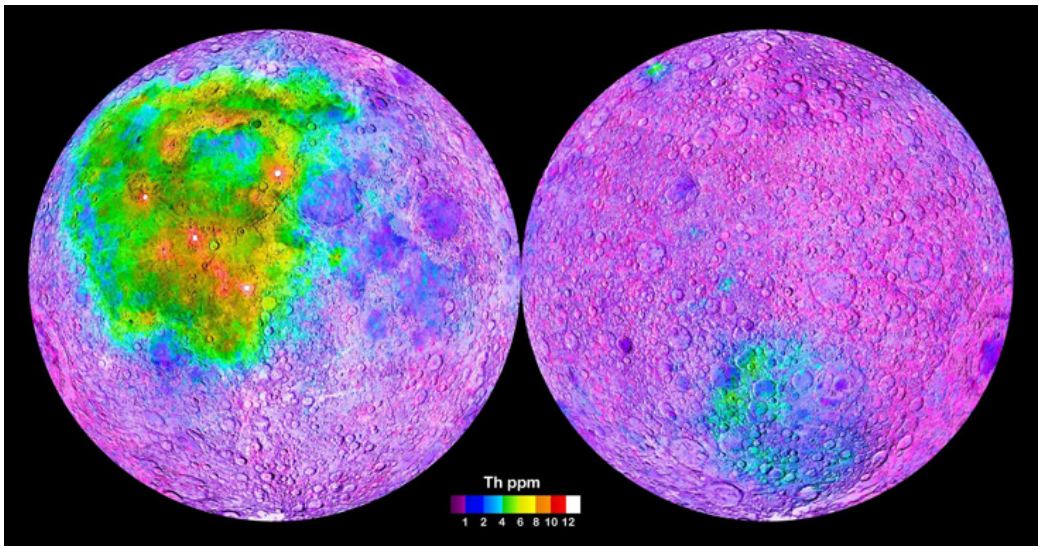


Figure 1-2: Global map of Th concentration from NASA Lunar Prospector showing Procellarum KREEP terrain has the high Th concentrations (left). There is also elevated Th in the South Pole Aitken Basin (left). Image Credit: NASA.

### 1.2 Early Lunar Impact History and The Late Heavy Bombardment

During the early magmatic evolution of the Moon described previously, the lunar surface was also being bombarded with left-over fragments from planet formation, called planetesimals, the largest of which formed the lunar basins. Recent gravity anomaly analyses from the NASA GRAIL mission have been used to identify additional lunar basins and raised the count of lunar basins (>200 km diameter) to 74 (Zuber et al., 2013; Neumann et al., 2015). Understanding the timing of the early basin forming impacts has implications beyond the Moon including constraining models of solar system evolution and understanding the

environment under which life first emerged on Earth (e.g. Ahrens, 1993; Abramov and Mojzsis, 2009; Morbidelli, 2013).

Some of the early analyses of Apollo samples revealed degassing ages and isotopic disturbances suggestive of multiple lunar basin formation during a short time interval centered around 3.95 Ga. Turner et al. (1973) was the first to propose an era of heightened bombardment and suggested that up to six basin forming events occurred between 3.88 and 4.05 Ga based on Ar-Ar ages of highlands material. Soon after, Tera et al. (1974) reported whole rock Pb-isotopic disturbances and Rb-Sr isochrones as additional evidence for multiple events at ~ 3.95 Ga; they termed this era the "terminal lunar cataclysm". Since then Ar-Ar ages of additional Apollo samples and lunar meteorites have been used to support the idea of a lunar cataclysm (e.g. Dalrymple and Ryder, 1996; Cohen et al., 2000). However, other authors have expressed skepticism towards this interpretation of the lunar data mostly because of the difficult nature of interpreting Ar-Ar ages for complex samples, and the inability to distinguish between a cataclysm and a simple drop in the impact flux bellow a saturation level (known as the "stonewall effect") (e.g. Hartmann, 1975, 2003; Harrison and Lovera, 2013). Other plausible impact histories have also been suggested such as the "sawtooth-like" timeline proposed by Morbidelli et al. (2012) or the possibility of multiple pre-3.9 Ga cataclysms. Figure 1-3 is modified from (Zahnle et al., 2007) and illustrates the range in possible lunar impact histories.

### 1.3 Lunar Zircons

In order to investigate the pre-3.9 Ga impact history of the Moon, it necessary to study samples which are older than the proposed terminal cataclysm and which can record signatures of impact bombardment. Lunar zircons are excellent candidates for this study for

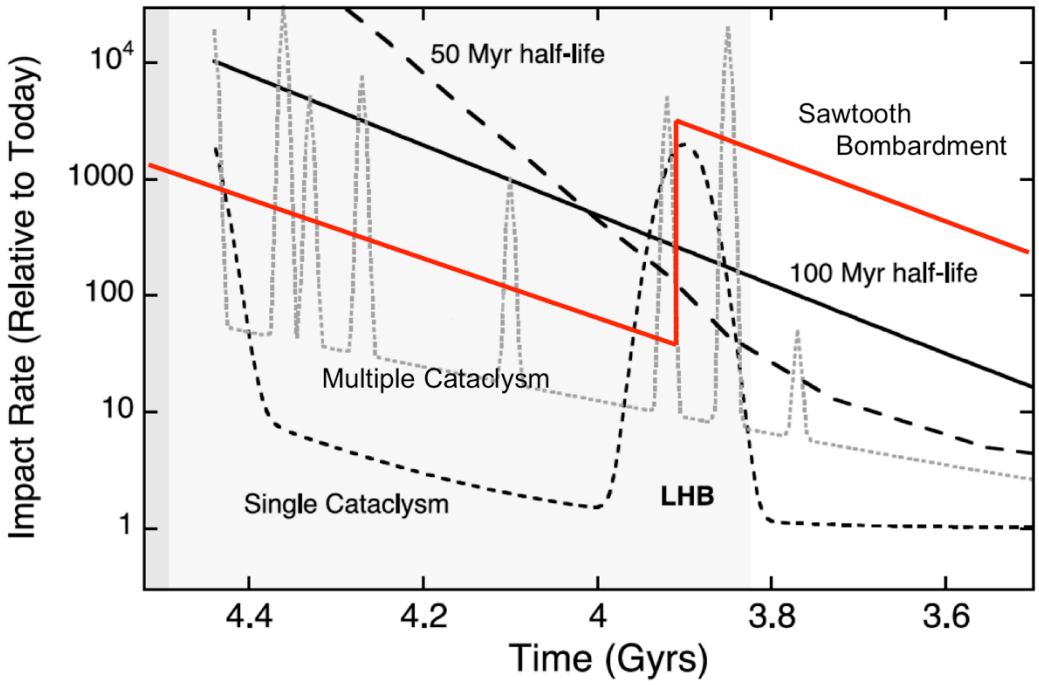


Figure 1-3: Modified figure from Zahnle et al. (2007) illustrating possible lunar impact histories that could explain the abundance of ~3.9 Ga degassing ages of lunar samples. The lunar zircons have crystallization ages pre-dating the proposed LHB and have been shown to record signatures of impact events making them idea for investigating the early lunar impact history.

multiple reasons, including their relatively old crystallization ages and their ability to retain structural and geochemical evidence of impact shock events.

Previous studies of zircons found in Apollo thin sections and in soils demonstrated that Pb-Pb crystallization ages for these minerals range between ~3.9 to 4.4 Ga (e.g. Meyer et al., 1996; Pidgeon et al., 2007; Nemchin et al., 2006, 2008; Taylor et al., 2009; Grange et al.,

2009, 2011). Most of these ages have been used to infer the timing of KREEP magmatism; however, in more recent studies the interpretations of some lunar zircon ages have been guided by microstructural observations such as those detailed in Grange et al. (2013) and Timms et al. (2012). Impact shock microstructures have been documented in zircons from terrestrial impact craters and in some cases Pb-loss associated with certain textures have been used to help confirm impact ages (Bohor et al., 1993; Krogh et al., 1993, 1996; Gibson et al., 1997a; Moser, 1997). Instances where zircons have undergone recrystallization or new growth due to an impact event are thought to provide some of the best constraints on the timing of impact events (Moser et al., 2011; Grange et al., 2013b). So far, only three lunar zircons with recrystallized regions have been identified, and their ages would suggest large impact events at ~ 4.1 and ~4.3 Ga (Nemchin et al., 2008; Grange et al., 2009, 20013b).

### 1.4 Apollo Landing Sites and Samples

The locations of the six Apollo landing sites are shown in Figure 1-1, and the sites which are represented by the samples herein (Apollo 14,15, and 17) are highlighted in yellow. Apollo 14 landed on the Fra Mauro Formation (Swann et al., 1971b) and samples from this mission are thought to contain both highlands material and ejecta from the Imbrium basin forming event thought to have occurred between 3770 and 3934 Ma (Deutsch and Stöffler, 1987; Stadermann et al., 1991; Dalrymple and Ryder, 1993; Shih et al., 1993; Liu et al., 2012; Merle et al., 2014). Apollo 15 sampled the edge of Mare Imbrium and the Apennine Mountains (eastern edge of Mare Imbrium). The samples from this landing site contain both mare and highlands material, which can be seen even within individual samples (Swann et al.,

1972). It is also worth mentioning the Apollo 14 and 15 landing sites are within the PKT terrain, which was discussed previously. Apollo 17 landed similarly on the edge of mare and highland terrains, and is located on the eastern edge of Mare Serenitatis. Like Apollo 15, the later Apollo 17 samples contain both highlands and mare material (Muehlberger et al., 1973).

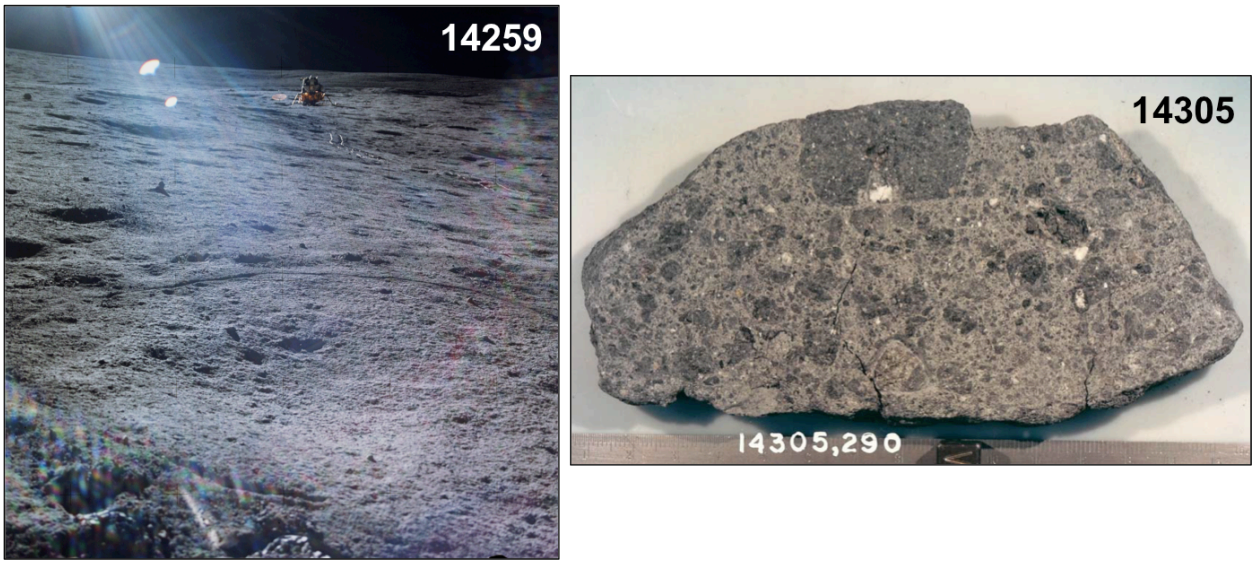


Figure 1-4: Two lunar samples used for the research reported in Chapters 2-4 illustrating the types of lunar materials included in our surveys. (Left) Image of sampling area for Apollo 14 soil 14259 (sampled from center of circle drawn in soil) with lunar module in the background. (Right) Apollo 14 breccia sample 14305 showing a range of darker clast material held together by a lighter gray matrix. Image Credit: NASA.

In considering chronological data obtained from Apollo samples, it is important to bear in mind that the vast majority of samples in the collection are breccias, not pristine rock fragments. Intensive bombardment of the surface has resulted in overturn of the top ~10 m of the lunar surface (Gault et al., 1974; Arnold, 1975). There are a few samples thought to be more pristine than others, however these samples too are breccias (e.g. Shervais et al., 1984; Shih et al., 1993). Also, based on their proximity to the large near side basins, all the Apollo

lunar samples to some extent, likely contain ejecta from Orientale, Imbrium, Serenitatis, and Nectaris basins to various extents (Heiken et al., 1991). Images of two samples representative of the suite used for the research reported herein are shown in Figure 1-4.

### 1.5 Overview of thesis

The research presented in this thesis utilizes isotopic, chemical, and microstructural data obtained on the lunar zircon population to investigate two facets of lunar history that remain to be well understood:

1. The timing and nature of KREEP magmatism.
2. The nature of the pre-3.9 Ga impact history, in particular the timing of the large basin forming impacts.

In this thesis, I present the results of coordinated analyses of individual zircons from samples collected by the Apollo 14, 15, and 17 astronauts. Chapters 2 and 3 present extensive surveys of U-Pb ages, trace element compositions, and impact shock microstructures for zircons extracted from both breccia and soil samples. With these large data sets, in addition to the previously published results, I place new constraints on the duration of KREEP magmatism and the large bolide flux on the early Moon. In these surveys, I also present analyses of Apollo 15 zircons, which up to now has been a poorly characterized population.

In Chapter 4, I investigate the application of the U-Pu-Xe in zircon chronometer to dating impact events. This chronometer has been only moderately studied in terrestrial zircons ( Shukoljukov et al., 1974; Teitsma et al., 1975; Krylov et al., 1993; Turner et al., 2007;

Shukolyukov et al., 2009) and has not been applied to impact environments. I present the first Xe isotopic analyses of individual lunar zircons and compare them with analyses of terrestrial analogues from the Vredefort impact structure in South Africa. The U-Xe analyses required that I synthesize and irradiate standard glass material, which allowed for the most precise measurement of Xe yields for neutron induced fission of $^{235}U$ currently reported.

In the conclusion chapter I revisit the goals of the coordinated lunar zircon analyses and detail how I have advanced our understanding of the early magmatic and impact histories of the Moon. I also suggest future work that will address remaining unanswered questions.

## Chapter 2: Ages and trace element distributions of Apollo 14, 15, and 17 zircons

### 2.1 Introduction

The lunar rock and crater record has been used to infer solar-system-wide parameters such as the ages of planetary surfaces and the dynamical evolution of the early solar system. Numerous studies have used the accessory mineral zircon to place constraints on the timing of the lunar magma ocean (LMO) crystallization, the duration of KREEP magmatism (LMO residual melt enriched in K, Rare Earth Elements, and P), and the ages of basin-forming impacts. Zircons are ideal geochronometers because they incorporate radioactive parents, such as U and Th, while preferentially excluding their daughter product Pb, allowing for precise U-Pb and Pb-Pb ages to be determined for individual grains (Hanchar and Hoskin, 2003). Zircons also incorporate other trace elements such as the rare earth elements (REEs) and titanium, which can give insight into the compositions and temperatures of their parent magmas (Hoskin and Schaltegger, 2003; Watson and Harrison, 2005). Microstructural studies of zircons from terrestrial and lunar impact sites have also found that certain types of shock deformation result in increased Pb mobility, and in the cases of the highest shock metamorphism, the ages of impacts can be determined (e.g. Krogh et al., 1996; Moser et al., 2011; Grange et al., 2013).

The lunar zircons analyzed to date have Pb-Pb ages that range from 3.9 to 4.4 Ga (e.g. Taylor et al., 2009; Grange et al., 2009, 2013), which mostly predate the hypothesized late heavy bombardment (LHB) (Tera et al., 1973). The ability of these grains to retain primary

crystallization ages in all but the highest degrees of shock metamorphism make them suitable for investigating the early magmatic history of the Moon. Additionally, the ability to identify shock textures suggestive of Pb-loss and age resetting makes them ideal for investigating the history of large impacts on the early Moon. Four large impacts have been previously proposed at ~ 3.9, 4.1, 4.2, and 4.3 Ga based on shock microstructural analyses and U-Pb ages of lunar zircons identified in Apollo thin sections (Nemchin et al. 2008; Grange et al. 2009, 2013; Norman and Nemchin 2014). Zircon trace element analyses have also been reported but are limited in numbers of analyses (Hinton and Meyer, 1991; Snyder et al., 1993; Wopenka et al., 1996; Taylor et al., 2009a; Nemchin et al., 2010).

We have conducted an extensive U-Pb, REE, and microstructural survey of Apollo zircons that, in combination with previous studies, represent a robust lunar zircon dataset from which we can draw constraints regarding the duration of KREEP magmatism, zircon formation mechanisms, and possibly the early impact history of the Moon. The focus of this chapter includes the age and trace element analyses; the microstructural survey is detailed in Chapter 3. Most previous zircon studies have focused on Apollo 14 and 17 samples. Here we report age analyses for 155 zircons from Apollo 14, 15, and 17 samples in addition to REE and Ti analyses for 90 of these zircons.

**2.2 Sample description**

Zircon grains were separated from three soil and six breccia samples, which were chosen based on high Zr content (see Appendix 1-1) and/or previously published zircon yields. All

lunar zircons discovered in Apollo thin sections to date are either detrital grains and not associated with co-crystallized material, or have textures suggestive of growth in an impact environment. A compositional understanding of the host rock from which the zircons were extracted does not provide petrographic information and is not imperative for this study. However, sample descriptions are provided here for completeness and include details of exposure ages and impact ages, which are informative for the U-Xe analyses reported in Chapter 4.

*14163 Soil*

Sample 14163 is a sub-mature soil collected nearby the Apollo 14 lunar module and is part of the lunar highlands suite reference material (Morris, 1978; Labotka et al., 1980). The soil has a large KREEP component and high percentage of glass (Labotka et al., 1980; Simon and Papike, 1981).

*14259 Soil*

Sample 14259 was collected from the top 1 cm of soil to the west of the Apollo 14 lunar module. The sample is a mature soil with a high concentration of agglutinates (McKay et al., 1972; Von Engelhardt et al., 1972) and carbon (Moore et al., 1972). The agglutinates in 14259 exhibit a Pb-loss discordia with a lower intercept between 0-300 Ma (Church et al., 1976). This recent Pb-loss event may be associated with formation of Cone Crater, which has been dated at 24.4 ± 1.1 Ma (Drozd et al., 1974) based on $^{81}$Kr-Kr spallation ages of Apollo 14 breccias. Tatsumoto et al. (1972) measured U-Th-Pb and Rb-Sr ages for a suite of Apollo 14 samples including 14259 and calculated Pb-Pb ages older than 4.75 Ga (obviously an

artifact of high cosmic ray exposure). Exposure ages of this sample were determined from the $^{236}U/^{238}U$ ratio and $^{126}Xe$ concentrations due to Ba spallation. These methods yield exposure ages of 450 Ma and 550 Ma respectively (Burnett et al., 1972; Fields et al., 1973).

*14304 Breccia*

Sample 14304 is a clast-rich impact melt breccia with a crystallized matrix (McGee et al., 1979). Shih et al. (1987) determined Rb/Sr ages of very high potassium (VHK) basalt clasts of 3.95 ± 0.04 and 3.99 ± 0.02 Ga, and they also measured a Sm/Nd age for VHK of 4.04 ± 0.11 Ga. However, Snyder et al. (1995) found older Rb/Sr and Sm/Nd ages for alkali anorthosite clasts of 4.336 ± 0.081 and 4.108 ± 0.053 Ga respectively.

*14305 Breccia*

Sample 14305 is a Fra Mauro breccia collected near the Apollo 14 lunar module. Like 14304, this sample is a clast-rich, crystalline matrix breccia with ~30% lithic clasts >1 mm (Wilshire and Jackson, 1972). This breccia has high concentrations of both KREEP and meteoritic material (Wanke et al., 1972; Palme et al., 1978), and highland gabbroic anorthosite, pink spinel, apatite and zircons have all previously been identified (Dence and Plant, 1972; Lovering et al., 1972).

This breccia is thought to have turned over or tumbled based on the distribution of cosmogenically produced $^{26}Al$ and $^{53}Mn$ on either side of the sample (Herpers et al., 1973). The $^{81}Kr$-Kr exposure age of 14305 is 27.6 ± 1.5 Ma (Eugster et al., 1984), while the Ar-Ar and Sm-Nd ages are ~3.9 Ga (Eugster et al., 1984; Shih et al., 1986). The Rb-Sr analyses

yield both a young whole rock age of 3.83 ±0.08 Ga and an older clast (olivine gabbronorite) age of 4.23 ± 0.05 Ga (Taylor et al., 1983; Shih et al., 1986). Three papers have previously reported U-Pb and Pb-Pb ages of zircons from 14305, with ages ranging between 3.97 and 4.35 Ga (Hinton and Meyer, 1991; Nemchin et al., 2008; Taylor et al., 2009).

*14321 Breccia*

This sample, also known as Big Bertha, was collected from the edge of Cone Crater and is thought to be part of the Fra Mauro Formation (Swann et al., 1971a, 1977; Wilshire and Jackson, 1972). Big Bertha is a clast-rich (about 30%), crystalline matrix breccia that contains anorthositic clasts considered pristine based on their very low Ir concentrations (Simonds et al., 1977; Warren et al., 1981). Sample 14321 also contains low-Ti, aluminous mare basalt clasts (Taylor et al., 1972). The REE patterns for these clasts are different than other mare basalts in that they do not exhibit the characteristic middle REE enrichment observed KREEP samples (Dickinson et al., 1985; Shervais et al., 1985).

There have been multiple dating studies on both clasts and matrix from sample 14321. Basalt clasts yield Rb-Sr ages ranging from 3.95 ± 0.04 to 4.33 ±0.12 Ga (Papanastassiou and Wasserburg, 1971; Dasch et al., 1987), while Ar-Ar gives younger ages from 3.83 to 3.94 Ga (York et al., 1972). There have been two studies of the exposure ages of this sample 14321: 24 ± 2 Ma by the $^{38}$Ar method and 27 Ma by the $^{81}$Kr method (Burnett et al., 1972; Lugmair and Marti, 1972). Burnett et al. (1972) interpret this to be the age of Cone Crater, near which the samples were collected.

Small zircons were identified in multiple thin sections by Grieve et al. (1975). Braddy et al. (1975) measured U concentrations of 93 zircons from sample 14321 counting fission tracks. The U concentrations ranged from 15-400 ppm with a median concentration of 50 ppm. Meyer et al. (1996) measured the zircon U-Pb ages of three zircons by sensitive high-resolution ion microprobe (SHRIMP). Two grains from a granitic clast give ages of 3956 ± 3 Ma (1σ) and 4004 ± 2 Ma (1σ), and the third zircon, found in sawdust, has an age of 4010 ± 2 (1σ) Ma. Another 29 zircons from 14321 sawdust and two from a thin section were measured by Nemchin et al. (2008, 2006). The $^{207}$Pb-$^{206}$Pb ages range between 3.89 to 4.40 Ga. Nemchin et al. (2006) also measured the oxygen isotopes of 14 of these zircons and found their $\delta^{18}$O to be within error of terrestrial mid-ocean ridge basalts. Taylor et al. (2009) reported $^{207}$Pb-$^{206}$Pb ages and Lu-Hf isotopes of 8 zircons from 14321 rock cuttings. The zircon ages ranged from 3987 ± 14 to 4282 ± 15 (1σ) Ma, which is consistent with previous studies. They also reported initial $^{176}$Hf/$^{177}$Hf ratios that suggest an age for the separation/formation of the KREEP reservoir of 4.478 ± 0.046 Ga (1σ).

*15311 Soil*

Soil 15311 is a rake sample collected in conjunction with soil 15301 as a part of a larger suite that collected material from the rim of Spur Crater, a small ~100 m crater on the edge of the Apennine front. The Apennine Mountains are located on the southeastern edge of the Imbrium basin and are thought to have formed partially due to uplift from the basin-forming impact (Swann et al., 1972; Heiken et al., 1991). Soil 15311 has significant amounts of green glass (Morris et al., 1983) and REE compositions suggestive of a KREEP basalt component

(Korotev, 1987). Dalrymple and Ryder (1991, 1993) measured the Ar-Ar degassing ages of five fragments of impact melt rocks separated from the soil ranging from 3858 ± 16 Ma to 3881 ±17 Ma. From these ages they infer an age of 3.87 Ga for the Imbrium basin forming impact.

*15405 Breccia*

Sample 15405 is a KREEP-rich breccia collected from a large boulder ~250 meters from Spur Crater (Swann et al., 1972). The clast population is dominated by KREEP basalt, with a few quartz monzodiorite (QMD), granite, and other clasts.

There were multiple attempts to measure the age of 15405, but only Ar-Ar and U-Pb methods were successful. A QMD clast gives a $^{39}$Ar-$^{40}$ Ar age of 1.29 ± 0.04 Ga (Bernatowicz et al., 1978), which is in agreement with the lower intercept of the U-Pb concordia diagram for zircons in the QMD clast. The two concordia intercepts are 4.294 ± 0.026 and 1.320 ± 0.250 Ga (Meyer et al. 1996). The older age is interpreted as the age of zircon formation and the younger age is thought to be the breccia formation age.

*15455 Breccia with Shocked Norite*

Sample 15455 was also collected from the rim of Spur Crater and consists of older shocked norite surrounded by a younger impact melt dark breccia. Shih et al. (1993) measured Rb/Sr and Sm/Nd ages of 4.59 ± 0.13 and 4.53 ± 0.29 Ga for norite clasts. Both the dark matrix and norite clasts have younger Ar-Ar ages of 3.94 ± 0.04 Ma and 3.82 ± 0.04 Ma respectively

(Alexander, Jr. and Kahl, 1974). The rock fragments obtained for this study contain both lithologies.

*72275 Breccia*

Sample 72275 is a feldspathic breccia that possibly represents ejecta from Serenitatis basin (Dalrymple and Ryder, 1996). This breccia has a high abundance of KREEPy non-mare basalt, and as a result has high concentrations of trace elements (Blanchard et al., 1975). Shih et al. (1992) also reported Rb-Sr and Sm-Nd ages for a KREEP basalt clast of 4.31 ± 0.08 and 4.08 ± 0.07 Ga respectively. These ages are ~ 200 My older than Apollo 15 KREEP basalts (e.g. Nyquist et al., 1973, 1975). Zircons previously measured from 72275 range in $^{207}$Pb-$^{206}$Pb age from 4.24 to 4.42 Ga (Nemchin et al., 2008, 2009).

## 2.3 Analytical Techniques

### *2.3.1 Sample Preparation*

Our sample preparation techniques follow those outlined in Taylor et al. (2009), in which zircons were mechanically separated from breccia and soil samples. The extraction of grains does not allow for petrologic context to be determined, but most lunar zircons identified in thin sections to date are detrital and not associated with material representative of parent magma composition. The advantage of the separation technique is it allows for larger numbers and sizes of zircons to be recovered.

Breccia samples were crushed by hand in an agate mortar, processed by standard heavy-liquid (methylene iodide [MI]) mineral separation, filtered, rinsed with acetone and allowed to dry. Soil samples were processed using the same method, except the soils were subjected to heavy-liquid separation before being crushed, and then processed a second time after crushing to maximize zircon yield. The high-density separate of each sample was then searched under an optical microscope using ultraviolet light because non-metamict zircons have been shown to fluoresce (Foster, 1948). After hand-picking, zircons were positively identified using energy-dispersive X-ray spectroscopy (EDS) in the UCLA Tescan Scanning Electron Microscope (SEM) and mounted in epoxy rounds. Each round was minimally polished using silicon carbide disks to expose a flat surface of the zircon necessary for SEM imaging and SIMS analyses. Maximizing retention of material during this step was a necessity for later noble gas analyses (see Chapter 4).

### *2.3.2 SEM and SIMS Measurements*

All mounted zircons were characterized by secondary electron (SE), backscattered electron (BSE) and cathodoluminescence (CL) images to look for primary zoning, inclusions, fractures, and recrystallization textures. A selection of the samples were also analyzed by electron backscatter diffraction (EBSD) at the Zircon and Accessory Phase (ZAP) Lab at the University of Western Ontario to search for evidence of recrystallization and other shock features (see Chapter 3). Prior to SIMS analyses, sample mounts were cleaned using a multistage ultrasonic bath protocol (ultrasonic cleaning solution, deionized water, 3N HCl, methanol) to reduce surface contamination. The mounts were then gold coated.

U-Pb and rare earth elements (REEs) were measured with the UCLA CAMECA *ims*1270 ion microprobe during multiple sessions between 2009 and 2014. U-Pb ages, Pb-Pb ages and U concentrations were measured with ~20-40 μm spots using the protocols described in Mojzsis et al., (2003). Ages and concentrations were calibrated against the AS3 zircon age standard and 91500 zircon U standard (Paces and Miller, 1993; Wiedenbeck et al., 2004). A $^{204}$Pb correction was made to account for common Pb contamination, but in most cases $^{204}$Pb was not detected. All of the lunar zircons have Pb that is above 97% radiogenic and the majority of grains are ≥99% radiogenic, so the U-Pb and Pb-Pb ages reported here are not affected by choice of using either a terrestrial Pb or lunar Pb isotopic compositions for the $^{204}$Pb correction (Taylor et al., 2009a).

Trace elements, including REE, Ti, Hf, Th, U, and Fe were measured in peak switching mode, following the protocol described by Bell and Harrison (2013). Sensitivity factors were calibrated using a combination of four NIST standard glasses and 91500 zircon standard. Ti temperatures were calculated using the revised Ti-in-zircon thermometer of Ferry and Watson (2007). Further discussion of assumptions for this calculation can be found in sections 2.4.2 and 2.5.2.3.

NanoSIMS analyses were also undertaken at the Lawrence Livermore National Laboratory to investigate the trace element and Pb contributions of impact melt glass inclusions. The new Hyperion II ion source allowed us to achieve a 2x3 μm spot size using a 600 pA $^{16}O^-$ primary beam. The beam was rastered over a 13 μm box, and data were collected in mapping mode from the inner 10 μm in order to exclude edge effects. A combination of multi-collection on

five electron multipliers and magnet cycling were used for the analyses. This was necessary because Fe and Pb could not be measured using the multi-collection system alone. AS3 was used to determine the instrumental U-Pb relative sensitivity factor, however no standard analysis of NIST610 was conducted, so the NanoSIMS Fe maps represent only relative concentrations.

## 2.4 Results

We recovered 117 zircons from Apollo 14 samples, 42 zircons from Apollo 15 samples, and 12 from the Apollo 17 sample. Figure 2-1 compares a typical zircon from the Moon with a terrestrial zircon of a similar age from Jack Hills, Australia. Lunar grains differ from their terrestrial counterparts in that lunar zircons are rarely euhedral except for grains with granular texture recrystallization (see section 2.5.1.1 and the discussion in Chapter 3). CL imaging of the lunar grains also suggests the majority are fragments of larger original zircons fragmented during subsequent impact events.

### *2.4.1 U-Pb and Pb-Pb Ages*

We measured U-Pb and Pb-Pb ages for 155 of the lunar zircons; the data are reported in Table 1 and shown as histograms in Figure 2-2. We note that some small zircons were lost during removal of coatings or polishing between imaging and SIMS analyses, and for these grains we have only images and/or trace element analyses, but no age information. Apollo 14 zircons exhibit the largest range in Pb-Pb ages spanning from 3942 ± 9 to 4408 ± 3 Ma (1σ), where as Apollo 15 and 17 zircon ages are between 4101 ± 14 Ma and 4378 ± 10 Ma (1σ).

Despite the variation in the range of Pb-Pb ages, all of the landing sites show a large abundance of grains with ages between 4320 and 4350 Ma; 80% of Apollo 17 zircons, ~50% of Apollo 15, and ~20% of Apollo 14 zircons analyzed fall within this age range. Most of the

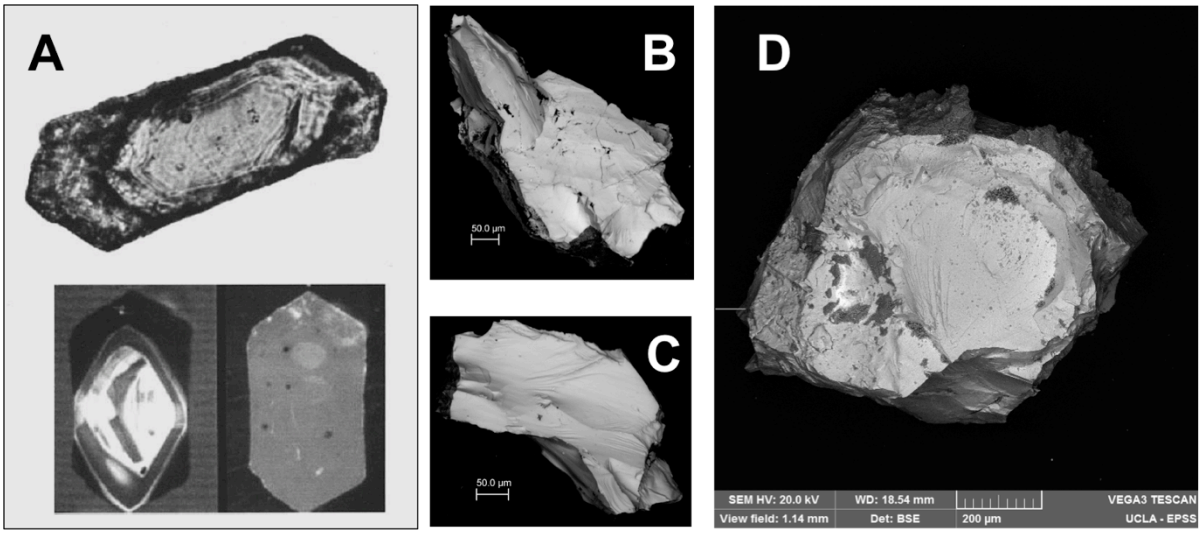


Figure 2-1: (A) Example of ancient terrestrial Hadean zircon from Jack Hills, Australia (Hoskin, 2005). Un-mounted grain shows euhedral core and altered rim (top), which is also visible in CL images (bottom left). The euhedral nature of the zircon is easily visible in a BSE (bottom right). SE images of typical lunar zircons prior to mounting in epoxy (B & C) illustrate the fragmented nature of the majority of lunar zircons. All lunar zircons are fragments of much lager original crystals. Even the larger zircon recovered in this study, ~900 μm in diameter, is a fragment of a larger parent zircon (D).

zircons are concordant within the errors of our analyses, suggesting relatively simple, closed-system behavior of the U-Pb age systems, but ~6% of the grains do show clear evidence of either Pb-loss (defined here as discordance exceeding 10%) or multiple age domains.

*2.4.2 REE and Ti Temperatures*

We collected 102 measurements of REE, Ti, Hf, Th, U, and Fe concentrations for 90

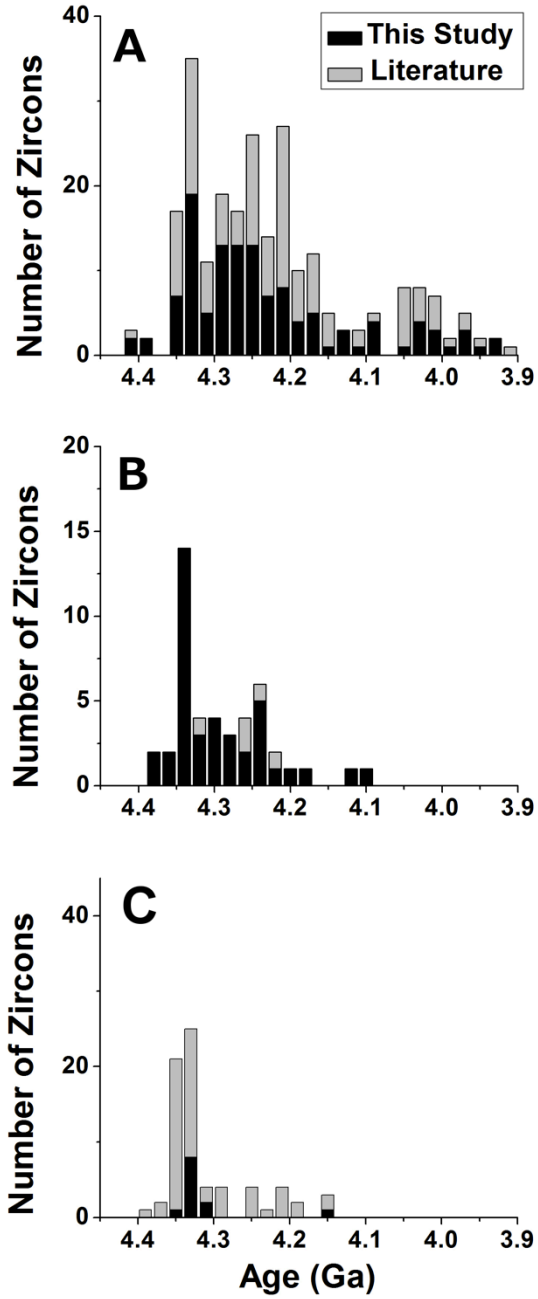


Figure 2-2: $^{207}Pb$-$^{206}Pb$ age histograms of Apollo 14 (A), 15 (B) and 17 (C) zircons (black – this study and Taylor et al. 2009; grey – literature data). These ages are considered lower limits on crystallization ages, so for zircons with multiple age analyses, only the oldest age is included in the histogram. Apollo 14 zircons span the full range of ages from 3.9 to just over 4.4 Ga, while all but one zircon from Apollo 15 and 17 are older than 4.1 Ga. The age distributions for the latter are also dominated by zircons between 4.30 and 4.35 Ga. This peak is less pronounced in the Apollo 14 data where the majority of zircons are between 4.2 and 4.35 Ga. (Apollo 14 – 307 zircons, Apollo 15 – 52 zircons, Apollo 17 – 76 zircons).

Apollo 14, 15, and 17 zircons. We filtered the results to remove analyses that included impact melt glass by inspection of SIMS analysis pits with SEM imaging (37 zircons) and by excluding measurements with anomalously high Fe concentration (17 zircons). The remaining pristine lunar zircon analyses can be characterized by one basic REE pattern, which varies in overall REE concentration between grains. In addition to the analyses reported herein, we reanalyzed the trace element data reported in Taylor et al. (2009) with the same set of criteria and filtered 16 of the 37 analyses (34 zircons) due to apparent impact melt glass contributions. The remaining pristine zircon measurements from Taylor et al. (2009) are consistent with the same REE pattern reported herein. The REE for both sets of analyses are shown in Figure 2-3, and trace element data for pristine analyses can be found in Appendix 3. All the zircons exhibit a steep positive slope with LREE depletion and large negative Eu anomalies.

The concentration of Ti in zircon has been shown to be a function of crystallization temperature, and the activities ($a$) of $SiO_2$ and $TiO_2$ in the melt (Watson and Harrison, 2005; Ferry and Watson, 2007), with relatively little to no influence from variations in pressure or $fo_2$ (Burnham and Berry, 2012; Ferriss et al., 2007). We calculated the Ti-in-zircon temperatures following the revised relationship of Ferry and Watson (2007):

$$\log\left(\frac{\left(Ti(ppm)\right)_{Zr}\cdot\left[a_{TiO_2}\right]_{Melt}}{\left[a_{SiO_2}\right]_{Melt}}\right)=\left(5.711\pm0.072\right)+\left(\frac{-4800\pm86}{T(K)}\right) \qquad (2.1)$$

Where $(Ti(ppm))_{Zr}$ is the concentration of Ti in zircon in (μg/g), $[a_{SiO2}]_{Melt}$ and $[a_{TiO2}]_{Melt}$ are the activities of $SiO_2$ and $TiO_2$ in the melt, and T is temperature in (K). We determined best

estimate values of $a_{SiO2} = 0.6$ and $a_{TIO2} = 0.25 \pm 0.05$ based on compositions of urKREEP from Warren and Wasson (1979) and KREEP-rich granite and quartz monzodiorite clasts from Apollo samples. More details on the methods for determining oxide activities can be found in section 2.5.2.3.

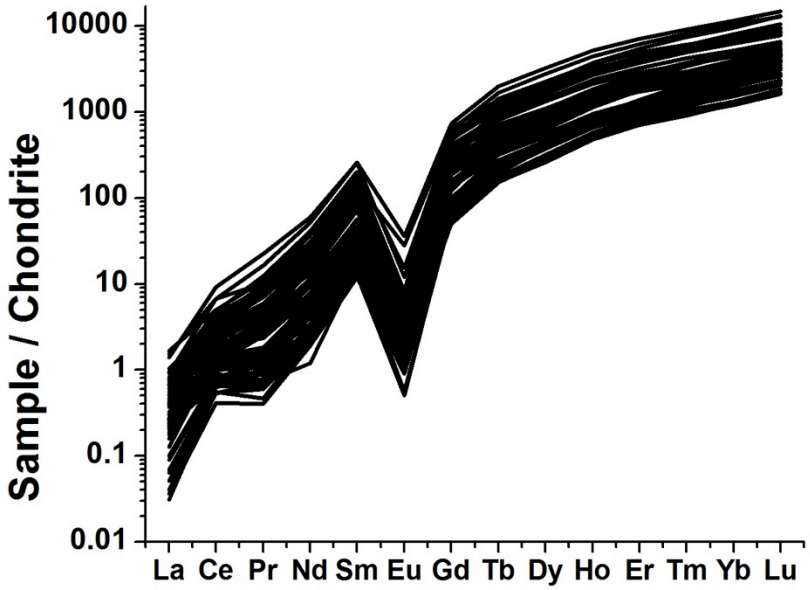


Figure 2-3: Chondrite normalized REE patterns for 38 zircons from this study and 21 zircons from Taylor et al. 2009. Analyses with Fe concentrations >400 ppm or visible sources of contamination were excluded. The zircons can general be described by one REE pattern with varying total concentrations. The pattern has a steep positive slope resulting from the zircon trace element partition coefficients, and all zircons have a negative Eu anomaly.

## 2.5 Discussion

### *2.5.1 U-Pb and Pb-Pb Ages: What are they dating?*

The distinct decay chains of $^{238}U$ to $^{206}Pb$ and $^{235}U$ to $^{207}Pb$ provide an important advantage as a chronometer of ancient samples. Following crystallization, if a sample experiences subsequent Pb-loss, both daughter isotopes will be lost with equal probability. If the Pb-loss

event is recent, then the Pb isotopic ratio remains unchanged and a $^{207}$Pb-$^{206}$Pb age can be computed and the open system behavior is recognized by discordance in the respective $^{238}$U/$^{206}$Pb and $^{235}$U/$^{207}$Pb ages. In the case of an ancient partial Pb-loss event, however, it can be difficult to recognize discordance in SIMS analyses with relatively large uncertainties in individual $^{238}$U/$^{206}$Pb and $^{235}$U/$^{207}$Pb ages due to uncertainties in inter-element relative sensitivity factors (average 1$\sigma$ is ~180 Ma for $^{207}$Pb-$^{235}$U age, and ~60 for $^{206}$Pb-$^{238}$U age). But even in such a case, the $^{207}$Pb-$^{206}$Pb age can be strictly interpreted as a lower limit on either the crystallization age of the sample or the time of last total Pb-loss.

On Earth, Pb-loss in zircons is facilitated by interactions with fluids or by metamictisation due to structural damage from U decay. The latter forms amorphous regions in crystals that provide accelerated diffusion pathways for Pb loss as they are easily infiltrated by fluids (e.g. Mezger and Krogstad, 1997). Despite recent findings of high OH contents in late-crystallizing phases, the lunar crust is dry (Boyce et al., 2014). Additionally, the majority of lunar zircons have U concentrations bellow 100 ppm, which is not high enough to cause appreciable amounts of metamictisation, so these two processes are not likely mechanisms for Pb-loss in zircons from the Moon (Wopenka et al., 1996; Garver and Kamp, 2002). This is also supported by the high crystallinity (i.e good band contrast) observed in electron backscatter diffraction analyses (EBSD) discussed in Chapter 3. Impacts are the dominant geologic alteration process on the surface of the Moon and are therefore the most likely source of U-Pb system disturbances.

In terrestrial impact structures zircons that have recrystallized, or contain structural damage in the form of crystal plastic deformation, show evidence of Pb-loss (post impact hydrothermal alteration can also cause Pb-loss, but this is not applicable to the Moon) (e.g. Moser et al., 2011). Grange et al. (2013) presented guidelines for interpreting lunar zircon U-Pb and $^{207}$Pb-$^{206}$Pb ages based on microstructural investigations of SEM and EBSD imaging. They suggest that the $^{207}$Pb-$^{206}$Pb ages of zircons are fully reset in the cases of zircon growth or recrystallization in an impact setting. They also observed variable amounts of Pb-loss in certain zircon grains wherein post impact strain caused high degrees of crystal plastic deformation. In these cases both the igneous crystallization ages and impact ages could be constrained. This is also true for grains that the show other types of open-system behavior such as discordant analyses or multiple concordant age domains. When there is no microstructural evidence of open-system behavior, the $^{207}$Pb-$^{206}$Pb ages can be used to place lower limits on the zircon igneous crystallization age.

*2.5.1.1 Overview of Age Distributions*

The distributions of the $^{207}$Pb-$^{206}$Pb ages for Apollo 14, 15, and 17 zircons reported herein agree well with previously reported ages of lunar zircons (summed histograms are shown in Figure 2-2) (Charles et al. 1996; Pidgeon et al. 2007; Nemchin et al. 2006; Nemchin et al. 2008; Taylor et al. 2009; Grange et al. 2009, 2013). Nemchin et al. (2008) observed that there is no variation in zircon age distributions among samples within a given Apollo landing site and concluded that it is appropriate to analyze summed, or composite, histograms of all zircons from a landing site. We therefore present the age histograms of zircons grouped by Apollo mission in Figure 2-2.

The age distributions are similar in that all three landing sites have a marked peak around ~4.33 Ga with relatively few zircons forming before this time. This could simply reflect the time at which zircon saturation was reached in residual KREEP magmas, or the ~ 4.33 Ga peak could represent a large zircon-forming event related to either LMO crystallization processes (such as mantle overturn) or a large impact basin (such as South Pole Aitken) (e.g. Elkins Tanton et al., 2002). Other than this peak, the age distributions vary between landing sites. Most notable is the lack of pre-4.1 Ga zircons from Apollo 15 and 17 samples, however the sample sizes for these two sites are much lower than that of Apollo 14.

We employed a Mann-Whitney U-test to determine if the variations between landing sites are statistically significant. This test compares the rank-sums of two samples to determine if they are sampling the same parent population (the Null hypothesis) (Mann and Whitney, 1947). Because we compared the differences among all three landing sites, we also applied a Bonferroni correction to account for multiple comparisons (Rice, 1989). This correction states that the probability for individual tests must be less than the desired significance level divided by the number of tests performed. This means that if we want to determine if the age distributions are statistically different to a significance level of 0.05, the probability of the Null must be less than 0.017 for each Mann-Whitney U-test. The probabilities that Apollo 15 and 17 are sampling the sample age distribution as Apollo 14 are both <0.0003, therefore we reject the null hypothesis that the Apollo zircons are sampling the same distribution. However, a similar comparison between Apollo 15 and 17 yields a probability of 0.022, which is not below 0.017, and therefore we fail to reject the null hypothesis; based on the age data, they could be sampling the same parent population.

Only ~10% of the lunar zircons are in the <4.1 Ga population, and most contain impact growth textures, have small grain sizes (most are <50 μm), or exhibit open system behavior. Previously reported Apollo 12 zircons also yield ages that are < 4.1 Ga (Meyer et al. 1996; Zhang et al. 2012). Similar to the Apollo 14 zircons, the younger grains from Zhang et al. (2012) exhibit microstructural textures that have been associated with age resetting or the grains are relatively small. The Apollo 12 and 14 landing sites are geographically close to each other (Figure 1-1), while Apollo 15 and 17 are located on the rims of Imbrium and Serenitatis basins respectively. One notable difference is Apollo 12 and 14 landing sites are thought to sample Imbrium ejecta, which has an estimate age between 3750 and 3938 Ma based on Rb-Sr, K-Ar, and Sm-Nd of Apollo 14 rocks and U-Pb ages of zircons and phosphates from similar samples (e.g. Deutsch and Stöffler, 1987; Shih et al., 1987; Stadermann et al., 1991; Liu et al., 2012; Merle et al., 2014). Imbrium eject could be the source of the younger, < 4.1 Ga zircon population either through Pb-loss and/or recrystallization during the impact event or through excavation of younger material that is not sampled by Apollo 15 and 17. A dedicated investigation of the younger zircon population would help in determining the extent of Imbrium influence on these samples. In the following two sections we will discuss the how the lunar zircons can be used to infer both impact and igneous crystallization ages.

*2.5.1.2 Impact Ages*

As previously mentioned there are multiple ways proposed to identify impact grown or altered zircons. Zircons that exhibit skeletal and granular texture are thought to have crystallized or recrystallized as a result of impacts. In terrestrial settings these grains are

associated with 80% to 100% Pb-loss with lower Concordia intercepts consistent with the age of the impact responsible for the growth or recrystallization (Moser et al., 2011). For this reason, ages of recrystallized regions of lunar zircons are interpreted as impact ages, and are often thought to yield the most reliable ages in both terrestrial and lunar impact settings. Additionally, if multiple analyses on a single zircon grain reveal multiple age domains or discordant analyses, it is possible to put limits on both crystallization and resetting ages (Grange et al., 2013b). Exact impact ages cannot be determined this way due to the difficulty constraining timing of ancient Pb-loss, as discussed in the previous section.

We measured the Pb-Pb ages of two granular texture zircons from breccia 15455 and one from soil 14259 (images are located in Appendix 3-2). One analysis of 15455 Z24 gives an age of 4332 ± 3 Ma (1σ) and two analyses of 15455 Z3 give ages of 4322 ± 4 and 4331 ± 3 Ma (1σ). These grains have a slight apparent reverse discordance due to small baddeleyite cores in some of the granules (affecting calibration of U/Pb relative sensitivity factors). The reverse discordance is a result of matrix effects from inclusion of both zircon and baddeleyite in analysis spots and is therefore an artifact of the SIMS analyses. Together, these two grains suggest an impact event at ~4.33 Ga, which could be related to an impact previously proposed to have formed the skeletal zircon from sample 73217 (Nemchin et al., 2008; Grange et al., 2009). This grain has weighted average $^{207}$Pb-$^{206}$Pb age of 4333 ± 5 Ma. Grange et al. (2013b) reported a second skeletal zircon from related sample 73215 that shows a spread of ages between 4305 and 4378 Ma. They suggested the zircon formed in an initial impact at ~4.38 Ga and underwent later Pb-loss at 4.31 Ga, but it is uncertain if these events are related to the impacts suggested by the Apollo 15 grains.

It is interesting to note the timing of some impact events coincides with the ~4.33 Ga peak seen in the age distributions of all three landings sites. It is difficult to determine if this suggests an impact trigger for a large, zircon-forming event from only a few zircons ages. It is equally likely that the coincidence may just stem from the paucity of pre-4.35 Ga zircons and the necessity to have pre-existing zircon grains to form granular recrystallization textures seen in the 15455 zircons. We also collected two analyses of granular soil zircon 14259,664 Z24 that both gave a concordant age of 4195 ± 7 Ma. This is age is similar to the 4.2 Ga basin forming age proposed based on zirconolite and apatite grains in Apollo sample 67955 (Norman and Nemchin, 2014).

In addition to textural analyses, evidence of age resetting can be identified in grains that exhibit open system behavior. In these cases of discordant analyses, the upper intercept is interpreted at the lower limit of the magmatic crystallization age and the lower intercept is thought to represent the upper limit on a Pb-loss event, which could be an impact age. Other zircons may contain multiple concordant Pb-Pb age domains that are not correlated to episodic igneous growth or impact recrystallization. These variations have generally been attributed to impact resetting with the oldest and youngest ages putting constraints on the crystallization and impact age respectively (e.g. Zhang et al., 2012). Only 6% of the grains we analyzed produced discordant analyses or revealed multiple age domains.

Seven of the Apollo 14 zircons, two Apollo 15 and one Apollo 17 zircon have U-Pb discordance greater than 10%. The discordant Apollo 14 soil and breccia grains appear to have experienced a recent Pb-loss event. Five analyses of the individual zircon 14321 Z14

define a discordia line with a lower intercept of 227 ± 360 Ma. The 14259 soil zircons also follow a similar trend with a Pb-loss event in the last 300 Myr. A similar event has also been noted in agglutinates from this soil sample (Church et al., 1976). Both Apollo 14 samples were collected close to the edge of Cone Crater (which is dated at 24.4 ± 1.1 Ma), so the Pb-loss in these grains could be due to high, post impact, temperatures (Drozd et al., 1974). The two discordant analyses of Apollo 15 zircons did not produce reliable intercept ages, but three analyses of 72275 Z1 define a discordia with a lower intercept of 245 ± 310 (1σ) Ma.

We collected multi-spot analyses for 26 zircons, and of these four show variations in the concordant ages outside of the 2σ errors. Most notable are grains 15311,18 Z6 and 14259,664 Z1. EBSD analyses of the former reveal that this grain is almost completely amorphous and crosscut by a complex pattern of planar and curviplanar features (see Chapter 2). Despite being almost fully amorphous, it does retain relatively old $^{207}$Pb-$^{206}$Pb ages ranging from 4245 ± 4 to 4332 ± 3 (1σ) Ma. These data suggest a lower limit on crystallization of 4.33 Ga and an upper age limit of Pb-loss of 4.25 Ga. The second grain, 14259,664 Z1, is ~900 μm in diameter (the largest zircon we have analyzed to date) and appears to be a fragment of an even larger parent zircon based on CL zonation. The Pb-Pb ages of this zircon span from 4075 ± 8 to 4313 ± 8 (1σ) with only slight discordance in a few analyses. The younger ages appear to be associated with cracks that may have served as pathways for increased Pb-loss during a thermal event; the upper age limit of which is 4.08 Ga. Here we stress again that multiple age domains and discordance can only be used to

place limits on impact ages, and impact grown or recrystallized zircons yield the most robust determination of impact ages.

In addition to the impact ages discussed above, two other impact events have previously been proposed based on lunar zircon ages. Grange et al. (2009) reported a $^{207}Pb$-$^{206}Pb$ age of 3929 ± 10 Ma for a granular texture zircon reaction rim surrounding a baddeleyite grain in sample 73217, and interpret this as an impact event at ~ 3.93 Ga. They also identified another grain, the "Tiger" zircon from 73235, which contains a recrystallized region with an age of 4106 ± 18 Ma. Our results combined with previous studies are shown in Figure 2-4 and provide strong evidence for large impacts, possibly basin forming events, occurring at least as often

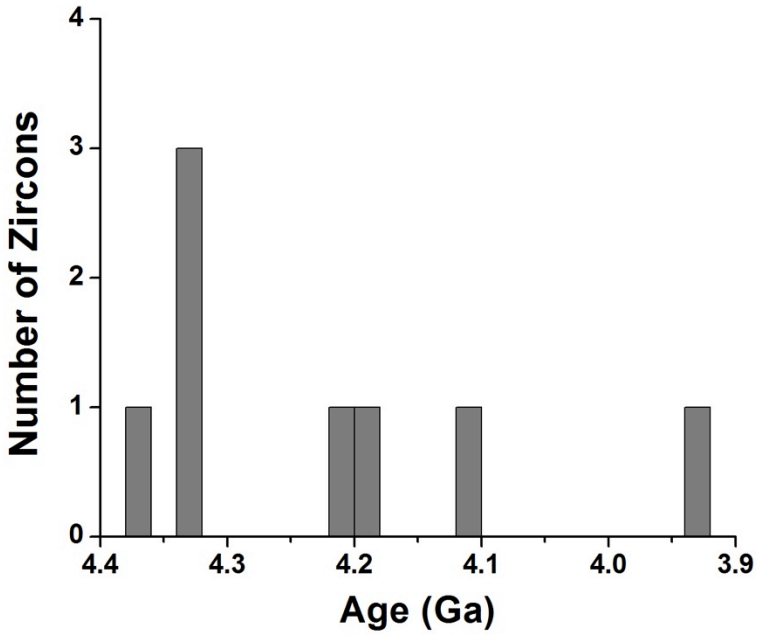


Figure 2-4: Histogram of ages of impact grown lunar zircons and associated mineral phases. These ages suggests large impacts at least as often as 100 Myr on the Moon during the pre-Late Heavy Bombardment era. See text for references.

as every 100 Myr after the initiation of zircon formation around 4.4 Ga. Additionally, the histogram of lunar zircon data in Figure 2-4 is not consistent with a late heavy bombardment at ~3.9 Ga.

*2.5.1.3 Igneous Crystallization Ages*

While zircons with impact growth textures (such as granular texture further discussed in Chapter 3) or open system behavior are useful in constraining the ages of impact events, they only make up a small percentage of the grains we analyzed. For the majority of the zircons reported herein, we find no textural evidence of recrystallization or deformation consistent with measurable Pb-loss, and their U-Pb ages are concordant. We therefore interpret their $^{207}$Pb-$^{206}$Pb ages as lower limits on magmatic crystallization ages. Even in the cases of open system behavior discussed above, the oldest age or Concordia intercept can still be interpreted as a limit on the crystallization age.

The age histograms that we find for Apollo 14, 15, and 17 zircons agree with previously reported ages, and 90% of the all zircon are older than 4.1 Ga while >90% of Apollo 15 and 17 grains are older than 4.2 Ga (Figure 2-2). All of the lunar zircons we analyzed are fragments of much larger zircons, and they range in size from ~20 to 900 μm. Primary igneous growth zoning, seen in CL images, suggests that some of these fragments came from zircon crystals larger than a millimeter in length. Zircons grown in terrestrial impact structures tend to be only a few 10s to 100 μm in length, which is much smaller than the original, parent lunar zircons (e.g. Moser et al., 2011; Wielicki et al., 2012). A magma that is highly enriched in zirconium is necessary to produce millimeter-sized zircons, and KREEP

magmatism is the most likely source for such highly enriched parent melts on the Moon. The majority of lunar zircons have concordant Pb-Pb ages older than 4.1 – 4.2 Ga suggesting that zircon producing magmatism had predominantly ceased by this time. If zircons were forming in KREEP-rich magmas, this suggests a maximum 200 - 300 Myr interval of KREEP magmatism, which is shorter than 3.9- 4.4 Ga span previously proposed based on the full range of zircon $^{207}$Pb-$^{206}$Pb ages (Meyer et al., 1989, 1996a).

Nemchin et al. (2008) proposed two explanations for the difference between Apollo 14 and 17 zircon age distributions. The first invokes contraction of a single KREEP reservoir towards the Procellarum KREEP terrain (PKT). In this scenario, zircon-producing magmatism spans a longer duration of time because it is closer to the center of the contracting PKT. The second explanation infers multiple pulses of KREEP magmatism triggered by large impacts, however identifying zircons produced in impact induced igneous systems as opposed to the last dregs of lunar magma ocean crystallization is difficult. Neither the single source or multiple parent magma scenarios can be ruled out by age alone, but paired trace element analyses may give more insight into the nature of early KREEP magmatism.

*2.5.2 Trace Elements*

Zircons incorporate ppm to wt% concentration levels of trace elements such as U, Th, Hf, REEs, and Ti (see Appendix 2-3 for trace element analyses of zircons in this study). The absolute and relative abundances of these elements have been used to infer aspects of zircon provenance, such as magma compositions, temperature, and oxidation state (Belousova et al.,

2002; Watson and Harrison, 2005; Schmitt and Zack, 2012; Trail et al., 2012). The CI-normalized REE patterns exhibited by zircons are usually characterized by a positive slope from La to Lu due to increasing compatibility of the REEs in the zircon crystal structure with increasing atomic mass. Cerium partitioning is sensitive to the oxidation state of the parent magma because oxidized magmas stabilize $Ce^{4+}$, which is more compatible in zircon than $Ce^{3+}$ (Trail et al., 2012). Negative Eu anomalies have also been used to indicate the removal of plagioclase by fractional crystallization prior to zircon formation because the plagioclase structure preferentially incorporates divalent Eu over the other REEs (Snyder et al., 1993; Hoskin and Ireland, 2000). Similar to Ce, the magnitude of the Eu anomaly is also affected by the oxidation state (Trail et al., 2012).

The Cl-chondrite normalized REE patterns for terrestrial igneous zircons are typically characterized by steep slope from LREE to HREE, a positive Ce-anomaly, and a negative Eu-anomaly (e.g. Hoskin and Schaltegger, 2003; Grimes et al., 2007; Bell and Harrison, 2013). The abundances of REEs range from 10s to 1000s ppm, with zircons from crustal rocks having higher concentrations than mantle rocks (Hoskin and Ireland, 2000; Belousova et al., 2002; Hoskin and Schaltegger, 2003). Terrestrial impact grown zircons have REEs that are similar to target rock zircons (Wielicki et al., 2012).

Nemchin et al. (2010) reported trace element analyses of 15 lunar zircons and identified four groups based on their REE patterns. They defined both Type 1 and 2 patterns as characterized by a positive slope from La to Lu and negative Eu anomalies, but with total REE concentration being higher in Type 2. Type 3 is differentiated by elevated LREE

concentrations, and the one zircon characterized as Type 4 has a positive Ce anomaly. We have analyzed REE concentrations in 90 zircons and combined them with the 34 zircon analyses from Taylor et al. (2009) to create a data set large enough to investigate characteristics of lunar zircon parent magmas.

*2.5.2.1 Identifying Contributions from Inclusions*

The LREE concentrations in zircon are up to four orders of magnitude lower than those of the HREEs, so they are more easily affected by even trace amounts of contamination (Hinton and Upton, 1991). Higher resolution SEM imaging compared to previously published lunar zircon images revealed that more than half of the lunar zircons we analyzed had potential sources of REE contamination exposed on the surface. These features include impact melt inclusions, cracks, annealed curviplanar fractures, or regions of trace element exchange between zircon and impact melt (visible in CL). Additionally, inspection of these samples under optical transmission microscopy revealed many grains have subsurface melt inclusions that could potentially be excavated during SIMS analyses. All of these microstructures can include materials that contain much higher trace element concentrations than the host zircon. We therefore discarded all trace element analyses where SIMS spots visibly overlapped these potential sources of contamination.

Iron is incompatible in the zircon structure; Hoskin and Schaltegger (2003) determined that primary igneous zircons incorporate at most a few hundred ppm Fe. These trace amounts of Fe are due to coupled substitution with REEs or Y necessary for charge balance (Hoskin and Ireland, 2000). Both $Fe^{2+}$ and $Fe^{3+}$ substitutions have been proposed, so variations in $fO_2$

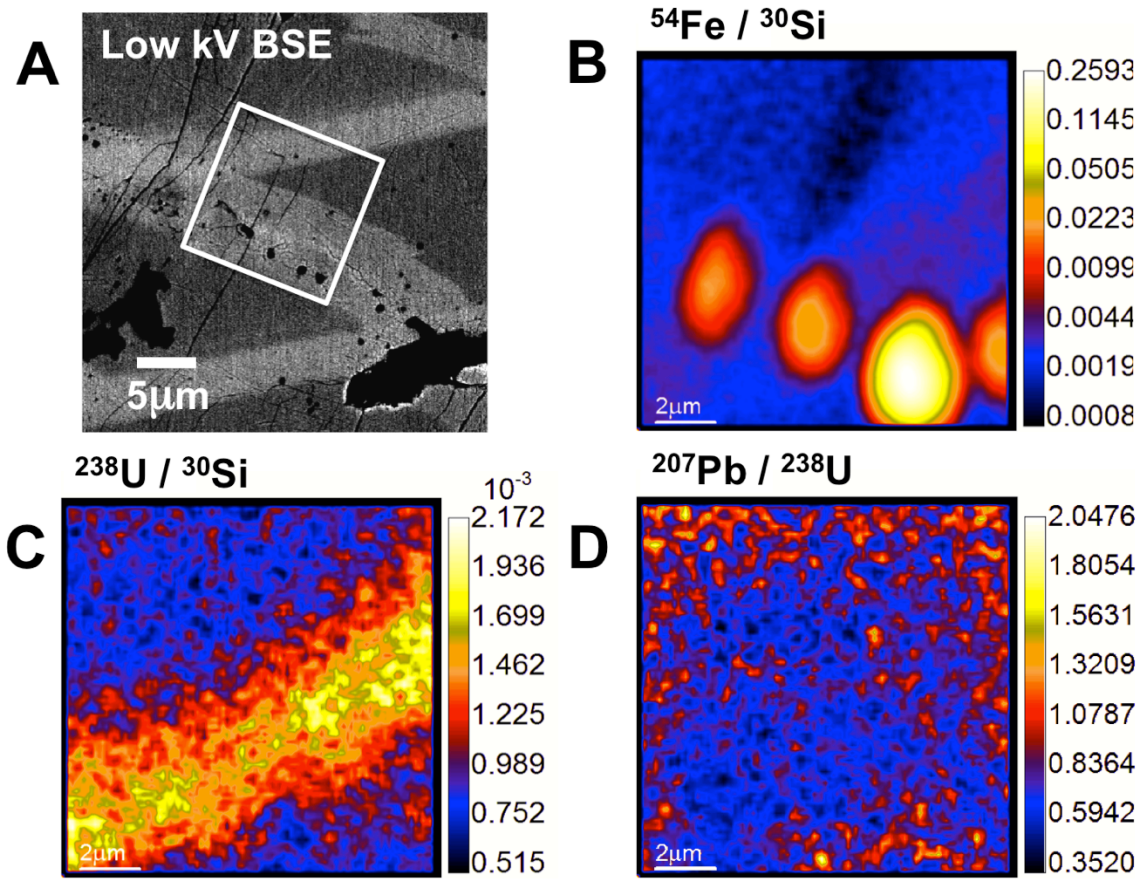


Figure 2-5: (A) Low accelerating voltage BSE image of lunar zircon 14305 Z34 showing region of NanoSIMS raster (white box). (B) Fe/Si map; bright regions of high Fe counts are impact melt glass inclusions. (C) U/Si map showing band of primary igneous zonation. The band is not perfectly aligned with the band in image (A) due to remounting and polishing between electron beam imaging and NanoSIMS analyses. (D) $^{207}Pb/^{238}U$ ratio shows no significant variation across primary zoning and glass inclusions. The higher counts around the edges of the image are edge effects due to long analyses times.

should not result in variations of Fe concentration between igneous terrestrial and lunar zircons. As such, we also used Fe concentration to identify analyses that contained trace element contaminants such as submicron inclusions that are not easily identifiable in SEM imaging. NanoSIMS maps of Fe/Si, U/Si, and $^{207}Pb/U$ ratios, along with a low accelerating voltage backscatter electron image, are shown in Figure 2-5. All maps are of the same raster

area on zircon 14305 Z34, which contains a curviplanar fracture with impact melt glass inclusions, primary zoning in U concentration, and a shock microtwin (see section 3.5.5 for discussion of shock microtwins). The impact melt glass inclusions are clearly visible in the Fe/Si map. This confirms our assumption that trace element analyses with elevated Fe concentrations contain contributions from glass inclusions or other regions, such as cracks, hosting material with trace element concentrations that differ from the host zircon. Monitoring Fe concentration can therefore be informative in monitoring SIMS analyses for potential sources of contamination.

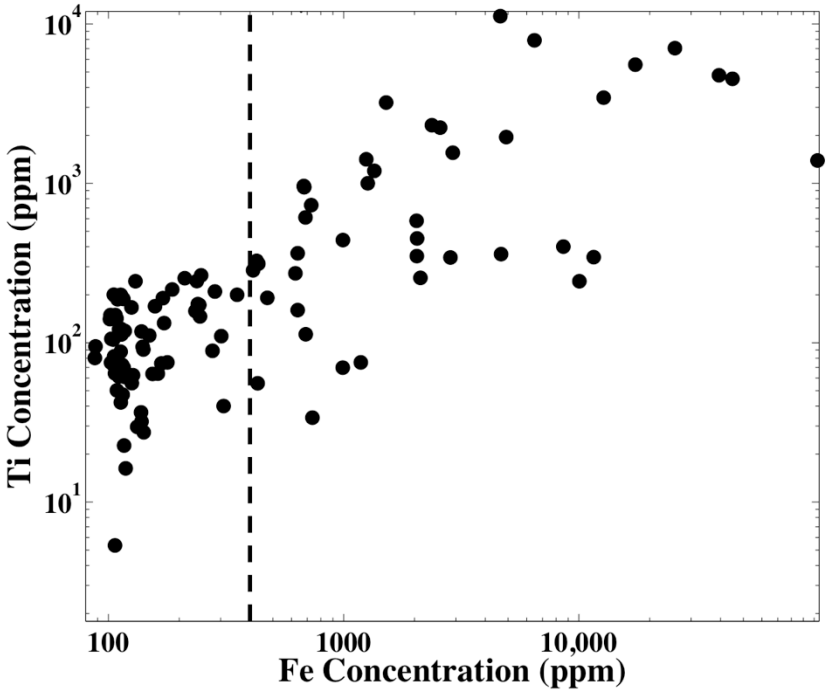


Figure 2-6: Ti vs Fe concentration of all REE analyses from this study and Taylor et al. 2009. We chose a cut off for acceptable Fe concentration of 400 ppm (dashed line) based on the average lunar zircon Fe concentration from Wopenka et al. (1996).

Wopenka et al. (1996) reported major and trace elements of a 200 μm zoned zircon from breccia 14161. They measured a transect of five SIMS analyses and observed FeO concentrations ranging between 200 ppm and 1000 ppm. Four of these analyses yield an average Fe concentration of ~ 400 ppm (the fifth SIMS spot appears to lie on a crack, so we excluded from the average). We therefore chose the cut off value for acceptable Fe concentration to be 400 ppm. This value is similar to the highest Fe concentrations found in Hadean Jack Hills zircons, which are of a commensurate ages as the lunar samples (Bell et al., in Review). Additionally, the plot of Ti vs Fe concentration in Figure 2-6 shows anomalously high Ti concentrations for some zircons with Fe >400 ppm, which also supports the cut of value. We discarded 54 of our 102 analyses and 16 of the 37 analyses from Taylor et al. (2009) due to visibly identifiable sources of contamination and/or Fe concentrations above ~400 ppm.

We conducted a simple mixing model using our highest Fe concentration zircon measurement (~40,000 ppm, Ti ~ 4500 ppm) and one of our visibly pristine zircon analyses. The results of the model suggest that small amounts of impact melt glass can readily produce the variations in trace element patterns observed. We were able to reproduce the LREE enrichment common in analyses with impact melt glass by a mixture of 5% high Fe analysis and 95% pristine zircon. We conducted this experiment with a range of end member analyses and found similar results. An example of the mixing model is shown in Figure 2-7. Additional evidence for the influence of impact melt glass contamination is that all measurements with positive Ce anomalies and relatively small Eu anomalies contained visibly identifiable impact melt glass inclusions within the SIMS analysis spots. This

suggests that a large percentage of lunar zircon REE data is contaminated and should not be interpreted in terms of zircon provenance, and monitoring Fe concentrations and high resolution SEM imaging may be a systematic way to filter lunar zircon trace element data.

After the removal of the analyses containing trace element contaminants, the lunar zircons can be characterized by one REE pattern with varying levels of total REE concentration (Figure 2-3). The REE pattern is characterized by a positive slope resulting from zircon partition coefficients along with negative Eu anomalies. The negative Eu anomaly suggests the zircons formed after appreciable amounts of plagioclase had been removed to form the flotation crust. Additionally, the absence of Ce anomalies is consistent with the zircons having formed in a reducing (i.e. dry) magma. Our analyses span the full range between group 1 and 2 zircons from Nemchin et al. (2010). All of our measurements that exhibited LREE enrichments and Ce anomalies similar to group 3 and 4 were discarded due to contamination. Thus, the four REE groupings suggested by Nemchin et al. (2010) collapse to a single group when the data are properly filtered to exclude impact melt or other contaminants. The similarity of the REE patterns of lunar zircons make it difficult to use the patterns alone to identify zircons of different provenance.

*2.5.2.2 Igneous Crystallization Trends*

Claiborne et al. (2010) showed that terrestrial zircons record trace element variations due to igneous fractional crystallization of parent magmas. As fractional crystallization progresses, Hf becomes increasingly concentrated in the melt due to its incompatible nature in most

minerals. The Hf concentration can therefore be used as a proxy for degree of crystallization within a given magma. Other trace elements also show similar trends diagnostic of fractional crystallization. These trends are most notable in the lunar zircon Ti, Th/U, Sm, and Yb/Gd systems. Figure 2-8 contains plots of four of systems relative to Hf. The trends in the lunar zircons are not as well-correlated as those for terrestrial zircons, possibly due to the smaller range in Hf concentrations in the lunar grains.

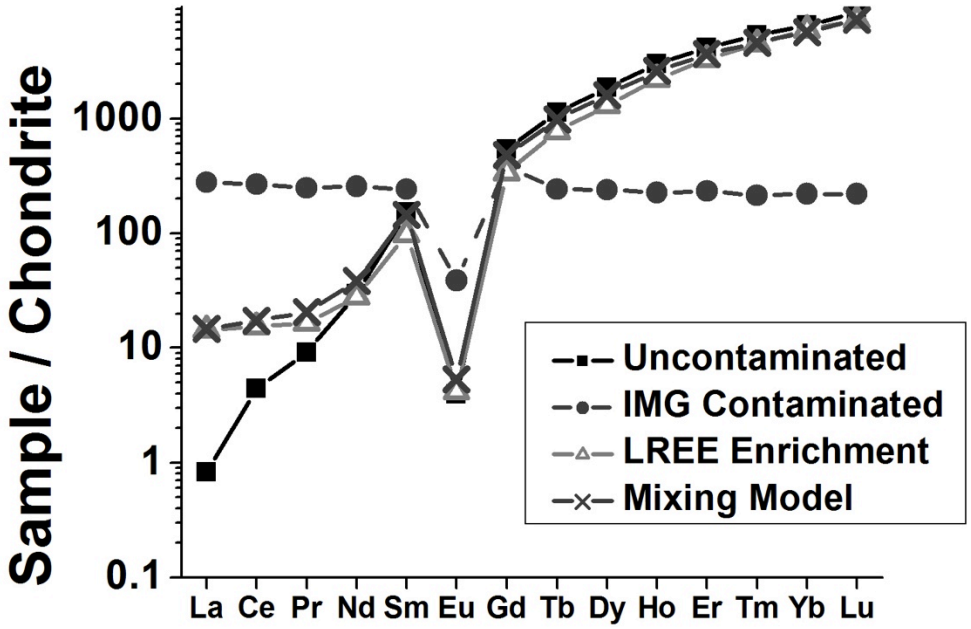


Figure 2-7: Linear mixing model between a pristine uncontaminated zircon measurements (square) and a contaminated zircon measurement, identified by high Fe concentration (circles). A mixture of 5% contaminated and 95% pure zircon is able to reproduce the LREE enrichment seen in some of the analyses with visible impact melt glass contamination.

Figure 2-8A shows a plot of Ti (proxy for temperature) vs Hf concentration. The Ti concentration of the lunar zircons decreases (and therefore temperature decreases) with

increasing degree of crystallization similar to the Spirit Mountain Batholith zircons(Claiborne et al., 2010). See section 2.5.2.3 for more discussion of Ti-in-zircon temperatures. The Th/U ratio (Figure 2-8B) also decreases with increasing Hf due to the higher compatibility of Th over U in most minerals (Claiborne et al., 2010). There is one anomalously high Th/U ratio of 1.8 in an Apollo 14321 zircon that cannot be explained by influences of impact melt glass inclusions. Sm shows a sharp decrease with degree of fractionation (Figure 2-8C). Claiborne et al. (2010) suggest this is due to co-crystallization of

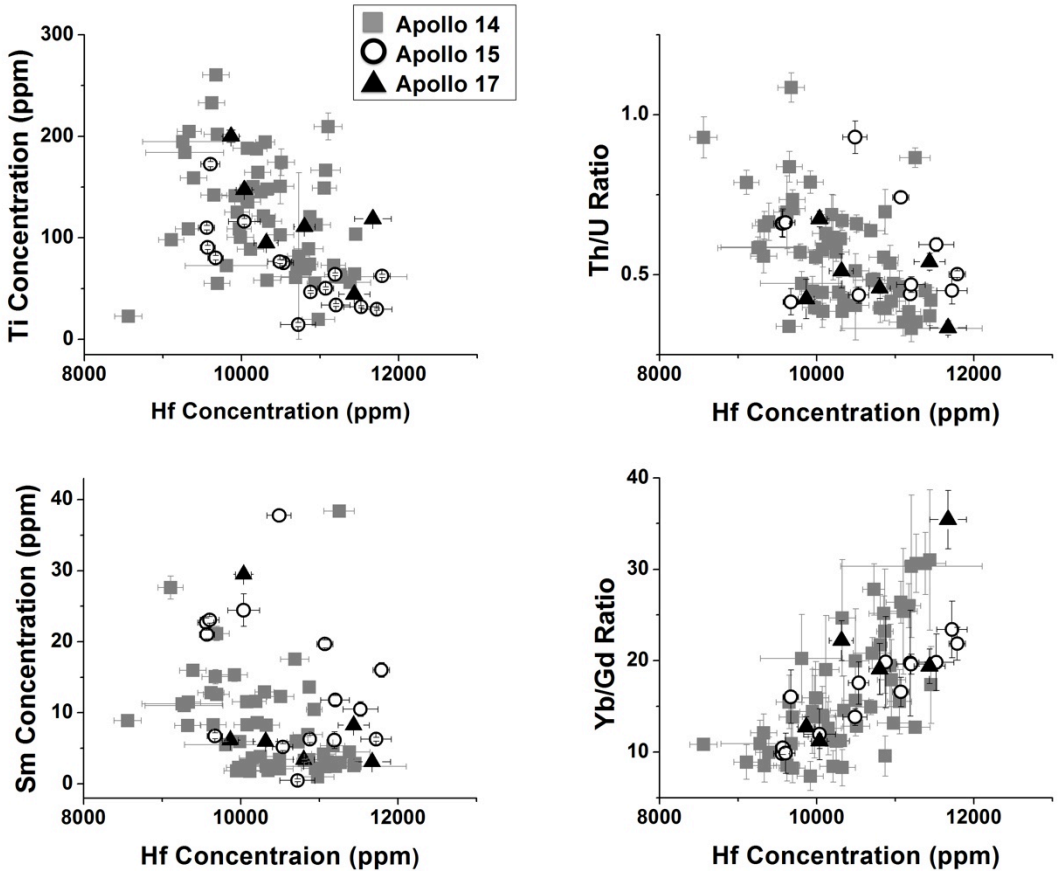


Figure 2-8: Trace element trends indicative of igneous fractional crystallization. Hf is concentrated in the melt and can be used as a proxy for percent fractionation. (A) Ti, proxy for temperature, decreases as crystallization progresses. (B) Th is more compatible than U in many minerals, so the Th/U ratio decreases as Hf increases. (C) Sm also decreases with time due to co-crystallization of middle REE favoring minerals. (D) The Yb/Gd ratio, indicative of REE slope, increases due to late crystallization of LREE favoring minerals.

LREE loving minerals, such as apatite (Watson and Green, 1981). The Yb/Gd ratio, indicative of REE slope, increases with Hf concentration (Figure 2-8D), most likely due to late co-crystallization of minerals that favor the middle REEs. All of these trends are similar to those reported in Claiborne et al. (2010) suggesting that the lunar zircons also formed by a fractional igneous crystallization process, generally similar to the processes that formed the Spirit Mountain Batholith zircons.

If all the lunar zircons formed from the same original magma, there should be a correlation between the Hf concentration and the Pb-Pb crystallization age, but the lunar zircons do not show this correlation. Even the oldest of the lunar zircons, >4300 Ma, do not show a distinct increase in Hf concentration with progressive crystallization (i.e., a decrease in age; Figure 2-9). This suggests that either there were multiple parent magmas producing zircons by fractional crystallization or that the Pb-Pb ages have been reset by subsequent impacts that did not simultaneously affect the trace element concentrations. The latter is possible because even at 1000° C, the diffusion coefficients for the REEs are between 4 and 300 times lower than that of Pb (Cherniak et al., 1997; Cherniak and Watson, 2000). Our data do not support the hypothesis of contraction of a single KREEP source region as an explanation for the age dichotomy in the Apollo landing sites, although it cannot be ruled out until there is a better understanding of how much impact induced Pb-loss the lunar zircons have experienced. Higher precision U-Pb analyses may be helpful in distinguishing between these scenarios by determining if the $^{207}$Pb-$^{206}$Pb ages are indeed concordant crystallization ages or if they lie on a discord almost parallel to Concordia.

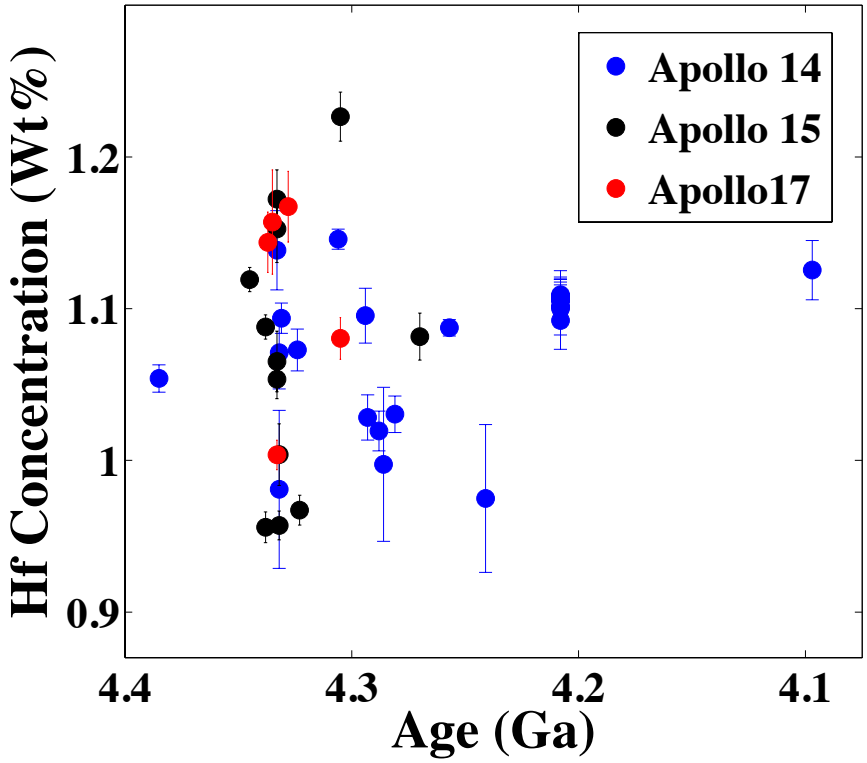


Figure 2-9: Plot of Hf concentration vs zircon $^{207}$Pb-$^{206}$Pb age for pristine zircon analyses. No correlation between the two parameters is seen. Since Hf can be used as a proxy for degree in fractional crystallization in a single source, the lack of correlation suggests multiple zircon forming sources on the early Moon. However potential Pb-loss and age resetting by subsequent impacts is unlikely, but it cannot be ruled out at this time (see discussion in text and in Chapter 3).

*2.5.2.3 Ti-in-zircon Temperatures and Zircon Saturation Temperatures*

As previously discussed, the partitioning of Ti into zircon is a function of temperature and the activities ($a$) of $TiO_2$ and $SiO_2$ in the melt. Since all lunar zircons, except for a few skeletal grains grown in an impact environments, are detrital, the compositions of their parent magmas are unknown. Even though we cannot directly measure the $a_{TiO2}$ and $a_{SiO2}$, we can still determine reasonable values based on the best estimates of KREEP parent melt compositions. To do this, we used the MELTS program to calculate temperatures, activities, and final mineral assemblages for four initial compositions (Asimow and Ghiorso, 1998;

Ghiorso and Sack, 1995): (1) estimated composition of urKREEP, or the KREEP parent (Warren and Wasson, 1979), (2) 15405 KREEP basalt granite (Ryder, 1976), (3) 15405 quartz monzodiorite (Taylor et al., 1980), and (4) 70215 high-Ti basalt (LSPET, 1973). The first three compositions are our best estimate of the KREEP parent magma composition (Warren, personal communication), and the latter was investigated to determine how higher Ti concentrations affect $a_{TiO2}$. Each MELTS run had the following conditions: fractional crystallization, P=0.540 kbar, starting log $fo_2$=IW-1 (Ghiorso and Sack, 1995; Wadhwa, 2008), and prohibition of spinel formation. The last parameter was necessary because starting compositions were for samples with little to no spinel, and crystallization of ulvospinel could influence the $a_{TiO2}$.

The average $a_{SiO2}$ for all starting compositions is 0.6 ± 0.1; there is a slight increase in activity with decreasing temperature and no variation between samples. The $a_{TiO2}$ also shows no variation between runs with different starting compositions and does not vary with temperature. Each composition yields maximum $a_{TiO2}$ values between 0.1 and 0.2. The Ti-temperatures for the lunar zircons calculated using $a_{SiO2}$ = 0.6 and $a_{TiO2}$ = 0.2 range between 989° - 1374°C. To test if the highest temperatures are reasonable, we can compare them with zircon saturation temperatures for the parent melts since Ti-temperatures recorded by a zircon cannot exceed the saturation temperature. The temperature at which zircon saturates depends on the composition of the melt and the relative concentrations of Zr in zircon and the melt. The equation for zircon saturation temperature was revised by Boehnke et al. (2013):

$$\frac{[Zr(ppm)]_{Zircon}}{[Zr(ppm)]_{Melt}} = \left(\frac{10108 \pm 32}{T}\right) - (1.16 \pm 0.15)(M - 1) - (1.48 \pm 0.09) \quad (2.2)$$

Where concentration of Zr in zircon, $[Zr(ppm)]_{Zircon}$, is assumed to be 500,000, $[Zr(ppm)]_{Melt}$ is the concentration of Zr in the melt, T is temperature in (K), and M is a parameter that describes the composition of the melt. M is determined using the normalized molar amounts of each element and using the following equation:

$$M = \left[\frac{Na + K + 2Ca}{Al \cdot Si}\right] \quad (2.3)$$

We calculated a zircon saturation temperature of 1250°C based on the Zr concentration and major element composition of urKREEP from Warren and Wasson (1979) (M=1.97), and a temperature of 1266°C for the 15405 KREEP basalt granite (M=1.82). (The M values for the QMD clast (M=2.49) and the high-Ti basalt (M=3.59) are outside the range calibrated by Bohenke et al. (2013)). The zircon saturation temperatures suggest that the highest Ti-temperatures recorded by lunar zircons should by ~1260°C. In order for our highest Ti concentrations to be consistent with this temperature with $a_{SiO2} = 0.6$, our $a_{TiO2}$ would need to be ~ 0.3. It is interesting to note that in all MELTS runs, ilmenite ($FeTiO_3$) begins to crystallize between ~ 980° and 1141°C, which is bellow the zircon saturation temperature suggesting zircons may be crystallizing before ilmenite. The activity of $a_{TiO2}$ could be higher prior to ilmenite formation, which would remove $TiO_2$ from the melt, so a value of ~ 0.3 is also reasonable for our high Ti zircons.

Based on the MELTS results and zircon saturation temperatures of KREEP rocks, our best estimates for oxide activities are $a_{SiO2} = 0.6 \pm 0.1$ and $a_{TiO2} = 0.25 \pm 0.05$. The Ti-in zircon

temperatures calculated using these values range from 958 ± 57° to 1321 ± 100°C (errors based range in $a_{SiO2}$ and $a_{TiO2}$, and 1σ analytical error in Ti concentration). The lower bound agrees well with the dry solidus for granite at near surface pressures (~950°C) (Robertson and Wyllie, 1971) and highest temperature is within error of the zircon saturation temperatures. (Note: the trace element analyses from Taylor et al. (2009) are included in this range.)

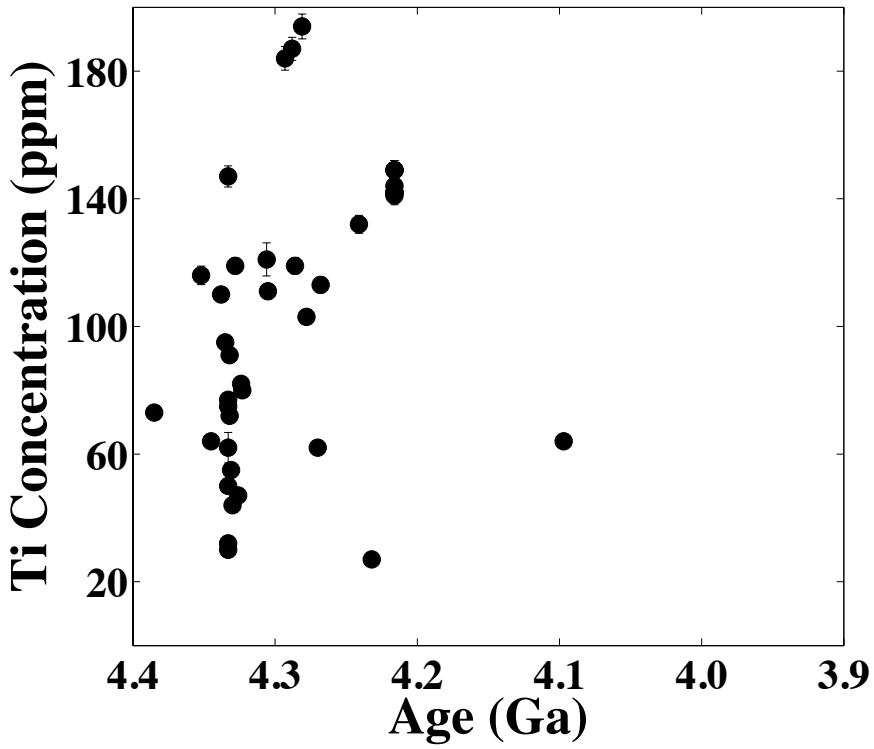


Figure 2-10: Plot of Ti concentration (μg/g) of pristine zircon analyses as a function of $^{207}Pb$-$^{206}Pb$ age, showing no correlation between the two parameters. The zircons from the ~4.33 Ga peak in age histograms show almost the full range of measured Ti-concentrations. This may suggest, similar to the other trace element systems, the lunar zircons formed in multiple KREEP-rich sources.

Our Ti concentrations are in agreement with the average Ti concentrations for zircons from Apollo 12, 14, 15, and 17 reported in Valley et al. (2014). They assumed equal values of

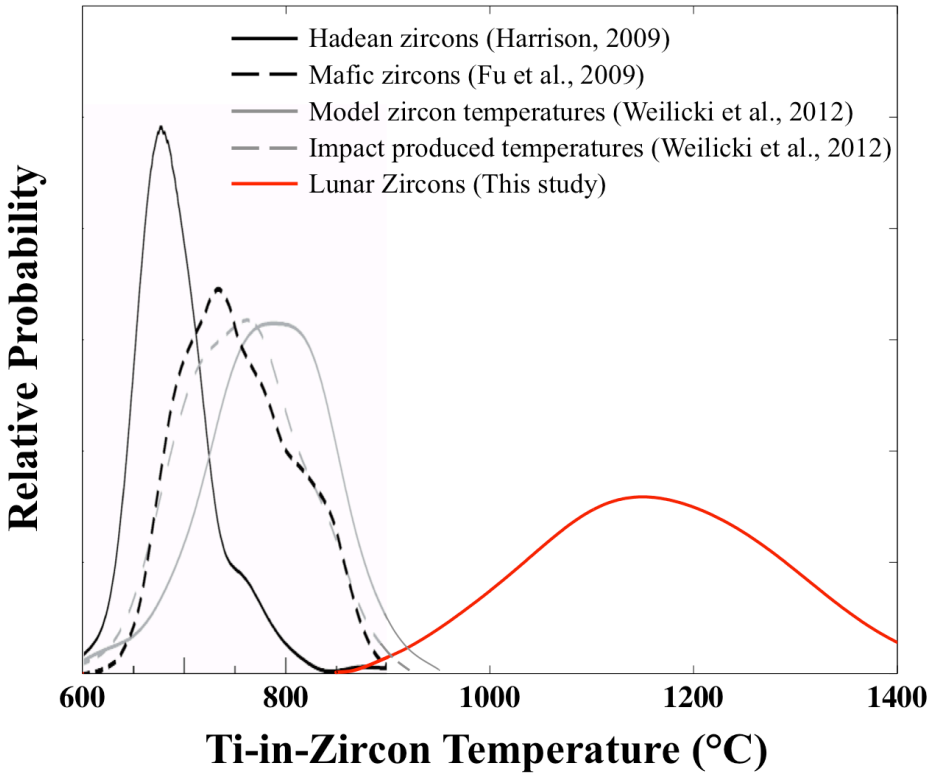


Figure 2-11: Probability density functions of Ti-in-zircon temperatures modified from Wielicki et al. (2012). The crystallization temperatures of the lunar zircons are all higher than those of terrestrial Hadean zircons (Harrison, 2009), mafic zircons (Fu et al., 2008), and measured and modeled temperatures of zircons produced in impact melts (Wielicki et al., 2012).

$a_{SiO2} = a_{TiO2} = 0.6$ and calculated temperatures range from 892° to 1085°C. Valley et al. (2014) suggested the subsolidus temperatures result from a lowering in solidus temperature due to enrichment of water and volatiles in late stage, residual magma such as KREEP. However, if we recalculate the temperatures for their zircons analyses using our new constraints on $a_{SiO2}$ and $a_{TiO2}$, the temperatures range from 1010 ± 55° to 1250 ± 78°C. These values agree well with the temperatures reported herein and do not require a hydrated late stage KREEP. The lunar zircon temperatures are higher than those of terrestrial Hadean zircons, which are all bellow 800°C (see Figure 2-11; Harrison and Schmitt, 2007; Bell and

Harrison, 2013). The higher lunar zircon temperatures are attributed to the anhydrous nature of the Moon relative to the Earth (Taylor et al., 2009).

## 2.6 Conclusions

The Pb-Pb age distributions of Apollo 14, 15 and 17 zircons from this study broadly agree with the ranges of previously reported ages. All three landing sites exhibit a peak in age around 4.33 Ga, although the peak in Apollo 14 is broader and extends down to 4.2 Ga. Apollo 14 is also the only landing site that contains zircons with Pb-Pb ages less than 4.1 Ga (~10% of the grains). These grains are usually smaller than 50 μm and/or show evidence of Pb-mobility, suggesting an increased likelihood of impact alteration. Based on microstructural analyses, our data, in combination with previously reported ages, suggest that lunar zircons are recording signatures of large impacts at least every 100 Myr during the first 500 Myr of the lunar history. Additionally, the lunar zircons do not record a signature of a LHB or spike in impact flux at ~3.9 Ga.

The majority (~90%) of the lunar zircons are older that 4.1 Ga, most of which are approximately concordant and show no evidence for open system behavior. The large size of the parent crystals, some over a millimeter in length, suggests formation in a highly enriched KREEP magma and not an impact environment. This suggests that the majority of zircon forming KREEP magmatism ceased by 4.1 Ga. This is older than the previously proposed age of 3.88 Ga, which was determined based on the total range of lunar zircon ages and not the probability densities of the age distributions (Meyer et al., 1989, 1996b). Microstructural

analyses, which were discussed briefly in this chapter and are the focus of Chapter 3, have also been key in interpreting the lunar zircon ages.

We compiled a REE dataset large enough to investigate characteristics of lunar zircon parent magmas. Inspection of the SIMS REE analysis spots and monitoring of Fe concentrations allowed us to filter our data to exclude measurements with potential trace element contamination from impact melt glass or cracks. In most cases, the contamination resulted in LREE enhancements, positive Ce anomalies, and/or a decrease in the magnitude of Eu anomalies. After the removal of contaminated measurements, the lunar zircons can be characterized by one REE pattern. The uncontaminated analyses also exhibit trace element trends (relative to Hf) indicative of fractional crystallization, but there is no correlation between Hf concentration and Pb-Pb age. This suggests that either there were multiple KREEP source regions forming zircons by fractional crystallization, or that there was one KREEP source region and the Pb-Pb ages have been modified while the trace elements remained unaltered.

The best estimates for oxide activities in the KREEP source are $a_{SiO2} = 0.6 \pm 0.1$ and $a_{TiO2} = 0.25 \pm 0.05$ based on the results of MELTS models for a range of likely parent melt compositions. The Ti-in-zircon temperatures of lunar zircons calculated using these values range from 958 ± 57° to 1321 ± 100°C. The lower bound of this range is above the dry solidus temperature of granite and the upper bound is within error of the zircon saturation temperatures of the stating MELTS compositions. The Ti concentrations (and temperatures)

do not correlate with age further supporting the suggestion of multiple KREEP source regions.

**Appendix 2-1: Zirconium Concentrations and Zircon Yields of Lunar Samples**

| Sample | Weight | Zircon Yield | Zr Concentration |
|---|---|---|---|
| 14163 | 15 g | 70 | 720-1022 ppm (1)(2) |
| 14259 | 15 g | 39 | 590-691 ppm (1)(2) |
| 14304* | 15 g | 28 | 28-850 ppm (3) |
| 14305* | 16 g | 13 | 840-1158 ppm (2)(4) |
| 14321* | 15 g | 9 | 670-1210 ppm (5)(6) |
| 15311 | 15 g | 10 | 407 ppm (7) |
| 15405 | 16 g | 21 | 500-1100 ppm (8)(9) |
| 15455 | 15 g | 12 | 230-270 ppm (10) |
| 72275 | 12.6 g | 12 | 613 ppm (11) |

* Samples were saw cuttings that contained diamonds, which made zircon recovery more difficult.

References for Zr concentrations of lunar samples:

(1) (Lindstrom et al., 1972)

(2) (Willis et al., 1972)

(3) (Goodrich et al., 1986)

(4) (Wiik et al., 1973)

(5) (LSPET, 1971)

(6) (Palme et al., 1978)

(7) (Korotev, 1987)

(8) (Laul and Schmitt, 1972)

(9) (Christian et al., 1976)

(10) (Lindstrom et al., 1988)

(11) (LSPET, 1973)

## Appendix 2-2: U-Pb and Pb-Pb Ages

| Sample Name | $^{207}Pb/^{206}Pb$ Age (Ma) | ± 1σ | $^{206}Pb/^{238}U$ Age (Ma) | ± 1σ | $^{207}Pb/^{235}U$ Age (Ma) | ± 1σ | % Disc. | % $^{206}Pb$ Radiogenic |
|---|---|---|---|---|---|---|---|---|
| *14163* | | | | | | | | |
| Z 18 | 4208 | 5 | 4235 | 90 | 4217 | 31 | -0.6 | 99.8 |
| Z 21 | 4253 | 7 | 3986 | 89 | 4165 | 30 | 6.3 | 99.7 |
| Z 23 | 4096 | 32 | 4041 | 47 | 4078 | 26 | 1.3 | 100 |
| Z 25 | 4249 | 7 | 4336 | 72 | 4277 | 23 | -2 | 99.8 |
| Z 26 | 4276 | 22 | 4346 | 83 | 4298 | 37 | -1.6 | 99.8 |
| Z 27 | 4265 | 8 | 4334 | 142 | 4287 | 46 | -1.6 | 99.8 |
| Z 29 | 4342 | 5 | 4401 | 122 | 4361 | 39 | -1.4 | 99.8 |
| Z 30 | 4357 | 8 | 4424 | 91 | 4378 | 30 | -1.5 | 99.2 |
| Z 31 | 3942 | 9 | 3794 | 174 | 3892 | 61 | 3.8 | 96.8 |
| Z 32 | 4252 | 10 | 4170 | 124 | 4226 | 40 | 1.9 | 97.8 |
| Z 33 | 4248 | 2 | 4235 | 64 | 4244 | 21 | 0.3 | 99.5 |
| Z 34 | 4271 | 9 | 4208 | 58 | 4250 | 21 | 1.5 | 97.5 |
| Z 35 | 4279 | 9 | 4132 | 157 | 4232 | 54 | 3.4 | 98.2 |
| Z 36 | 4203 | 4 | 4091 | 69 | 4166 | 24 | 2.7 | 99.4 |
| Z 37 | 4329 | 4 | 4255 | 85 | 4305 | 28 | 1.7 | 99 |
| Z 38 | 4247 | 5 | 3901 | 94 | 4133 | 31 | 8.1 | 98.9 |
| Z 43 | 3976 | 27 | 3586 | 158 | 3840 | 64 | 9.8 | 97 |
| Z 46 | 4334 | 5 | 4339 | 84 | 4336 | 27 | -0.1 | 99.2 |
| Z 48 | 4333 | 5 | 4265 | 91 | 4311 | 29 | 1.6 | 99.9 |
| Z 49 | 4259 | 5 | 4111 | 88 | 4211 | 29 | 3.5 | 99.9 |
| Z 51 | 4123 | 8 | 3944 | 88 | 4063 | 30 | 4.3 | 99.8 |
| Z 52 | 4263 | 8 | 4333 | 189 | 4285 | 62 | -1.6 | 98 |
| Z 53 | 3979 | 6 | 4025 | 156 | 3994 | 51 | -1.2 | 98.9 |
| Z 54 | 4097 | 8 | 3987 | 92 | 4061 | 30 | 2.7 | 99.8 |
| Z 55 | 4296 | 7 | 4575 | 627 | 4383 | 194 | -6.5 | 98.5 |
| Z 58 | 4213 | 5 | 4153 | 86 | 4193 | 29 | 1.4 | 99.9 |
| Z 59 | 4333 | 4 | 4080 | 89 | 4251 | 30 | 5.8 | 99.9 |
| Z 60 | 4342 | 3 | 4232 | 91 | 4307 | 29 | 2.5 | 99.9 |
| Z 61 | 4317 | 15 | 4421 | 126 | 4350 | 40 | -2.4 | 99 |
| Z 62 | 4248 | 3 | 4254 | 103 | 4250 | 33 | -0.1 | 99.5 |
| Z 63 | 4280 | 27 | 4155 | 175 | 4240 | 66 | 2.9 | 99 |
| Z 64 | 4254 | 7 | 4108 | 90 | 4207 | 31 | 3.4 | 99.8 |
| Z 66 | 4282 | 10 | 4180 | 168 | 4249 | 56 | 2.4 | 99.1 |
| Z 67 | 4221 | 9 | 4242 | 190 | 4228 | 62 | -0.5 | 98.2 |
| Z 69 | 4287 | 6 | 4199 | 129 | 4259 | 43 | 2.1 | 99.4 |
| Z 70 | 4226 | 6 | 4073 | 89 | 4176 | 29 | 3.6 | 99.7 |
| Z 71 | 4323 | 7 | 4231 | 92 | 4293 | 30 | 2.1 | 99.9 |
| Z 72 | 4335 | 5 | 4235 | 94 | 4303 | 31 | 2.3 | 99.9 |
| Z 74 | 4329 | 2 | 4195 | 63 | 4286 | 20 | 3.1 | 99.7 |

| | | | | | | | | |
|---|---|---|---|---|---|---|---|---|
| Z 83 | 4238 | 13 | 4406 | 85 | 4291 | 29 | -4 | 99.9 |
| Z 89 | 4313 | 6 | 4251 | 60 | 4293 | 18 | 1.4 | 99.9 |
| Z89 @2 | 4309 | 6 | 4189 | 51 | 4270 | 16 | 2.8 | 99.9 |
| Z 90 | 3988 | 11 | 3953 | 65 | 3976 | 22 | 0.9 | 99.8 |
| *14259, 658* | | | | | | | | |
| Z1 | 4232 | 9 | 4524 | 555 | 4324 | 172 | -6.9 | 99.8 |
| Z2 | 4332 | 4 | 3864 | 274 | 4177 | 94 | 10.8 | 100 |
| Z 3 | 4205 | 7 | 4357 | 389 | 4254 | 124 | -3.6 | 100 |
| Z 3 @2 | 4221 | 18 | 3592 | 276 | 4006 | 100 | 14.9 | 100 |
| Z 3 @3 | 4196 | 5 | 4071 | 305 | 4155 | 101 | 3 | 100 |
| Z 6 | 4251 | 4 | 4167 | 305 | 4224 | 100 | 2 | 100 |
| Z 7 | 4190 | 12 | 3113 | 252 | 3803 | 100 | 25.7 | 100 |
| Z 8 | 4331 | 12 | 4303 | 204 | 4322 | 64 | 0.6 | 100 |
| Z 8 @2 | 4341 | 2 | 3877 | 154 | 4188 | 53 | 10.7 | 100 |
| Z 12 @2 | 4306 | 4 | 4519 | 187 | 4373 | 58 | -4.9 | 100 |
| Z 13 | 4257 | 7 | 5101 | 331 | 4512 | 93 | -19.8 | 99.9 |
| Z 13 @2 | 4278 | 13 | 4586 | 264 | 4374 | 80 | -7.2 | 99.8 |
| Z 14 | 3987 | 10 | 4069 | 220 | 4014 | 72 | -2.1 | 99.9 |
| Z 14 @ 2 | 4030 | 7 | 4180 | 268 | 4079 | 86 | -3.7 | 99.8 |
| *14259, 664* | | | | | | | | |
| Z 1 | 4218 | 11 | 3982 | 284 | 4141 | 99 | 5.6 | 99.9 |
| Z 1 @ 2 | 4237 | 15 | 4097 | 326 | 4191 | 111 | 3.3 | 99.9 |
| Z 1 @ 3 | 4156 | 14 | 3926 | 266 | 4080 | 92 | 5.5 | 100 |
| Z 1 @ 4 | 4153 | 13 | 3591 | 242 | 3961 | 89 | 13.5 | 99.9 |
| Z 1 @ 5 | 4313 | 8 | 4100 | 159 | 4244 | 54 | 4.9 | 99.9 |
| Z 1 @ 6 | 4075 | 8 | 3956 | 182 | 4035 | 61 | 2.9 | 99.8 |
| Z 1 @ 7 | 4275 | 6 | 4094 | 186 | 4216 | 61 | 4.2 | 99.9 |
| Z 1 @ 8 | 4163 | 20 | 3986 | 204 | 4105 | 68 | 4.3 | 100 |
| Z 1 @ 9 | 4183 | 19 | 4062 | 165 | 4143 | 57 | 2.9 | 100 |
| Z 1 @ 11 | 4206 | 15 | 4044 | 228 | 4153 | 79 | 3.9 | 99.9 |
| Z 1 @ 12 | 4292 | 32 | 3818 | 183 | 4134 | 57 | 11 | 100 |
| Z 1 @ 13 | 4310 | 12 | 3527 | 150 | 4043 | 53 | 18.2 | 99.9 |
| Z 1 @ 14 | 4263 | 10 | 3982 | 195 | 4171 | 65 | 6.6 | 99.9 |
| Z 1 @ 15 | 4219 | 32 | 4147 | 219 | 4196 | 77 | 1.7 | 99.9 |
| Z 1 @ 16 | 4106 | 9 | 4031 | 192 | 4081 | 65 | 1.8 | 100 |
| Z 2 | 4199 | 6 | 3873 | 102 | 4090 | 34 | 7.8 | 100 |
| Z 3 | 4025 | 14 | 1955 | 30 | 3144 | 18 | 51.4 | 99.8 |
| Z 4 | 4093 | 4 | 4124 | 104 | 4103 | 34 | -0.8 | 99.8 |
| Z 5 | 3932 | 9 | 3928 | 136 | 3931 | 47 | 0.1 | 99.9 |
| Z 6 | 4338 | 3 | 4345 | 112 | 4341 | 35 | -0.2 | 100 |
| Z 7 | 4128 | 6 | 3929 | 98 | 4062 | 32 | 4.8 | 100 |
| Z 11 | 4137 | 8 | 4113 | 115 | 4129 | 39 | 0.6 | 100 |
| Z 11@2 | 4115 | 7 | 4065 | 111 | 4098 | 37 | 1.2 | 100 |
| Z 12 | 4241 | 2 | 4270 | 56 | 4250 | 33 | -0.7 | 100 |

| | | | | | | | | |
|---|---|---|---|---|---|---|---|---|
| Z 15 | 3922 | 8 | 3806 | 146 | 3882 | 50 | 3 | 100 |
| Z 16 | 4327 | 4 | 4286 | 105 | 4314 | 34 | 0.9 | 100 |
| Z 17 | 4323 | 4 | 3963 | 113 | 4205 | 39 | 8.3 | 99.9 |
| Z 18 | 4274 | 5 | 3853 | 86 | 4134 | 30 | 9.9 | 99.8 |
| Z 19 | 4041 | 10 | 3932 | 103 | 4004 | 36 | 2.7 | 99.8 |
| Z 20 | 4329 | 4 | 4526 | 226 | 4390 | 69 | -4.6 | 99.9 |
| Z 21 | 4001 | 10 | 4070 | 270 | 4024 | 88 | -1.7 | 99.9 |
| Z 21 @2 | 3983 | 10 | 3968 | 244 | 3978 | 85 | 0.4 | 100 |
| Z 23 | 4306 | 16 | 4712 | 330 | 4431 | 99 | -9.4 | 100 |
| Z 24 | 4194 | 7 | 4392 | 208 | 4257 | 65 | -4.7 | 100 |
| Z 24 @2 | 4196 | 11 | 4088 | 215 | 4161 | 73 | 2.6 | 99.9 |
| Z 25 | 4212 | 15 | 4049 | 362 | 4159 | 119 | 3.9 | 100 |

*14304*

| | | | | | | | | |
|---|---|---|---|---|---|---|---|---|
| Z 1* | 4001 | 10 | 3962 | 91 | 3988 | 30 | 1 | 99.8 |
| Z 2* | 4279 | 5 | 4306 | 94 | 4288 | 30 | -0.6 | 99.9 |
| Z 3* | 4265 | 6 | 4126 | 89 | 4220 | 30 | 3.3 | 99.9 |
| Z 4* | 4114 | 14 | 4036 | 94 | 4088 | 33 | 1.9 | 99.8 |
| Z 5* | 4024 | 5 | 3922 | 85 | 3990 | 29 | 2.5 | 99.9 |
| Z 8* | 4176 | 16 | 4136 | 108 | 4163 | 38 | 1 | 99.7 |
| Z 9* | 4185 | 6 | 4390 | 93 | 4251 | 29 | -4.9 | 99.9 |
| Z 13* | 4196 | 4 | 4191 | 89 | 4194 | 29 | 0.1 | 99.9 |
| Z 13 @2 * | 4282 | 13 | 4154 | 93 | 4241 | 32 | 3 | 99.8 |
| Z 22* | 4321 | 7 | 4242 | 89 | 4295 | 29 | 1.8 | 99.9 |
| Z 25* | 4177 | 10 | 4090 | 100 | 4149 | 33 | 2.1 | 99.7 |

*14305*

| | | | | | | | | |
|---|---|---|---|---|---|---|---|---|
| Z 1* | 4292 | 6 | 4144 | 43 | 4244 | 14 | 3.4 | 99.6 |
| Z 1@2* | 4276 | 14 | 4226 | 37 | 4260 | 12 | 1.2 | 99.3 |
| Z 3* | 4016 | 4 | 4043 | 85 | 4025 | 28 | -0.7 | 99.9 |
| Z 5* | 4160 | 6 | 4426 | 94 | 4245 | 30 | -6.4 | 99.9 |
| Z 12* | 4274 | 9 | 4194 | 95 | 4248 | 31 | 1.9 | 99.8 |
| Z 15 | 4206 | 16 | 4043 | 122 | 4153 | 42 | 3.9 | 99.2 |
| Z 16 | 4338 | 3 | 4270 | 67 | 4316 | 22 | 1.6 | 99.9 |
| Z 17 | 4317 | 14 | 4372 | 145 | 4335 | 48 | -1.3 | 99.7 |
| Z 18 | 4288 | 8 | 4013 | 171 | 4198 | 58 | 6.4 | 99.4 |
| Z 19 | 4287 | 9 | 4334 | 134 | 4302 | 41 | -1.1 | 99.5 |
| Z 20 | 4293 | 8 | 4274 | 150 | 4287 | 49 | 0.4 | 99.6 |
| Z 22 | 4219 | 11 | 4194 | 135 | 4211 | 44 | 0.6 | 99.6 |
| Z 23 | 4332 | 4 | 4246 | 81 | 4305 | 26 | 2 | 99.8 |
| Z 24 | 3977 | 5 | 3873 | 72 | 3942 | 25 | 2.6 | 99.8 |
| Z 25 | 4265 | 5 | 4106 | 99 | 4213 | 33 | 3.7 | 99.7 |
| Z 26 | 4233 | 4 | 4272 | 64 | 4246 | 20 | -0.9 | 99.8 |
| Z 27 | 4333 | 7 | 4283 | 104 | 4317 | 35 | 1.2 | 99.7 |
| Z 27 @2 | 4331 | 6 | 4043 | 189 | 4237 | 62 | 6.6 | 99.8 |
| Z 27 @3 | 4341 | 9 | 4039 | 226 | 4243 | 77 | 7 | 99.8 |

| | | | | | | | | |
|---|---|---|---|---|---|---|---|---|
| Z 28 | 4344 | 3 | 4290 | 59 | 4326 | 19 | 1.2 | 99.9 |
| Z 29 | 4254 | 6 | 4191 | 96 | 4233 | 31 | 1.5 | 99.7 |
| Z 30 | 4334 | 5 | 4305 | 73 | 4325 | 23 | 0.7 | 99.9 |
| Z 31 | 4020 | 12 | 3849 | 113 | 3962 | 39 | 4.3 | 99.6 |
| Z 32 | 4334 | 4 | 4196 | 77 | 4289 | 25 | 3.2 | 99.8 |
| Z 33 | 4324 | 5 | 4231 | 94 | 4294 | 30 | 2.2 | 99.8 |
| Z 36 | 4281 | 5 | 4383 | 129 | 4313 | 42 | -2.4 | 99.4 |
| Z 38 | 4151 | 5 | 4114 | 64 | 4139 | 21 | 0.9 | 99.9 |
| Z 39 | 4353 | 8 | 4334 | 137 | 4347 | 43 | 0.4 | 99.5 |
| Z 42 | 4334 | 1 | 4188 | 53 | 4287 | 17 | 3.4 | 100 |
| Z 42 @2 | 4332 | 9 | 4160 | 117 | 4277 | 39 | 4 | 99.5 |
| *14321* | | | | | | | | |
| Z 1* | 4248 | 15 | 3846 | 135 | 4114 | 46 | 9.5 | 99.7 |
| Z 4* | 4176 | 14 | 4025 | 98 | 4126 | 34 | 3.6 | 99.9 |
| Z 7 * | 4224 | 13 | 4147 | 67 | 4199 | 24 | 1.8 | 99.8 |
| Z 8 | 4236 | 13 | 4194 | 108 | 4222 | 35 | 1 | 99.7 |
| Z 8 @2 | 4209 | 41 | 4215 | 136 | 4211 | 51 | -0.1 | 99.7 |
| Z 9* | 4268 | 3 | 4200 | 39 | 4246 | 13 | 1.6 | 99.9 |
| Z 9 @2 | 4273 | 4 | 4266 | 41 | 4271 | 14 | 0.2 | 99.9 |
| Z 9 @3 | 4271 | 3 | 4232 | 41 | 4259 | 14 | 0.9 | 100 |
| Z 9 @4 | 4281 | 4 | 4245 | 47 | 4270 | 16 | 0.8 | 99.9 |
| Z 9 @5 | 4266 | 5 | 4161 | 50 | 4232 | 18 | 2.5 | 99.8 |
| Z 10 | 4294 | 37 | 4407 | 549 | 4330 | 172 | -2.6 | 99.3 |
| Z 10 @2 | 4268 | 10 | 4312 | 523 | 4282 | 166 | -1 | 99.2 |
| Z 11 | 4385 | 4 | 4281 | 324 | 4352 | 104 | 2.4 | 99.8 |
| Z 12 | 4164 | 3 | 4202 | 331 | 4177 | 107 | -0.9 | 99.9 |
| Z 13 | 4327 | 6 | 4228 | 195 | 4295 | 62 | 2.3 | 98.4 |
| Z 13 @2 | 4400 | 3 | 4351 | 312 | 4385 | 99 | 1.1 | 99.9 |
| Z 14 | 4208 | 6 | 3819 | 314 | 4078 | 109 | 9.2 | 99.7 |
| Z 14 @2 | 4216 | 17 | 3010 | 174 | 3779 | 70 | 28.6 | 99.9 |
| Z 14 @3 | 4134 | 31 | 2805 | 225 | 3637 | 95 | 32.1 | 98.9 |
| Z 14 @4 | 4188 | 11 | 5049 | 916 | 4450 | 263 | -20.6 | 98.8 |
| Z 14 @5 | 4205 | 18 | 3980 | 346 | 4130 | 120 | 5.4 | 97.2 |
| Z 15 | 4265 | 7 | 3140 | 212 | 3864 | 84 | 26.4 | 99.8 |
| Z 16 | 4398 | 3 | 4569 | 289 | 4451 | 88 | -3.9 | 99.7 |
| Z 17 | 4097 | 2 | 3917 | 226 | 4037 | 77 | 4.4 | 99.9 |
| Z 19 | 4408 | 3 | 4365 | 288 | 4395 | 91 | 1 | 99.7 |
| Z 20 | 4241 | 5 | 4007 | 251 | 4164 | 84 | 5.5 | 99.7 |
| Z 21 | 4286 | 6 | 4094 | 317 | 4224 | 105 | 4.5 | 99.6 |
| *15311,18* | | | | | | | | |
| Z 1 | 4358 | 7 | 4783 | 519 | 4488 | 154 | -9.8 | 100 |
| Z 2 | 4342 | 4 | 4404 | 415 | 4362 | 130 | -1.4 | 100 |
| Z 5 | 4373 | 31 | 4434 | 190 | 4392 | 60 | -1.4 | 100 |
| Z 6 | 4245 | 4 | 4112 | 176 | 4202 | 53 | 3.1 | 99.9 |

| | | | | | | | | |
|---|---|---|---|---|---|---|---|---|
| Z 6 @2 | 4332 | 3 | 4492 | 189 | 4383 | 58 | -3.7 | 100 |
| Z 6 @3 | 4327 | 3 | 4160 | 150 | 4273 | 49 | 3.9 | 100 |
| Z 7 | 4338 | 4 | 4106 | 189 | 4263 | 62 | 5.3 | 99.9 |
| *15311* | | | | | | | | |
| Z 1 | 4352 | 19 | 4348 | 349 | 4350 | 109 | 0.1 | 100 |
| Z 1 @2 | 4326 | 25 | 4354 | 274 | 4335 | 84 | -0.6 | 100 |
| *15405,75* | | | | | | | | |
| Z 1 | 4338 | 4 | 4182 | 162 | 4288 | 52 | 3.6 | 99.9 |
| Z 4 | 4337 | 10 | 4641 | 307 | 4431 | 95 | -7 | 99.7 |
| Z 5 | 4321 | 6 | 4449 | 141 | 4361 | 44 | -3 | 99.8 |
| Z 6 | 4332 | 5 | 4389 | 138 | 4350 | 43 | -1.3 | 99.9 |
| Z 7 | 4241 | 5 | 4909 | 266 | 4445 | 77 | -15.8 | 99.7 |
| Z 8 | 4323 | 9 | 4004 | 140 | 4219 | 49 | 7.4 | 99.9 |
| Z 9 | 4293 | 4 | 4039 | 113 | 4210 | 38 | 5.9 | 99.8 |
| Z 10 | 4233 | 10 | 4518 | 270 | 4323 | 85 | -6.7 | 99.6 |
| Z 11 | 4332 | 5 | 4323 | 190 | 4329 | 61 | 0.2 | 99.9 |
| Z 12 | 4299 | 5 | 4162 | 188 | 4255 | 62 | 3.2 | 99.8 |
| Z 13 | 4333 | 10 | 4427 | 187 | 4363 | 57 | -2.2 | 98.3 |
| Z 13 @2 | 4333 | 5 | 4748 | 146 | 4461 | 44 | -9.6 | 99.8 |
| *15405,9* | | | | | | | | |
| Z 1 | 4258 | 12 | 3242 | 125 | 3900 | 49 | 23.9 | 100 |
| Z 1 @2 | 4255 | 19 | 3246 | 133 | 3900 | 54 | 23.7 | 100 |
| Z 2 | 4378 | 10 | 4196 | 162 | 4320 | 52 | 4.2 | 99.1 |
| Z 6A | 4305 | 7 | 4482 | 191 | 4360 | 61 | -4.1 | 99.3 |
| Z 6B | 4232 | 7 | 4108 | 289 | 4192 | 96 | 2.9 | 99.6 |
| Z 9B | 4125 | 11 | 3013 | 156 | 3719 | 65 | 27 | 99.9 |
| Z 12 | 4307 | 5 | 3538 | 303 | 4045 | 111 | 17.9 | 99.8 |
| Z 13B | 4333 | 5 | 3652 | 154 | 4104 | 55 | 0.8 | 99.2 |
| Z 15 | 4332 | 13 | 4709 | 183 | 4448 | 56 | -8.7 | 99.4 |
| Z 16 | 4260 | 6 | 4227 | 172 | 4249 | 56 | 0.8 | 99.4 |
| Z 17A | 4270 | 10 | 4173 | 200 | 4239 | 66 | 2.3 | 99.8 |
| Z 17B | 4284 | 4 | 3377 | 287 | 3970 | 109 | 21.2 | 99.9 |
| *15455* | | | | | | | | |
| Z 3 | 4322 | 4 | 4897 | 192 | 4497 | 56 | -13.3 | 99.7 |
| Z 3@2 | 4331 | 3 | 4597 | 331 | 4414 | 101 | -6.1 | 99.7 |
| Z 4 | 4175 | 19 | 3952 | 208 | 4101 | 73 | 5.3 | 99.6 |
| Z 7 | 4320 | 10 | 4605 | 87 | 4409 | 26 | -6.6 | 100 |
| Z 9 | 4101 | 14 | 3992 | 261 | 4065 | 87 | 2.7 | 99.5 |
| Z 10 | 4345 | 4 | 4436 | 296 | 4374 | 93 | -2.1 | 99.8 |
| Z 10@2 | 4347 | 5 | 4139 | 218 | 4281 | 71 | 4.8 | 99.7 |
| Z 11 | 4241 | 18 | 4089 | 220 | 4191 | 76 | 3.6 | 99.8 |
| Z 12 | 4235 | 11 | 4320 | 230 | 4262 | 75 | -2 | 99.8 |

| | | | | | | | | |
|---|---|---|---|---|---|---|---|---|
| Z 19 | 4221 | 9 | 4253 | 219 | 4231 | 70 | -0.8 | 99.6 |
| Z 20 | 4206 | 8 | 4236 | 193 | 4216 | 63 | -0.7 | 99.8 |
| Z 23 | 4280 | 15 | 4233 | 226 | 4265 | 74 | 1.1 | 99.6 |
| Z 24 | 4332 | 3 | 5035 | 315 | 4544 | 91 | -16.2 | 99.6 |
| Z 26 | 4335 | 4 | 4038 | 147 | 4238 | 50 | 6.9 | 99.8 |
| | | | | | | | | |
| *72275* | | | | | | | | |
| Z 1 | 4335 | 5 | 4042 | 141 | 4240 | 48 | 6.8 | 99.9 |
| Z 1 @2 | 4331 | 10 | 3791 | 116 | 4151 | 42 | 12.5 | 100 |
| Z 1 @3 | 4343 | 14 | 4373 | 207 | 4353 | 68 | -0.7 | 99.9 |
| Z 2 | 4334 | 4 | 3952 | 159 | 4209 | 53 | 8.8 | 99.9 |
| Z 14 | 4337 | 3 | 4039 | 164 | 4240 | 55 | 6.9 | 100 |
| Z 14 @2 | 4322 | 9 | 4575 | 193 | 4401 | 61 | -5.9 | 99.9 |
| Z 17 | 4335 | 4 | 4336 | 173 | 4335 | 55 | 0 | 99.9 |
| Z 21 | 4334 | 2 | 4179 | 201 | 4284 | 65 | 3.6 | 99.9 |
| Z 22 | 4334 | 2 | 4412 | 316 | 4359 | 99 | -1.8 | 100 |
| Z 23 | 4140 | 2 | 4224 | 304 | 4167 | 98 | -2 | 99.9 |
| Z 23 @2 | 4339 | 5 | 4488 | 331 | 4386 | 102 | -3.4 | 100 |
| Z 24 | 4328 | 9 | 4616 | 318 | 4417 | 97 | -6.7 | 100 |
| Z 29 | 4305 | 12 | 4440 | 292 | 4348 | 91 | -3.1 | 100 |
| Z 48 | 4333 | 8 | 4087 | 233 | 4253 | 76 | 5.7 | 99.8 |
| Z 49 | 4307 | 4 | 4583 | 238 | 4394 | 73 | -6.4 | 99.2 |

* Annalyses from Taylor et al. 2009 used for age histograms.

**Appendix 2-3: REE and Trace Element Concentrations (ppm)**

| Sample | La | ± 1σ | Ce | ± 1σ | Pr | ± 1σ | Nd | ± 1σ | Sm | ± 1σ | Eu | ± 1σ |
|---|---|---|---|---|---|---|---|---|---|---|---|---|
| 14259 Z8 | 0.12 | 0.02 | 1.82 | 0.07 | 0.49 | 0.06 | 6 | 0.3 | 10.4 | 0.4 | 0.26 | 0.03 |
| 14259 Z9 | 0.08 | 0.01 | 0.88 | 0.1 | 0.09 | 0.03 | 1.3 | 0.1 | 3.3 | 0.2 | 0.07 | 0.03 |
| 14259 Z10 | 0.05 | 0.01 | 0.49 | 0.04 | 0.06 | 0.01 | 1.1 | 0.1 | 2.5 | 0.2 | 0.03 | 0.01 |
| 14259 Z11 | 0.06 | 0.01 | 0.7 | 0.13 | 0.1 | 0.02 | 1.3 | 0.2 | 3.4 | 0.2 | 0.08 | 0.02 |
| 14259 Z13 | 0.04 | 0.01 | 0.66 | 0.05 | 0.08 | 0.01 | 1.3 | 0.1 | 2.9 | 0.2 | 0.06 | 0.03 |
| 14259 Z12 | 0.16 | 0.02 | 1.94 | 0.1 | 0.65 | 0.08 | 9.8 | 0.4 | 13.6 | 0.9 | 0.28 | 0.05 |
| 14305 Z14 | 0.1 | 0.01 | 1.31 | 0.03 | 0.46 | 0.02 | 6.9 | 0.1 | 11.3 | 0.3 | 0.23 | 0.02 |
| 14305 Z18 | 0.1 | 0.01 | 1.34 | 0.06 | 0.4 | 0.05 | 7.3 | 0.3 | 11.6 | 0.4 | 0.22 | 0.03 |
| 14305 Z20 | 0.1 | 0.01 | 1.31 | 0.09 | 0.43 | 0.06 | 6.5 | 0.3 | 11 | 0.8 | 0.22 | 0.03 |
| 14305 Z21 | 0.09 | 0.01 | 1.27 | 0.06 | 0.4 | 0.05 | 6.5 | 0.3 | 11.6 | 0.4 | 0.22 | 0.03 |
| 14305 Z23 | 0.06 | 0.01 | 0.69 | 0.04 | 0.15 | 0.02 | 2.9 | 0.4 | 5.5 | 0.4 | 0.1 | 0.04 |
| 14305 Z23@2 | 0.06 | 0.01 | 0.74 | 0.04 | 0.23 | 0.03 | 3.2 | 0.2 | 6 | 0.3 | 0.1 | 0.02 |
| 14305 Z27 | 0.05 | 0.01 | 0.41 | 0.03 | 0.07 | 0.01 | 1.1 | 0.1 | 2.5 | 0.3 | 0.06 | 0.02 |
| 14305 Z33 | 0.07 |  | 0.81 |  | 0.2 |  | 3 |  | 5.9 |  | 0.19 |  |
| 14305 Z36 | 0.09 | 0.01 | 1.45 | 0.06 | 0.48 | 0.06 | 7.5 | 0.3 | 12.9 | 0.4 | 0.26 | 0.03 |
| 14305 ZC8 | 0.14 | 0.02 | 1.26 | 0.06 | 0.25 | 0.04 | 4.3 | 0.2 | 6.9 | 0.3 | 0.29 | 0.03 |
| 14305 ZC13 | 0.05 | 0.01 | 0.45 | 0.03 | 0.07 | 0.01 | 1.4 | 0.1 | 3 | 0.2 | 0.08 | 0.03 |
| 14305 ZC15 | 0.11 | 0.02 | 0.77 | 0.04 | 0.09 | 0.02 | 1.3 | 0.1 | 2.4 | 0.3 | 0.08 | 0.02 |
| 14305 ZC19 | 0.18 | 0.05 | 1.04 | 0.2 | 0.12 | 0.04 | 1.6 | 0.1 | 3.1 | 0.3 | 0.19 | 0.07 |
| 14321 Z10 | 0.06 | 0.01 | 0.56 | 0.05 | 0.06 | 0.02 | 1 | 0.1 | 2.2 | 0.2 | 0.07 | 0.03 |
| 14321 Z11 | 0.06 | 0.01 | 0.59 | 0.05 | 0.12 | 0.02 | 2.4 | 0.1 | 5.3 | 0.2 | 0.12 | 0.01 |
| 14321 Z14@1 | 0.05 | 0.01 | 0.47 | 0.03 | 0.09 | 0.02 | 2.2 | 0.6 | 4.2 | 0.2 | 0.12 | 0.02 |
| 14321 Z14@2 | 0.05 | 0.01 | 0.59 | 0.04 | 0.09 | 0.02 | 1.7 | 0.1 | 3.4 | 0.2 | 0.09 | 0.02 |
| 14321 Z14@3 | 0.05 | 0.01 | 0.54 | 0.04 | 0.11 | 0.02 | 1.7 | 0.2 | 3.3 | 0.3 | 0.1 | 0.02 |
| 14321 Z14@4 | 0.05 | 0.01 | 0.57 | 0.06 | 0.11 | 0.02 | 1.8 | 0.2 | 3.9 | 0.2 | 0.09 | 0.03 |
| 14321 Z14@5 | 0.03 | 0.01 | 0.51 | 0.03 | 0.09 | 0.02 | 1.3 | 0.1 | 3 | 0.2 | 0.07 | 0.03 |
| 14321 Z14@6 | 0.06 | 0.01 | 0.53 | 0.04 | 0.11 | 0.02 | 1.7 | 0.2 | 3.2 | 0.2 | 0.08 | 0.02 |

| Sample | La | ± 1σ | Ce | ± 1σ | Pr | ± 1σ | Nd | ± 1σ | Sm | ± 1σ | Eu | ± 1σ |
|---|---|---|---|---|---|---|---|---|---|---|---|---|
| 14321 Z14@7 | 0.05 | 0.01 | 0.53 | 0.03 | 0.11 | 0.02 | 1.5 | 0.1 | 3.5 | 0.3 | 0.09 | 0.02 |
| 14321 Z17 | 0.22 | 0.04 | 4.07 | 0.13 | 1.52 | 0.14 | 23.5 | 1 | 38.4 | 0.9 | 2.01 | 0.1 |
| 14321 Z20 | 0.14 | 0.02 | 1.72 | 0.07 | 0.52 | 0.07 | 8.7 | 0.4 | 14.5 | 0.5 | 0.23 | 0.03 |
| 14321 Z21 | 0.07 | 0.01 | 0.56 | 0.04 | 0.13 | 0.02 | 2.6 | 0.2 | 6.3 | 0.3 | 0.12 | 0.02 |
| 15311 Z7 | 0.05 | 0.01 | 0.84 | 0.09 | 0.16 | 0.03 | 3.1 | 0.2 | 6.3 | 0.5 | 0.08 | 0.02 |
| 15311 Z6@1 | 0.39 | 0.08 | 3.04 | 0.1 | 1.01 | 0.14 | 16.8 | 0.6 | 24.4 | 2.3 | 0.37 | 0.04 |
| 15405,9 Z6 | 0.14 | 0.02 | 0.81 | 0.07 | 0.16 | 0.03 | 2.3 | 0.3 | 4.5 | 0.3 | 0.09 | 0.02 |
| 15405, 9 Z7B | 0.18 | 0.02 | 1.69 | 0.06 | 0.54 | 0.06 | 7.6 | 0.3 | 11.8 | 0.7 | 0.31 | 0.03 |
| 15405,9 Z13B@1 | 0.06 | 0.01 | 1.13 | 0.08 | 0.22 | 0.05 | 3.4 | 0.2 | 6.3 | 0.3 | 0.08 | 0.02 |
| 15405,9 Z13B@2 | 0.09 | 0.01 | 1.58 | 0.13 | 0.43 | 0.07 | 6.8 | 0.4 | 10.5 | 1 | 0.17 | 0.03 |
| 15405,9 Z13B@3 | 0.16 | 0.02 | 2.55 | 0.12 | 0.88 | 0.11 | 12.9 | 0.9 | 19.7 | 0.6 | 0.32 | 0.04 |
| 15405,9 Z13B@4 | 0.33 | 0.03 | 5.6 | 0.15 | 2.08 | 0.17 | 27.3 | 0.8 | 37.8 | 0.9 | 0.66 | 0.06 |
| 15405,9 Z17A | 0.24 | 0.02 | 2.16 | 0.08 | 0.68 | 0.06 | 10 | 0.4 | 16 | 1 | 0.18 | 0.03 |
| 15405,9 Z26 | 0.36 | 0.03 | 4.11 | 0.63 | 0.95 | 0.16 | 14.1 | 0.5 | 23.1 | 0.5 | 0.38 | 0.07 |
| 15405,75 Z1 | 0.2 | 0.02 | 2.73 | 0.09 | 0.85 | 0.09 | 13.5 | 0.7 | 22.7 | 0.6 | 0.22 | 0.03 |
| 15405,75 Z8 | 0.07 | 0.01 | 0.85 | 0.1 | 0.23 | 0.05 | 3.6 | 0.3 | 6.7 | 0.4 | 0.11 | 0.03 |
| 15405,75 Z11 | 0.17 | 0.02 | 2.18 | 0.1 | 0.85 | 0.1 | 13.5 | 0.5 | 21 | 0.6 | 0.22 | 0.03 |
| 15405,75 Z13 | 0.05 | 0.01 | 0.74 | 0.07 | 0.14 | 0.04 | 2.7 | 0.3 | 5.2 | 0.5 | 0.07 | 0.02 |
| 15455,226 Z10 | 0.12 | 0.01 | 1.11 | 0.06 | 0.26 | 0.05 | 3.3 | 0.5 | 6.1 | 1.2 | 0.27 | 0.05 |
| 72274 Z14 | 0.17 | 0.02 | 1.75 | 0.09 | 0.39 | 0.04 | 4.8 | 0.3 | 8.2 | 0.5 | 0.18 | 0.03 |
| 72275 Z17 | 0.07 | 0.01 | 0.87 | 0.04 | 0.17 | 0.02 | 2.8 | 0.2 | 5.9 | 0.3 | 0.34 | 0.03 |
| 72275 Z24 | 0.05 | 0.01 | 0.61 | 0.04 | 0.11 | 0.02 | 1.3 | 0.1 | 3.1 | 0.2 | 0.08 | 0.02 |
| 72275 Z29 | 0.07 | 0.01 | 0.78 | 0.08 | 0.11 | 0.02 | 1.8 | 0.2 | 3.4 | 0.2 | 0.11 | 0.03 |
| 72275 Z43 | 0.16 | 0.02 | 1.54 | 0.08 | 0.22 | 0.03 | 3.2 | 0.2 | 6.2 | 0.3 | 0.18 | 0.03 |
| 72275 Z48 | 0.22 | 0.03 | 2.89 | 0.09 | 1.14 | 0.1 | 18.3 | 0.6 | 29.5 | 0.7 | 0.87 | 0.06 |

| Sample | Gd | ± 1σ | Tb | ± 1σ | Dy | ± 1σ | Ho | ± 1σ | Er | ± 1σ | Tm | ± 1σ |
|---|---|---|---|---|---|---|---|---|---|---|---|---|
| 14259 Z8 | 41 | 2 | 21 | 1 | 264 | 8 | 101 | 5 | 438 | 14 | 93 | 12 |
| 14259 Z9 | 17 | 2 | 8 | 1 | 105 | 3 | 42 | 3 | 184 | 8 | 41 | 18 |
| 14259 Z10 | 12 | 1 | 7 | 1 | 95 | 3 | 40 | 3 | 187 | 6 | 41 | 14 |
| 14259 Z11 | 17 | 3 | 9 | 1 | 116 | 3 | 47 | 3 | 206 | 6 | 46 | 10 |
| 14259 Z13 | 15 | 1 | 7 | 1 | 92 | 3 | 35 | 3 | 149 | 5 | 31 | 13 |
| 14259 Z12 | 50 | 2 | 22 | 1 | 232 | 8 | 83 | 6 | 319 | 10 | 60 | 11 |
| 14305 Z14 | 44 | 1 | 20 | 1 | 221 | 3 | 80 | 4 | 317 | 5 | 61 | 7 |
| 14305 Z18 | 47 | 2 | 22 | 1 | 237 | 2 | 87 | 3 | 337 | 4 | 67 | 9 |
| 14305 Z20 | 44 | 3 | 19 | 1 | 214 | 6 | 77 | 6 | 303 | 9 | 59 | 9 |
| 14305 Z21 | 43 | 2 | 21 | 1 | 223 | 4 | 82 | 3 | 316 | 6 | 62 | 8 |
| 14305 Z23 | 27 | 2 | 15 | 2 | 175 | 5 | 69 | 6 | 297 | 9 | 64 | 23 |
| 14305 Z23@2 | 27 | 2 | 15 | 1 | 183 | 1 | 70 | 3 | 304 | 4 | 66 | 12 |
| 14305 Z27 | 13 | 1 | 7 | 1 | 99 | 7 | 40 | 6 | 186 | 15 | 42 | 13 |
| 14305 Z33 | 26 |  | 15 |  | 191 |  | 77 |  | 344 |  | 79 | 11 |
| 14305 Z36 | 52 | 2 | 24 | 1 | 264 | 2 | 97 | 4 | 375 | 8 | 73 | 9 |
| 14305 ZC8 | 29 | 2 | 17 | 1 | 214 | 2 | 86 | 4 | 381 | 4 | 86 | 10 |
| 14305 ZC13 | 14 | 1 | 9 | 1 | 115 | 1 | 47 | 3 | 219 | 3 | 49 | 16 |
| 14305 ZC15 | 10 | 1 | 5 | 1 | 71 | 1 | 30 | 3 | 131 | 3 | 29 | 6 |
| 14305 ZC19 | 14 | 3 | 8 | 1 | 98 | 1 | 40 | 3 | 181 | 2 | 40 | 14 |
| 14321 Z10 | 11 | 1 | 5 | 1 | 68 | 2 | 26 | 2 | 112 | 4 | 23 | 9 |
| 14321 Z11 | 24 | 2 | 15 | 1 | 180 | 1 | 73 | 3 | 325 | 4 | 74 | 15 |
| 14321 Z14@1 | 20 | 3 | 10 | 3 | 113 | 3 | 43 | 3 | 176 | 4 | 37 | 7 |
| 14321 Z14@2 | 16 | 1 | 8 | 1 | 99 | 2 | 39 | 3 | 164 | 2 | 34 | 7 |
| 14321 Z14@3 | 16 | 1 | 9 | 1 | 104 | 2 | 39 | 4 | 168 | 2 | 34 | 7 |
| 14321 Z14@4 | 19 | 2 | 10 | 1 | 119 | 1 | 45 | 3 | 188 | 3 | 39 | 11 |
| 14321 Z14@5 | 16 | 1 | 8 | 1 | 99 | 1 | 40 | 3 | 166 | 5 | 34 | 17 |
| 14321 Z14@6 | 16 | 1 | 8 | 1 | 101 | 1 | 38 | 3 | 161 | 3 | 34 | 10 |

| Sample | Gd | ± 1σ | Tb | ± 1σ | Dy | ± 1σ | Ho | ± 1σ | Er | ± 1σ | Tm | ± 1σ |
|---|---|---|---|---|---|---|---|---|---|---|---|---|
| 14321 Z14@7 | 16 | 1 | 8 | 1 | 101 | 2 | 39 | 4 | 160 | 2 | 34 | 7 |
| 14321 Z17 | 144 | 4 | 71 | 3 | 783 | 21 | 285 | 11 | 1122 | 33 | 227 | 14 |
| 14321 Z20 | 64 | 2 | 30 | 1 | 323 | 10 | 117 | 5 | 459 | 14 | 87 | 11 |
| 14321 Z21 | 29 | 2 | 14 | 1 | 168 | 5 | 62 | 3 | 260 | 8 | 52 | 9 |
| 15311 Z7 | 29 | 3 | 15 | 1 | 180 | 5 | 70 | 6 | 305 | 10 | 66 | 14 |
| 15311 Z6@1 | 94 | 5 | 44 | 3 | 482 | 22 | 175 | 20 | 696 | 36 | 139 | 16 |
| 15405,9 Z6 | 31 | 3 | 14 | 2 | 190 | 2 | 77 | 7 | 367 | 4 | 84 | 23 |
| 15405, 9 Z7B | 40 | 2 | 22 | 1 | 256 | 2 | 97 | 6 | 413 | 11 | 90 | 9 |
| 15405,9 Z13B@1 | 27 | 2 | 15 | 1 | 184 | 12 | 74 | 5 | 325 | 15 | 72 | 20 |
| 15405,9 Z13B@2 | 40 | 4 | 21 | 2 | 249 | 11 | 97 | 11 | 416 | 21 | 90 | 13 |
| 15405,9 Z13B@3 | 70 | 4 | 36 | 3 | 419 | 7 | 157 | 9 | 654 | 11 | 139 | 17 |
| 15405,9 Z13B@4 | 121 | 5 | 60 | 4 | 674 | 8 | 242 | 13 | 973 | 14 | 203 | 20 |
| 15405,9 Z17A | 59 | 3 | 33 | 2 | 395 | 7 | 154 | 13 | 681 | 10 | 150 | 26 |
| 15405,9 Z26 | 110 | 17 | 41 | 2 | 459 | 8 | 165 | 8 | 659 | 6 | 131 | 24 |
| 15405,75 Z1 | 107 | 4 | 41 | 2 | 455 | 5 | 165 | 7 | 668 | 7 | 133 | 20 |
| 15405,75 Z8 | 40 | 5 | 17 | 2 | 205 | 3 | 79 | 6 | 342 | 6 | 73 | 20 |
| 15405,75 Z11 | 95 | 4 | 37 | 2 | 415 | 6 | 153 | 7 | 607 | 10 | 123 | 19 |
| 15405,75 Z13 | 32 | 3 | 13 | 2 | 167 | 2 | 65 | 7 | 292 | 4 | 63 | 21 |
| 15455,226 Z10 | 31 | 6 | 13 | 3 | 163 | 24 | 65 | 16 | 287 | 41 | 65 | 16 |
| 72274 Z14 | 41 | 3 | 18 | 2 | 232 | 2 | 90 | 6 | 399 | 4 | 89 | 11 |
| 72275 Z17 | 26 | 2 | 14 | 1 | 174 | 5 | 68 | 5 | 291 | 9 | 64 | 8 |
| 72275 Z24 | 14 | 1 | 9 | 1 | 112 | 2 | 48 | 3 | 224 | 3 | 53 | 11 |
| 72275 Z29 | 17 | 2 | 9 | 1 | 111 | 1 | 43 | 3 | 181 | 5 | 38 | 10 |
| 72275 Z43 | 26 | 2 | 12 | 1 | 139 | 3 | 50 | 3 | 200 | 2 | 40 | 6 |
| 72275 Z48 | 104 | 5 | 51 | 3 | 554 | 7 | 199 | 10 | 773 | 12 | 151 | 12 |

| Sample | Yb | ± 1σ | Lu | ± 1σ | Y | ± 1σ | $^{178}$Hf | ± 1σ | Th | ± 1σ | U | ± 1σ |
|---|---|---|---|---|---|---|---|---|---|---|---|---|
| 14259 Z8 | 800 | 183 | 162 | 10 | 1933 | 100 | 10937 | 100 | 51 | 2.6 | 96 | 8.7 |
| 14259 Z9 | 361 | 83 | 77 | 8 | 842 | 43 | 10808 | 92 | 19 | 1.9 | 49 | 2.7 |
| 14259 Z10 | 372 | 85 | 80 | 9 | 1273 | 41 | 11439 | 55 | 14 | 0.7 | 37 | 2.4 |
| 14259 Z11 | 402 | 93 | 86 | 14 | 928 | 48 | 10871 | 103 | 20 | 1.2 | 50 | 3.8 |
| 14259 Z13 | 266 | 61 | 54 | 6 | 696 | 37 | 11458 | 66 | 5 | 0.4 | 13 | 0.9 |
| 14259 Z12 | 478 | 109 | 94 | 6 | 1590 | 102 | 10874 | 54 | 15 | 1.2 | 22 | 1.4 |
| 14305 Z14 | 493 | 22 | 99 | 6 | 1600 | 39 | 9254 | 512 | 13 | 0.4 | 22 | 1 |
| 14305 Z18 | 529 | 24 | 109 | 6 | 2688 | 88 | 10194 | 131 | 14 | 0.5 | 20 | 1.7 |
| 14305 Z20 | 476 | 109 | 96 | 6 | 1538 | 81 | 10283 | 149 | 11 | 0.6 | 18 | 1.1 |
| 14305 Z21 | 504 | 25 | 103 | 5 | 2514 | 80 | 10075 | 183 | 11 | 0.7 | 20 | 1.4 |
| 14305 Z23 | 553 | 127 | 114 | 17 | 1350 | 70 | 9809 | 521 | 28 | 1.3 | 59 | 3.6 |
| 14305 Z23@2 | 564 | 34 | 119 | 8 | 2151 | 65 | 10710 | 239 | 28 | 0.7 | 57 | 2 |
| 14305 Z27 | 383 | 88 | 82 | 12 | 800 | 106 | 11385 | 261 | 14 | 1 | 42 | 4.5 |
| 14305 Z33 | 711 | 51 | 153 |  | 2307 | 91 | 10728 | 138 | 40 | 0.9 | 82 | 3 |
| 14305 Z36 | 581 | 26 | 117 | 7 | 1797 | 98 | 10304 | 120 | 15 | 0.6 | 24 | 0.9 |
| 14305 ZC8 | 740 | 39 | 154 | 9 | 2546 | 95 | 10855 | 184 | 43 | 1 | 77 | 1.7 |
| 14305 ZC13 | 443 | 33 | 95 | 10 | 1467 | 45 | 11268 | 129 | 17 | 0.6 | 47 | 1.7 |
| 14305 ZC15 | 261 | 16 | 57 | 6 | 893 | 28 | 11074 | 187 | 12 | 0.5 | 26 | 0.9 |
| 14305 ZC19 | 359 | 69 | 77 | 7 | 1248 | 39 | 11103 | 177 | 11 | 0.7 | 32 | 3.2 |
| 14321 Z10 | 199 | 46 | 41 | 6 | 520 | 27 | 10954 | 181 | 4 | 0.3 | 11 | 0.9 |
| 14321 Z11 | 633 | 40 | 135 | 8 | 2232 | 47 | 10540 | 90 | 15 | 1.3 | 38 | 3 |
| 14321 Z14@1 | 313 | 50 | 65 | 19 | 1330 | 40 | 11057 | 152 | 7 | 0.6 | 16 | 1.8 |
| 14321 Z14@2 | 286 | 20 | 62 | 6 | 1219 | 39 | 11092 | 158 | 5 | 0.3 | 17 | 0.7 |
| 14321 Z14@3 | 287 | 20 | 62 | 8 | 1242 | 47 | 11001 | 174 | 6 | 0.3 | 16 | 1.4 |
| 14321 Z14@4 | 324 | 34 | 68 | 6 | 1417 | 66 | 11018 | 139 | 8 | 0.4 | 19 | 2.2 |
| 14321 Z14@5 | 285 | 22 | 60 | 6 | 1229 | 39 | 10922 | 190 | 7 | 0.6 | 18 | 1 |
| 14321 Z14@6 | 286 | 21 | 61 | 7 | 1209 | 38 | 11079 | 114 | 6 | 0.4 | 14 | 0.6 |

| Sample | Yb | ± 1σ | Lu | ± 1σ | Y | ± 1σ | $^{178}$Hf | ± 1σ | Th | ± 1σ | U | ± 1σ |
|---|---|---|---|---|---|---|---|---|---|---|---|---|
| 14321 Z14@7 | 288 | 22 | 61 | 6 | 1208 | 37 | 11060 | 136 | 6 | 0.3 | 16 | 2.2 |
| 14321 Z17 | 1834 | 406 | 371 | 22 | 8443 | 277 | 11254 | 195 | 92 | 4.2 | 106 | 7.1 |
| 14321 Z20 | 140 | 152 | 134 | 8 | 3559 | 117 | 9749 | 487 | 21 | 1.4 | 39 | 2 |
| 14321 Z21 | 88 | 96 | 87 | 7 | 1952 | 67 | 9974 | 508 | 9 | 1.3 | 20 | 1.4 |
| 15311 Z7 | 574 | 132 | 115 | 9 | 1363 | 76 | 10879 | 80 | 34 | 1.6 | 81 | 4.5 |
| 15311 Z6@1 | 1121 | 257 | 214 | 21 | 3285 | 297 | 10038 | 203 | 74 | 10.3 | 105 | 10.5 |
| 15405,9 Z6 | 762 | 84 | 154 | 1 | 2221 | 18 | 12266 | 162 | 67 | 0.6 | 149 | 2.5 |
| 15405, 9 Z7B | 789 | 34 | 157 | 7 | 2884 | 86 | 11202 | 183 | 93 | 2.5 | 199 | 8.9 |
| 15405,9 Z13B@1 | 638 | 68 | 131 | 10 | 2199 | 165 |  |  | 54 | 3.8 | 120 | 7.1 |
| 15405,9 Z13B@2 | 783 | 86 | 157 | 15 | 2867 | 166 | 10652 | 200 | 89 | 1.7 | 150 | 4.6 |
| 15405,9 Z13B@3 | 1168 | 84 | 230 | 21 | 4482 | 270 | 11722 | 193 | 169 | 2.1 | 228 | 4.1 |
| 15405,9 Z13B@4 | 1672 | 88 | 320 | 22 | 6848 | 446 | 11525 | 221 | 309 | 8 | 333 | 16 |
| 15405,9 Z17A | 1291 | 79 | 263 | 18 | 4446 | 167 | 10816 | 155 | 196 | 2.3 | 390 | 6.4 |
| 15405,9 Z26 | 1085 | 179 | 197 | 2 | 4877 | 15 | 9607 | 120 | 63 | 0.9 | 96 | 2.3 |
| 15405,75 Z1 | 1048 | 43 | 211 | 12 | 4853 | 265 | 9559 | 101 | 54 | 1.3 | 82 | 4.7 |
| 15405,75 Z8 | 637 | 81 | 131 | 12 | 2397 | 147 | 9672 | 98 | 28 | 2.2 | 68 | 3.9 |
| 15405,75 Z11 | 999 | 51 | 193 | 9 | 4469 | 263 | 9571 | 95 | 63 | 3.5 | 95 | 3.7 |
| 15405,75 Z13 | 554 | 51 | 113 | 13 | 1964 | 107 | 10535 | 128 | 39 | 1.7 | 90 | 3.4 |
| 15455,226 Z10 | 611 | 142 | 118 | 14 | 1804 | 242 | 11192 | 80 | 25 |  | 56 |  |
| 72274 Z14 | 804 | 62 | 151 | 13 | 1691 | 76 | 11438 | 199 | 50 | 1.8 | 92 | 3 |
| 72275 Z17 | 576 | 43 | 117 | 12 | 1988 | 73 | 11571 | 344 | 19 | 1.8 | 38 | 1.7 |
| 72275 Z24 | 497 | 32 | 107 | 11 | 1469 | 44 | 11672 | 233 | 23 | 1.3 | 70 | 2.5 |
| 72275 Z29 | 323 | 33 | 68 | 6 | 1334 | 44 | 10804 | 138 | 6 | 0.3 | 14 | 0.7 |
| 72275 Z43 | 328 | 20 | 65 | 5 | 1573 | 74 | 9867 | 102 | 6 | 0.5 | 13 | 1.5 |
| 72275 Z48 | 1167 | 65 | 230 | 14 | 5839 | 222 | 10036 | 98 | 47 | 1 | 70 | 2.1 |

| Sample | $^{49}$Ti | ± 1σ | $^{57}$Fe | ± 1σ | Ti-Temp (°C) | Error* |
|---|---|---|---|---|---|---|
| 14259 Z8 | 55 | 1.2 | 439 | 5 | 1064 | 64 |
| 14259 Z9 | 69 | 1.7 | 108 | 4 | 1101 | 68 |
| 14259 Z10 | 64 | 1.6 | 107 | 4 | 1089 | 67 |
| 14259 Z11 | 74 | 1.8 | 104 | 4 | 1114 | 69 |
| 14259 Z13 | 103 | 2.3 | 107 | 4 | 1174 | 75 |
| 14259 Z12 | 121 | 5.2 | 115 | 5 | 1205 | 82 |
| 14305 Z14 | 195 | 3 | 109 | 4 | 1305 | 88 |
| 14305 Z18 | 187 | 3.6 | 109 | 2.8 | 1296 | 87 |
| 14305 Z20 | 184 | 3.7 | 107 | 4 | 1292 | 87 |
| 14305 Z21 | 188 | 3.6 | 116 | 2.8 | 1297 | 87 |
| 14305 Z23 | 72 | 1.8 | 113 | 4.2 | 1109 | 69 |
| 14305 Z23@2 | 72 | 1.7 | 114 | 2.8 | 1109 | 68 |
| 14305 Z27 | 62 | 4.8 | 125 | 11.4 | 1083 | 75 |
| 14305 Z33 | 82 | 1.9 | 106 | 3.9 | 1132 | 71 |
| 14305 Z36 | 194 | 3.9 | 109 | 2.7 | 1304 | 88 |
| 14305 ZC8 | 89 | 2 | 277 | 40.2 | 1146 | 72 |
| 14305 ZC13 | 61 | 1.5 | 111 | 3.9 | 1081 | 66 |
| 14305 ZC15 | 167 | 3.3 | 125 | 3 | 1271 | 85 |
| 14305 ZC19 | 209 | 13.3 | 284 | 26.1 | 1321 | 100 |
| 14321 Z10 | 113 | 2.5 | 110 | 4.1 | 1191 | 77 |
| 14321 Z11 | 73 | 1.5 | 107 | 2.9 | 1111 | 68 |
| 14321 Z14@1 | 149 | 3 | 102 | 5 | 1247 | 82 |
| 14321 Z14@2 | 142 | 2.9 | 107 | 2.8 | 1237 | 81 |
| 14321 Z14@3 | 144 | 2.9 | 105 | 2.7 | 1240 | 81 |
| 14321 Z14@4 | 149 | 3 | 107 | 3.5 | 1247 | 82 |
| 14321 Z14@5 | 142 | 2.9 | 108 | 2.8 | 1237 | 81 |
| 14321 Z14@6 | 142 | 2.9 | 106 | 4.6 | 1237 | 81 |

*Errors include the range in activities and the 1σ errors in Ti-concentrations.

| Sample | $^{49}$Ti | ± 1σ | $^{57}$Fe | ± 1σ | Ti-Temp (°C) | Error* |
|---|---|---|---|---|---|---|
| 14321 Z14@7 | 141 | 2.9 | 101 | 2.7 | 1236 | 81 |
| 14321 Z17 | 64 | 1.4 | 115 | 4.3 | 1089 | 66 |
| 14321 Z20 | 132 | 2.8 | 111 | 4.2 | 1222 | 80 |
| 14321 Z21 | 119 | 2.6 | 104 | 4.1 | 1201 | 78 |
| 15311 Z7 | 47 | 1.2 | 117 | 4.2 | 1039 | 62 |
| 15311 Z6@1 | 116 | 2.9 | 141 | 5.7 | 1196 | 78 |
| 15405,9 Z6 | 27 | 1.1 | 78 | 10.2 | 958 | 57 |
| 15405, 9 Z7B | 34 | 1.3 | 737 | 38 | 990 | 59 |
| 15405,9 Z13B@1 | 30 | 1 | 133 | 7.5 | 972 | 57 |
| 15405,9 Z13B@2 | 32 | 1 | 138 | 6.9 | 982 | 57 |
| 15405,9 Z13B@3 | 50 | 1.3 | 206 | 11.3 | 1049 | 63 |
| 15405,9 Z13B@4 | 77 | 1.7 | 216 | 9.4 | 1120 | 69 |
| 15405,9 Z17A | 62 | 1.5 | 653 | 20.8 | 1083 | 66 |
| 15405,9 Z26 | 173 | 2.7 | 244 | 28.6 | 1279 | 85 |
| 15405,75 Z1 | 110 | 2.3 | 302 | 20.6 | 1186 | 76 |
| 15405,75 Z8 | 80 | 2.2 | 88 | 9.8 | 1127 | 71 |
| 15405,75 Z11 | 91 | 2.1 | 141 | 11.7 | 1150 | 73 |
| 15405,75 Z13 | 75 | 2.9 | 178 | 13.9 | 1116 | 72 |
| 15455,226 Z10 | 64 | 1.4 | 162 | 16.3 | 1089 | 66 |
| 72274 Z14 | 44 | 1 | 266 | 5.7 | 1029 | 61 |
| 72275 Z17 | 95 | 2.1 | 88 | 2.4 | 1158 | 73 |
| 72275 Z24 | 119 | 2.5 | 117 | 2.8 | 1201 | 77 |
| 72275 Z29 | 111 | 2.4 | 149 | 4.3 | 1188 | 76 |
| 72275 Z43 | 200 | 6.1 | 352 | 16.6 | 1311 | 92 |
| 72275 Z48 | 147 | 3.3 | 203 | 9.6 | 1244 | 82 |

*Errors include the range in activities and the 1σ errors in Ti-concentrations.

## Chapter 3: Survey of Shock Microstructures in Zircons from Apollo 14 and 15

### 3.1 Introduction

The crystalline structures of minerals are susceptible to deformation via pressure shocks induced by impact events. Zircon shock microstructures were first reported in grains from the Sudbury impact structure (Krogh et al., 1984), and later the Chicxulub impact crater and K/T boundary ejecta (Bohor et al., 1993; Krogh et al., 1993). Both planar defect features and recrystallization textures were observed and found to be associated with varying levels of Pb-loss. Shock-recrystallized zircons have also been used to constrain the age of the Vrederfort impact structure in South Africa in tandem with unshocked grains crystallized from impact-related magmas (e.g. Gibson et al., 1997; Moser, 1997). More recent studies have identified a range of impact induced microstructures in Vrederfort zircons including shock microtwin lamellae and crystal-plastic deformation (Moser et al., 2011). Additionally, the shock conditions necessary to form zircon microstructures and the sequence in which they manifest have been better constrained through laboratory experiments and detailed study of both terrestrial and lunar zircons (e.g. Deutsch and Schärer, 1990; Leroux et al., 1999; Timms et al., 2012).

Shock microstructures have been documented in lunar zircons, but the degree of associated Pb-loss appears to be less than in similarly shocked terrestrial grains, except in cases of polycrystalline texture where Pb-loss is assumed to be ~100% (e.g. Grange et al., 2013; and references therein). Grange et al. (2013) presented guidelines for interpreting U-Pb ages of lunar zircons based on microstructural analyses of 12 grains. They observed

varying amounts of Pb-loss accompanying crystal-plastic deformation (CPD), planar features, and shock microtwin lamellae, and they suggest that in some cases limits can be placed on both impact and crystallization ages.

An inventory of shock microstructures in lunar zircons would be potentially informative as to the pressure and temperature conditions experienced by the Apollo samples, and would thus aid in interpreting the large datasets of lunar zircon U-Pb and $^{207}Pb$-$^{206}Pb$ ages. We have conducted a survey of 34 zircons separated from Apollo 14 and 15 soil and breccia samples to better characterize the abundance of individual shock microstructures in the lunar zircon population.

### 3.2 Overview of Shock Microstructures

Moser et al. (2011), Timms et al. (2012), and Erickson et al. (2013) have all made notable advancements towards understanding the of mechanisms for forming, and the sequence of forming, shock microstructures in zircon, generally in the crater floor environment. Together, their findings (based on EBSD structural analyses and cross-cutting relationships) can be summarized into the following sequence of microstructure formation with increasing shock pressures:

1. Planar features with (010) and (100), or c-axis parallel orientation

    1A. Fine grained granular recrystallization and decomposition to baddeleyite and $SiO_2$ in ejecta zircons.

2. Planar features with {112} orientation (all four orientations have previously been observed)
3. Curviplanar features and impregnation of impact generated melt (later referred to as impact melt glass inclusions)
4. Planar features with (011) orientation
5. Microtwins in {112} orientation (Erickson et al. (2013) place this along with the formation of planar features in step 2)
6. Crystal-plastic deformation (thought to form at lower pressures and higher temperatures)
7. Granular texture recrystalliation and decomposition of zircon to $ZrO_2$ and $SiO_2$ (thought to occur in high pressure and high temperature environments)

Shock experiments have also been used to constrain the pressures at which these microstructures form (Leroux et al., 1999). Planar fractures parallel to {100} were observed in experimental runs with pressures above 20 GPa, and zircon converted to its high pressure phase, reidite, at pressures above 40 GPa. Reidite has thus far not been observed in lunar zircons, but has recently been identified in terrestrial zircons from the Ries and Chesapeake Bay impact structures (Glass and Liu, 2001). In the shock experiments, more reidite domains were observed at >60 GPa, in addition to microtwins with {112} orientation, granular texture, and planar features hosting amorphous zircon. Wittmann et al. (2006) produced the first time-temperature history schema for zircon microstructures and Timms et al. (2012) produced a more detailed shock deformation map (Figure 3-1, reproduced from Timms et al. (2012)) that combines experimental data

and recent observations of natural samples. The map can be used to help determine the P-T paths experienced by zircons based on their microstructural characteristics, although caution must be used because some of the P-T domains are not well constrained (in particular the decomposition of zircon to its constituent oxides).

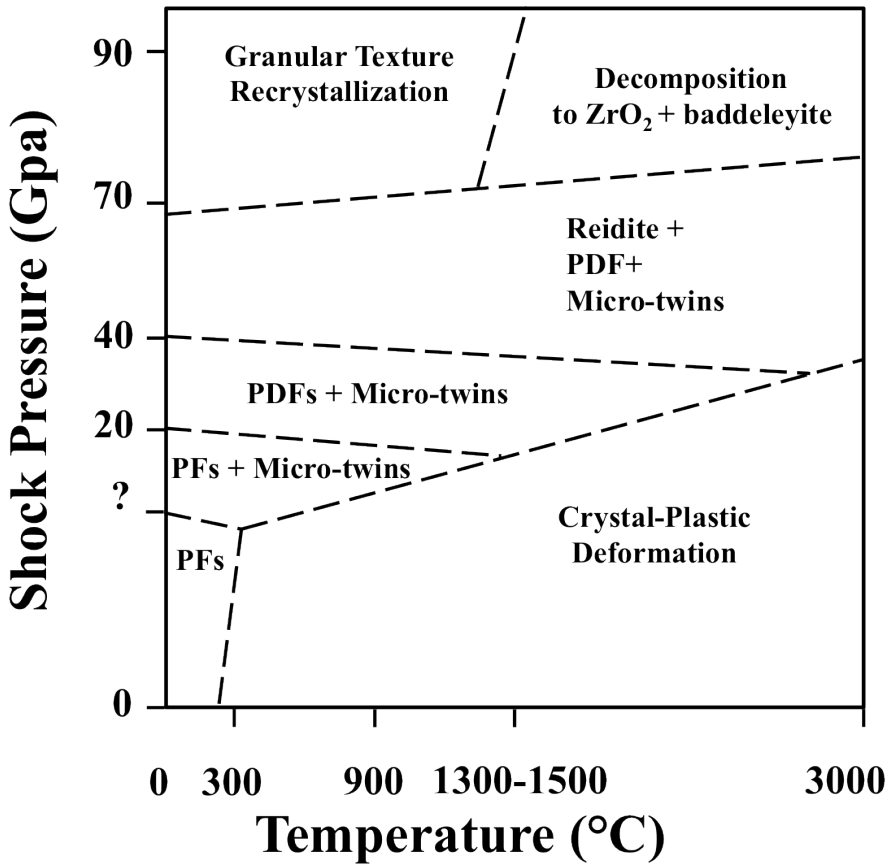


Figure 3-1: Diagram reproduced from Timms et al. (2012) illustrating the pressure and temperature conditions required for the formation of shock microstructures in zircon. The boundaries were constrained using both experimental data and observations of zircons from terrestrial impact structures.

## 3.3 Sample Descriptions

Our survey included a subset of the lunar zircons discussed in Chapter 2. The zircons were separated from soils 14259 and 15311, as well as breccias 14305 and 14321. Detailed descriptions of these samples can be found in section 2.2.

## 3.4 Analyses

### *3.4.1 Sample Preparation*

Zircons were separated from lunar breccia and soil samples by crushing, standard heavy liquid (methylene iodide) density separation, and hand picking under an optical microscope aided by ultraviolet light (see Chapter 2). Zircons then were positively identified by energy-dispersive X-ray spectroscopy (EDS) on the UCLA Tescan Scanning Electron Microscope (SEM). The samples were then mounted in 1-inch epoxy rounds and polished with a 1 μm alumina slurry on a Vibromet automatic polisher for 45 minutes. The last step prior to SEM analyses was to coat the samples with a thin layer of carbon to make them conductive and reduce sample charging that interferes with electron imaging.

### *3.4.2 Microbeam Analyses*

We collected SEM micrographs (SE, BSE, CL)and electron backscatter diffraction (EBSD) measurements for 30 lunar zircons following the analytical methods outlined in Moser et al. (2011). Analyses were made using the Hitachi SU6600 field emission gun

(FEG)-SEM in the Zircon and Accessory Phase ("ZAP") Laboratory at the University of Western Ontario. Secondary electron (SE) and backscatter electron (BSE) images of carbon coated epoxy mounts containing lunar zircons were collected using a 5kV accelerating voltage. The relatively low voltage can produce a channeling effect from the lattice planes that most efficiently diffract electrons. This has the effect of accentuating any variations in crystallographic orientation and is a useful comparison with proxy images of chemical variation and zoning in average atomic number exhibited by grey scale variations in conventional higher voltage (15kV) backscatter electron (BSE) images. For EBSD analyses the mount was tilted at a 70° angle relative to the detector and positioned at a working distance of 19.0 mm. We were therefore able to use these images to identify zircons or zones that would be interesting for EBSD analyses. (In the discussion, we have included granular texture zircons that are were not initially part of the survey and for which we only have SEM images. These images can be found in Appendix 3-2).

A higher accelerating voltage of 20 kV was used for EBSD analyses. We first conducted electron backscatter pattern (EBSP) analyses in point detection mode to test for orientation changes related to features in the low kV BSE images. We then selected four zircons for which we collected larger EBDS maps where a grid EBSPs were collected in ~ 125 nm steps across the sample surface. The mean angular deviation (MAD), or the angle between the measured EBSP and the reference Kikuchi bands for a given mineral phase, was set to 1.7° as an accuracy threshold based on laboratory experience. If the MAD was higher than this value, the EBSD software (Oxford HKL Channel 5) did not

index the EBSP and the step was excluded when producing the EBSD map (black pixels in maps). The angular resolution (noise level) for orientation differences between pixels is a maximum of 0.5+/0.2 degrees and can be as low as 0.2+/-0.1 degrees are very highly polished specimens. The software was set up to index for zircon, baddeleyite, and reidite (high pressure polymorph of zircon). Maps can be produced for multiple EBSD parameters including Kikuchi band contrast, MAD, mineral phase, textural component (misorientation), Euler angle, and crystallographic orientation.

We also collected color cathodoluminescence (CL) images of the zircons using the ZAP lab customized Gatan Chroma CL detector and the UCLA Tescan Color CL. In most cases, the summed CL or blue band images show the greatest contrast for identifying trace element zoning.

### 3.5 Results

We analyzed a total of 30 lunar zircons and observed every type of shock microstructure previously reported for both terrestrial and lunar impact zircons (except for the formation of reidite, a high pressure polymorph of zircon). In addition, we observed, to the best of our knowledge, a previously unreported class of shock microtwins with curved boundaries. Below are descriptions of the types and range of individual shock structures we identified in the lunar zircons in this survey. Table 3-1 lists the microstructures observed in each zircon, while more detailed descriptions and images of each grain in this survey can be found in Appendix 3-1 (Appendix 3-3 overviews previously published

lunar zircon microstructure analyses). Information on the $^{207}$Pb-$^{206}$Pb and U-Pb ages discussed can be found in Chapter 2.

### *3.5.1 Homogeneous Zircons*

Five of the zircons analyzed contained no apparent shock microstructures or primary

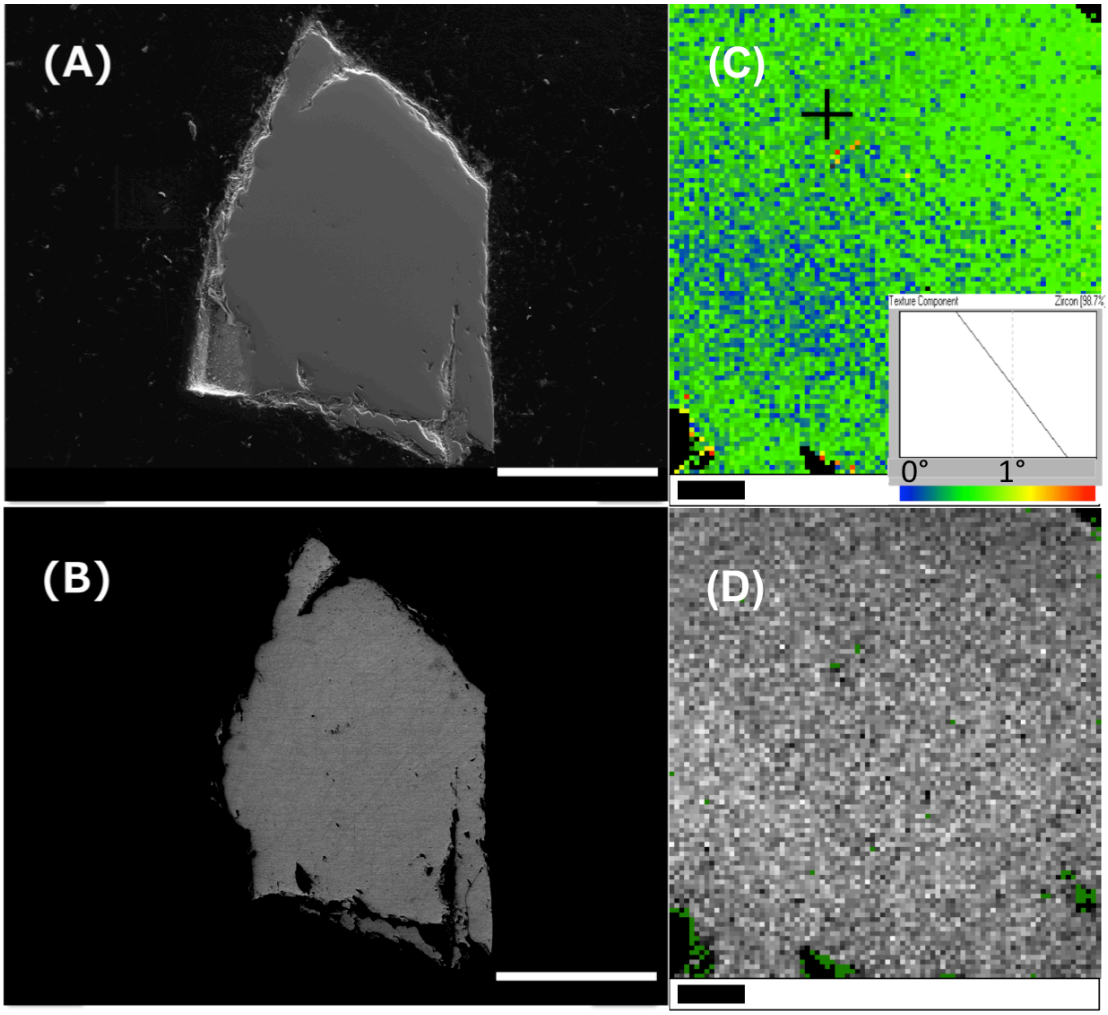


Figure 3-2: Images and EBSD analyses of homogeneous zircon 14321 Z14. Scale bars for panels A and B are 100 mm. Scale bars for panels C and D are 50 mm. (A) SE image showing no curviplanar features or impact melt glass inclusions exposed on the surface. (B) Low kV BSE image revealing no variations in composition or structure. (C) EBSD map of misorientation relative to black '+' reveals less than 1° of variation in crystal orientation across the grain. (D) EBSD band contrast map shows no variation in band contrast.

magmatic zoning on the polished surface. Further inspection of these grains with an optical transmission microscope often revealed subsurface fractures or impact melt glass inclusions. Breccia zircon 14321 Z21 is the best example of this type of grain (Appendix 3-1, Figure 3-35). It does have some small cracks, but otherwise does not show any evidence of shock or igneous zonation in CL or BSE imaging. One analysis of this grain gives a concordant U-Pb age of 4286 ± 6 (σ) Ma. Zircon 14321 Z14 is another interesting example of an apparently featureless grain (Figure 3-2A). EBSD analyses show the grain is structurally homogeneous with <1° of variation in crystal orientation across the grain (Figure 3-2C). Seven REE and Ti analyses reveal that it is also homogeneous in trace elements, but five U-Pb age analyses show that it has experienced significant Pb-loss (up to 30% discordance) with $^{207}$Pb-$^{206}$Pb dates ranging from 4134 ± 31 (σ) to 4216 ± 17 (σ).

*3.5.2 Primary Igneous Zoning*

Primary oscillatory and sector zoning was identified in about 38% (13/30) lunar zircons via features in CL and low-kV BSE images (5 oscillatory zoning, 6 sector zoning, 2 contain both). Breccia zircon 14305 Z27 exhibits well-preserved primary oscillatory zoning (Figure 3-3A). The CL zoning patterns suggest an oscillatory zoned dark core (likely due to higher-U concentration) surrounded by a brighter oscillatory zoned overgrowth zone. EBSD point analyses show that the bright outer growth zone is epitaxial. There is a slight change in band contrast due to either the lattice strain from extra REE and trace elements responsible for variations in CL activity and/or changes in metamictisation. The bands of oscillatory zoning range from submicron to ~10 μm in

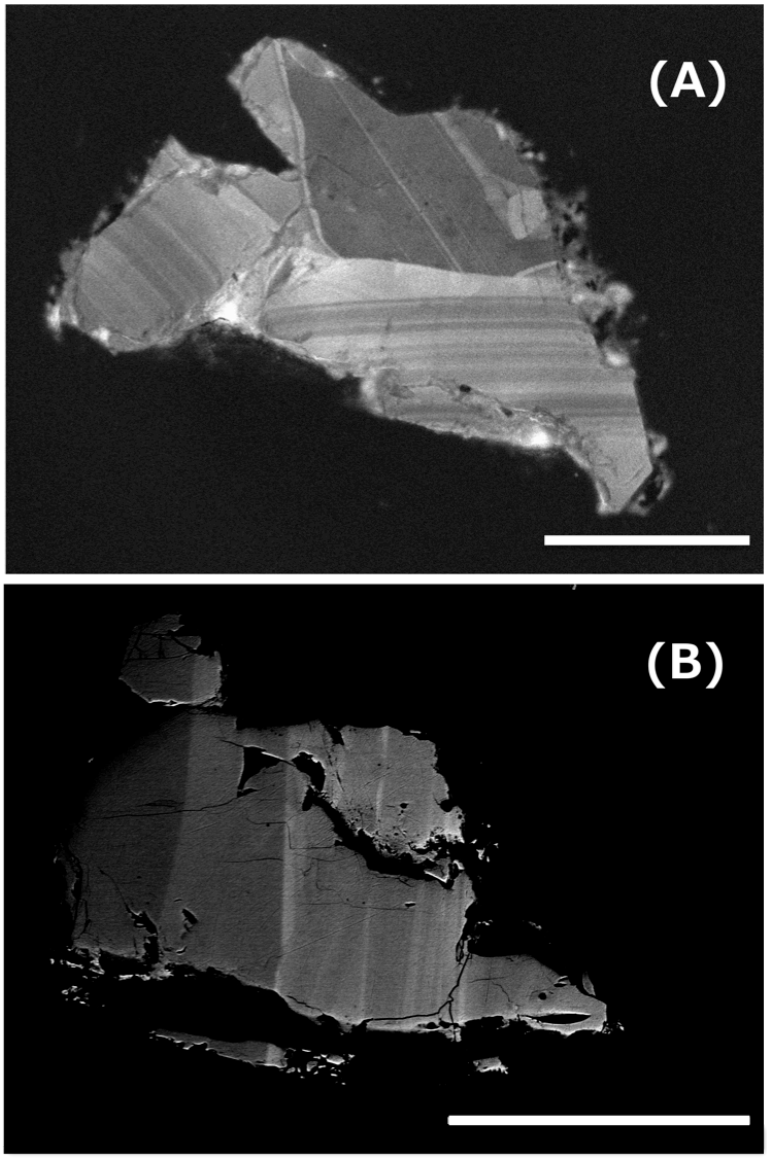


Figure 3-3**:** Zircons exhibiting primary igneous zoning. All scale bars are 50 mm. (A) CL image of 14305 Z27 showing well-preserved oscillatory zoning suggestive of a high-U core (dark in CL image). (B) Low kV BSE image of 14305 Z29 showing primary sector zoning. There are not variations in $^{207}Pb$-$^{206}Pb$ ages with zonation in either of the grains shown here.

width. SIMS analyses of core and rim both give Pb-Pb age within error of 4331 ± 6 Ma ($1\sigma$) with <6% discordance.

Breccia zircon 14305 Z29 contains sector zoning (Figure 3-3B). CL and low kV BSE images reveal three regions of sector zoning. Like Z27, EBSD line scans show no variation in crystallographic orientation across the sector zoning and a slight reduction in band contrast for the dark CL region consistent with increased metamictisation. To date we have only one SIMS age analysis of Z29, which yields 4254 ± 6 Ma (1σ). Previous age analyses of sector-zoned zircons (see Chapter 2) suggest that there is no variation outside of error between the zones, but multiple magmatic events cannot be ruled out at this time.

*3.5.3 Curviplanar Features and Impact Melt Glass Inclusions*

Curviplanar features (CPF) and impact melt glass (IMG) inclusions are the two most prevalent shock microstructures observed in this survey (~67% of zircons), and they are commonly spatially associated. A wide range in both CPF and IMG properties were noted, and the following describes the most common types of these shock features. More details can be found in Appendix 3-1.

Only two grains contained distinctly planar features (PF) and these too were associated with chains of IMG inclusions. Breccia zircon 14305 Z15 contains multiple sets of PFs and CPFs that are easily identifiable in BSE images by their associated chains of dark inclusions (Figure 3-4A). This grain has some of the smallest inclusions observed in the microstructure survey, and all are less than 1 μm in diameter. There appear to be two larger olivine inclusions, but these are most likely exposed contact materials and not actually primary inclusions. The larger IMG inclusions are often associated with bright

CL regions suggestive of trace element exchange during zircon-melt reactions or annealing of the CPF [note; as seen in Vredefort grains].

Breccia zircon 14305 Z36 contains IMG inclusions that are larger than the previous example grain; some are up to 2 μm in diameter. In the low kV BSE image, these inclusions are surrounded and connected by bright thin bands (Figure 3-4C). A comparison between the low kV BSE and the SE image reveals topographical depressions corresponding to the bright band, which suggests this region is more easily polished or eroded than the host grain. The most likely explanation for this feature is that it is an annealed CF that appears bright in the low-kV BSE image due to the higher crystallinity of the annealed zircon. Breccia zircon 14321 Z10 is similar to the previously described grain except that instead of a chain of micron sized inclusions, long segments of the curviplanar fracture (up to ~50 μm in length) have been filled with impact melt glass (Appendix 3-1, Figure 3-28). Thin bands that appear bright in low kV BSE and correspond to depressions in SE images also connect the glass filled regions. The annealing of CPFs and zircon-melt trace element exchange suggests these grains were exposed to elevated post-impact temperatures.

We also observed re-crystallized IMG inclusions. Breccia zircon 14321 Z12 has a long, ~70 μm curviplanar chain of inclusions that are between ~ 1 to 3 μm in size. In SE images, these inclusions appear to contain euhedral submicron crystals (Figure 3-4D). The crystals are too small to be reliably indexed with EDS or EBSD, although two pixels indexed as baddeleyite (MAD= 0.7). The chain of inclusions is also associated with small,

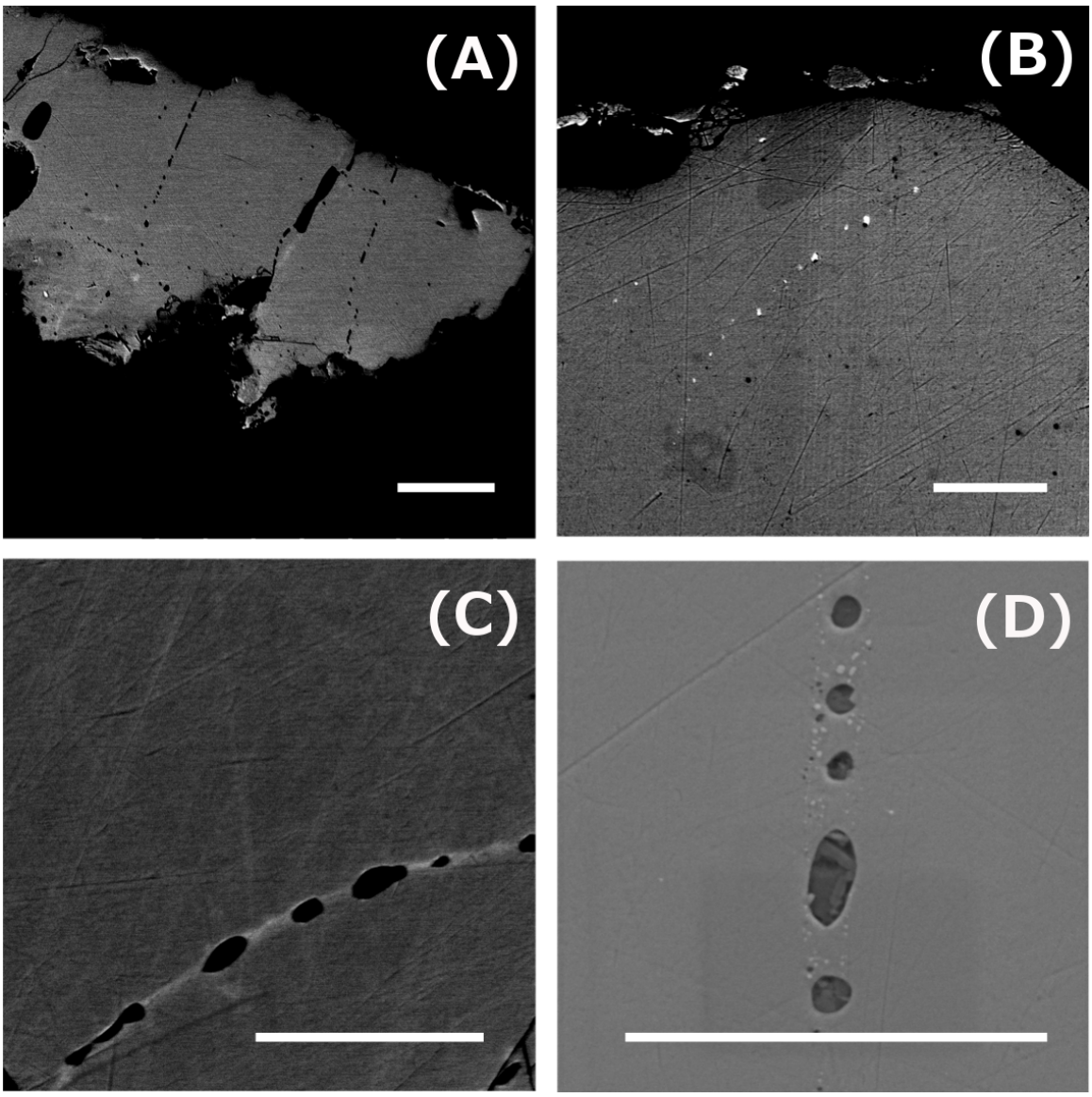


Figure 3-4: Four examples showing a range of curviplanar features and impact melt glass inclusions. All scale bars are 10 mm. (A) Low kV BSE image of planar features containing impact melt glass in zircon 14305 Z15. (B) The chain of bright inclusions in 14305 Z31 identifiable in low kV BSE image, are not associated with fractures seen in SE imaging. (C) Bright low kV BSE regions (dark in CL images) associated with impact melt glass inclusions suggestive of CPF annealing or trace element exchange between melt and zircon (14305 Z36). (D) A chain of inclusions in 14321 Z12 contains euhedral recrystallized grains suggesting slow cooling or reheating of melt inclusions. Bright spherical features surrounding inclusions are too small to be indexed by EBSD.

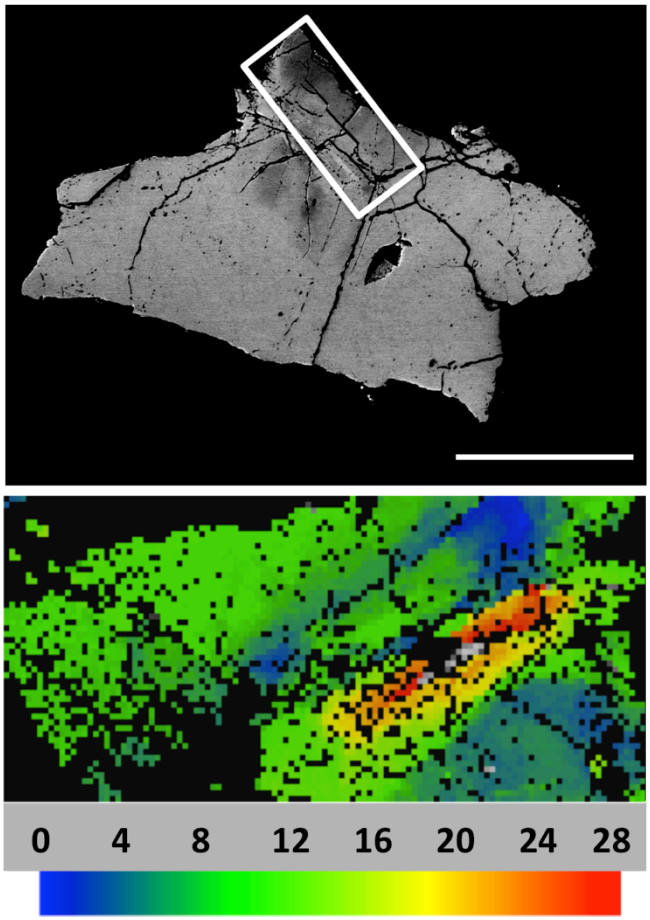


Figure 3-5: BSE image of zircon 15311 Z6 reveal an intricate network for CPF and impact melt glass inclusions (top). Bright areas yielded no or un-indexed BSE diffraction patterns but are compositionally zircon in EDS analyses, suggesting that these regions are amorphous. An EBSD map for the regions that did produce reliably indexed patterns reveals up to 28° of CPD (bottom).

10s of nanometer spots of both bright and dark material in the low kV and BSE images. These also are too small to index with EBSD, but are possibly regions where zircon has decomposed to its constituent oxides baddeleyite ($ZrO_2$) and $SiO_2$. The presence of the crystalline IMG inclusions suggests that this zircon was exposed to elevated temperatures for an extended period of time, which was long enough to allow for devitrification.

We also found cases where curviplanar features and IMG inclusions are identifiable, but not spatially related. For example, inspection of the SE image for breccia zircon 14305 Z31 reveals a relatively homogenous, unshocked grain. However, the low kV BSE image contains a curved chain of submicron spherules of significantly brighter material (Figure 3-4B). These regions are not easily identifiable in the SE image, which is not sensitive to atomic number suggesting that they are most likely recrystallized zircon or baddeleyite. Soil zircon 15311 Z5 is another example (Appendix 3-1, Figure 3-38). It contains a larger ~1μm and a smaller submicron IMG inclusions that are not associated with any other features visible in SE, BSE, or CL imaging. This could be an effect of the orientation of the CPF with respect to the exposed surface, but further investigation would be needed to determine if this is the cause.

*3.5.4 Amorphous Zircon*

Only one in the suite of grains analyzed, soil zircon 15311 Z6, contained regions of completely amorphous zircon. (A second zircon, 14321 Z20 had small areas where the band contrast was too poor to index, but was still visible.) Z6 is highly shocked and contains numerous CPFs and PFs entirely or partially filled with impact melt glass. Almost the entire grain is amorphous, and only the darker regions in the low kV BSE image (Figure 3-5) were indexed by EBSD. The indexed region contains up to 28° of CPD, one of the highest reported for lunar zircons to date (Grange et al., 2013b). This grain has a U concentration of 114 ppm, which is slightly higher than the average lunar zircon concentration (average of our samples is ~50 ppm), but most likely not high enough to cause the large amount of metamictisation (Mezger and Krogstad, 1997;

Garver and Kamp, 2002). Despite its amorphous nature and the high degree of CPD, three age analyses give concordant Pb-Pb ages between 4245 ± 4 and 4332 ± 3 (σ) Ma. This suggests the zircon experienced some amount of Pb-loss early in its history, but regions have retained Pb since ~4250 Ma. The REE pattern, collected in a region containing no impact melt glass, is consistent with other pristine lunar zircon analyses (see Chapter 2).

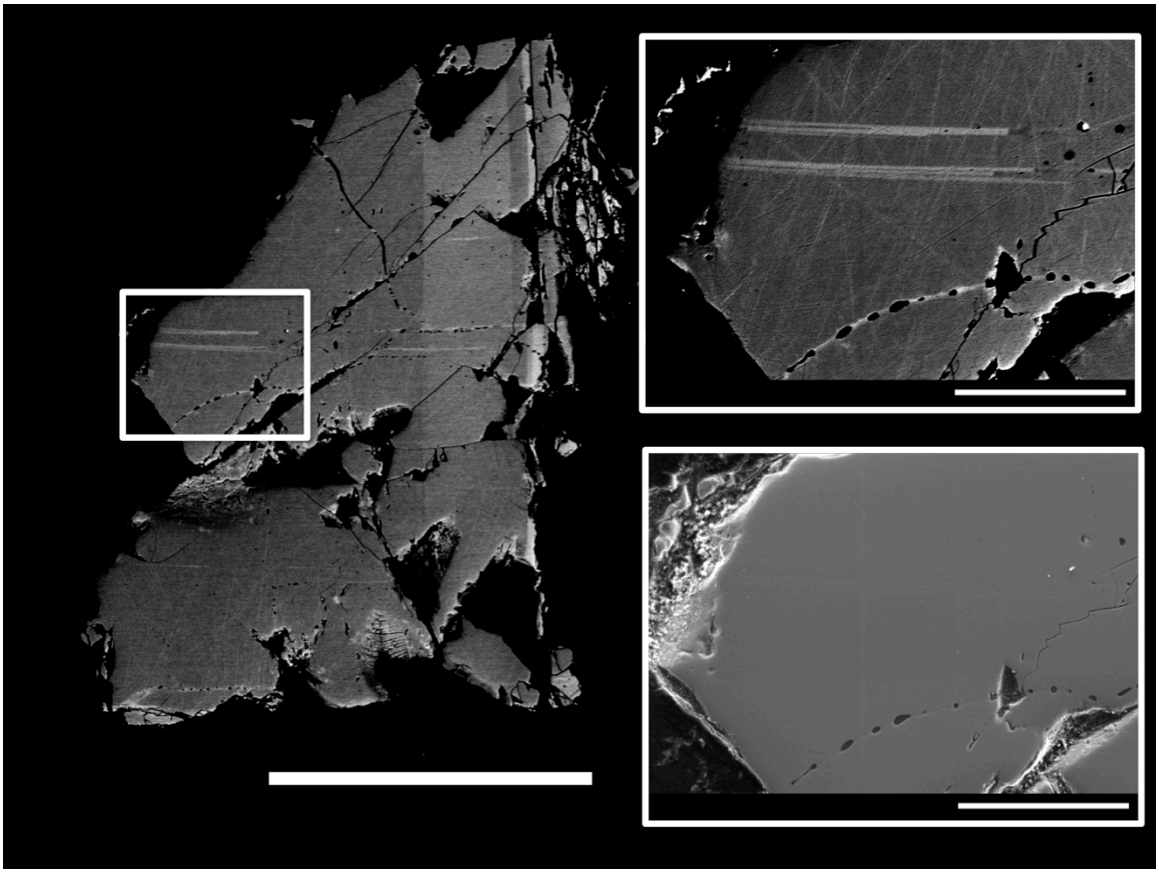

Figure 3-6: Low kV BSE (left) for 14305 Z36 and higher resolution image of region defined by white box in BSE image (top right – low kV BSE, bottom right – SE). The horizontal bright bands in the BSE images are shock microtwins that are orientation in the {1K2} plane and rotated 65° around {110} relative to the host zircon. These features are produced in experimentally shocked zircons at pressures above 60 GPa.

*3.5.5 Shock Microtwins*

We identified shock microtwins in three lunar zircons, all of which were separated from breccia samples. EBSD analyses were used to determine the orientation of the twins, and all sets of twins have {112} orientation and are rotated 65° around {110} relative to the host zircon. Breccia zircon 14305 Z36 contains two bands that are comprised of three individual, sometimes overlapping, sub-micron, twins. The twins on the left edge of the grain sharply terminate near the center where there is a high concentration of cracks, curviplanar features, and impact melt glass inclusions. On the right edge of the grain in Figure 3-6, the twins are visible, but not as well defined and are parallel to two planar features, which contain impact melt glass inclusions. The less defined twins also overlap a region of c-axis parallel CPD (vertical bands in Figure 3-6). There are also appear to be parallel relic microtwins towards the zircon towards the top and bottom of the grain, but these were not indexed.

Breccia zircon 14305 Z34 contains two sets of shock microtwins (Figure 3-7), both of which have {112} orientation. These planes are perpendicular to directions of high Young's modulus or stiffness in the zircon structure (Timms et al., 2012). The first is a linear ~1-2 μm twin that offsets a second set of three curved microtwins, which have not previously been reported in literature. The curved twins are wider than the typical planar microtwins, in places up to ~5-6 μm thick, and are associated with curviplanar chains of impact melt glass inclusions. The plane of the curved twins is rotated 65° around {110} relative to the polished surface suggesting that the curved nature of the twins is real and not an artifact of polishing.

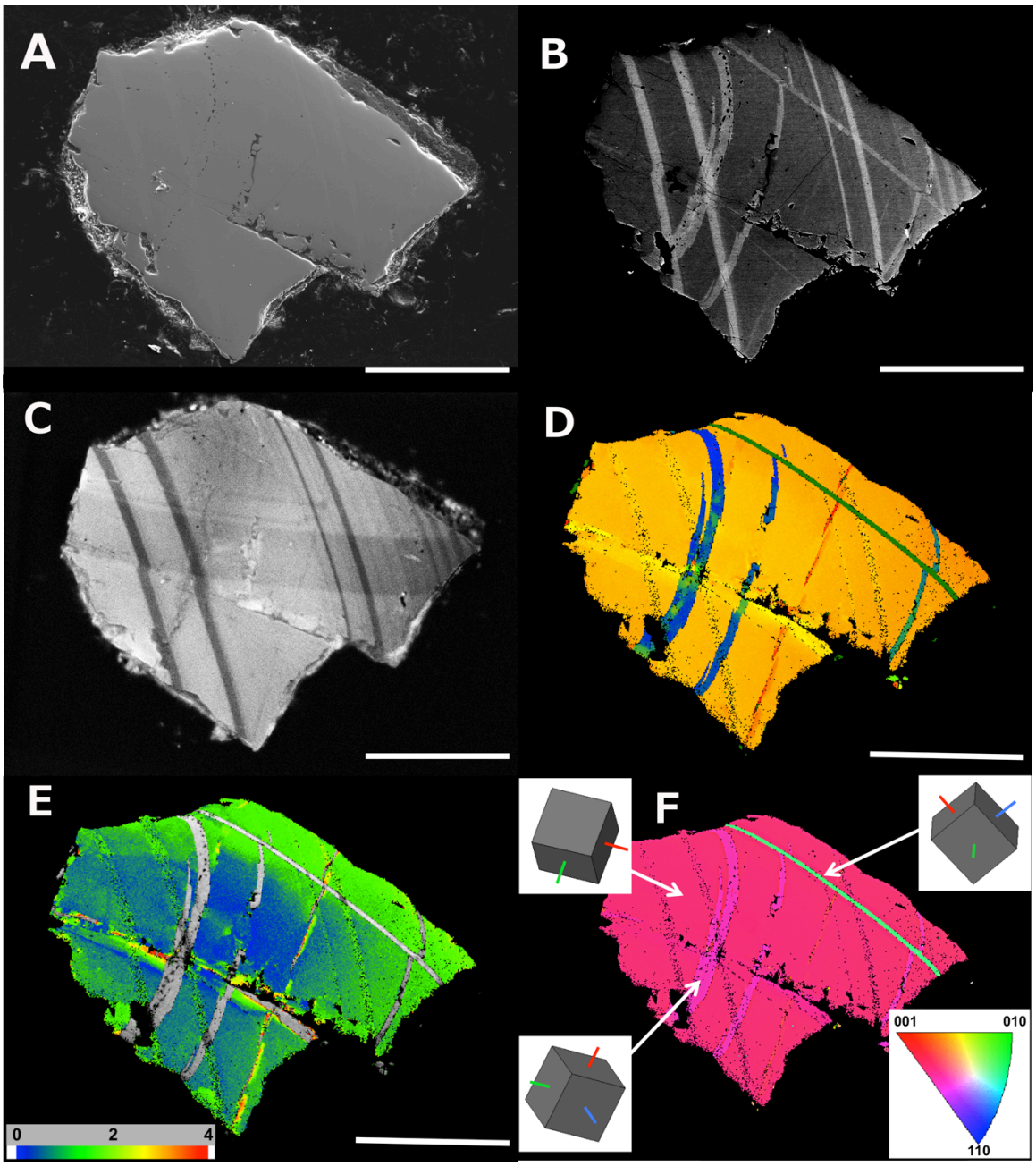


Figure 3-7: Images of zircon 14305 Z34, which exhibits curved shock microtwins that have not been previously reported in literature. (A) SE image. (B) Low kV BSE image. (C) CL image. Dark bands are zones of high-U concentration due to primary oscillator zoning. (D) EBSD crystal orientation map. The curved microtwins (blue) are offset by a second straight shock microtwin (green) that appears slightly curved due to drift during EBSD mapping. (E) Map of misorientation in host zircon, shows up to 4° of CPD mostly associated with a crack running the length of the grain and a perpendicular band. (D) Euhler angle map and pole orientations (c-axis is red).

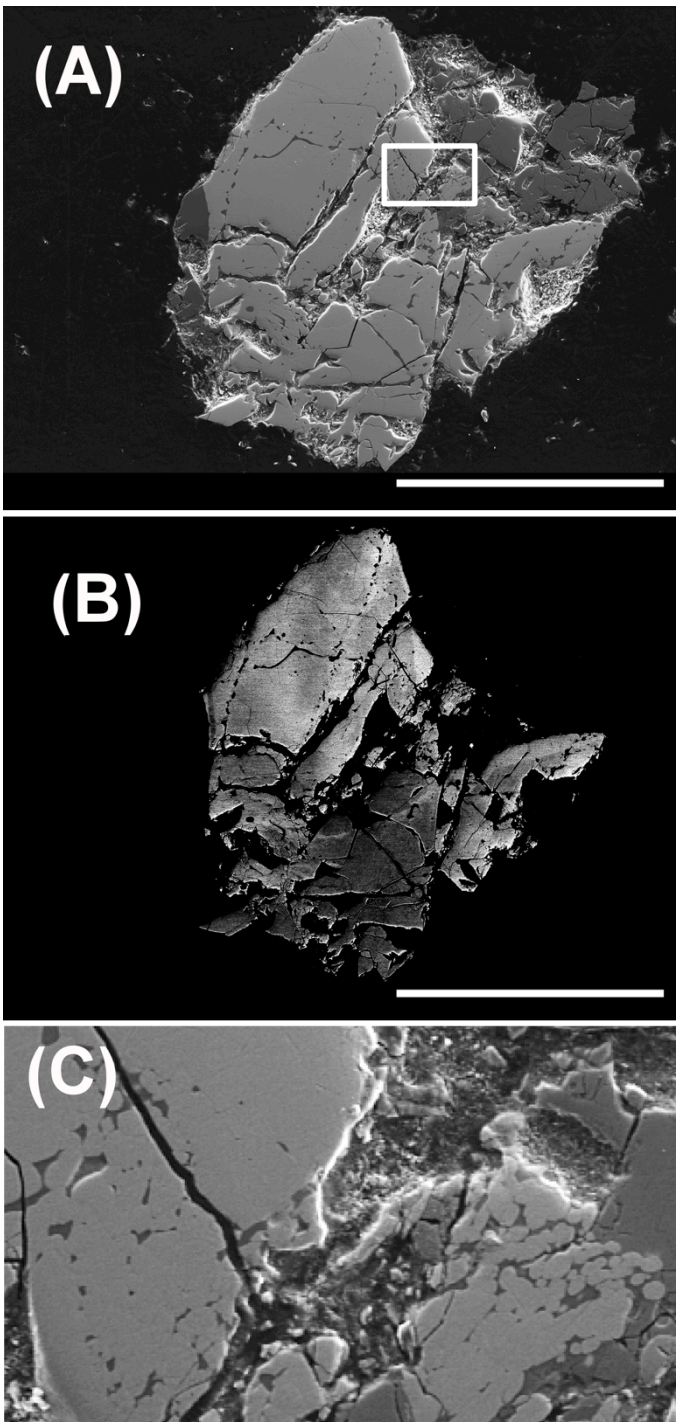


Figure 3-8: Images of highly shocked zircon 14305 Z30 (scale bar is 50 mm). The SE image (A) reveals a fragmented zircon with many CPF and impact melt glass inclusions. The low kV BSE image (B) is relatively consistent with the CL image (Appendix 3-1, Figure 3-22). The higher resolution image (C) of the central region (~17 mm white box in A) reveals sub micron granular texture recrystallization.

*3.5.6 Granular Texture Recrystallization*

Granular texture recrystallization was only observed in one of the lunar zircon in the initial microstructural survey, 14305 Z30 (Figure 3-7). Granular texture zircons are very rare in lunar samples. Out of the 214 zircons analyzed at UCLA to date, only four zircons contain this thermal recrystallization texture. Images of two of the additional granular zircons from the UCLA collection are presented in Appendix 3-2 and are included in this chapter's discussion due to their significance in determining impact ages.

In addition to granular texture recrystallization, zircon 14305 Z30 has a high concentration of cracks, CPF, and impact melt glass inclusions suggesting that it is a highly shocked grain. The recrystallized region contains many micron to submicron zircon granules with random orientations relative to the host zircon. The CL pattern of this grain shows a mottled texture and some bright reaction regions surrounding CPF and melt inclusions, but no primary igneous zonation. It is interesting to note that even though this zircon has experienced some of the highest shocked pressure and temperature conditions in this study, there are no indexed regions with baddeleyite or reidite (high pressure polymorph of zircon).

*3.5.7 Crystal Plastic Deformation*

CPD was identified in eight (~ 25%) of the lunar zircons. Three of the zircons contain bands of deformation parallel to the c-axis. This type of deformation is most pronounced in breccia zircon 14305 Z25. The EBSD map in Figure 3-9, reveals that the bands are between ~3-10 μm in width and are shifted by up to ~5° around the c-axis relative to a

host grain reference point. The boundaries between the bands appear as slight depressions in SE images due to preferential polishing, and in some places the boundaries host impact melt glass inclusions. This grain also has primary igneous zoning seen in the CL image (Figure 3-9C), which does not correlate with the banded deformation.

Four of the lunar zircons exhibit CPD that is related to c-axis parallel twisting. Most of the non-c-axis parallel deformation appears to be associated with cracks. Breccia zircon 14305 Z34 has localized deformation up to ~4° surrounding a large crack that runs the full length of the grain (Figure 3-7). It also contains a second band of deformation that is not associated with any cracks or other features, but it is parallel to {112}. The band is not coherent like banded deformation in 14305 Z25, but is instead comprised of smaller ~ 20 μm segments. In all cases of CPD in the lunar zircons analyzed, accept for amorphous zircon 15311 Z6, the misorientation did not exceed ~6° relative to the host grain.

### 3.6 Discussion

In this survey, we collected electron beam analyses including SEM imaging (SE, BSE, CL) and EBSD measurements for 30 lunar zircons separated from Apollo 14 soil and breccia samples. The objectives of these analyses were to better understand the range of impact shock features in lunar samples and to compare them with shocked terrestrial zircons to better understand the impact conditions experienced by the lunar samples. A secondary objective was to produce a catalog of high-resolution SEM images of impact shock features that could be useful for identifying similar microstructures in other lunar

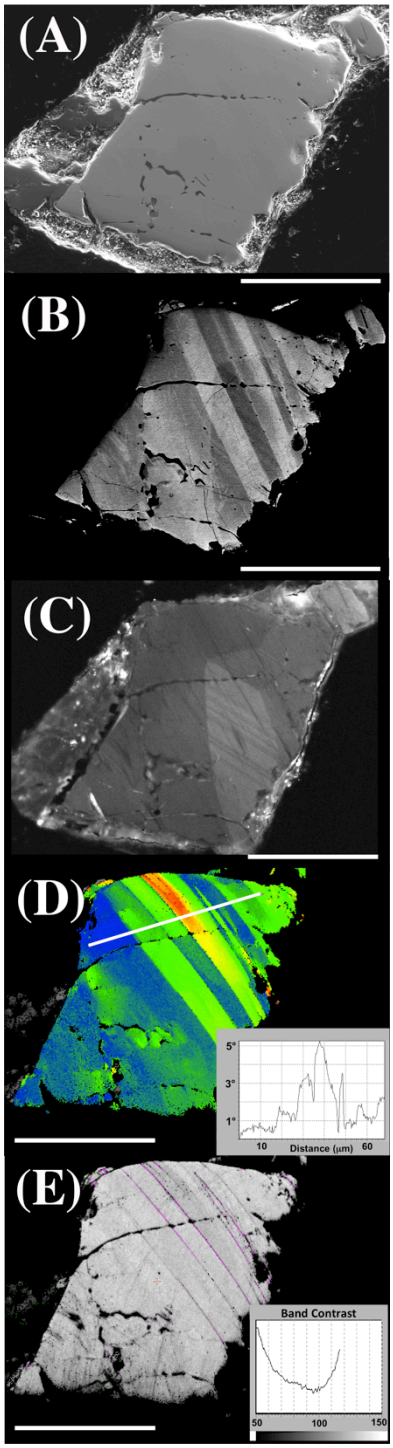


Figure 3-9: Images of zircon 14305 Z25. (A) SE image revealing impact melt and CPF. (B) Low kV BSE image. (C) CL image exhibiting primary sector and oscillatory zoning. The CL zoning is associated with slight variations in BSE zoning in image (B). (D) EBSD orientation map and profile showing up to 5° misorientation in c-axis parallel bands. These bands are the dominant feature in the BSE image (B). (E) EBSD band contrast map reveals that the crystallinity of the zircon is consistent across the zircon.

zircon samples (Appendix 3-1). Moser et al. (2011) produced a similar catalog of shock microstructures for terrestrial zircons, but most previous lunar zircon studies (combined total of 22 zircons) have published low-resolution or incomplete sets of images making it difficult to search for new shock structures.

*3.6.1 Microstructural Survey Results*

The lunar zircons we analyzed exhibit the complete range of shock microstructures. In the case of breccia 14305, all previously described microstructures were observed in individual zircon grains from a single 16 g rock fragment. We also observed some previously unreported morphologies of zircon shock features including non-linear shock microtwins and crystalline impact melt glass inclusions, which are discussed bellow. The findings of the survey are detailed in Table 1, which includes the shock features and Pb-Pb ages measured for each zircon. A similar table has been compiled for previously reported lunar zircons for which images and/or EBSD analyses were available (Appendix 3-3). Although the survey size of 30 zircons may not be large enough to be statistically robust, there are still interesting generalizations that can be made about the lunar zircon shock microstructures. Primary oscillatory and sector igneous zoning were identified in ~40% of the zircons, all of which are older than 4.2 Ga and have grain sizes ranging from 60-160 μm. All but one of the lunar zircons with primary zoning reported in literature also have $^{207}$Pb-$^{206}$Pb ages ≥ 4.2 Ga (Pidgeon et al., 2007; Nemchin et al., 2009b; Grange et al., 2011, 2013b) This suggest a potential difference between the pre- and post-4.2 Ga zircon forming magmatic systems. Impact alteration in general does not erase primary

igneous zonation, but instead produces mottled textures, which was noted in some of the zircons from this survey.

Curviplanar and planar features, along with associated impact melt glass inclusions, are the most common shock features in the lunar grains. They are present in grains that span almost the full range of zircon $^{207}$Pb-$^{206}$Pb ages. The CPF we observed are similar to those previously described in Moser et al. (2011), and their prevalence is not surprising because their formation requires the lowest level of shock pressures. It was difficult to find CPF in previously published lunar zircon analyses due to low resolution images, however planar features were described or visible in ~35% of grains (Appendix 3-3). We note here that fractures were not included as a shock microstructure because almost all lunar zircons are fragments of primary grains, so at some level they contain fractures. Even some impact grown zircons show later fracturing.

Higher pressure shock microstructures, such as shock microtwins, were also identified only in ~ 10% of zircons, and all are older than 4.2 Ga. Shock twins have been produced in the laboratory in zircons that were subject to shock pressures > 60 GPa and were often found to be associated with reidite (a high pressure polymorph of zircon). The small population of grains containing microtwins in our survey would suggest that only a small fraction of zircons in the Apollo sample collection have experienced the conditions necessary for microtwin formation. The current understanding of the formation and preservation of shock microtwins is limited. However, the observation of multiple, offsetting shock twins within in an individual grain, in addition to granulites with twin

orientation in Moser et al. (2011), suggests that twin orientation may be preserved during subsequent shock and thermal events (discussed in section 5.2).

Similar to the previous microstructure discussed, CPD was only identified in zircons older than 4.2 Ga, and in most cases the misorientation was relatively low (<6°). Previous lunar zircon studies also observe CPD only in this older population of grains, but the degree of deformation is often higher than reported herein (Nemchin et al., 2009a; Timms et al., 2012; Grange et al., 2013b). CPD can be categorized into two groups: banded and un-banded. The latter has been reported in both lunar and terrestrial zircons and is often associated with Pb-loss. Grange et al. (2011) reported Pb-mobility in a lunar zircon with ~4° of misorientation, and Moser et al. (2011) noted Pb-loss in a Vrederfort shocked zircon across regions of only 3-4° misorientation. Our similarly un-banded CPD only exhibit 1-2° misorientation, which may explain the absence of appreciable Pb-mobility in these grains. Although Pb-loss due to an ancient impact event that is not resolvable from the Pb-Pb crystallization age cannot be ruled out.

The higher degrees of CPD identified in survey zircons were in {100} parallel deformation bands. This {100} parallel banding has been noted in both terrestrial and lunar grains where it is commonly rotated about {010} (e.g. Leroux et al., 1999; Moser et al., 2009; Nemchin et al., 2009; Timms et al., 2012). Zircon 14305 Z25 (Figure 3-9E) is the best example in our survey of this type of banded deformation. Two SIMS U-Pb analyses of the banded and un-banded regions give consistent, concordant ages of 4265 Ma. The EBSD band contrast map (Figure 3-9E) is also relatively homogenous across the

grain, save for the boundaries between deformation bands. This may suggest that for this zircon the mechanical formation of the bands does not cause enough structural damage by itself to lead to appreciable Pb mobility in the rotated section, or conversely that deformation facilitated 100% Pb loss to produce a concordant composition. However, Nemchin et al. (2009) and Timms et al. (2012) report variations in U-Pb ages associated with regions of banded deformation in zircon #1 from 72215,195, but the Pb mobility appears to be localized to a small region of high deformation reaching ~12°. Unlike the bands reported herein, previously reported zircons have poor band contrast suggesting that the deformation may have caused enough structural damage to facilitate Pb diffusion in this region. EBSD band contrast maps are therefore equally important as, if not more so than, misorientation maps in investigating Pb-loss associated with impact produced CPD.

Of the 30 zircons in the survey, only one exhibited granular texture recrystallization (Figure 3-7). This recrystallization texture has been well documented in terrestrial impact settings and is associated with almost, if not total Pb-loss (Moser et al., 2011). Zircons with this texture are therefore thought to produce the most accurate impact ages. We have identified four additional granular texture zircons from the suite of 214 zircons recovered from the Apollo collection at UCLA (the total number includes zircons reported in Chapter 2 and in Taylor et al. (2009)). We discuss these additional zircons here due to their implications for the early lunar impact history (ages can be found in Chapter 2 and images in Appendix 3-2). Overall, only 2% of the zircons in the UCLA collection exhibit granular texture recrystallization. These zircons differ from the “pomegranate” zircon,

73235,82 #1, reported in Pidgeon et al. (2007), which consists of a mechanically fragmented primary grain surrounded by secondary zircon matrix. The fragments of that primary grain retain remnant primary igneous zonation suggesting that they were once part of a larger magmatic zircon.

The granular zircons reported here are instead similar to those reported in Moser et al. (2011) in which the granules recrystallized in an impact environment, which contained no remnant CL zonation or Pb from a parent grain. These recrystallized regions are thought to provide the some of the most accurate constraints on impact ages due to their high degree of age resetting (see Chapter 2). Two of the granular texture zircons herein, 15455 Z3 and Z24, contain the first reported occurrence of the decomposition of lunar zircon to its oxide constituents (Figure in Appendix 3-2). This is in contrast to the report by Grange et al. (2009) in which a baddeleyite grain occurs with a granular texture zircon rim (73217,52 type-3). In this Apollo 17 grain, the fractures in the baddeleyite core that terminate at the zircon-baddeleyite interface. This suggests that the granular texture zircon postdates the core and is most likely a product of a reaction of the primary baddeleyite ($ZrO_2$) with $SiO_2$ in the surrounding material, and not the result of a decomposition reaction.

Timms et al. (2012) suggest that both high shock pressure and elevated temperatures are required to decompose zircon to $ZrO_2$ and $SiO_2$, although these parameters are not well constrained. Regardless, these two zircons may be evidence for large basin sized impacts on the early Moon. Future investigations into the composition of the interstitial melt

adjacent to the granules, such as Ti concentrations, should give more insight into the temperatures required for the decomposition and recrystallization, and help constrain the size of the early impact these zircons are dating.

We observed no skeletal growth texture zircons similar to those seen in Grange et al. (2011, 2013) and Nemchin et al. (2008). The method of extracting zircons by crushing, as used in this study, essentially obviates the recoverability of thin or fragile skeletal and granular texture zircons. Further investigation into the preservation of zircons, in both impact and lab environments, would be useful in interpreting the significance of the survey results.

*3.6.2 Observation of new morphologies of shock microstructures*

We have observed two previously unreported variations of shock microstructures. The first is crystalline impact melt glass inclusions as seen in 14321 Z12 (Figure 3-4). The curviplanar feature containing these inclusions is similar in form to those seen in other grains, and there are no CL reaction regions surrounding the inclusions. This suggests that the inclusions were initially formed by rapid quenching of injected melt to form a glass. A later heating event, associated with slow cooling during the same or second impact, most likely melted and slowly cooled the glass inclusions allowing for the crystallization of euhedral grains. There also exist potential regions of decomposition of the zircon to its oxide constituents, $ZrO_2$ and $SiO_2$ (bright and dark spherules respectively in Appendix 3-1, Figure 3-21), around the inclusions and the edges of the CPF, although the regions are generally too small to index by EBSD.

The second new morphology observed is represented by a set of curved shock microtwins in zircon 14305 Z34 (Figure 2-7). The zircon within the curved twins has orientation and rotation consistent with planar microtwins, as previously reported (e.g. Erickson et al., 2013; Moser et al., 2011). However, they differ from planar twins in that they exhibit curved boundaries, which in three dimensions are perhaps spherical, and moreover they are associated with inclusions of impact melt glass. The physical association of these two features suggests that the twins nucleated on a previously existing CPF, and supports similar conclusions of both Moser et al. (2011) and Timms et al. (2012) that shock twins are genetically related to CPFs. A second planar shock twin with a different {1K2} orientation, but similar {110} rotation offsets the curved twins in Z34. If the twins formed as a result of the same shock event, it would suggest a progression of twin formation by nucleation on fractures followed by formation along planes perpendicular to values of high Young's modulus; in other words, in planes perpendicular to the directions which accommodate the most amount of strain. The curved twin domains are a new phenomenon that to our knowledge has not been produced experimentally. Rapid shock unloading in metals can produce cavitation and curved microfaults and these mechanisms remain to be explored.

Moser et al. (2011) noted granular crystallites in twin orientation and concluded that twin orientation is preserved, at least in some cases, even during recrystallization at high temperatures. The resilience of the microtwin structures to later shock events may suggest that the survey observation that only zircons older that 4.2 Ga contain twins, is

real and not an artifact of preservation. However, experiments in which zircons are exposed to multiple shock and thermal events would be useful in understanding the preservation of these features in zircon.

### 3.7 Conclusion

The findings in the 30 zircon shock microstructure survey reported herein, together with results from previous authors (see Appendix 3-3), suggest the following:

1. Well preserved, primary igneous zonation is found in lunar zircons that have crystallization ages ≥ 4.2 Ga (except for zircon 14083,35 #1 reported in Grange et al. (2013)).
2. Over two-thirds of lunar zircons contain curviplanar features and/or impact melt glass inclusions. Thus over two-thirds of the zircons have experienced shock pressures of at least 20 GPa.
3. Shock microtwins are only found in zircons with crystallization ages ≥ 4.2 Ga. They were identified in ~10% of zircons form both this study and from prior work by other researchers (for which EBSD analyses were collected). The minimum pressure value for microtwin could be as low as 20 GPa based on occurrence of these features in the relatively low-shock collar region of the Vredefort impact structure. Mictrowins in old lunar grains could reflect exposure to a lower pressure, 'ambient' shock history.
4. Crystal plastic deformation occurred in ~ 25% of the survey zircons and has two forms: banded and un-banded. Both have previously been observed in lunar

grains with similar frequency. Current understanding is that zircon manifests CPD in rocks undergoing ductile flow, within or beneath central uplifts during the crater modification stage (e.g. Moser et al. 2009), and therefore this subpopulation may reflect this aspect of lunar crust dynamics. Reduction in zircon crystallinity as a result of deformation, not necessary the maximum degree of deformation, appears to be correlated with Pb-loss and age resetting.

5. Only ~2% of the zircons from the Apollo collection at UCLA exhibit granular texture recrystallization. We observe no other recrystallized regions or impact growth texture suggesting that only a very small fraction of the grains were exposed to the high shock pressures and prolonged elevated temperatures necessary to recrystallize zircon. However, issues with preservation of skeletal zircons during sample crushing could represent a bias accounting for the low numbers observed.
6. We report the first evidence of the decomposition of lunar zircon to its oxide constituents. Future investigation of these grains may help constrain the temperature conditions for the decomposition and recrystallization of zircon and the size of the impact they are dating.

We also observed two previously unreported morphologies of zircon shock microstructures. The first is crystalline impact melt inclusions. Their form suggests suggest that they were initially similar to melt glass inclusions, but a subsequent heating event melted and cooled slowly enough to allow for the formation of euhedral grains. The second morphology is a set of curved shock microtwins. The curved nature of the former

and their association with impact melt glass inclusions suggest the twins nucleated on a preexisting CPF. Additionally, the offset of these twins by a second linear shock twin may imply a progression of twin formation; first by reworking of preexisting fractures, followed by formation perpendicular to directions of high Young's modulus.

In the process of this survey, we have produced a robust catalog of zircon shock microstructure imaging and EBSD characteristics that can be used to help identify and classify shock structures in future zircon analyses.

## Table 3-1: Inventory of Shock Microstructures

| Sample | Primary Ocillatory Zoning | Primary Sector Zoning | Diffuse CL | CPF[1] | Melt Inclusions | CPD[2] | Amorphous Zircon | Shock Twins | Granular Texture | Pb-Pb[3] Age (Ma) | 1σ |
|---|---|---|---|---|---|---|---|---|---|---|---|
| 14259 *Soil* | | | | | | | | | | | |
| Z8 | X | | X | X | X | | | | | 4336 | 12 |
| Z9 | | X | | | | | | | | | |
| Z10 | | | | | | | | | | | |
| Z12 | | X | X | | | X* | | | | 4306 | 4 |
| Z13 | | | | | | | | | | 4268 | 15 |
| Z14 | | | | X | X | | | | | 4009 | 12 |
| 14305 *Breccia* | | | | | | | | | | | |
| Z15 | | | | X | X | | | | | 4206 | 16 |
| Z22 | | X | X | X | X | | | | | 4219 | 11 |
| Z23 | | | | X | | | | | | 4332 | 4 |
| Z25 | X | X | X | X | X | X* | | | | 4265 | 5 |
| Z27 | X | | | X | X | | | | | 4335 | 13 |
| Z29 | | X | | | | | | | | 4254 | 6 |
| Z30 | | | X | X | X | X | | | X | | |
| Z31 | | | | X | X | | | | | 4334 | 5 |
| Z33 | | | | | | X* | | | | 4334 | 4 |
| Z34 | X | | | X | X | X | | X | | 4324 | 5 |
| Z36 | | | | X | X | X* | | X | | 4281 | 5 |
| Z42 | | | | X | ? | | | | | | |
| 14321 *Breccia* | | | | | | | | | | | |
| Z10 | | X | | X | X | | | | | 4281 | 38 |
| Z11 | X | | | X | X | | | | | 4385 | 4 |
| Z12 | | | | X | X | | | | | 4164 | 3 |
| Z14 | | | | | | | | | | 4190 | 42 |
| Z17 | | | | | | | | | | 4097 | 2 |
| Z19 | | | | X | X | | | | | 4408 | 3 |
| Z20 | | | | X | X | X | X | X | | 4241 | 5 |
| Z21 | | | | | | | | | | 4286 | 6 |
| 15311 *Soil* | | | | | | | | | | | |
| Z3 | X | | | X | X | | | | | | |
| Z5 | | X | | | X | | | | | 4373 | 31 |
| Z6 | | | | X | X | X | X | | | 4301 | 6 |
| Z7 | X | X | X | X | X | | | | | 4338 | 4 |

* Banded Deformation

[1] Curviplanar features

[2] Crystal-plastic Deformation

[3] Ages are reproduced from Appendix 2-2

## Appendix 3-1: Secondary Electron Images and Descriptions of All Lunar Zircons in Study

This appendix contains images of all zircons within this survey. The figures are arranged such that secondary electron (SE) images are on top, followed by low-kV backscatter electron (BSE), and cathodoluminesence images are on the bottom (CL). All SE and low-kV BSE images were collected using the customized Gatan Chroma CL detector in the Zircon and Accessory Phase ("ZAP") Laboratory at the University of Western Ontario using a 5kV accelerating voltage. CL images were also collected in the ZAP lab unless the figure number is followed by (*) which designates CL images taken using the UCLA Tescan Color CL.

Figure 3-10: 14259,658 Z8

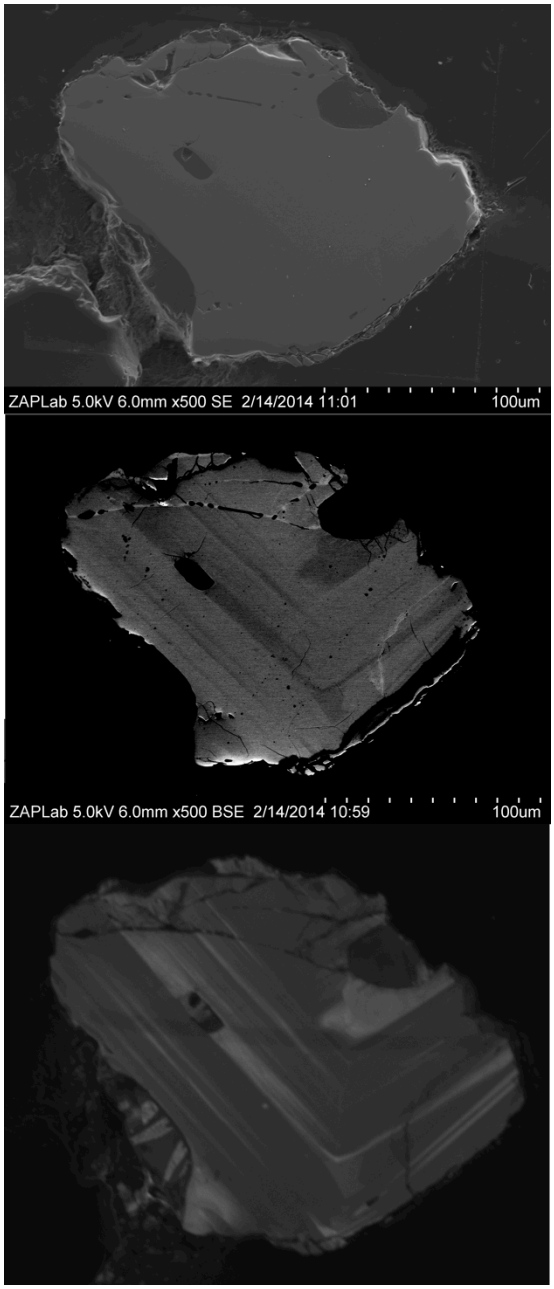


Figure 3-11: 14259,658 Z9

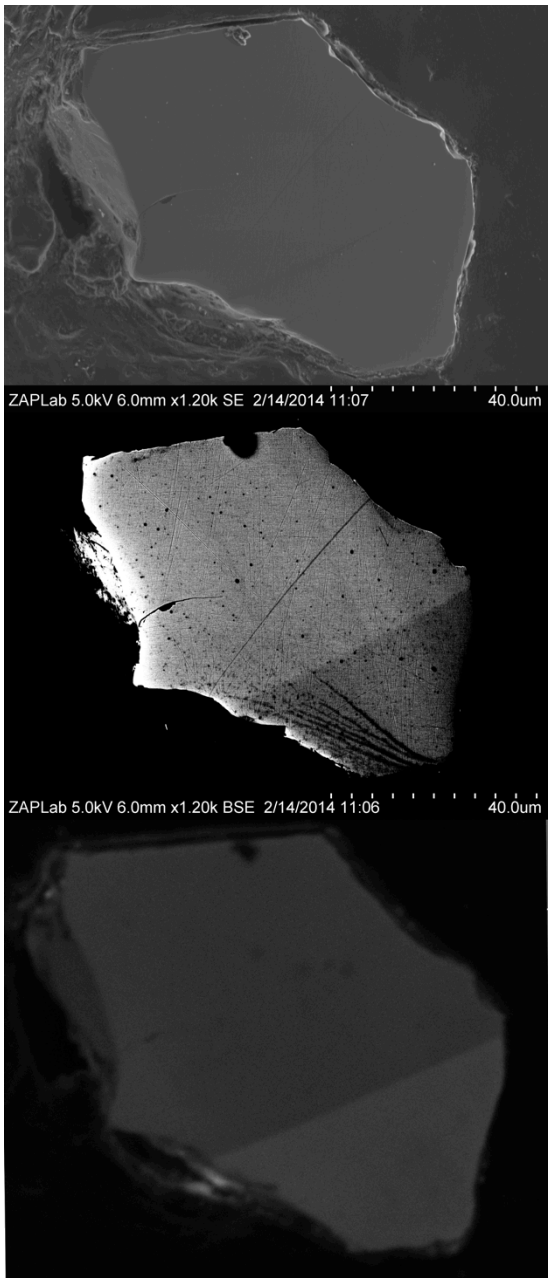

Figure 3-12: 14259,658 Z10

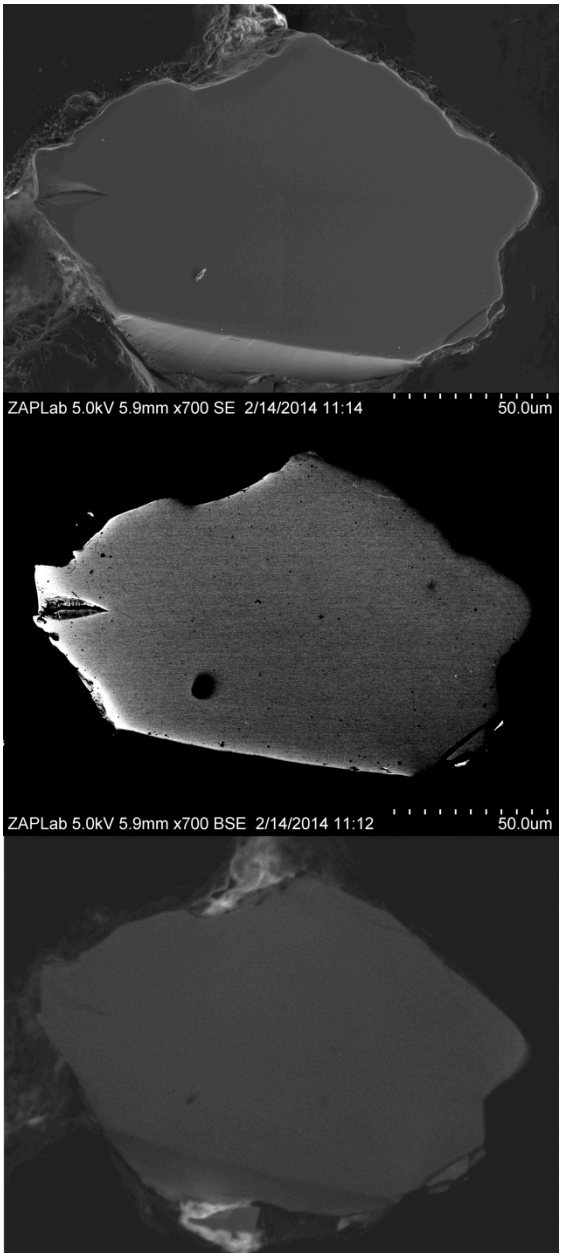


Figure 3-13: 14259,658 Z12

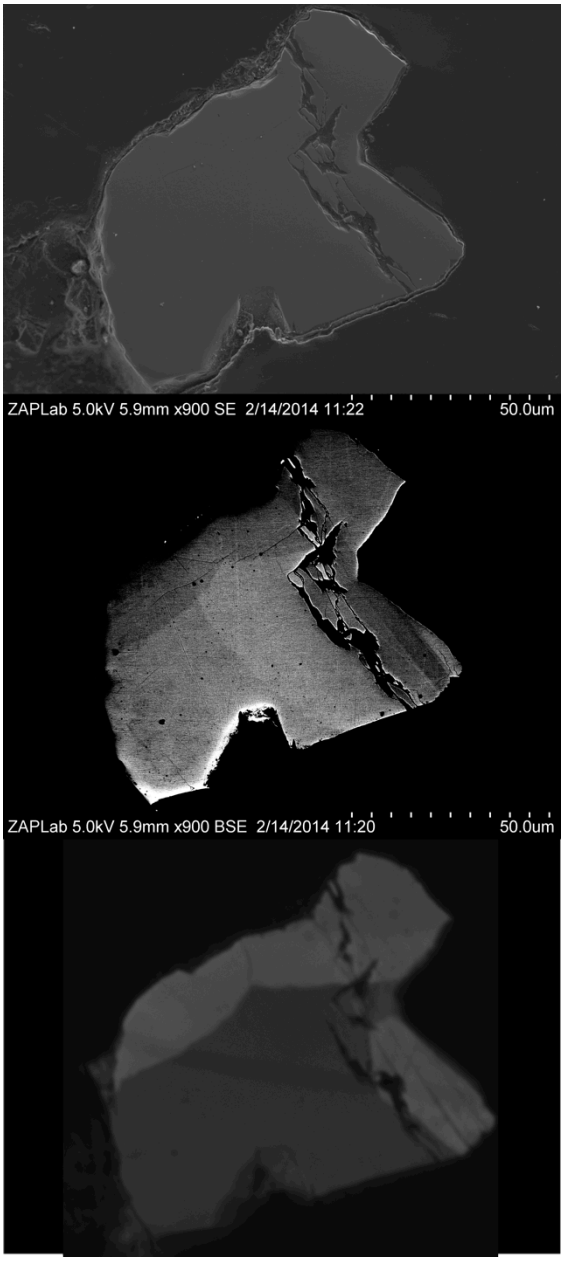

*14259 Z8* (Figure 3-10)

Zircon 14259 Z8 is a moderately sized zircon, ~ 150 μm. Grain Z8 exhibits both primary and secondary microstructures. There is primary oscillatory zoning that intersects at an almost 90° angle with a potential CL dark core. Pb-Pb ages of both the supposed core and rim regions are within error of 4331 ± 12 Ma (σ), but the rim is discordant by 11%. A possible inclusion ~ 5 x 10 μm is situated along one of the bands of oscillatory zoning. In CL this potential inclusion appears to have some internal structure, which may be a sign of recrystallization. A second potential inclusion is situated within the core region. Both inclusions have the same composition as the surrounding material, so it is possible that they are not primary inclusions, but instead contact material exposed by polishing an uneven zircon grain boundary. There are multiple curviplanar features with impact melt inclusions. At least one, if not two of the inclusions have recrystallized. The annealed curviplanar features appear bright in low-kV BSE and a crack in the lower right of Figure 1 has bright wispy regions propagating from it. The latter is also identifiable in CL images and may therefore represent trace element diffusion along the crack.

*14259 Z9* (Figure 3-11)

Zircon 14259 Z9 is a smaller ~60-80 μm grain, which contains primary sector zoning with a corresponding change in electron backscatter diffraction pattern (EBSP) band contrast. This is most likely due to a higher U concentration in regions of lower band contrast. There do not appear to be any secondary impact features.

*14259 Z10* (Figure 3-12)

Zircon 14259 Z10 is another ~ 100 μm homogeneous grain that does not exhibit any primary or secondary microstructures.

*14259 Z12* (Figure 3-13)

Zircon 14259 Z9 has a Pb-Pb age of 4306 ± 4 Ma (σ) and both primary and secondary features. CL images reveal primary sector zoning that correlates with some of the zonation in low-kV BSE images. There is a large crack running through the grain and to its right there are bands of ~ 5° of misorientation (determined from EBSD point analyses) visible in the BSE image. These are most likely similar to the twisting around the C-axis seen in grain 14305 Z25.

*14259 Z13* (Figure 3-14)

Zircon 14259 Z13 is a homogeneous grain with very good EBSP band contrast, which does not exhibit any primary or secondary microstructures. Two analyses of Z13 give an average Pb-Pb age of 4268 ± 8 Ma (σ). Both analyses are reversely discordant by up to 20%.

*14259 Z14* (Figure 3-15)

Zircon 14259 Z14 is a relatively homogeneous grain with very good EBSP band contrast, suggesting high crystallinity. It exhibits no primary zoning, but does contain one curviplanar feature (CPF) with one impact melt inclusion. The annealed feature has regions that appear both bright and dark in CL. Two U-Pb analyses give a concordant average age of 4008 ± 10 Ma (s).

*14305 Z15* (Figure 3-16)

Zircon 14305 Z15 is a large grain ~200 μm in size and attached to a fragment of Plagioclase. The Pb-Pb age is 4206 ± 16 Ma (σ) and is ~4% discordant. The grain has multiple planar features (PFs) and curviplanar features (CPFs) that are associated with strings of impact melt glass inclusions. There appears to be two large inclusions ~ 5 mm in size with forsterite compostion. It is also possible that these inclusions are exposed contact mineral with the subsurface grain boundary of the zircons. In low-kV BSE images, this zircon is relatively homogeneous with no evidence of reaction regions around the impact melt glass inclusions. This is also reflected in CL images, which show small wispy bright regions and potential sector zoning. Point EBSD measurements also showed no variation in band contrast or orientation across the grain.

Figure 3-14: 14259,658 Z13

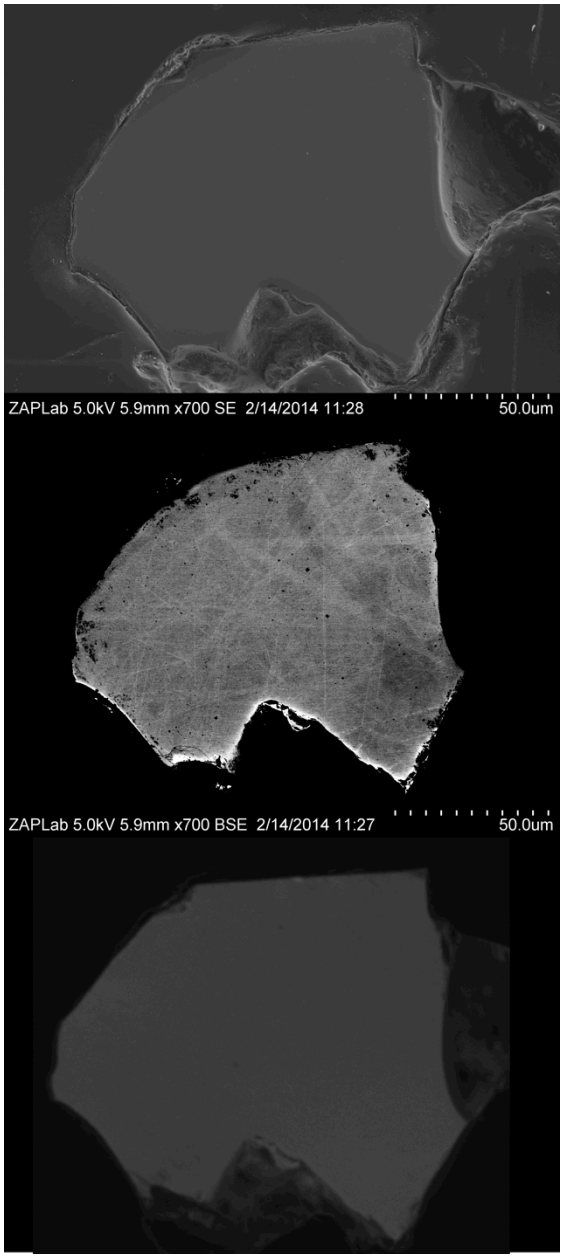


Figure 3-15: 14259,658 Z14

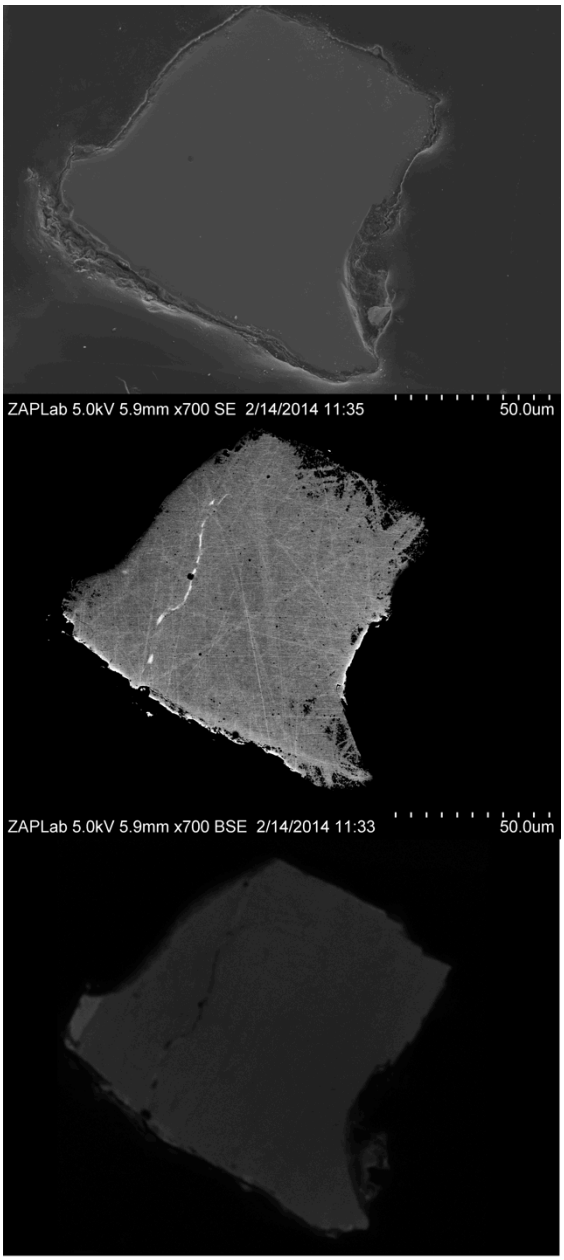


Note: The linear marks in Figures 3-13 and 3-14 are due to polishing and do not reflect structural or compositional variations.

Figure 3-16: 14305 Z15

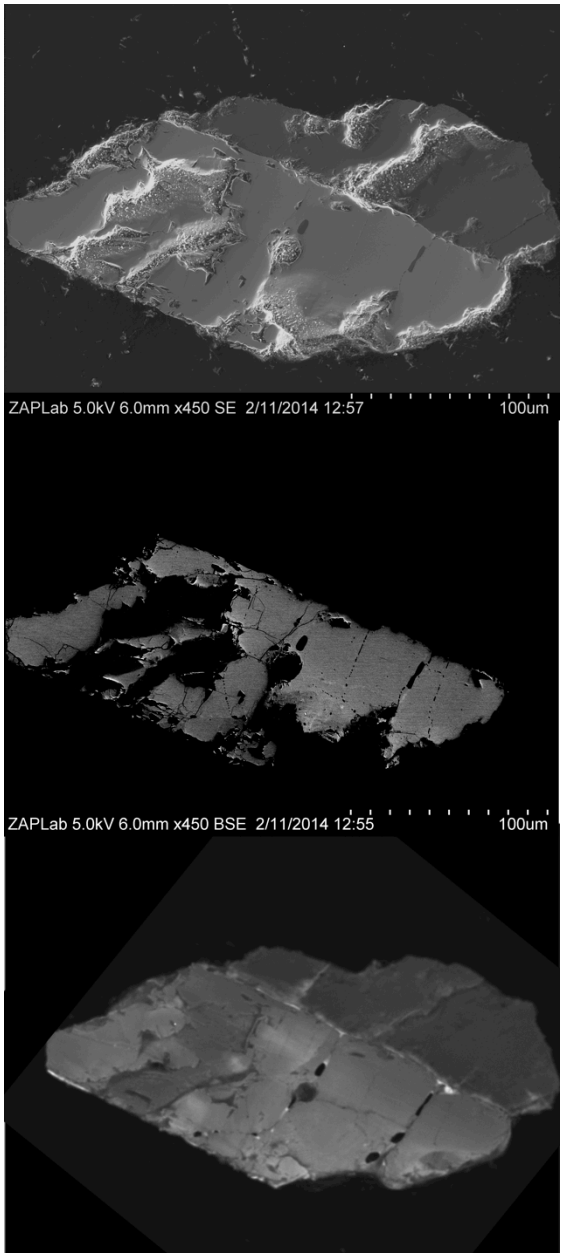


Figure 3-17: 14305 Z22

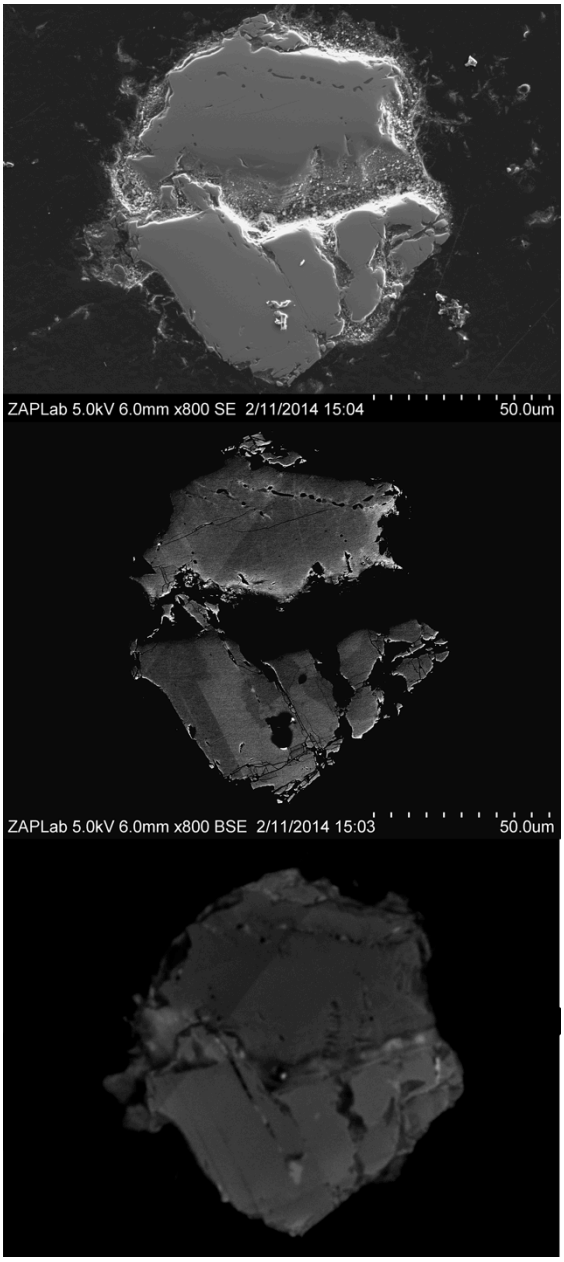

Figure 3-18: 14305 Z23

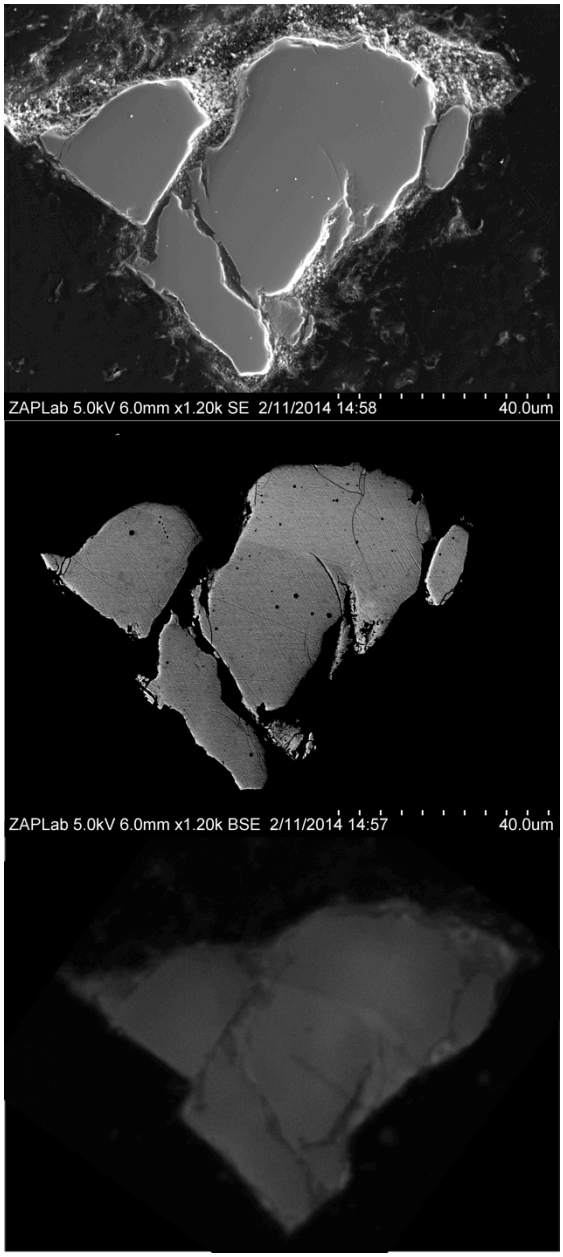


Figure 3-19: 14305 Z25

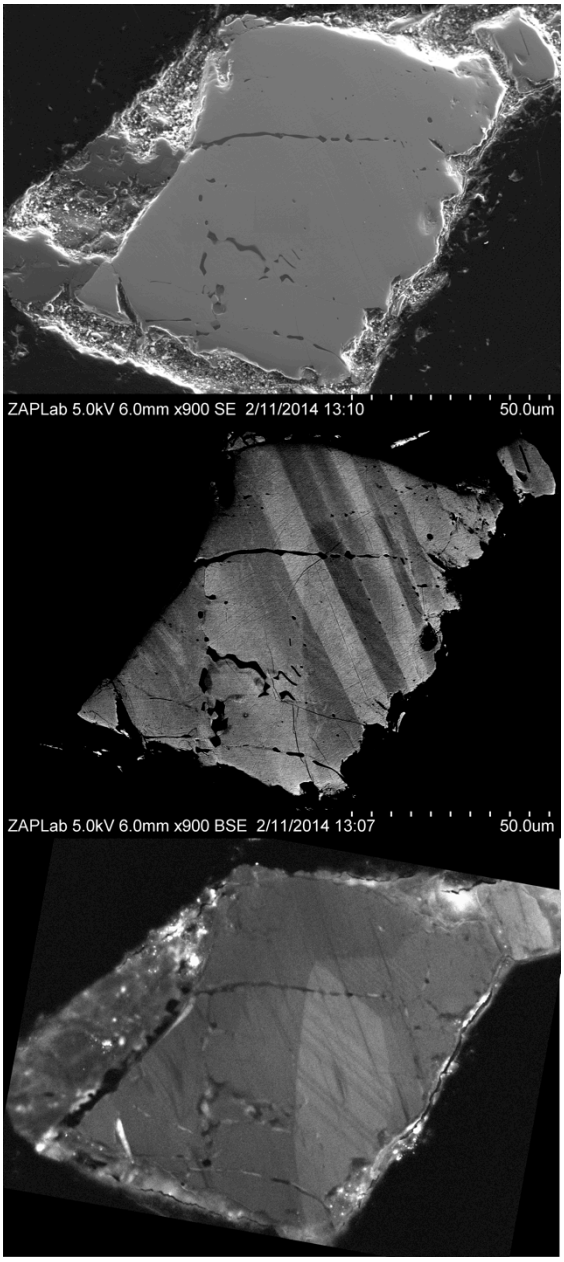

*14305 Z22* (Figure 3-17)

Zircon 14305 Z22 is an ~ 80 μm zircon that has multiple curviplanar fractures with impact melt glass inclusions on the order of a few microns in size. CL and low-kV BSE images reveal some primary sector zoning and diffuse bright regions surrounding the impact melt glasses. The latter may be evidence of reaction between the melt and host zircon due to prolonged, elevated temperatures. Point EBSD measurements do not show any variation in band contrast or orientation across the grain. Z22 has a concordant Pb-Pb age of 4219 ± 10.7 Ma (σ).

*14305 Z23* (Figure 3-18)

Zircon 14305 Z23 is a ~100 μm, relatively featureless grain in both low-kV and CL imaging. It does have one small CPF in the upper left region of the grain. Most of the other dark circular features in low kV BSE images are associated with surficial dust seen in SE. There are slight variations in CL activity possibly suggestive of primary sector zoning, but the variations are too small to be conclusive. Z23 has an old concordant Pb-Pb age of 4332 ± 4 Ma (σ).

*14305 Z25* (Figure 3-19)

Zircon 14305 Z25 is a very complex grain that has a range of both primary and shock features. It is about ~ 100 μm in size and has a relatively concordant age of 4265 ± Ma (σ). Z25 has regions of primary sector zoning that appear in CL to have banding within them, possibly oscillatory zoning. There are multiple CPFs that have impact melt inclusions and some annealed CPFs that appear bright in CL. EBSD analyses reveal that half of the zircon has bands of c-axis parallel dislocation, that are shifted by up to ~5°. Similar banded crystal plastic deformation (CPD) has previously been identified in both lunar and terrestrial zircons.

*14305 Z27* (Figure 3-20)

Zircon 14305 Z27 is an ~120 μm grain that is, so far, the best example of primary oscillatory zone that we have observed in lunar grains. This grain appears to be a fragment of a much larger zircon based on the zoning. There is part of a CL dark core, presumably due to high U concentration, with surrounding primary oscillatory zoning preserved on the bottom and left of the grain. There is one small curviplanar feature with included impact melt glass, but there does not seem to be other evidence of impact shock exposed on the grain surface. The core and oscillatory zoned region have the same crystallographic orientation, suggesting the zoning is of primary nature. The core has a slightly lower EBSD band contrast than the surrounding zircon most likely due to the larger structural damage in the higher U regions and the lattice strain from other REE substitutions. The core of Z27 yields a Pb-Pb age of 4331 ± 6 Ma (σ), which is within error of the rim ages 4341 ± 9 Ma (σ).

*14305 Z29* (Figure 3-21)

Zircon 14305 Z29 is an ~100 μm Ma grain that exhibits primary sector zoning and a concordant Pb-Pb age of 4254 ± 6 Ma (σ). The grain has three major zones in CL imaging, the darkest of which may have internal oscillatory or sector zoning. The zircon is fractured, but the cracks do not appear to be PFs or CPFs, and they are not filled with impact melt glass. EBSD point analyses show no change in orientation across the CL regions, which is consistent with primary zonation. The dark CL region has slightly low band similar to 14305 Z27 described above.

*14305 Z30* (Figure 3-22)

Zircon 14305 Z30 exhibits some of the highest shock alteration features of the lunar zircons in this survey. The zircon is surrounded by pigeonite and anorthite from the host breccia, which appear to be void of shock features (see Figure 3-7 C for higher resolution image). Z30 is a highly fractured heart-shaped ~ 150 x 200 μm grain. The grain is riddled with PFs and CPFs that are entirely or partially filled with impact melt glass. A region of granular recrystallization texture cuts through the center of the zircon. The individual granules are small with most under

Figure 3-20: 14305 Z27

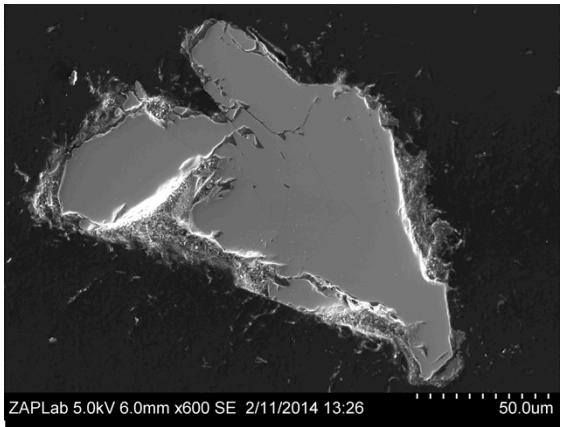


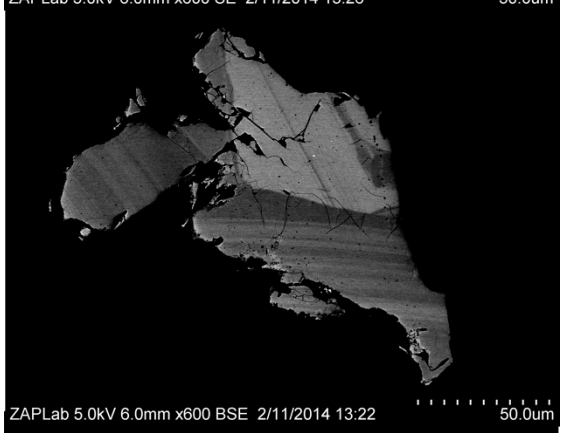


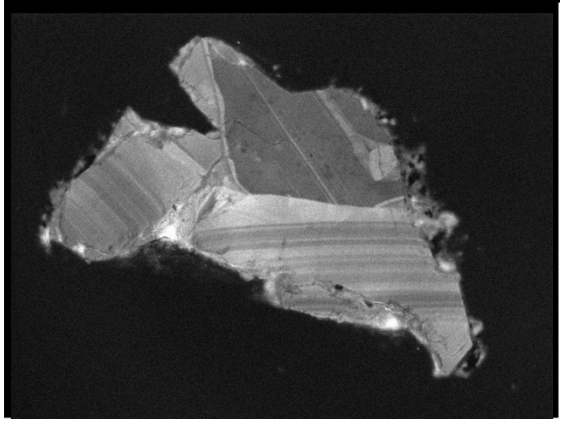

Figure 3-21: 14305 Z29

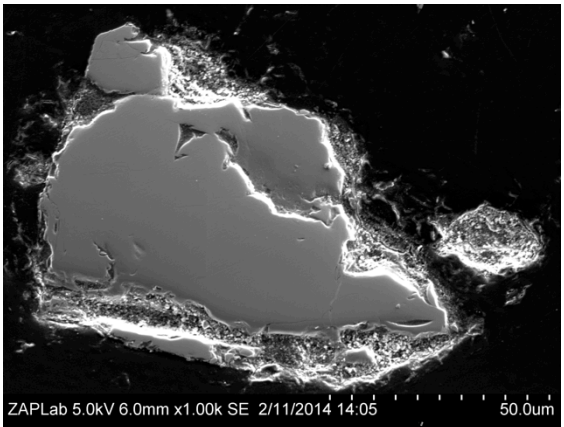


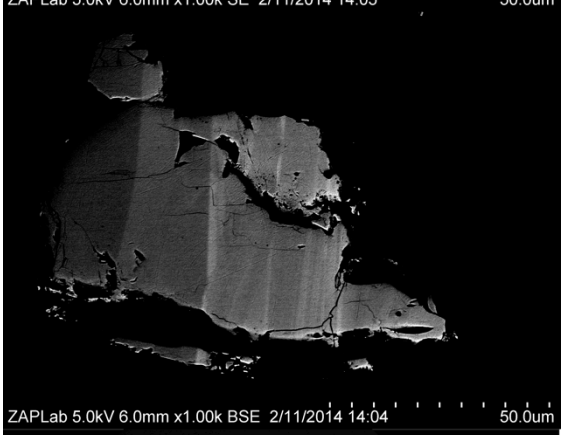


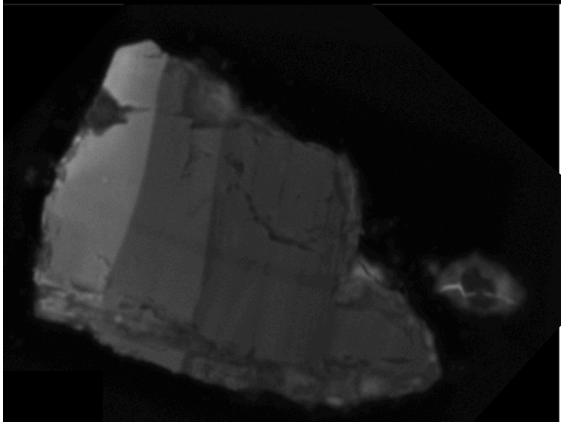

Figure 3-22: 14305 Z30

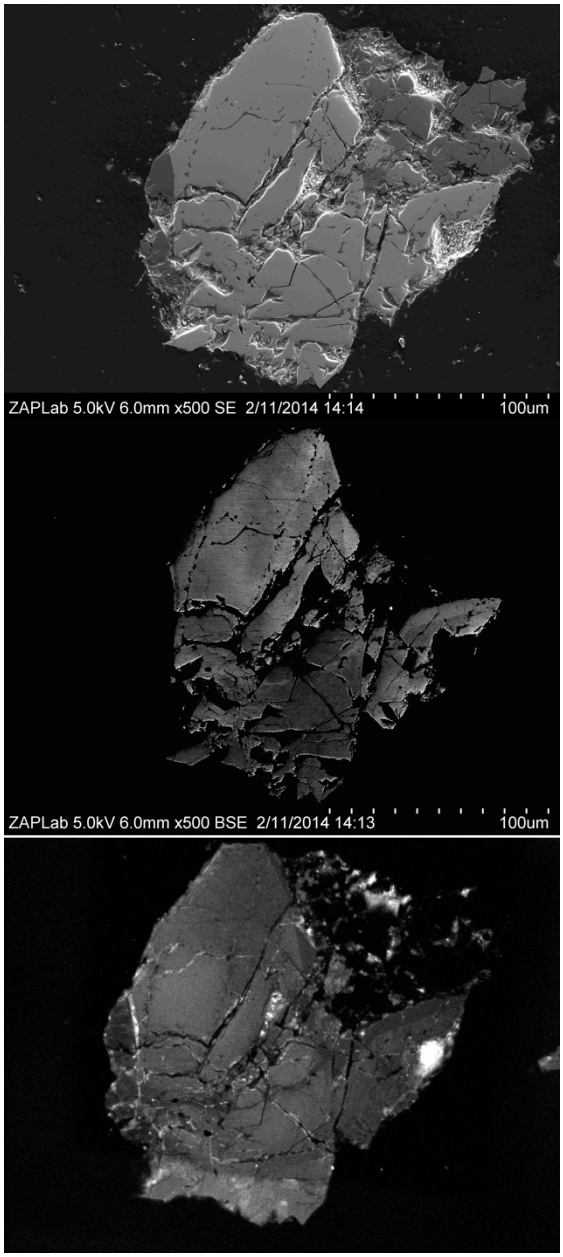


Figure 3-23: 14305 Z31

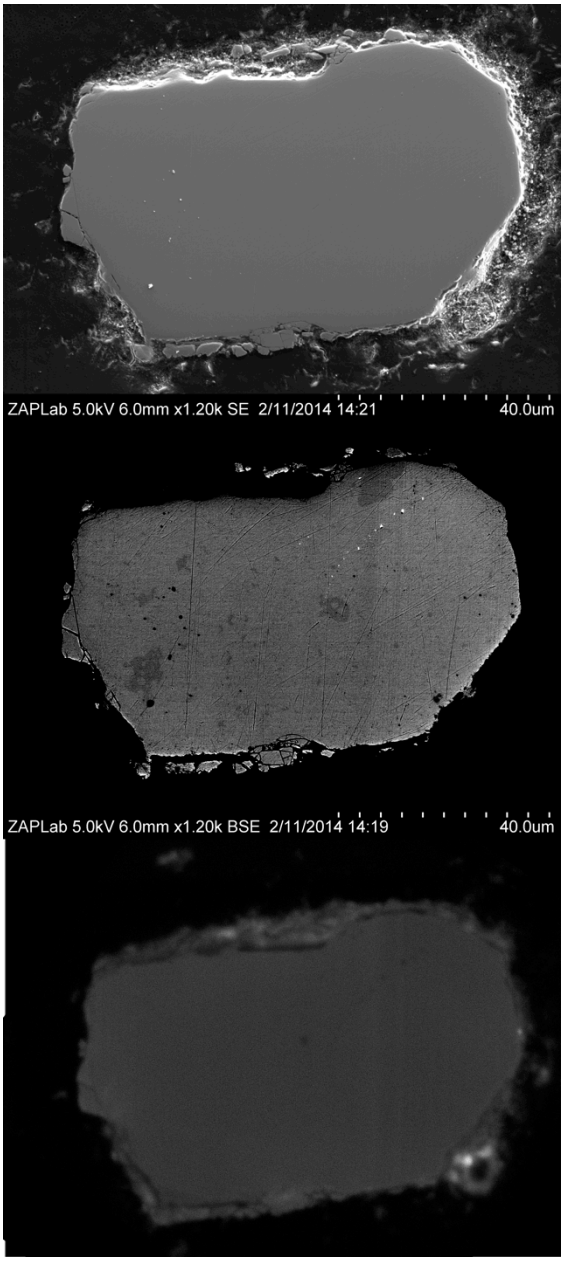

1 mm in diameter. Granular texture has been observed in experimentally shocked zircons at pressures above 60 GPa (Leroux et al. 1999). Moser et al. 2011 observed that this texture is usually accompanied by partial to total Pb-loss in terrestrial impact zircons from the Vrederfort impact structure. EBSD analyses show that the two halves of the grain on either side of the granular zone are slightly rotated relative to each other, and the recrystallized granules have orientations largely offset from the host zircon. CL imaging of Z30 show diffuse or modeled texture through out most of the grain and bright regions along the edges of CPFs with large amounts of impact melt glass. The latter also suggests exposure to elevated temperatures.

*14305 Z31* (Figure 3-23)

Zircon 14305 Z31 is an ~ 100 μm zircon that has a concordant Pb-Pb age of 4334 ± 5 Ma (σ). Low kV backscatter and CL images reveal an annealed CPF identified by a chain of bright spheres in the upper right quadrant of the grain. The dark regions seen in the low-kV BSE images are not associated with any features in CL imaging, so are potentially due to surface contamination. These features were present in the 15311 soil zircon images, which had to be re-cleaned and re-coated due to surface contamination, further strengthening the assumption that these are artifacts.

*14305 Z33* (Figure 3-24)

Zircon 14305 Z33 is an ~ 150 μm zircon with a Pb-Pb age of 4334 ± 4 Ma (σ). In CL, Z33 appears to have sector zoning, mostly likely primary. There is one region on the right most part of the zircon that is bright in CL and dark in low-kV BSE that has a higher band contrast, but same crystallographic orientation as the rest of the grain supporting the interpretation of primary zoning. Some fragments along the central crack in the zircon are misoriented by ~6° (bright in low-kV BSE). These pieces do not appear to be attached to the host grain, so this could be caused during the mounting process. Z33 also has dark spots similar to Z31 that do not correspond to CL or EBSD features. They are therefore most likely due to surface contamination.

Figure 3-24: 14305 Z33

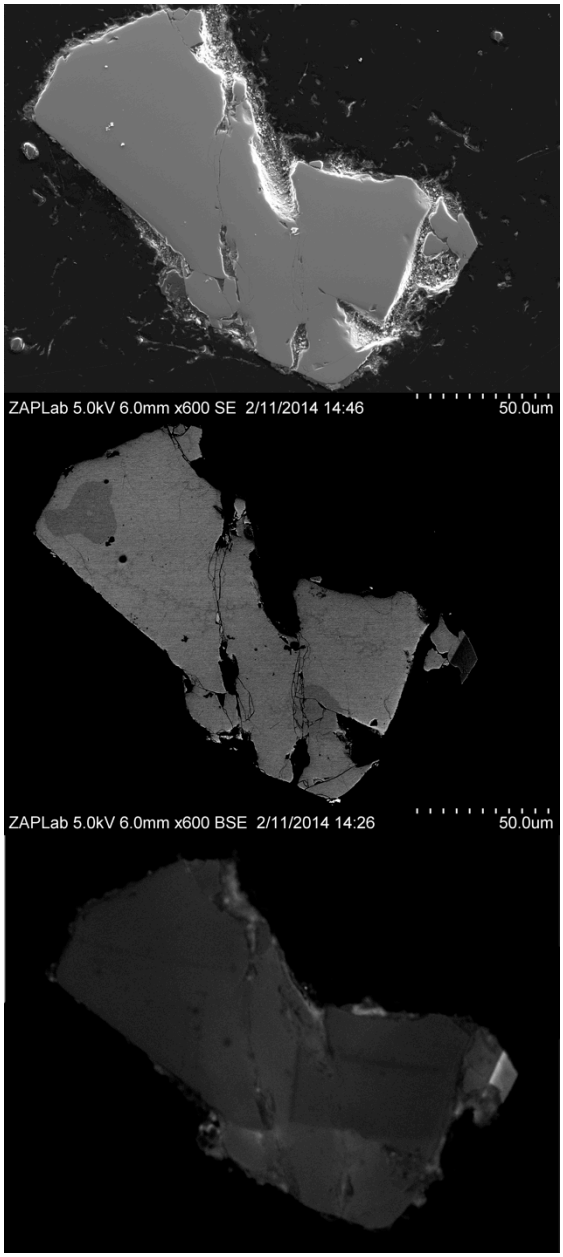


Figure 3-25: 14305 Z34

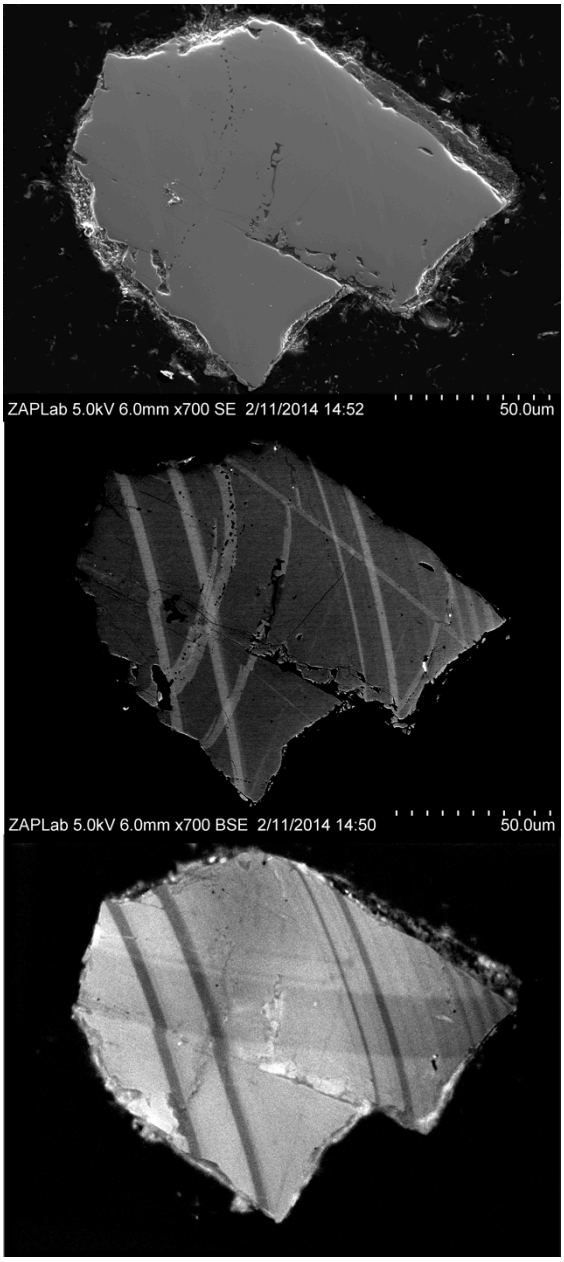

*14305 Z34* (Figure 3-25)

Zircon 14305 Z34 is a highly shocked ~ 100 μm zircon with a concordant Pb-Pb age of 4324 ± 5 Ma (σ) and which exhibits both primary and secondary features. In CL, there is a series of dark thin (~5 μm) parallel bands that are offset in the lower left quadrant by the crack running the length of the grain. EBSD analyses show that these bands have a slight offset of ~1° to 2° and are accompanied by a decrease in band contrast. These bands are most likely primary bands of high U concentration, although it is unusual for primary zoning to be offset from the surrounding grain suggesting they may have been affected by impacts. Grain Z35 also contains two sets of microtwins. The first set has three twins that are parallel and curved. The plane of these twins is near perpendicular to the grain surface, so the curvature is real and not an artifact of polishing. All three are spatially associated with impact melt inclusions that look similar to CPFs. One of the impact melt inclusions is crystalline, but is neither zircon nor reidite. The second linear shock microtwin offsets the previous set of microtwins, although it does not offset the CL dark bands. This second microtwin also offsets a band of variable deformation (up to ~ 4°) that runs across the grain perpendicular to the microtwin (see in EBSD map Figure 3-6). This deformation does not appear to be associated with a crack or melt inclusions. The zircon as a whole has about 1.5° of deformation across the grain and there is up to 4° of deformation along the crack running the length of the grain.

*14305 Z36* (Figure 3-26)

Zircon 14305 Z36 is a large ~130 x 250 μm zircon with a Pb-Pb age of 4281 ± 5 Ma (σ). Grain Z36 has multiple secondary microstructures; CL images need to be taken to determine the presence of primary zonation. There are bands of 4° rotation or crystal plastic deformation around the c-axis running the length (light band on right of low-kV BSE image). There are multiple curviplanar and planar features that have impact melt inclusions with evidence of annealing and/or reaction with the surrounding zircon. The grain also has two parallel microtwins that are perpendicular to and cross (but not offset) the bands of rotation around the c-axis. Each twin is itself made up of three smaller parallel microtwins and part of one twin is

accompanied by impact melt inclusions in the region of crystal plastic deformation. The twins appear to terminate near a region of high concentration of CPFs and fractures. There are also defuse planar features (bright in low-kV BSE images) parallel to the well-defined twins that could potentially be remnant twins, but we did not index them with EBSD analyses.

*14305 Z42* (Figure 3-27)

Zircon 14305 Z42 is ~100 x 50 μm, 4333 ± 5 Ma (σ) zircon. Only part of the grain is exposed on the mount surface. Comparison of the low-kV BSE and SE images reveals that some of the fragmented appearance in the BSE image is due to topography and not interstitial material or matrix. Grain Z42 has two small CPFs with impact melt inclusions (left most part of grain in low-kV BSE image), but is otherwise featureless.

*14321 Z10* (Figure 3-28)

Zircon 14321 Z10 is a large ~160 μm zircon with a Pb-Pb age of 4268 ± 10 Ma (σ). This grain has two regions of primary sector zoning that are crosscut by a large CPF. This CPF is partially annealed (the annealed regions appear brighter in low-kV BSE than the surrounding host grain) and partially filled with impact melt glass. There is a second, almost completely annealed CPF in the lower left of the grain. EBSD analyses show homogeneity in crystal orientation across the grain, which is consistent with primary zoning.

*14321 Z12* (Figure 3-29)

Zircon 14321 Z12 is a large 100 x 200 μm zircon with a Pb-Pb age of 4160 ± 3 Ma (σ). Grain Z12 has a large ~ 80 μm long, almost linear CPF that is filled with impact melt inclusions. Most of melt inclusions have recrystallized and individual euhedral crystals are visible in the SEM. The composition of these minerals or the impact melt glass has not yet been measured. There are also small circular bright and dark areas surrounding the recrystallized melt inclusions. Most are too small to index with EBSD, but one contained a pattern indexed as baddeleyite. The

Figure 3-26: 14305 Z36

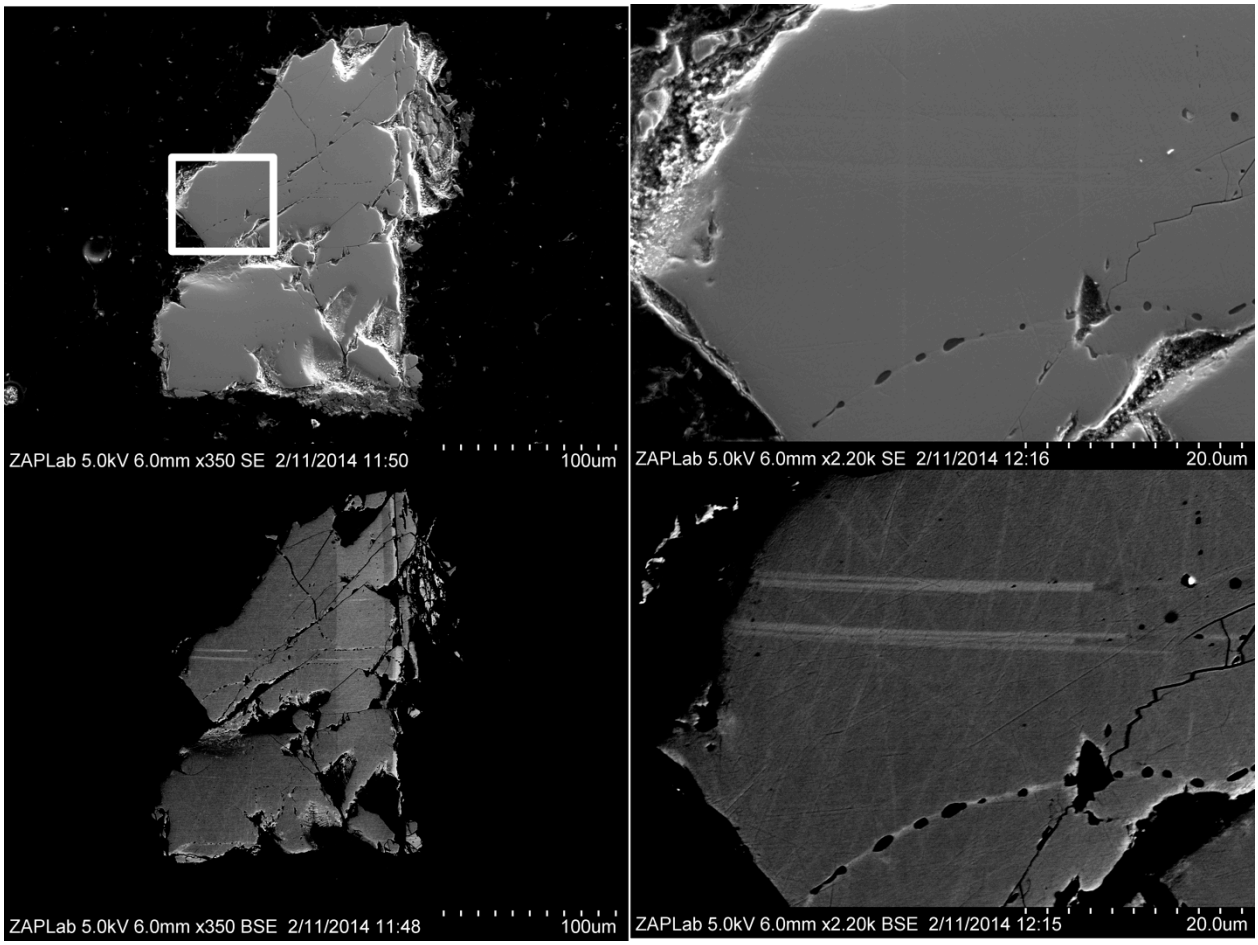

Figure 3-27: 14305 Z42

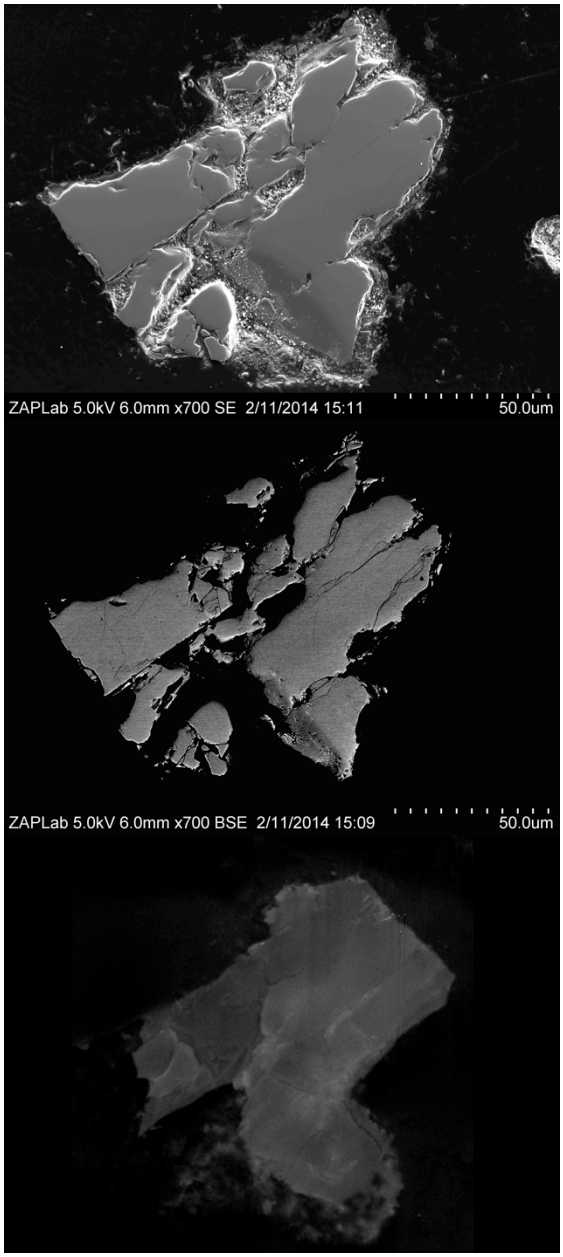


Figure 3-28: 14321 Z10

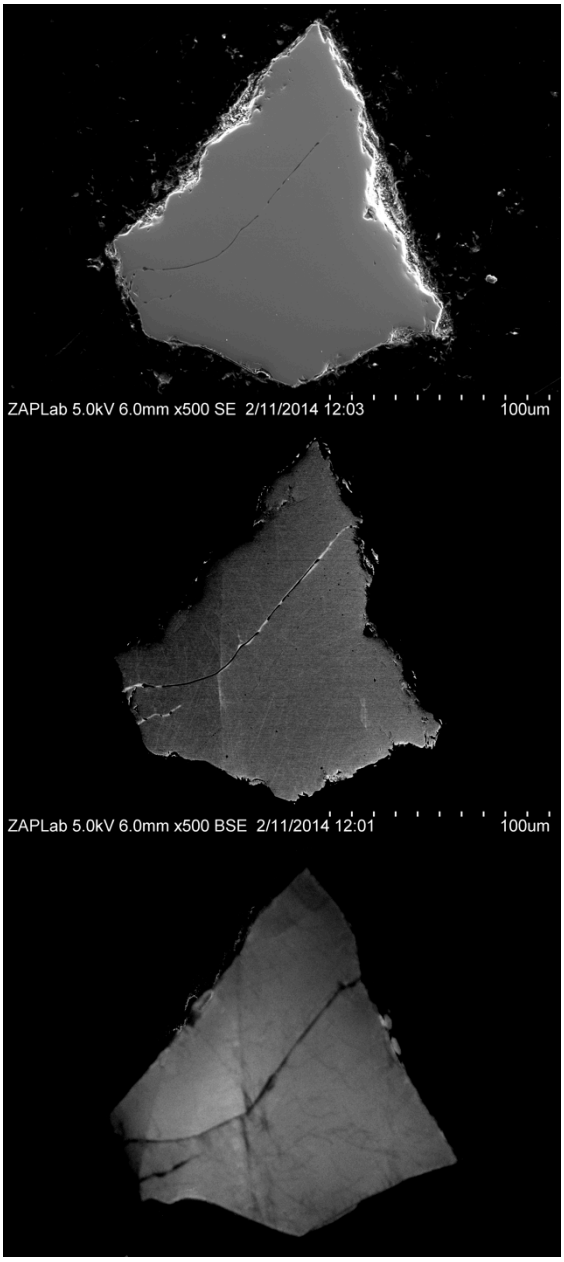

Figure 3-29: 14321 Z12

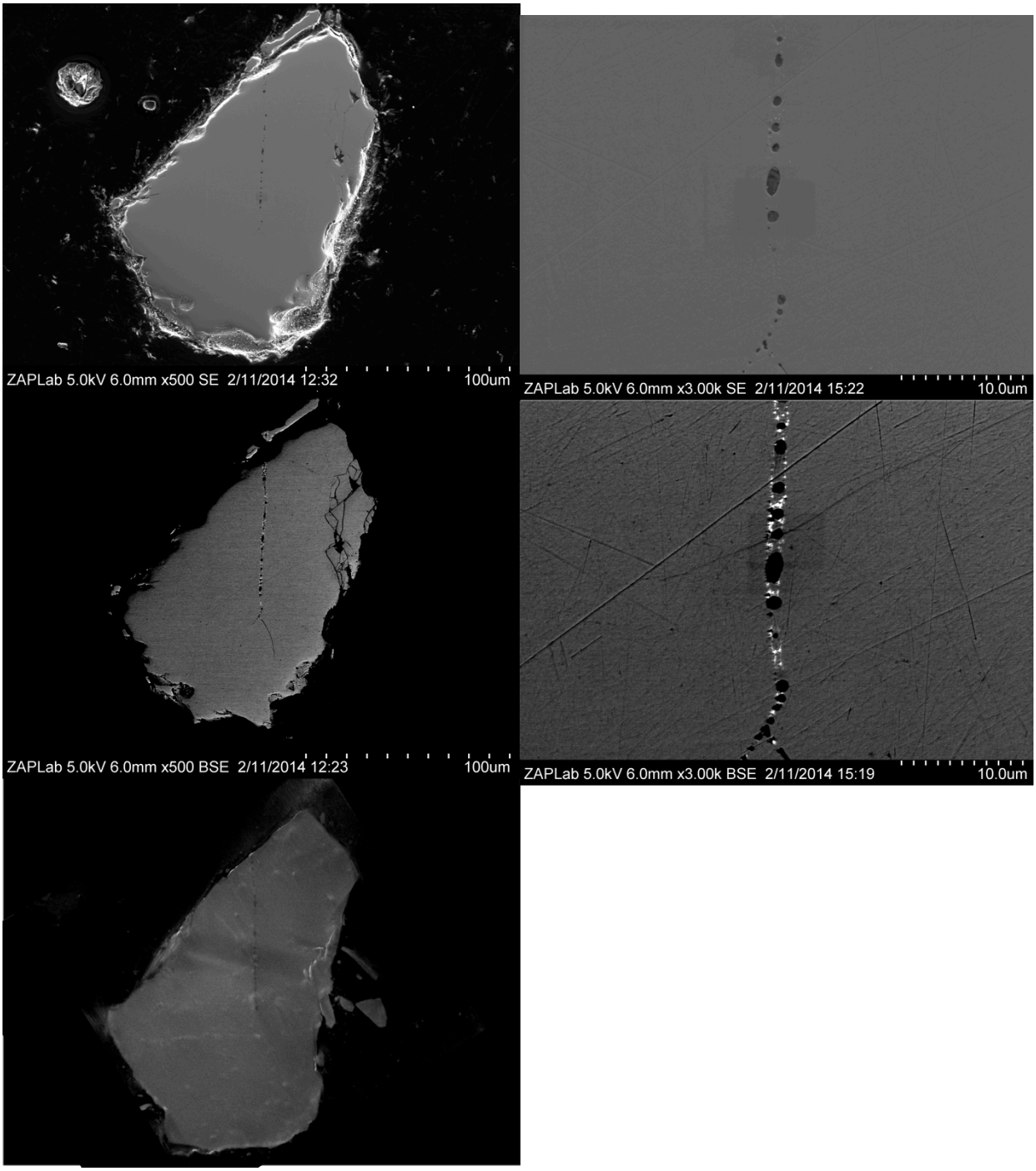

recrystallization of the impact melt suggests this grain may have elevated temperatures long enough to result in devitrification of the IMG inclusions.

*14321 Z11* (Figure 3-30)

Zircon 14321 Z11 is large 100 x 160 μm zircon with a typical REE pattern and Pb-Pb age of 4385 ± 4 Ma (σ). Z11 has two regions of primary oscillatory zoning and only minimal secondaryshock features. There is a small curviplanar fracture with ~2 μm melt inclusions along the bottom edge of the grain. There are also larger fractures not filled with glass.

*14321 Z14* (Figure 3-31)

Zircon 14321 Z14 is a large ~300 μm zircon that appears to have no primary or secondary features. REE analyses of six different locations reveal that the zircon is homogeneous in trace elements. EBSD analyses also show a high degree of homogeneity with variations in crystallographic orientation less than 1°. Despite it's Z14's chemical and structural uniformity, Pb-Pb ages range from 4134 ± 31 to 4208 ± 6 Ma (σ) with discordance ranging from 5 - 32%. The Pb disturbance is puzzling given the absence of secondary shock features.

*14321 Z17* (Figure 3-32)

Zircon 14321 Z17 is 100 x 200 μm zircon that is homogeneous in low-kV BSE and does not appear to have any impact shock features although it does have a few cracks. The dark patches in the low-kV BSE image are similar to those seen in 14305 Z31 and Z33, and are most likely due to surface contamination. Grain Z17 has a younger Pb-Pb age than most samples investigated (4097 ± 2 Ma (σ)).

*14321 Z19* (Figure 3-33)

Zircon 14321 Z19 is a ~ 100 μm zircon with a concordant Pb-Pb age of 4408 ± 3 Ma (σ), making this grain the oldest zircon analyzed in this study. This zircon is relatively homogeneous except for a small, mostly annealed CPF in the center of the grain. It is easiest to identify the CPF in low-kV BSE by the bright spots of annealed zircon or impact melt glass. Surface dust particles, seen in the SE image, correlate to black spots in the BSE images. The larger amorphous dark regions in the BSE are also likely due to surface contamination.

*14321 Z20 Ghost* (Figure 3-34)

Zircon 14321 Z20 is roughly 150 x 250 μm grain and with a slightly discordant, 6%, Pb-Pb age of 4241 ± 5 Ma (σ). Grain Z20 has a large crack that runs through almost the entire grain, and propagating away from the crack are bright CL wisps. This diffuse, bright CL band crosscuts the whole grain even though the associated crack terminates a little over half way across. The brightest CL zones are associated with a reduction in EBSP band contrast. There is also a string of small impact melt inclusions or CPF that crosscuts the grain to the right of the crack in Figure 25. The inclusions are easiest to identify in the SE image because there are no bright, annealed regions or reaction rims in BSE. EBSD analyses show that the entire grain has been bent ~ 3° around the crack. We are uncertain if this is inherent or due to shifting during the mounting process. There is also one shock microtwin and two possible other microtwins that are oriented ~45° relative to each other (the twins appear dark in low-kV BSE).

*14321 Z21 The Lobsta* (Figure 3-35)

Zircon 14321 Z21 is an ~ 100 μm grain with a Pb-Pb age of 4286 ± 6 Ma (σ). The grain is homogeneous in CL, low-kV BSE and SE images. There are no visible shock features evident on the exposed surface.

*15311 Z3* (Figure 3-36)

Zircon 15311 Z3 is a fractured zircon that exhibits both primary and secondary features. The

Figure 3-30: 14321 Z11

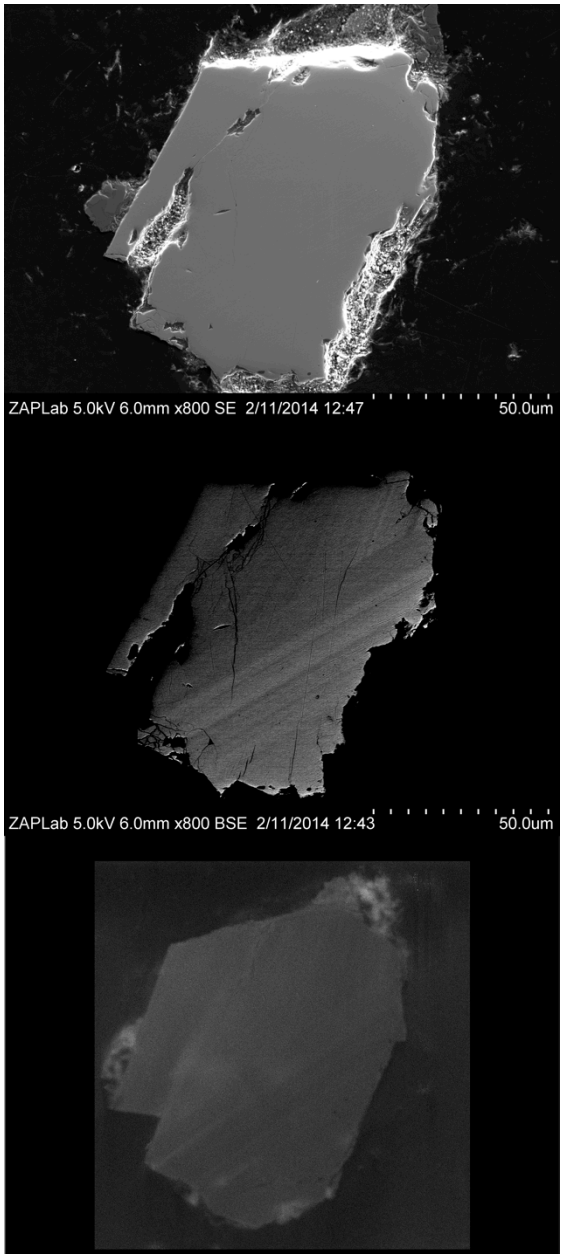


Figure 3-31: 14321 Z14

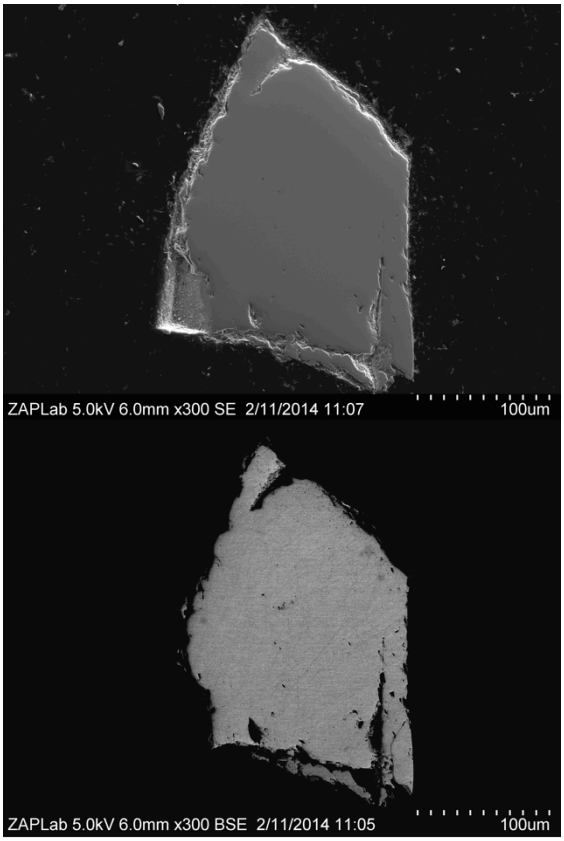

Figure 3-32: 14321 Z17

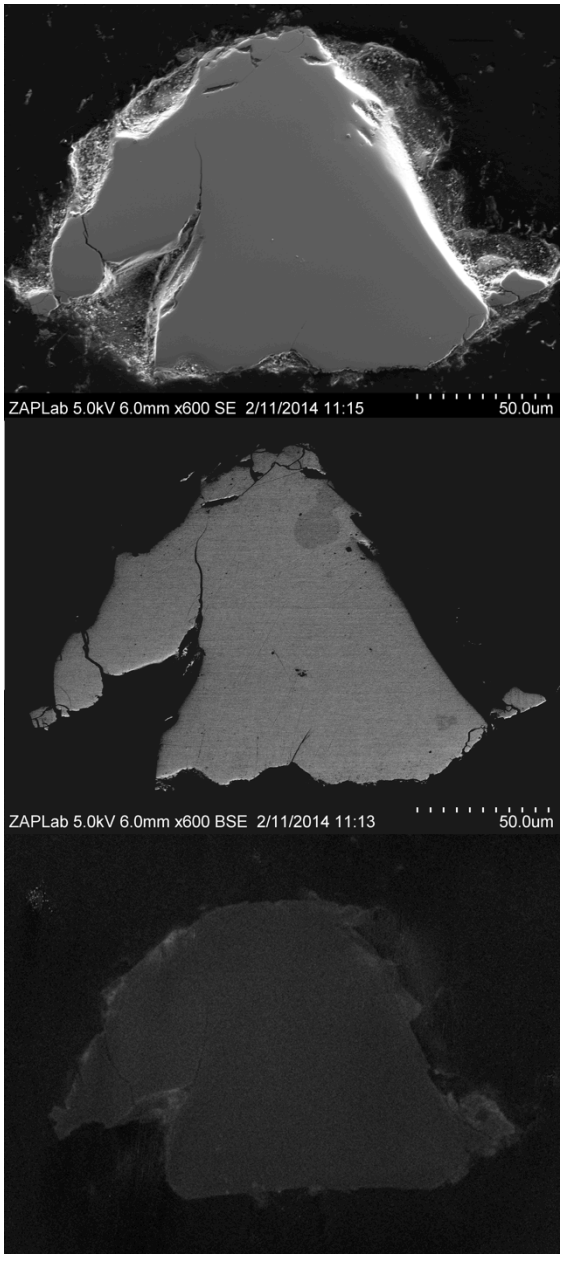


Figure 3-33: 14321 Z19

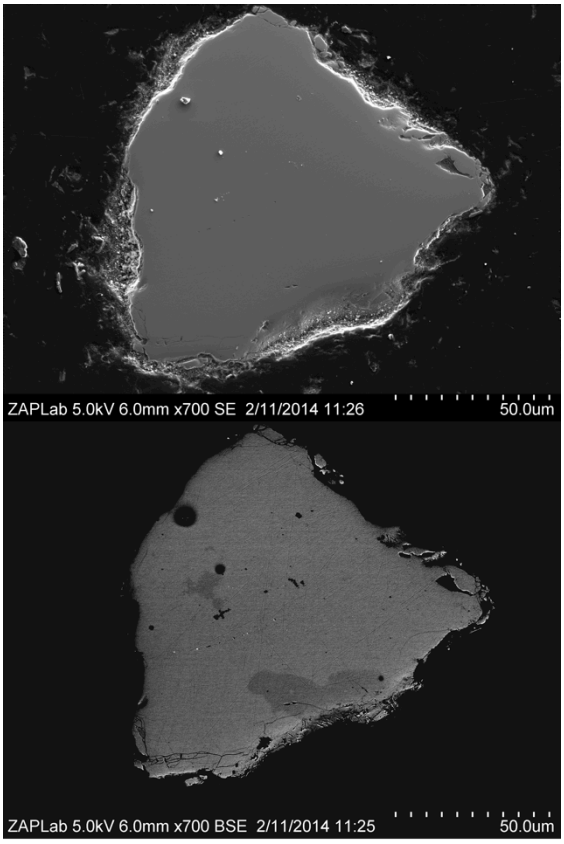

Figure 3-34: 14321 Z20

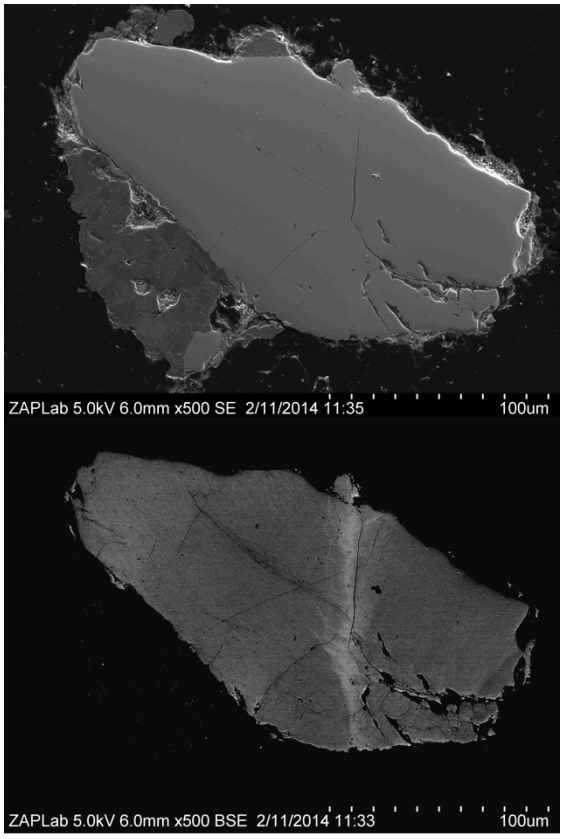


Figure 3-35: 14321 Z21

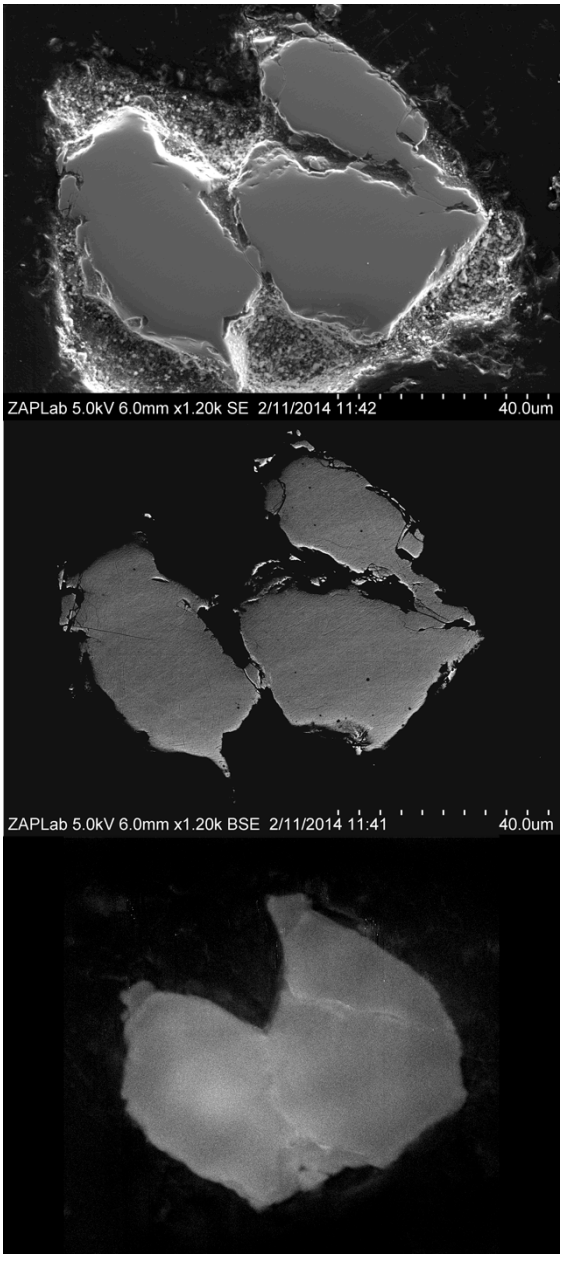

largest fragment of the grain has primary oscillatory zoning and a PF partially filled with impact melt. Each of the fragments is offset from one another by a few degrees, but this could be due to shifting during the mounting process. Grain Z3 was lost during polishing before a Pb-Pb age could be determined.

*15311 Z5 Kite* (Figure 3-37)

Zircon 15311 Z5 has primary sector zoning and possibly some oscillatory zoning. There are a few small impact melt glass inclusions along an annealed CPF that appears bright in CL. There is also diffuse wispy features towards the bottom, right tip of the grain that are visible in both Cl and low-kV BSE images. Wispy CL zones have been seen in other grains associated with cracks and are possibly due to trace element diffusion along the boundary. Z5 has a concordant Pb-Pb age of 4373 ± 30 Ma (σ).

*15311 Z6* (Figure 3-38)

Zircon 15311 Z6 is a highly altered grain with multiple curviplanar fractures filled or partially filled with impact melt glass. Most of the grain is dark in CL and has no indexable EBSP suggesting that this region is amorphous. The small region where the grain is bright in CL has variations in crystallographic orientation up to 28°. Three Pb-Pb analyses of Z6 give old ages of 4245 ± 4, 4327 ± 3 and 4332 ±3 Ma (σ), suggesting portions of this zircon have experienced Pb-loss. Although it is remarkable that other regions of this grain, despite the high degree of shock deformation, have retained their radiogenic Pb for 4.3 Ga.

*15311 Z7* (Figure 3-39)

Zircon 15311 Z7 has a Pb-Pb age of 4338 ± 4 Ma (σ), and it exhibits primary oscillatory zoning with a CL bright boundary crosscutting the grain. There is a large crack through the grain and one CPF with impact melt glass inclusions.

Figure 3-36: 15311,18 Z3

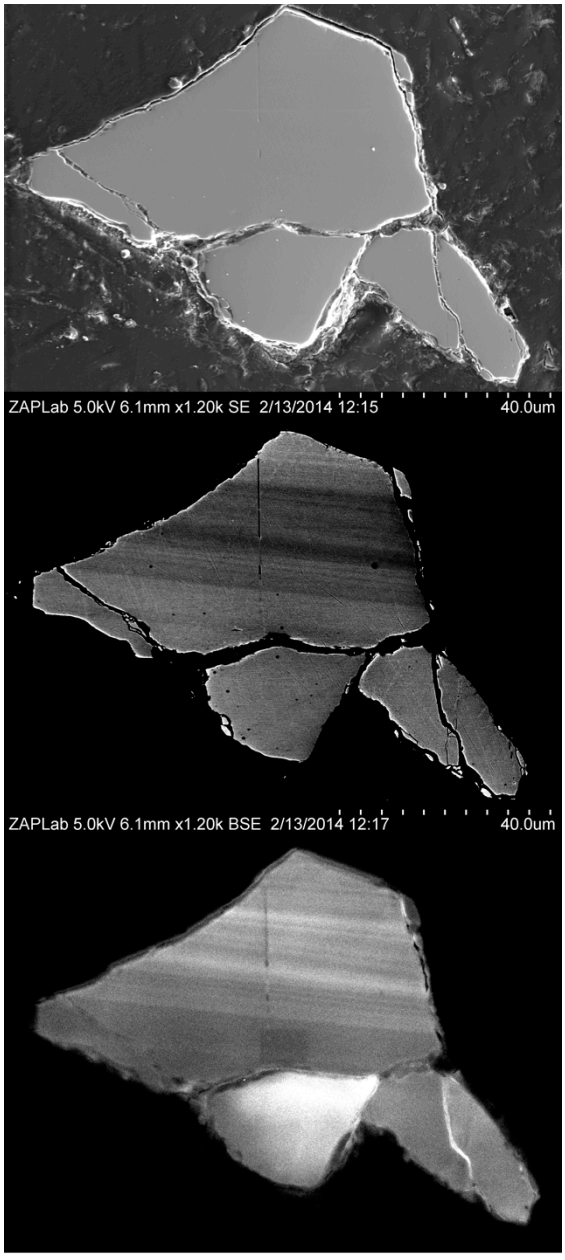


Figure 3-37: 15311,18 Z5

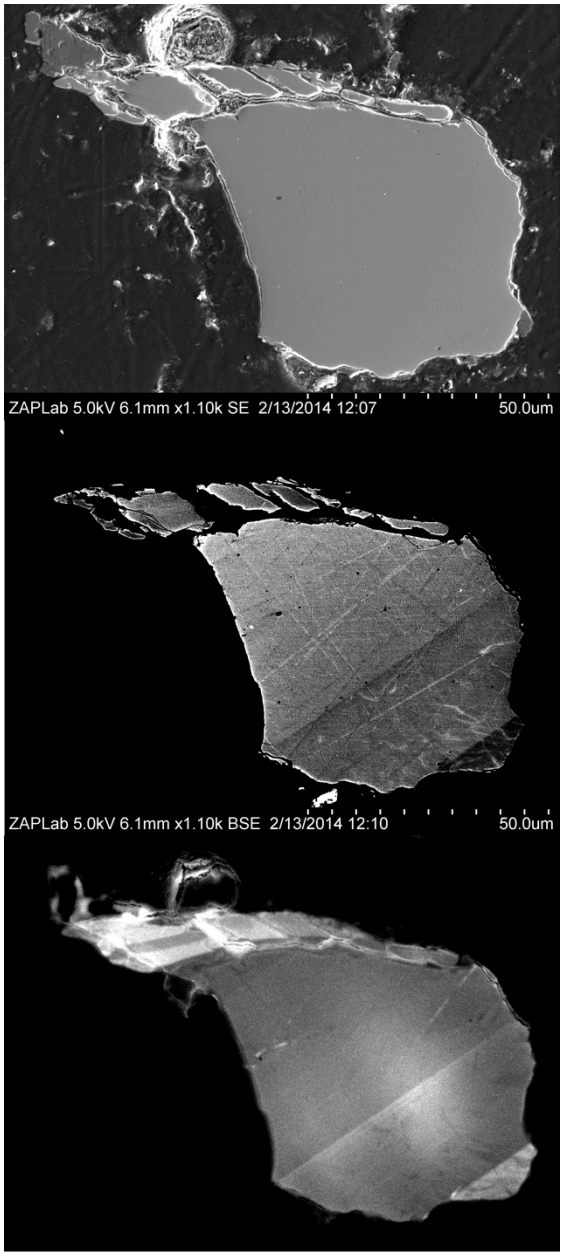

Figure 3-38: 15311,18 Z5

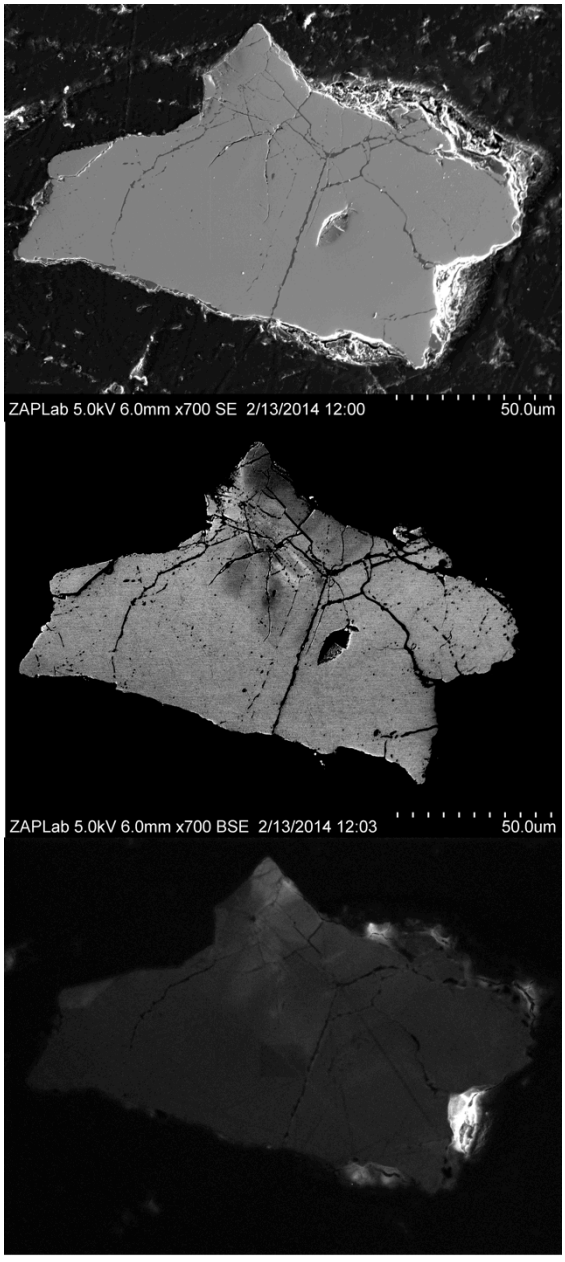


Figure 3-39: 15311,18 Z7

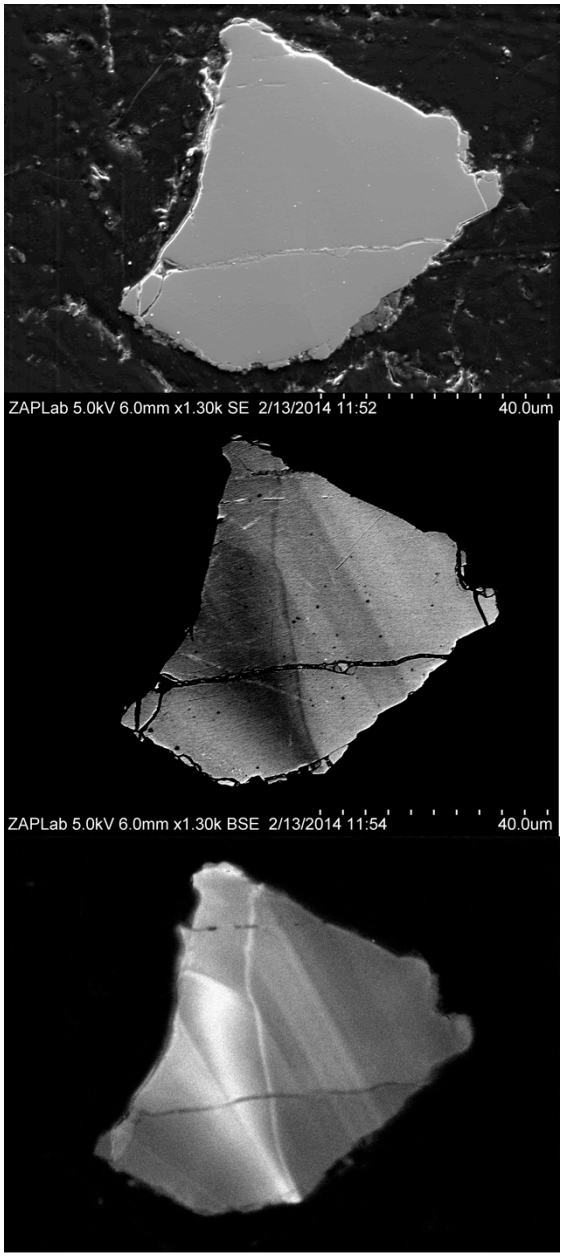

**Appendix 3-2: Granular Texture Zircons and Decomposition of Zircon to $ZrO_2$ and $SiO_2$**

In addition to the granular texture zircons discussed in Chapter 3, we identified three additional zircons with this recrystallization texture. Additionally, we report the first observation of the decomposition of lunar zircon to its constituent oxides baddeleyite ($ZrO_2$) and $SiO_2$. Bellow are pictures of two granular zircons separated from Apollo breccia 15455 and one from 14259.

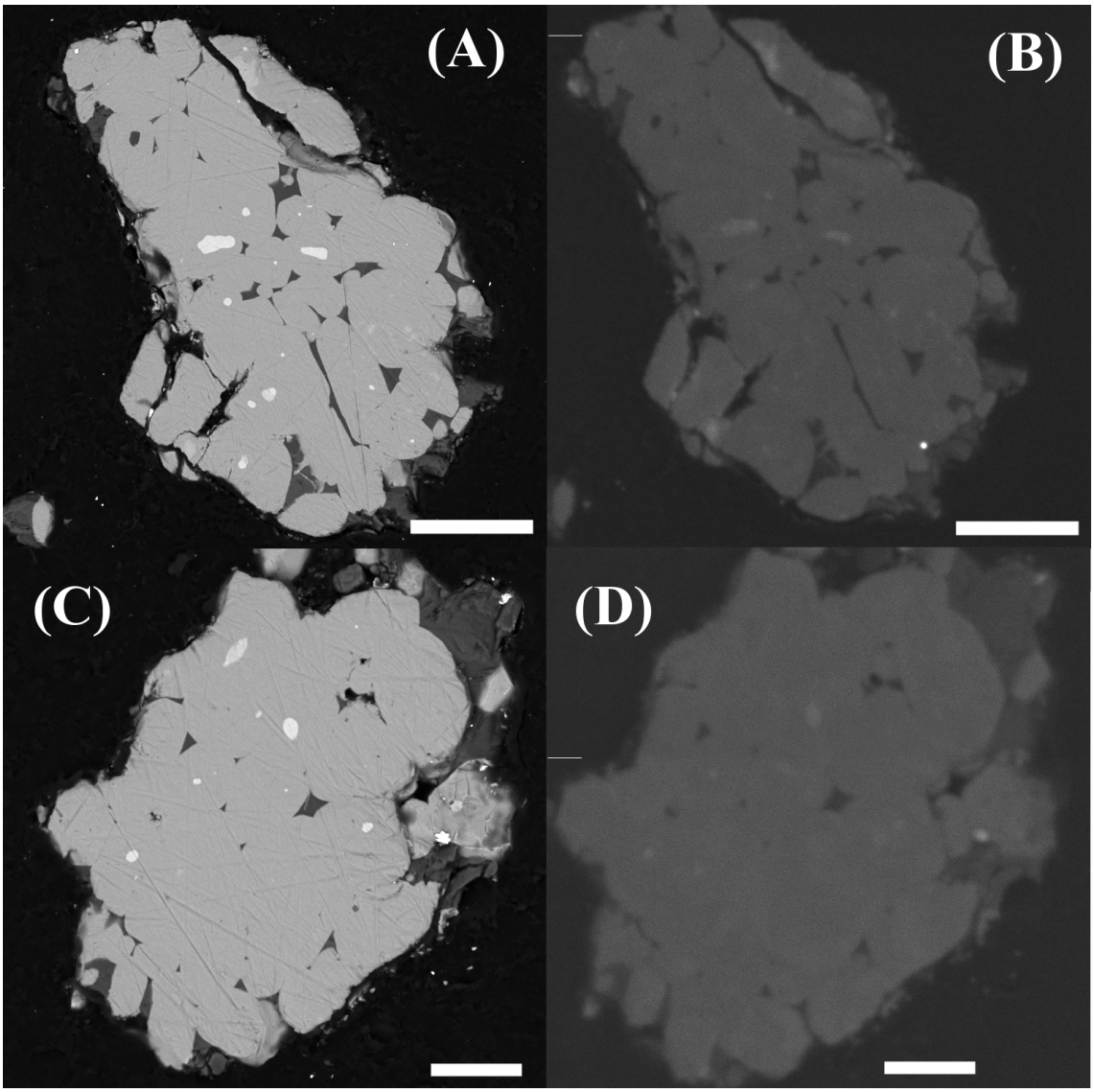


Figure 3-40: Granular texture zircons with decomposition to baddeleyite and $SiO_2$. (A) SE image and (B) CL image of 15455 Z3 (scale bar 20 μm). (C) SE image and (D) CL image of 15455 Z24 (scale bar 10 μm). Both zircons have large recrystallized granules, so up to 20μm in length. The brightest regions in both SE and CL images are consistent with $ZrO_2$ and dark interstitial material has $SiO_2$ composition. Two SIMS analyses of Z3 yield $^{207}Pb$-$^{206}Pb$ ages of 4322 ± 4 and 4331 ± 3 Ma (σ) and one of Z24 give an age of 4332 ± 3 Ma (σ).

**Appendix 3-2 (Continued):**

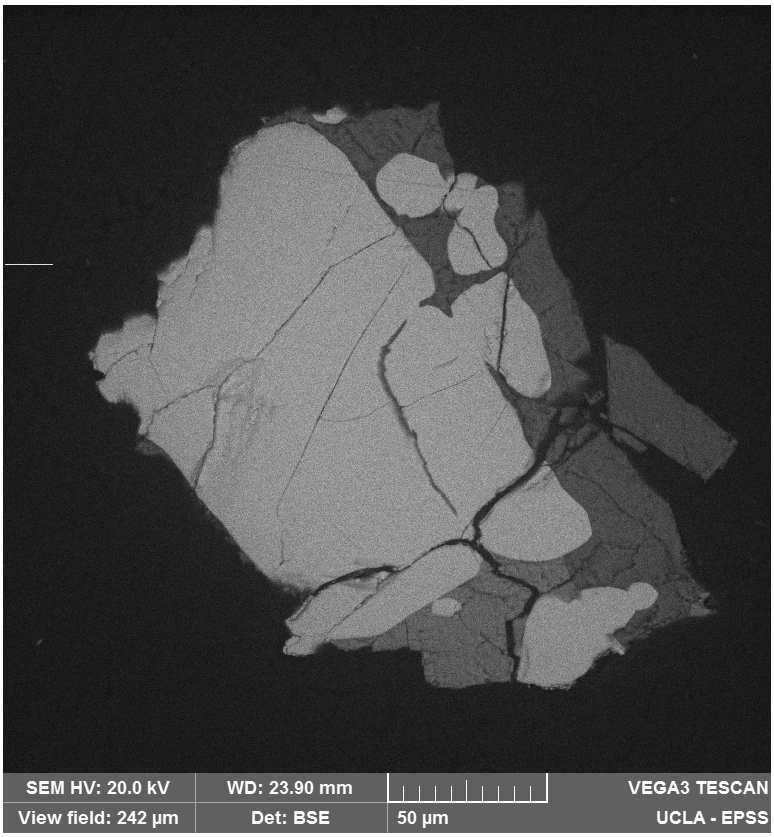


Figure 3-41: Granular texture zircon 14259,664 Z24. Two $^{207}Pb$-$^{206}Pb$ analyses yield concordant ages of 4195 ± 7 Ma. This age is similar to the 4.2 Ga basin forming event proposed by Norman and Nemchin (2014) based on zirconolite and apatite grains from Apollo 16 sample 67955.

## Appendix 3-3: Previously Reported Lunar Zircon Shock Microstructures

| Sample | Primary Ocillatory Zoning | Primary Sector Zoning | Diffuse CL | CPF[1] | Melt Inclusions | CPD[2] | Amorphous Zircon | Shock Twins | Granular/ Skelital Texture | Pb-Pb Age (Ma) | 1σ | Source |
|---|---|---|---|---|---|---|---|---|---|---|---|---|
| 14083,35 #1* | X | | | | | | | | | 4036-4043 | 5/7 | (A) |
| 14303,49 #1* | X | | | ? | | | | | | 4228-4339 | 4 | (A) |
| 14303,49 #3* | | | | X | | | | | | | | (A) |
| 14163 #10* | X | | | | | | | | | 4343 | 7 | (A) |
| 14305,93 #1* | | | | | | | | | | 4159-4216 | 15/18 | (A) |
| 14306,60 #1* | X | X | | ? | | | | | | 4198-4221 | 6/5 | (A) |
| 14306,60 #2* | | X | | ? | | | | | | 4205-4208 | 17/5 | (A) |
| 14306,60 #62* | | | | X | | | | | | | | (A) |
| 14321,1613 #1* | | X (faint) | | | | | X | | | 3972-4004 | 4 | (A) |
| 14321,1613 #2* | | X (faint) | | | | | X | | | 3959-3990 | 5 | (A) |
| 73215,122 #6[S]* | | | | | | X | X | | X | 4292-4378 | 21 | (A) (B) |
| 76295,91 #2* | | X | | X | | X | | X | | 4110-4243 | 9/12 | (A) |
| 73235,82 #1[3]* | | X | | | | X | | | | 4315 | 15 | (C) |
| 73235,82 #1[4]* | | | | | | | X | | X | 4187 | 11 | (C) |
| 73235,60 #4* | | | | | | | | | | 4353-4369 | 6 | (D) (B) |
| 73215,122 #5* | | | | | | X | X | | | | | (B) |
| 73235,60 #5* | | | | | X | ? | X | | | 4175-4219 | 7/5 | (E) (B) |
| 72215,195 #1* | X | X | | | | X | X | | | 4417 | 6 | (F) (B) |
| 73235,59 #3* | | | X | X | | X | | X | X | 4331-4395[5] | 7/11 | (D) (B) |
| 73235,60 #2* | | | | | | | X | | | 4241-4361 | 5/6 | (D) |
| 73235,60 #3* | | | | | | | X | | | 4347 | 25 | (D) |
| 73235,80 #2 | | | | X | | | | | | 4339 | 6 | (D) |
| 73217,52 #1 | | | | | | | | | ? | 4332 | 7 | (H) |
| 73217,52 #2[S] | | | | X | ? | | | | X | 4335 | 5 | (G) (H) |
| 73217,52 #3* | | | | | | | | | X | 3929 | 10 | (H) |

* EBSD analyses have been collected for these zircons.

[1] Curviplanar features

[2] Crystal plastic deformation

[3] Primary fragmented zircon

[4] Secondary matrix zircon

[5] One analysis of this grain has a $^{207}Pb$-$^{206}Pb$ age of 4106 ± 9 Ma.

[S] Skeletal texture.

(A) Grange et al. (2013)
(B) Timms et al. 2012
(C) Pidgeon et al. (2007)
(D) Grange et al. (2011)
(E) Meyer et al. (1996)
(F) Nemchin et al. (2009)
(G) Nemchin et al. (2008)
(H) Grange et al. (2009)

## Chapter 4: U-Xe Ages of Terrestrial and Lunar Impact Shocked Zircons

### 4.1 Introduction

The U-Xe (or $Xe_S$-$Xe_N$) dating technique was detailed by Shukoljukov et al. (1974), Teitsma et al. (1975), and Teitsma and Clarke (1978) for application to zircon and other uranium bearing minerals. The method uses Xe produced by spontaneous fission of $^{238}U$ and neutron induced fission of $^{235}U$ to determine a Xe closure or degassing age. The neutron irradiation of the samples allows for ages to be calculated without precisely measuring the U abundance of a sample. These early studies, along with later zircon step heating analyses, suggest that the U-Xe system in zircon has high thermal stability, possibly as stable as the U-Pb system (Shukolyukov et al., 2009). However, Krylov et al. (1993) analyzed zircons from the Archean Napier Complex in East Antarctica and found variations in the Xe ages for gasses released at low and high temperatures. They found the low temperature step (<1200°C) ages to correspond with known local events while the oldest high temperature steps were commensurate with U-Pb SHRIMP ages for zircons from the same region. This suggests that the U-Xe system in zircon may be useful in determining the ages of both primary crystallization and secondary thermal events.

Turner et al. (2004, 2007) measured Xe isotopes for a suite of Hadean zircons from western Australia and also noted varying amounts of Xe loss. They also found evidence for Xe produced by the extinct radionuclide $^{244}Pu$ ($t_{1/2}$ = 82 Myr). Comparison between the U-Xe and Pu-Xe ages allows for constraints to be placed on the age of and fraction of Xe degassing. The lunar zircons are of a similar age as, or older than, the Hadean zircon population which do show evidence of the incorporation of $^{244}Pu$. If the lunar grains have not experienced total degassing since ~3.9 Ga,

they should also retain a signature of plutogenic Xe. The pairing of U-Pb and U-Pu-Xe system in zircon allows for crystallization and degassing ages to be determined for individual grains. Currently most crystallization and degassing ages are measured on whole rock or mineral separates (see discussion in Borg et al. (2015)). This poses potential problems for returned lunar samples, which are mostly breccias comprised of a mixture of material with varying thermal histories. This ability to measure both crystallization and degasing ages for individual zircon grains could be a potentially useful method for investigating the impact history of the Moon. Additionally, the high thermal stability of the Xe in zircon makes it promising for studying the pre-late heavy bombardment (LHB) era for which the timing of basin forming impacts is not well constrained.

In this study we have measured Xe isotopes and U/Xe ages for a suite of lunar zircons and terrestrial zircons from the Vrederfort impact structure in South Africa. The goal was to investigate the response of the U-Xe system to terrestrial bolide impact settings and use these findings to help understand the U-Pu-Xe ages of the lunar samples.

## 4.2 Methods

### *4.2.1 U-Xe Dating*

During magmatic crystallization, the actinide isotopes $^{235}U$, $^{238}U$, and $^{244}Pu$ partition favorably into zircon. The latter two radioactive parents can spontaneously fission producing, among other fission fragments, the heavy isotopes of Xe ($^{131}Xe$, $^{132}Xe$, $^{134}Xe$, and $^{136}Xe$). Additionally, fission can be induced in $^{235}U$ by thermal neutron bombardment in a nuclear reactor (e.g. Shukoljukov et al., 1974; Teitsma et al., 1975; Teitsma and Clarke, 1978). Zircons that form

before, and have retained their fission Xe since, extinction of $^{244}$Pu (~ 600 Myr after solar system formation) should retain a plutogenic Xe signature allowing for two Xe ages to be determined: one calculated using the spontaneous fission Xe from $^{238}$U and $^{244}$Pu (denoted U-Pu-Xe dating), and the second using the spontaneous and neutron fission Xe from the U nuclides (denoted U-Xe dating).

The method of U-Xe dating is similar to that of Ar-Ar and I-Xe dating (Shukoljukov et al., 1974; Teitsma et al., 1975; Turner et al., 2004). If we assume the distribution of $^{235}$U/$^{238}$U is homogeneous within a zircon grain, then the ratio of Xe from neutron induced fission of $^{235}$U to Xe from spontaneous fission of $^{238}$U (S/N) can be used to calculate a U-Xe age. Below is a derivation based on the method outlined by Shukoljukov et al., 1974 and Teitsma et al., 1975.

The number of spontaneous fissions (S) of $^{238}$U is a function of the spontaneous fission and alpha decay constants ($\lambda_s$, $\lambda_a$), the number of $^{238}$U atoms, and the age (T).

$$S = \left(\frac{\lambda_s}{\lambda_\alpha}\right)^{238}U\left(e^{\lambda_\alpha T} - 1\right) \tag{4.1}$$

We can redefine $\lambda_s/\lambda_a$ of $^{238}$U as the branching ratio as $B_8$ to simplify equation 4.1.

$$S = B_8 \cdot {}^{238}U\left(e^{\lambda_\alpha T} - 1\right) \tag{4.2}$$

The number of neutron induced fissions (N) of $^{235}$U is a function of its thermal neutron cross section ($\sigma_5$), the thermal neutron fluence (*f*), and the number of $^{235}$U atoms.

$$N = \sigma_5 \cdot f \cdot {}^{235}U \tag{4.3}$$

The number of atoms of a given isotope of Xe, *i*, is the product of the number of fissions and the yield of isotope *i* per fission, which is dependent on the fissioning parent. We are most interested in *i* = 131, 132, 134, 136 as the light isotopes 124, 126, 128, and 130 are shielded and 129 is complicated due to contributions from $^{129}$I.

$$^{i}Xe_{S} = Y_{S}^{i}S$$
$$^{i}Xe_{N} = Y_{N}^{i}N$$

If we ratio equations 4.2 and 4.3 we create the new expression:

$$\frac{S}{N} = \left(\frac{B_8}{\sigma_5 \cdot f}\right)\left(\frac{^{238}U}{^{235}U}\right)\left(e^{\lambda_\alpha T} - 1\right) \tag{4.4}$$

This equation can be rearranged to solve for the U-Xe age (T).

$$T = \frac{1}{\lambda_\alpha}\ln\left[1 + \left(\frac{^{235}U}{^{238}U}\right)\left(\frac{\sigma_5 \cdot f}{B_8}\right)\left(\frac{S}{N}\right)\right] \tag{4.5}$$

The thermal neutron fluence (*f*) is determined by measuring the number of Xe atoms/mg in a U bearing glass that is irradiated with the samples. The glass has a known U concentration and mass, so the number of $^{235}$U atoms can be calculated and used in equation 4.3. For this work, we produced and characterized this flux monitor (see discussion in section 4.3.1). Values of all constants used in age calculations and references can be found in Table 4-1.

The ratio of (S/N) can be determined by using the ratio of any two heavy isotopes of Xe (131, 132, 134, 136). For zircons that have crystallization ages younger than ~4.0 Ga (no contribution from $^{244}$Pu), we can determine the contributions from $^{235}$U and $^{238}$U by solving a set of simultaneous equations with the following form, based on known (and measured) fission yields:

$$\left(\frac{^{i}Xe}{^{j}Xe}\right)_{M} = f_5\left(\frac{^{i}Y}{^{j}Y}\right)_{5} + f_8\left(\frac{^{i}Y}{^{j}Y}\right)_{8} \quad (4.6)$$

Where measured value of $^{i}$Xe is ratioed to $^{j}$Xe, Y corresponds to the fission yields of isotopes *i* and *j* for $^{235}$U (5) and $^{238}$U (8). Xe isotopic values for end member fission products are listed in Table 4-2, and discussion of the fission yields used can be found in section 4.2.4.

The errors in the U-Xe ages are not greatly influenced by the errors in fission yields, which are relatively small, and are therefore are mostly dependent on the error in the measured Xe isotope ratios. The errors are large for older U-Xe ages due to the dependence of the $^{238}$U contribution on ($e^{\lambda T}$-1). This is also the reason for the asymmetric positive and negative errors for the ancient lunar zircons in section 4.6.2.2.

*4.2.2 U-Pu-Xe Dating*

In addition to U, zircons can incorporate $^{244}$Pu. The half-live of $^{244}$Pu, 82 Myr, is much shorter than that of $^{238}$U, and consequently, only ancient zircons that crystallized before ~ 4.0 Ga can contain a signature of having incorporated now-extinct $^{244}$Pu. At younger ages, the natural fission Xe signal is only from $^{238}$U fission and thus only U-Xe ages can be determined.

If the samples are not reactor irradiated, only two ratios of the fission isotopes of Xe need be used to determine the relative contributions from the two parents. If the samples have been irradiated, three ratios of fission isotopes must be used following the matrix multiplication method, described in the previous section, to determine the contributions from all three parent

isotopes. The ratio of $^{i}$Xe from $^{244}$Pu and $^{238}$U can then be calculated by using the yields of isotope *i*. The U-Pu-Xe age is then calculated by solving for T in the following equation.

$$\frac{\left(^{136}Xe_4\right)_M}{\left(^{136}Xe_8\right)_M} = \left(\frac{^{244}Pu}{^{238}U}\right)_0 \frac{B_4 \cdot {}^{136}Y_4 \cdot \exp\left(-\lambda_4\left(4560-T\right)\right)}{B_8 \cdot {}^{136}Y_8 \cdot \left(\exp\left(-\lambda_8\left(4560-T\right)\right) - \exp\left(-\lambda_8\left(4560\right)\right)\right)} \tag{4.7}$$

Where the subscript 4 and 8 correspond to radiogenic parents $^{244}$Pu and $^{238}$U respectively. The subscript M also denotes the measured values and ($^{244}$Pu/$^{238}$U)$_0$ is taken to be 0.008 (the upper limit of Hudson et al., 1989). Additionally, in this equation the age of the Moon is taken to be 4560 Ma.

*4.2.3 U-Pu Ternary Diagram*

The U-Pu-Xe systematics can be represented by a ternary diagram in three-isotope space (Turner et al., 2007). A cartoon example of the ternary diagram and the determination of U-Xe and U-Pu-Xe ages can be seen in Figure 4-1. Any three fission isotopes of Xe can be used to create a ternary diagram, but we have used $^{132}$Xe, $^{134}$Xe, and $^{136}$Xe because these isotopes have the largest fission yields and are not dominant products of REE spallation (see section 4.4). The vertices of the triangle represent pure end-member fission compositions, such that a sample that contains Xe produced solely from $^{238}$U would plot on the vertex labeled $^{238}$U, and the same applies to the $^{235}$U and $^{244}$Pu end-members.

A sample that contains Xe derived only from a combination of all three end-member fission parents will fall inside the ternary diagram (Figure 4-1B). If we assume that the zircon has undergone no Xe degassing, the U-Xe and U-Pu-Xe ages can be represented by projections from an end-member parent onto the mixing line between the two other fission parents (Figure 4-1C,

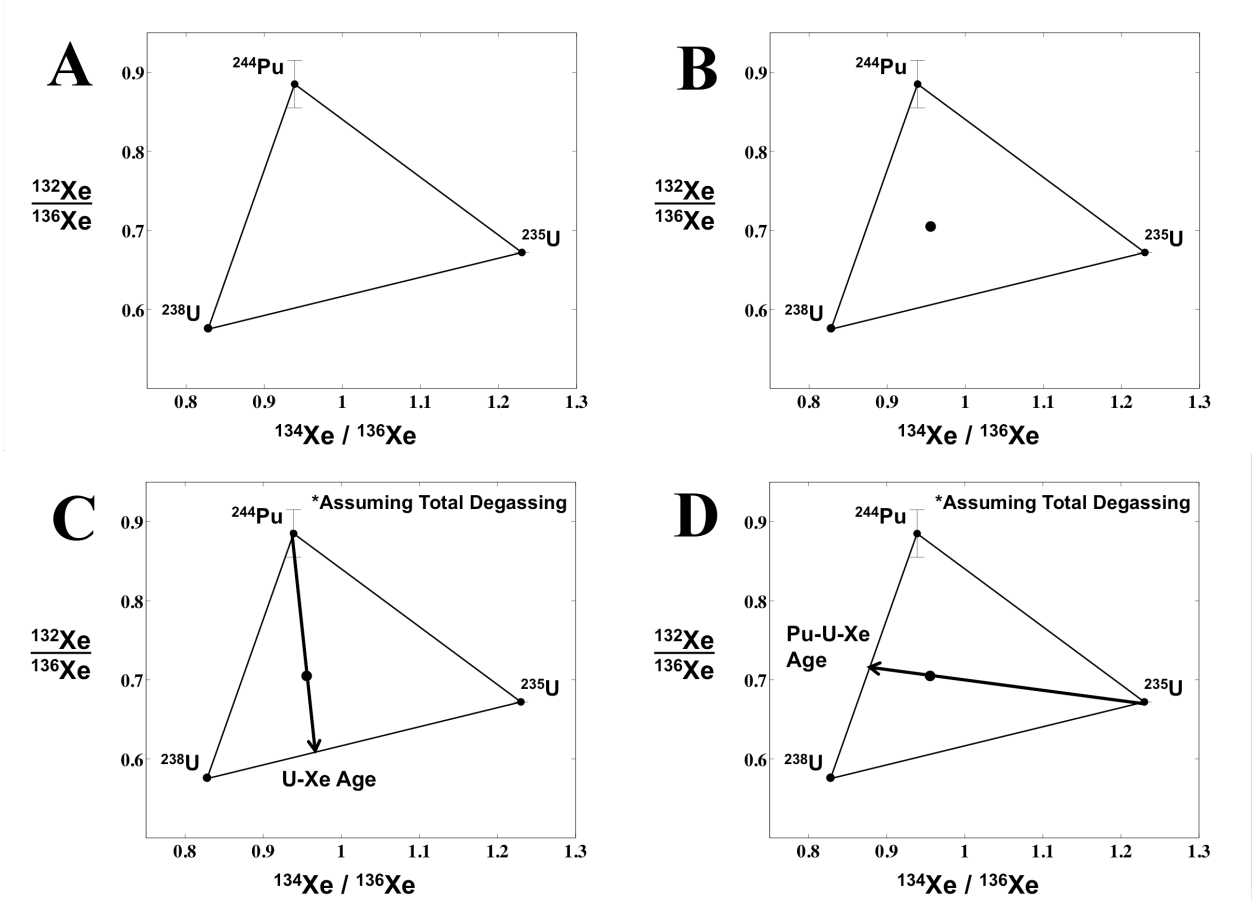


Figure 4-1: Illustration to demonstrate interpretation of U-Pu-Xe ternary diagram. (A) Vertices represent Xe compositions of pure end-member fission parent. Errors are shown or are within the vertex symbol. (B) A sample that contains Xe from a combination of all three fission parents will plot in the center of the ternary diagram. (C) Assuming no or total degassing, the U-Xe age of a sample can be represented by a projection from $^{244}$Pu onto the $^{238}$U and $^{235}$U mixing line. Older samples will plot closer to the $^{238}$U end-member. (D) If zircons are >3.9 Ga, and have not since experienced total degassing, they will contain measureable amounts of plutogenic Xe. The Pu-U-Xe age can be represented by a projection from $^{235}$U onto the $^{238}$U and $^{244}$Pu mixing line. Older samples will plot closer to the $^{244}$Pu end-member.

D). In cases of partial degassing the projections become more complicated, but limits on degassing ages and percent of loss can be determined, and are described below.

### *4.2.4 End Member Xe Yields and Compositions*

The calculated U-Pu-Xe ages can vary depending on what end member values are chosen for

data corrections (SW, air, spallation) and calculations of fission parent contributions ($^{235}$U, $^{238}$U, $^{244}$Pu). We therefore need to use the most appropriate values for our samples to ensure we are calculating the most accurate ages. For air subtractions and corrections for instrumental mass fractionation, we used the Xe composition for air measured by Basford et al. (1973). We chose to use the solar wind Xe composition measured in Genesis samples by Crowther and Gilmour (2013) (analyses conducted on RELAX), which are in agreement with the values measured in lunar soils by Pepin et al. (1995).

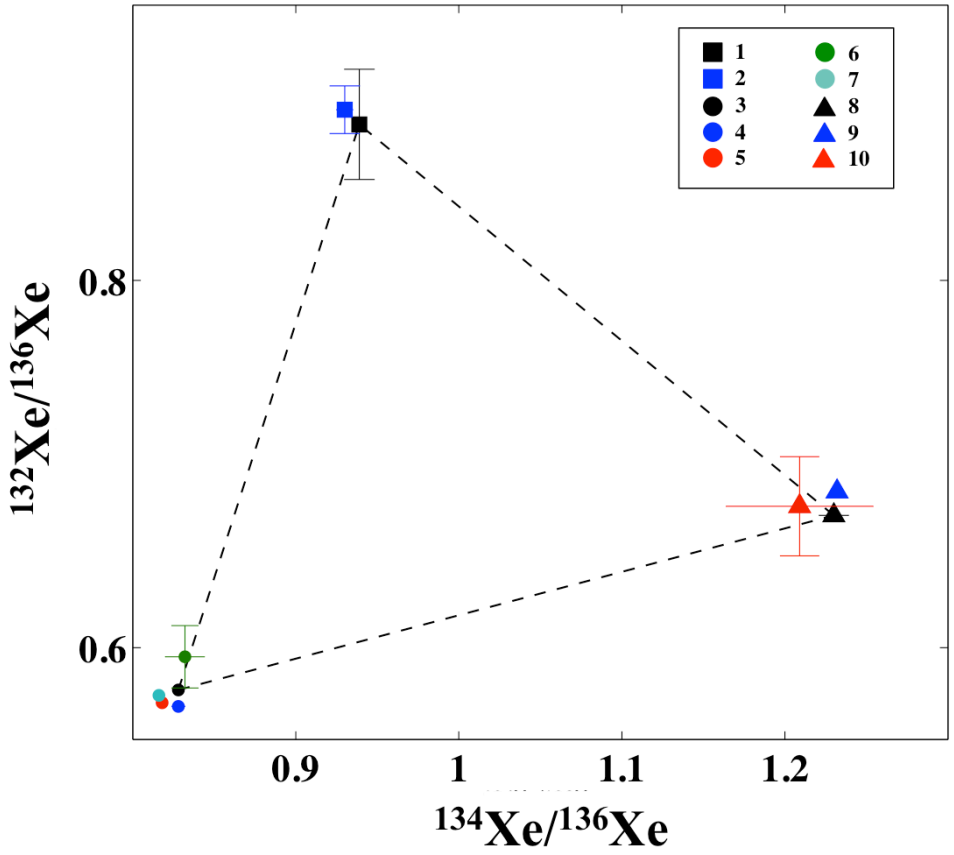


Figure 4-2: Ternary diagram illustrating reported fission parent Xe yields. The errors for reported data are shown or are inside data points. The values used we used for our age analyses are in black. The references for all the data points are: (1) Ozima and Podosek (1983); (2) Ozima and Podosek (2002); (3) Ragettli et al. (1994); (4) Hebeda et al. (1987); (5) Eikenberg et al. (1993); (6) Wetherill (1953); (7) Young and Thode (1960); (8) Irradiated UCLA standard glass (this study); (9) Crouch (1977); (10) Irradiated NIST610 glass (this study).

Figure 4-2 shows the range in reported fission end member concentrations. For induced fission of $^{235}U$, we used the Xe isotope ratios of the UCLA standard glass, which was irradiated with the zircon samples (black triangle Figure 4-2). These values are within error of those listed in Ozima and Podosek (2002) (which are based on the report by Crouch (1977) – blue triangle Figure 4-2), but our analyses have 3-10 times smaller errors than previously reported yields. Our measurement of the ULCA standard glass is therefore the most precise measurement to date of induced fission Xe yields of $^{235}U$. Also plotted in Figure 4-2 are the values measured for an irradiated NIST610 glass (red triangle). The errors are large on for this sample due to the smaller sample size of the NIST610 compared with the UCLA glass, but it is also within error of the values we chose.

The Xe yields of $^{238}U$ have been reported for a range of materials including U oxides and zircons. Ragettli et al. (1994) conducted a study dedicated to determining the branching ratio and yields of $^{238}U$ spontaneous fission for application to U-Xe dating of zircons. They found the values of Xe yields determined on U oxides to be slightly different than those reported for zircon samples. We use their values of branching ratio and Xe yields because they were also measured on zircon samples. The Xe yields for spontaneous fission of $^{244}Pu$ are not as well constrained as the U parents. We used the values from Ozima and Podosek (1983) because we feel that it better reflects the uncertainty in the $^{244}Pu$ yields.

The Xe yields of REE spallation are even less well defined than the fission parents. Hohenberg and Rowe (1970) and Hohenberg et al. (1981) report Xe yields of irradiated doped glasses (both

individual REE glasses and a mixture similar to Angra dos Reis meteorite). The samples were bombarded with 730 MeV protons to induce spallation of REEs. The yields they report show, in some cases, over an order of magnitude variation between analyses of the same doped glass (this effect is largest in the heavy isotopes of Xe). As a result, the values commonly used to correct for REE spallation have errors up to 100% (Hohenberg et al., 1981). Adding to the difficulty in correcting the lunar zircon analyses, the experimental glasses were not compositionally similar to zircons, which are enriched in the HREEs and other elements such as Hf. As of this writing, these are the only reported values of REE spallation, the complications of which will be discussed further later in this chapter.

## 4.3 Sample Preparation and Analyses

### *4.3.1 Irradiation Flux Monitor*

We created a U bearing standard glass at UCLA to serve as a flux monitor during sample irradiation at the UC Irvine nuclear reactor. Previous authors used NIST610 standard glass, but this is problematic due to its high concentrations of Ba and other trace elements (Turner et al., 2007). There are several potential deleterious effects of these minor elements: some (e.g., Ba) can produce Xe in the reactor and others (e.g., B or Gd) capture neutrons producing radioactivity. The net results are that the calculation of Xe produced by $^{235}$U fission may not be accurate because either the calculated thermal neutron fluence seen by the U in the zircons is not the same as that in the flux monitor or because additional heavy Xe is produced that is not derived from U fission. Finally, there is the practical problem that the samples become radioactively 'hot' and require a long cooling period (1-2 years) before they can be safely handled. Below we describe the procedure for synthesizing and the composition of the UCLA standard glass.

*4.3.1.1 Standard Glass Compositional Requirements*

The suitability of the irradiation standard glass for U-Xe analyses is dependent on the Ba and B concentrations of the glass because of their respective propensities to produce Xe and to absorb neutrons. Neutron capture on $^{130}$Ba can result in an excess $^{131}$Xe via $^{130}$Ba(n, β+)$^{131}$Cs, which undergoes β+ decay to $^{131}$Xe with a half-life of 9 days. The $^{131}$Xe excess is seen in the irradiated NIST610 in comparison with the Xe isotopic values for $^{235}$U fission from literature and the UCLA standard glass, as shown in Table 4-4. To avoid potential contributions from Ba, we calculated the reactor fluence based on the $^{136}$Xe concentration of the standard glass. Additionally, the UCLA standard glass has a Ba concentration of 5.38 ppm (we measured the concentration with UCLA ims 1270 using NIST 610 as a reference material), which is below the concentration at which the Ba produced $^{131}$Xe signal would be 1% of the $^{131}$Xe produced by $^{235}$U (this value is based on the U concentration of the glass and the thermal neutron cross-sections). As a result, we also measured the $^{235}$U fission yields of Xe with higher precision and accuracy than previously reported (see Table 4-4 and Ozima and Podosek (2002)).

The thermal neutron cross section of $^{10}$B is larger than that of $^{235}$U, so a concentration of only ~ 5 ppm of B will reduce the thermal neutron flux to the $^{235}$U by ~5% (based on the thermal neutron cross sections, U concentration of the glass, and average sample size of 3 mg). A 5% reduction in the calculated fluence would result in a 100 Myr reduction in the U-Xe age, which is significant relative to the average error of the U-Xe ages. Thus, it was important to minimize the B concentration in the flux monitor.

*4.3.1.2 Standard Glass Synthesis*

We attempted to make a zircon based standard glass by using $ZrSiO_4$ powder (1 g) and adding U solution (0.076g). The mixture was heated in a graphite crucible at ~1200°C for 30 minutes, but it did not fuse due to the high melting temperature of zircon. We therefore decided to make a glass with the same major element composition as NIST610 and dope it with U (Jochum et al., 2011). The major element composition of the standard glass is in Table 4-3.

To make the standard glass we first weighed the $SiO_2$ powder and then used a syringe to drop the U solution on top. The other major element powders were weighed individually and all were placed in a mortar. All were mixed together with ethanol to minimize the loss of material and the mixture was put into an oven to aid the ethanol evaporation. The powder was then loaded into a pre-cleaned platinum crucible for heating. (The crucible was cleaned by filling the vessel with $Na_2CO_3$ and heating it until melted. It was then rinsed with $H_2O$ to dissolve the $Na_2CO_3$ and heated in an oven to dry.)

The platinum crucible was loaded into a 1350˚C furnace, heated for 1.5 hours, and rapidly quenched. The resulting glass was full of bubbles and SIMS analyses of the U concentration revealed heterogeneities on the mm scale. We therefore re-crushed the glass and left the sample at 1350°C in the furnace overnight (~10 hours). The high Si content glass resulted in a high viscosity, but the longer time allowed for most of the bubbles to dissipate.

We characterized the standard glass at UCLA using electron microprobe and SIMS. Electron probe major element analyses show that our glass does have a similar composition as NIST610

(Table 4.3). We also measured the U concentration with the UCLA ims 1270 using a ~25nA $O^-$ beam, a ~60 μm spot size, and the NIST610 standard glass as a concentration standard. All isotopes were measured on the axial EM by magnet cycling, and we included 35 seconds of pre-sputtering to obtain sputtering equilibrium of $^{30}Si$. Eight SIMS analyses give an average U concentration of 211 ± 20 ppm (1σ). Two fragments of the glass, 7 and 90 mg, were sent to Ian Hutcheon at Lawrence Livermore National Lab (LLNL) where the U concentrations were measured with the Nu Plasma MC-ICP-MS. The ICPMS data corroborate the SIMS measurements but are more precise and thus we used the average U concentration of 226 ± 2 ppm (2σ) measured by LLNL for the U-Xe age analyses.

*4.3.1.3 Analyses of Irradiated Standard Glass*

The Xe abundance and isotopic composition of irradiated standard glass samples were measured by Vernoika Herber and Henner Busemann in the Noble Gas Laboratory at ETH Zürich. Glass fragments were heated to above 1450°C in order to melt the samples. The released gas was then separated into three batches that contained He + Ne, Ar, and Kr + Xe by cold finger distillation. The amount of Xe in the Ar portion was less than 0.8% for all analyses. The $^{136}Xe$ abundance and Xe isotope ratios for the irradiated glasses are listed in Table 4-4. The isotope ratios for the irradiated UCLA glass are consistent with or slightly lower than published values for $^{235}U$ fission (Ozima and Podosek, 2002). The errors listed in Table 4-4 include errors in masses, blanks, instrument sensitivity, mass fractionation, and counting statistics. Air corrections were done based on the $^{130}Xe$ abundance (because $^{130}Xe$ is not produced by fission) and in most cases resulted in only a 2% reduction in the $^{136}Xe$ peak.

*4.3.1.4 Reactor Flux and Fluence Optimization*

At high fluxes of thermal neutrons, captures on $^{135}$Xe (a short-lived fission product of $^{235}$U, $t_{1/2}$ = 9.1 hour) can produce excess $^{136}$Xe. Turner et al. (2007) noted this complication, and therefore used $^{134}$Xe as their reference isotope despite seeing no evidence of this effect in analyses of a uranium bearing glass. The neutron flux of the UC Irvine reactor used for our samples was less than that used for the irradiations in Turner et al. (2007), and the Xe isotope abundances of our irradiated standard glass are similar to literature values for $^{235}$U fission yields. Thus, we concluded that any effect of $^{135}$Xe neutron capture is not a significant concern for our analyses.

The optimal reactor fluence is such that the contribution of Xe from induced fission of $^{235}$U is equal to that from spontaneous fission of $^{238}$U in the natural sample. For the first irradiation of lunar and Vredefort zircons we were unsure of the sample U-Xe ages, so we used a similar fluence to that employed by Turner et al. (2007), who analyzed Hadean grains of a similar $^{207}$Pb-$^{206}$Pb ages to our lunar samples. For the second irradiation we determined the optimal fluence by assuming a U-Xe age of ~3.0 Ga. The irradiation parameters can be found in Table 4-5.

The lunar and terrestrial zircons analyzed for fission Xe in this study are all >200 μm, and most are >300 μm. Fission recoil tracks in zircon are typically on the scale of 1-10 μm. This suggests that the recoil loss of fission derived Xe is negligible for the samples reported herein.

*4.3.2 RELAX Measurements*

RELAX is a resonance ionization, time of flight mass spectrometer designed solely for analyses of xenon isotopes (Gilmour et al., 1992; Crowther et al., 2008). A schematic of the instrument is

shown in Figure 4-3. The instrument operates on the principle of resonance ionization in which a species in the sample is excited and ultimately ionized by exposure to photons of specific wavelengths (Hurst et al., 1979; Payne et al., 1981). The photon energies correspond to the

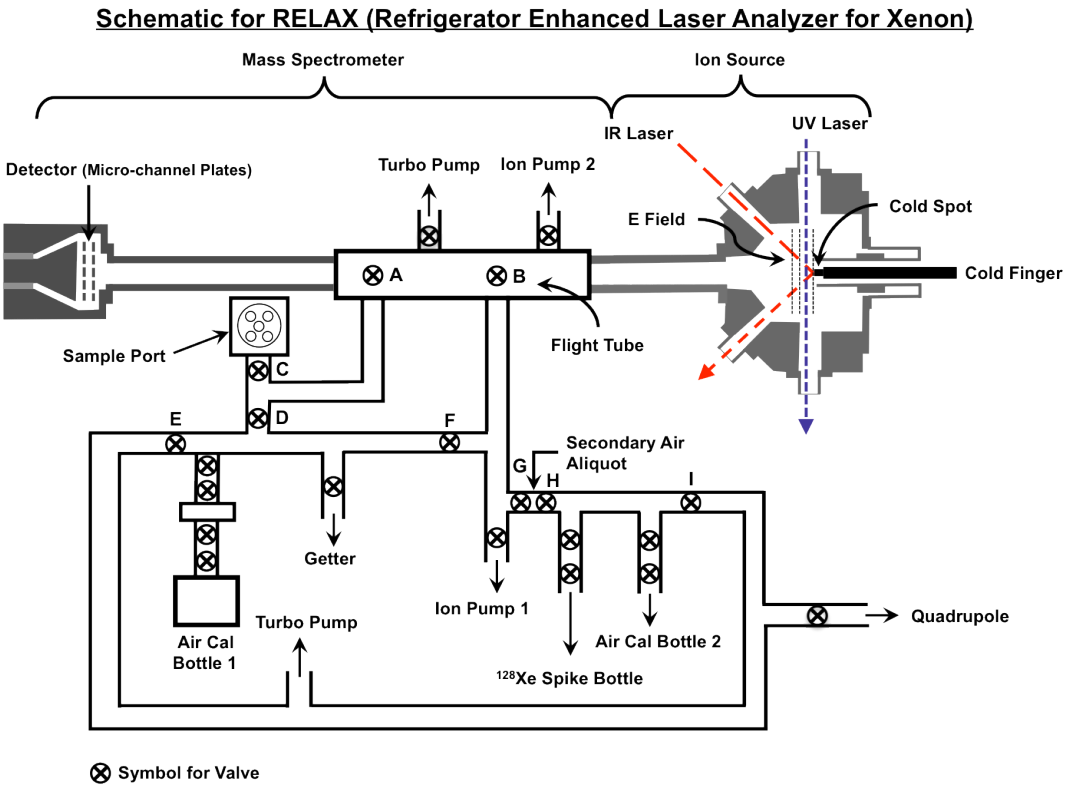


Figure 4-3: Schematic of RELAX at the University of Manchester.

resonant steps necessary to excite and then ionize a particular element, in this case Xe, and the ionization is thus chemically selective since resonant steps vary between elements. The selectivity of this method results in extremely high sensitivity and hence low detection limits; Gilmour et al., 1992 cite an ~1000 atom detection limit for RELAX based on 3 times the standard deviation of the blank (Crowther et al., 2008). The ionization of Xe only requires one

laser because only three photons of λ = 249.6 nm are necessary, two for excitation and a third for ionization (Chen et al., 1980).

Samples are loaded into holder made of molybdenum containing five sample positions. Three holders can be loaded into the sample chamber, allowing for measurements of 15 samples per analysis session. Once samples are loaded, the sample chamber and instrument are pumped and baked at 180°C for ~12 hours to remove air that entered the system during sample changing. The blank and air calibrations are checked prior to any sample analyses to ensure no leaks are present, to optimize the instrument sensitivity, and calibrate detection efficiency.

During analyses, the sample chamber is isolated from the mass spectrometer while samples are heated using a Spectron Nd:YAG laser ((λ = 1064 nm, max 13 W). After the gas is cleaned by exposure to reactive Ti metal (getters), it is allowed to enter the mass spectrometer where it is condensed on a cold trap in order to concentrate the sample (normal operating procedure is outlined in the following section). A second Nd:YAG laser (λ = 1064 nm, energies listed in next section) is pulsed (10 ns width) to heat the cold spot and release the trapped gas. The pulsing (10 ns) of the ionizing UV Continuum laser (249.6 nm, 1.5-2 mJ per pulse) is offset from the heating laser by between 0.5 and 0.6 μs to maximize the ionization yield of the released plume. The ionization yield is estimated to be ~97% based on analyses of residual gas remaining after air calibration measurements (Crowther, personal communication). The ionized Xe is accelerated into the time of flight mass spectrometer and the signal is measured on a microchannel plate.

*4.3.2.1 Standard Operating Procedure*

Air calibrations, blanks, and sample analyses are conducted following a similar procedure. Initially, the mini YAG laser, which heats the cold spot, is turned up to 600 mV (10.2 mJ) to reduce the amount of hydrocarbons that condense on the cold spot. The gas line is then isolated by closing the values to the gas line ion pump and to the flight tube. If an air calibration is being measured, the air is let into the gas line and gettered for two minutes. If a sample is being measured, the Spectron YAG laser current is set and the samples are heated. For our analyses the samples were heated between one and five minutes, with a minimum gettering time of two minutes. In the cases of blanks, the sample holder was not heated and the gas line is gettered for two minutes. Following this step, the protocol is identical for all types of analyses.

The gas line is gettered for an additional 30 seconds, after which the mini YAG is turned down to 540 mV (~4.5 mJ) for another 30-second wait time. The valve to the flight tube ion pump is closed and the valve between the gas line and the flight tube is opened to allow the gas into the ion source/mass spectrometer. The mini YAG shutter is closed allowing the gas in the line to condense on the cold spot for 45 seconds. The flight tube – gas line value is then closed to trap the condensed gas in the spectrometer/flight tube volume and the mini YAG shutter is opened. We waited ten seconds before turning the mini YAG down to 530 mV (~3.6 mJ) and an additional ten seconds before letting the UV Continuum laser beam through the source. These ten-second wait times allow for an initial release and resettling of gas condensed on the cold spot. Once the UV laser is let through the source we started data collection.

*4.3.2.2 Data Collection*

The RELAX software sums spectra from 100 individual laser pulses (about 10 seconds for 100 pulses), and for each analysis we collected 30 of these summed spectra (examples of fission, air, and REE spallation dominated spectra are shown in Figures 4-4, 4-5, and 4-6). To assess variations in sensitivity between analyses, the peak areas for the $^{132}$Xe peak in the air calibrations were plotted as a function of spectrum number and extrapolated back to determine the initial signal value. We aimed for a value above 50,000 (a value based on recent instrument performance; the unit are arbitrary and are used only in tuning the signal and the data reduction

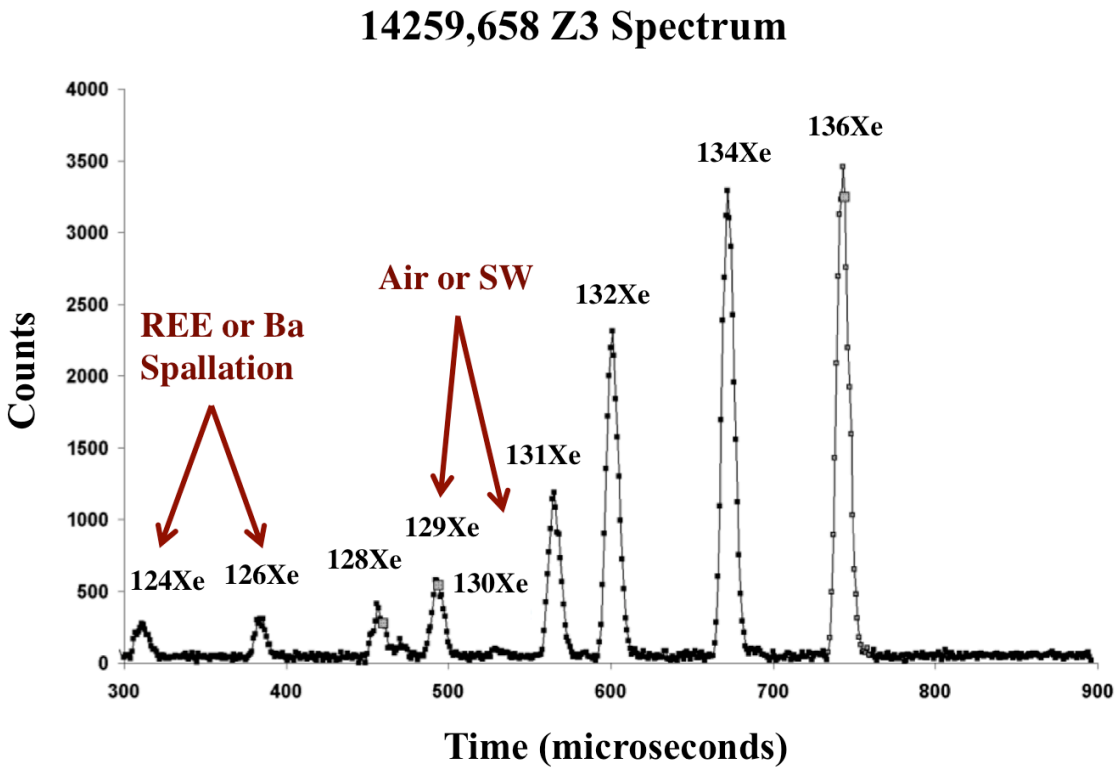


Figure 4-4: Example Xe spectrum as collected by RELAX for zircon 14259,658 Z3. The instrument is a time of flight mass spectrometer, so counts are plotted as a function of time. This spectrum is dominated by the heavy isotopes of Xe – 132, 134, and 136. There is little to no evidence for air or solar wind (we used $^{130}$Xe to correct for these two contributions). The presence of $^{124}$Xe and $^{126}$Xe peaks indicates contributions from spallation Xe produced by exposure to cosmic rays on the surface of the moon. For zircons this is mainly due to spallation of rare earth elements.

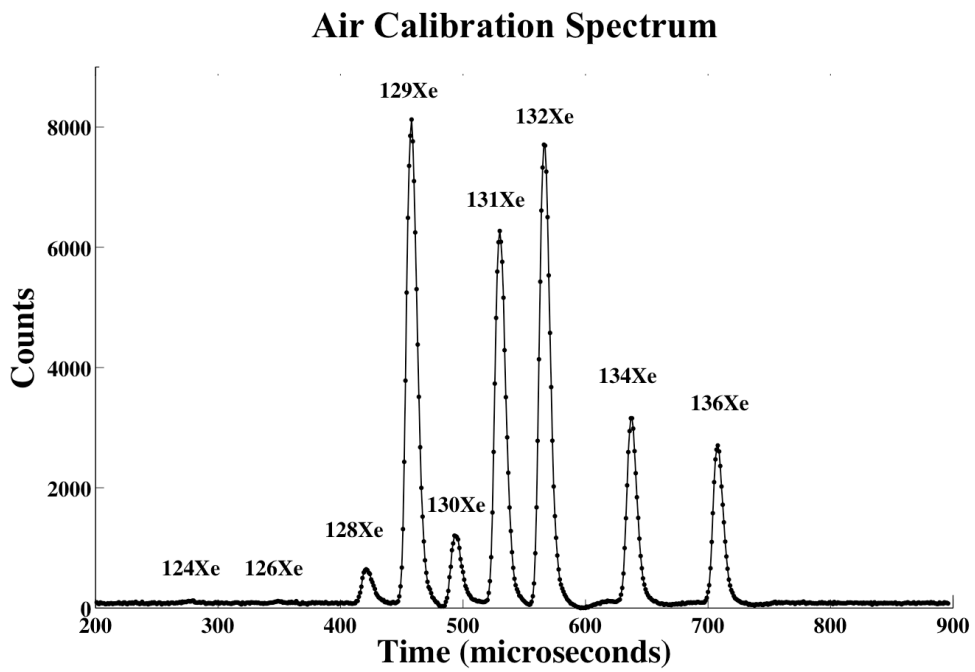


Figure 4-5: Example RELAX air calibration spectrum. The average values of air calibrations are compared with known air Xe concentrations to correct for instrumental mass fractionation. Also air subtractions of samples are assessed using the $^{129}$Xe or the $^{130}$Xe peak areas.

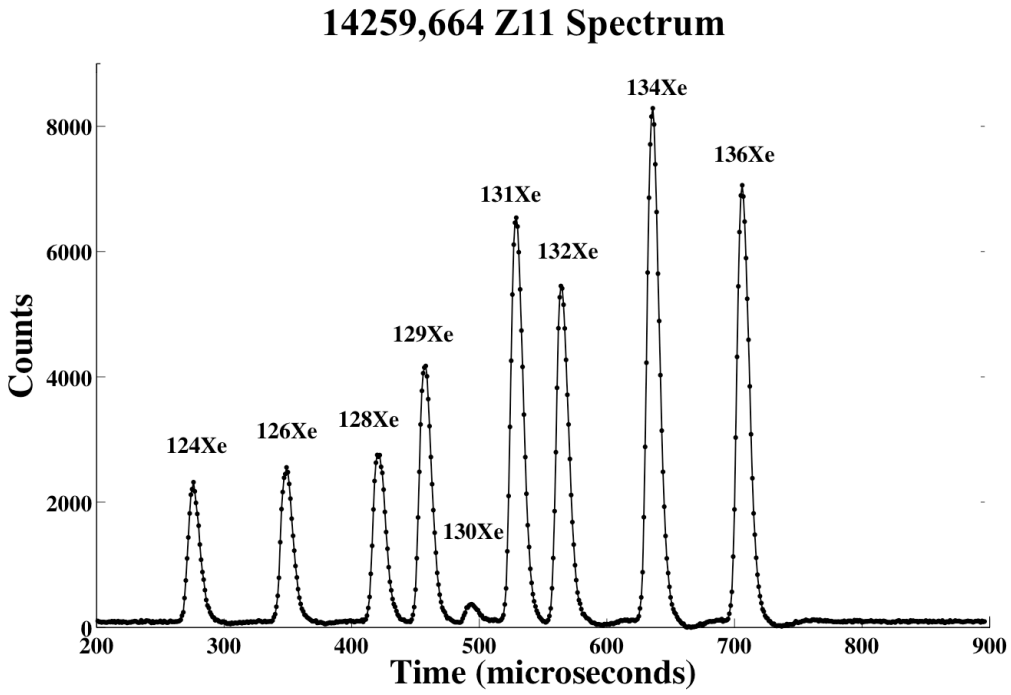


Figure 4-6: This high temperature release (20.5 A) of 14259,664 Z11 is dominated by fission and spallation components. The contribution of the latter is identified by the excess $^{124}$Xe and $^{126}$Xe.

spreadsheet) and adjusted the position of the ionizing laser when the signals dropped below this limit. The Xe signal decreased with time due to removal of ionized gas, so the decay constant for the exponential fit is an indicator of the ionization efficiency. A value between 0.07 and 0.10 is favorable; high values indicate contributions from hydrocarbon interferences and lower values are usually due to small initial signals.

For data reduction and analysis, described below, we used the sum of first five spectra because the low signal to noise of the later spectra introduces large errors. Figure 4-7 illustrates the change in isotopic ratio as a function of time for zircon 14259,658 Z3 and for an air calibration. In most cases the sum of the last five spectra differ from the previous spectra and have much larger errors due to small signal intensities.

## 4.4 Data Reduction

### *4.4.1 Blank Correction*

The number of Xe atoms in individual blank measurements was determined by multiplying the peak area of a given isotope *i* by the ratio of the average number of $^{136}$Xe atoms in an air calibration (3.95 x $10^4$ atoms) over the average air calibration $^{136}$Xe peak area.

$$\left({}^{i}Xe_{atoms}\right)_{blank} = \left({}^{i}Xe_{counts}\right)_{blank}\left(\frac{{}^{136}Xe_{atoms}}{{}^{136}Xe_{counts}}\right)_{air} \tag{4.8}$$

The average number of each isotope in all blank analyses and the standard deviation were determined. Average blank values are on the order of$10^4$ counts (sum of first five spectra), whereas large sample releases values are ~2x$10^5$ or higher. Blank subtractions have little effect

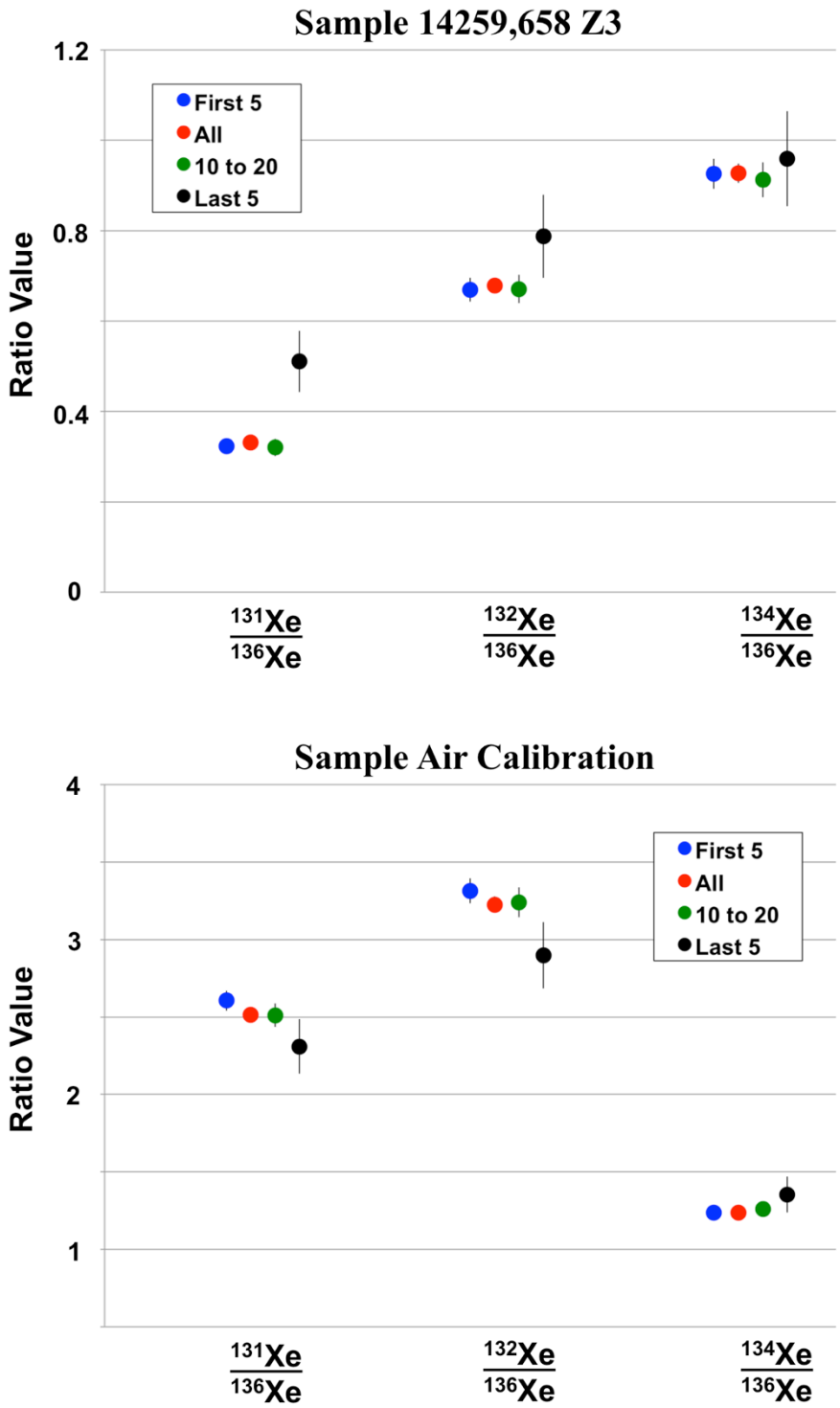


Figure 4-7: Comparison of heavy Xe isotope ratios for various groups of spectra for sample 14259,658 Z3 (top) and air calibration (bottom). The last five spectra show the most variation due to small signal intensities. We use the sum of the first five spectra for all calculations in this chapter.

on the results reported herein accept for $^{128}Xe$, which has a known hydrocarbon interference. For this reason, we do not use $^{128}Xe$ for any data corrections or age calculations.

*4.4.2 Instrumental Mass Fractionation (Air Correction Factor)*

Instrumental mass fractionation is accounted for by determining the air correction factor (ACF). For each air analysis, the blank subtracted peak areas of each isotope were normalized to $^{136}Xe$, and the average value for all air calibration measurements was determined. The ACF for a given isotope *i* is the ratio of the actual air ratio to the measured air ratio:

$$ACF = \frac{\left(\frac{^{i}Xe}{^{136}Xe}\right)_{Actual}}{\left(\frac{^{i}Xe}{^{136}Xe}\right)_{Measured}} \tag{4.9}$$

*4.4.3 Sample Data Reduction*

Prior to data reduction, analyses were filtered according to $^{136}Xe$ peak areas. The accuracy of RELAX drops when peak areas fall below ~ 80,000 counts (average air calibration) and above ~ 3 x $10^6$ counts. With larger gas releases and higher count rates the peaks widen and become more difficult to resolve (this was seen in some of the 14259,664 Z1 analyses), and at lower count rates the errors increase due to poor counting statistics and contributions from the blank. After filtering for signal strengths, the following data reduction routine was performed on each measurement collected, while U-Xe ages were only calculated for the largest Xe releases. The peak areas of each Xe isotope were determined for each sample analysis and the average blank values were subtracted. The blank-corrected values were then multiplied by the ACFs to account for instrumental mass fractionation. Blank subtraction has minimal to no effect on the measured

peak areas (usually <2% for air calibrations). The ACF also has minimal effect on the Xe isotope values (usually between 0.95 and 1.02 for fission Xe isotopes). The effect of these corrections on the lunar data are illustrated in Figure 4-8.

Terrestrial zircons were then corrected for contributions from air assuming that all of the $^{130}$Xe in a measurement is from air. This assumption can be made because $^{130}$Xe is shielded and thus is effectively not produced by fission. If, after considering the uncertainty on the blank correction, there was no resolved detection of $^{130}$Xe, no air correction was necessary. The air component (AC) subtracted from Xe isotope, *i,* is

$$\left(\frac{^{i}Xe}{^{136}Xe}\right)_{AC} = \left(\frac{^{130}Xe}{^{136}Xe}\right)_{M}\left(\frac{^{i}Xe}{^{130}Xe}\right)_{Air} \tag{4.10}$$

where M is the measured isotope ratio. The fission component (FC) of isotope *i* is therefore the measured ratio minus the air component.

$$\left(^{i}Xe_{FC}\right) = \left(^{i}Xe\right)_{M} - \left(^{130}Xe\right)_{M}\left(\frac{^{i}Xe}{^{130}Xe}\right)_{Air} \tag{4.11}$$

These air corrected values are used to calculate the U-Xe age of the terrestrial zircons using the parameters from their associated irradiations.

Blank subtraction and ACFs were both applied to the lunar data in the same manner as the terrestrial grains, however after this point the lunar zircons were treated slightly differently. This is because in addition to fission derived Xe, the lunar zircons contain at least two more components: a solar wind contribution (similar in composition to the air component above), and

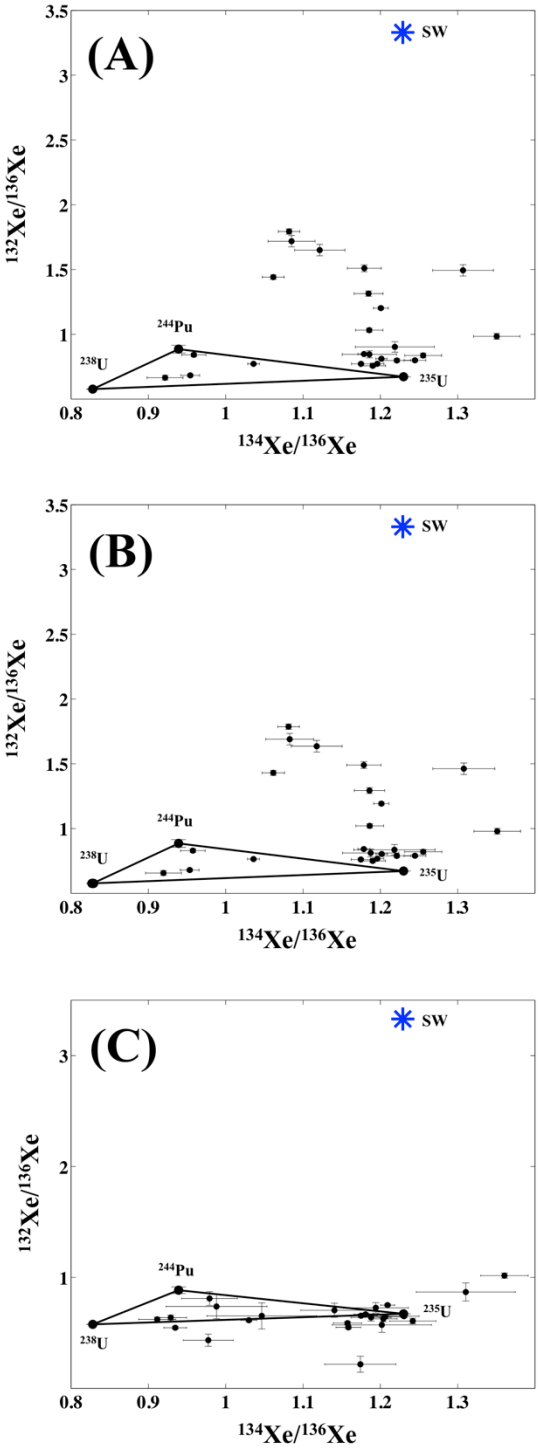


Figure 4-8: This figure illustrates the affects of the blank subtraction (A), adjustment for instrumental mass fractionation (B), and a solar wind correction based on the $^{130}$Xe peak height (C). The blank subtraction has no affect on the Xe isotope ratios, so the raw data has not been shown. Out of all data corrections, the solar wind correction has the largest effect on the final isotope ratios.

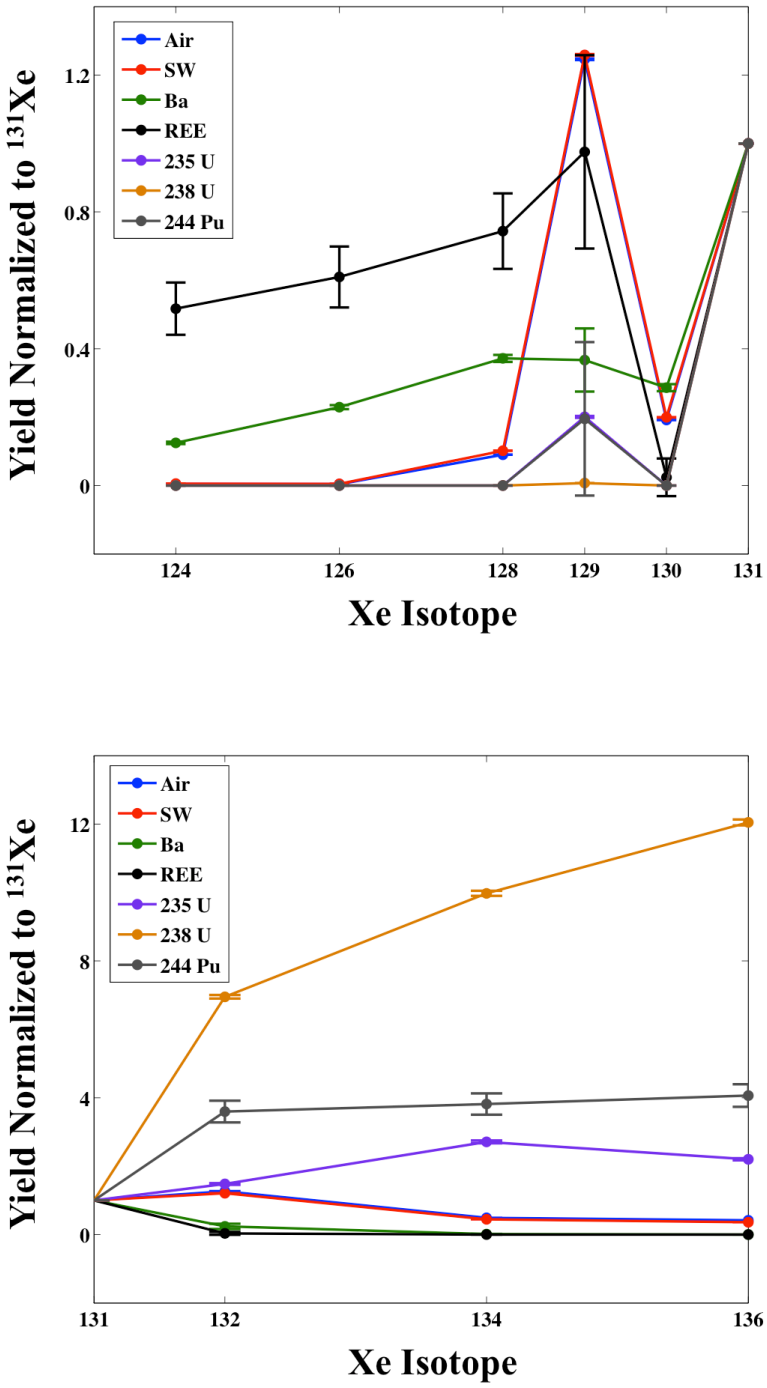


Figure 4-9: Xe isotope compositions for the six end member components normalized to $^{131}$Xe. The heavy isotopes are dominated by $^{244}$Pu, $^{238}$U, and $^{235}$U fission products, while the lighter isotopes are dominated by Ba and REE spallation. See table 4-2 for values and references.

Xe produced by spallation of REEs, and potentially Ba, due to cosmic ray exposure near the surface of the Moon. Similar to air correction, $^{130}$Xe is used to monitor contributions from solar wind. REE spallation Xe yields, reported by Hohenberg et al. (1981), are dominated by light isotopes, so $^{124}$Xe and $^{126}$Xe are used to assess the contributions from this component The relative yields of all six parent components relative to $^{131}$Xe are shown in Figure 4-9 and the values with references are listed in Table 4-2. The spallation yields are the least well defined of any end member and they were determined on samples containing only light REEs (Hohenberg and Rowe, 1970; Hohenberg et al., 1981). However, zircon REEs are dominated by the heavy species, as seen in Chapter 2. Additionally, most zircons contain percent level Hf, which, being a heavy element, is a spallation target. Due to this uncertainty, we filtered our data to include only analyses with very little spallation contributions following the process below.

After blank and mass fractionation corrections, the lunar data were divided into three categories and reduced accordingly:

1. The first group contained analyses with $^{124}$Xe, $^{126}$Xe and $^{130}$Xe values within error of zero. Satisfying this criterion suggests these signals contain no measurable solar wind or spallation component. Therefore, no solar wind correction was applied to these data and the blank and ACF corrected data were used to investigate fission contributions.
2. Group 2 exhibited analyses with $^{124}$Xe and $^{126}$Xe within error of zero, but with measurable amounts of $^{130}$Xe. These analyses must contain some solar wind component (or trapped air), but show no evidence of spallation contribution. The solar wind correction for data in this category was performed similar to the air correction above, by assuming that all $^{130}$Xe was from solar wind.

3. For the rest of the samples, the spectra show evidence of both solar wind and spallation components. The fraction of the $^{130}$Xe peak from solar wind was determined from the $^{126}$Xe/$^{130}$Xe ratio. The $^{130}$Xe/$^{126}$Xe and the $^{124}$Xe/$^{126}$Xe were used to determine if Ba or REE yields should be used for this calculation. Figure 4-10 shows that most of the light isotopes are consistent with REE spallation, but a few low current heating steps yield data that are consistent with Ba spallation. A possible explanation for this phenomenon is that these low temperature steps are releasing shallow Xe that is not inherent to the zircon, and may be from Ba spallation in surrounding material. Figure 4-11 shows a mixing

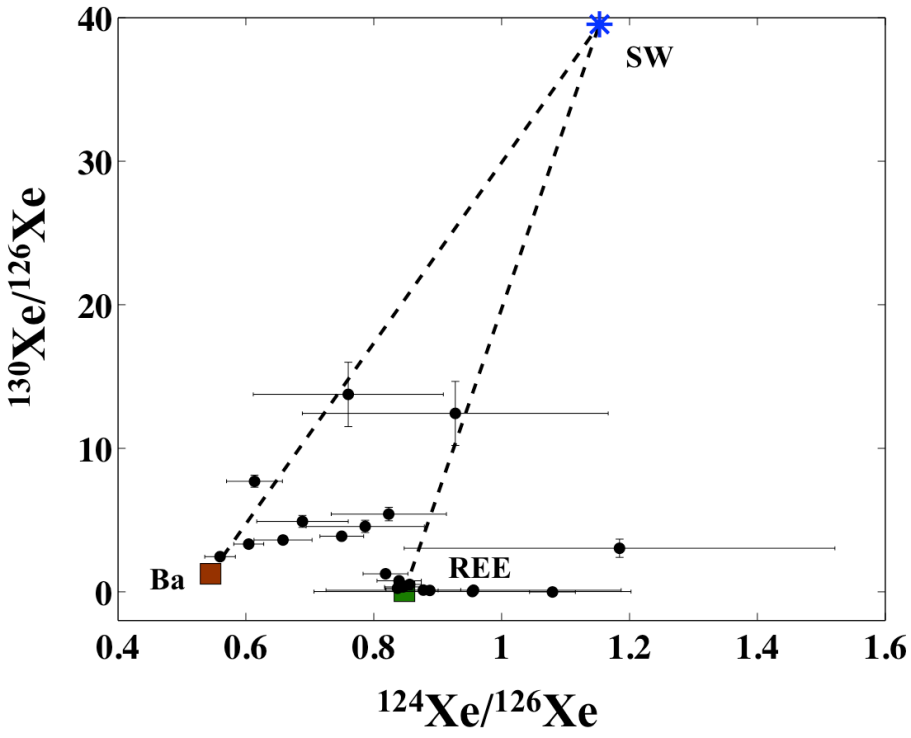


Figure 4-10: In the lunar samples, the lighter isotopes of Xe consist of a mixture between Ba and rare earth element (REE) spallation, and trapped solar wind. This figure contains data for the largest gas releases (reported in Table 4-6 and 4-7). The light isotopes are mostly consistent REE spallation, however a few low current (temperatures) releases correspond to the Ba spallation. See text for more details.

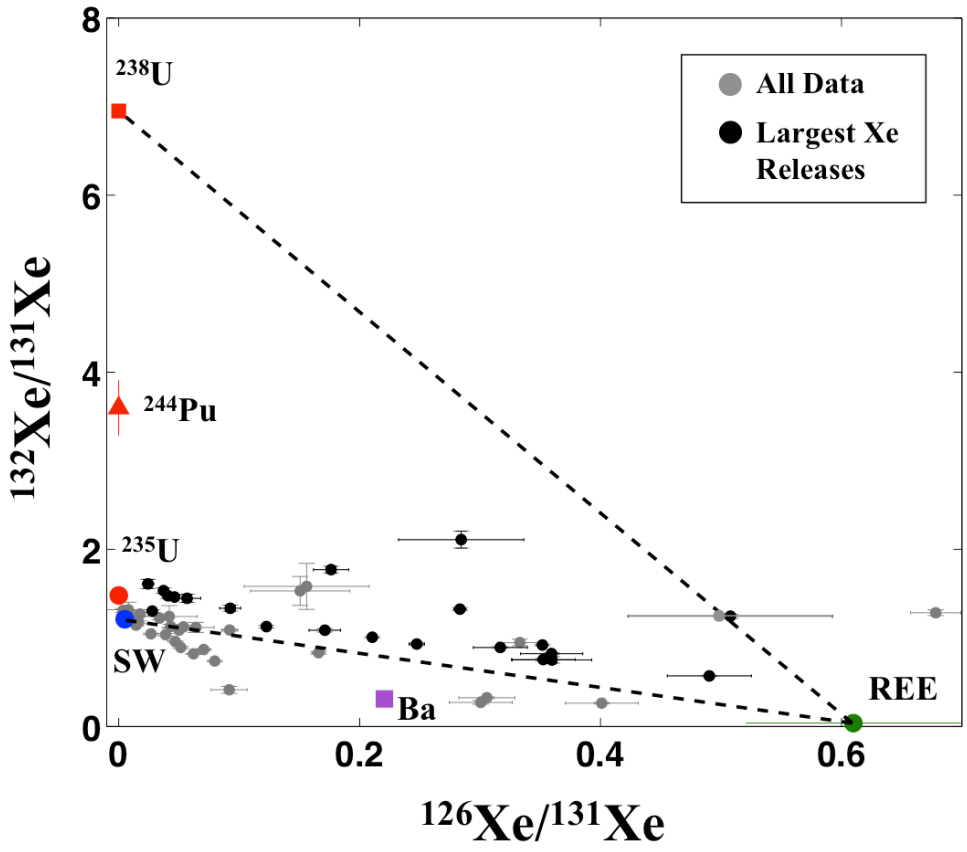


Figure 4-11: Mixing diagram of lunar zircon analyses showing all six end member components. The grey data points are all releases with measurable Xe, and the black data points are the largest releases also shown in Figure 4-10. All the large releases fall above the SW and REE mixing line indicating they contain a fission component. This diagram should not be used to interpret the amount of fission component. Instead the diagram illustrates that most of the lunar samples contain both SW and a spallation component.

diagram of all six end-member parents and illustrates that most of the lunar zircons contain both solar wind and spallation trapped components.

Samples whose $^{130}$Xe peak contained >98% solar wind were corrected assuming that all $^{130}$Xe was from solar wind. For the remaining samples, the correction was made using the fraction of

the $^{130}$Xe peak from solar wind. Most of these grains contained significant $^{124}$Xe and $^{126}$Xe after the correction, confirming a contribution from spallation. Because of remaining ambiguities in the full spallation correction, these data were not included in this study. After all subtractions were made, the final values were normalized to $^{136}$Xe to produce ternary diagrams and calculate U-Xe and U-Pu-Xe ages.

## 4.5 Sample Descriptions

### *4.5.1 Vredefort Samples*

We analyzed zircons from four Vredefort samples that represent a range of pressure and temperature conditions associated with both the bolide impact and a subsequent local intrusive event at ~1 Ga (Reimold et al., 2000). The aim for investigating this set of samples was to characterize the response of the zircon U-Xe system to P-T domains common in impact environments.

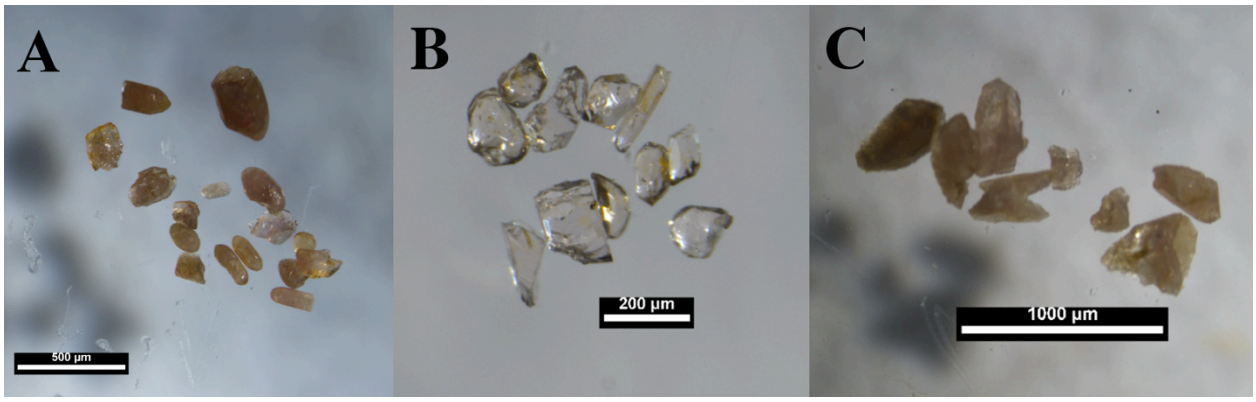


Figure 4-12: Optical images of Vrderfort zircons. (A) V49-2 zircons extracted from a foliated tonalite dyke ~15 km radially out from the geologic center of the impact structure. (B) V58-1 gem-quality, unshocked zircons from the geographic center of the impact structure. These zircons crystallized at 2019 ± 2 Ma, shortly after the Vrederfort impact (Moser et al., 2011). (C) V62 zircons collected near the collar of the central uplift. These zircons show evidence of Pb-loss associated with the ~ 1 Ga local intrusive event (Anna's Rust Sheet) (Moser et al., 2011; Reimold et al., 2000).

*V58-1*

V58-1 is from a recrystallized norite dike located near the geographic center of the Vredefort impact structure (Moser, 1997). About 80% of the zircons from this sample are shocked, while the remaining 20% are unshocked gem-quality grains. The shocked grains show a range of microstructures including planar features, overgrowth rims and polycrystalline texture. The presence of these features suggest that these grains experienced shock pressures >20 GPa and post impact temperatures of >900°C (Moser et al., 2011). Single grain analyses of polycrystalline and shocked grains yield $^{207}$Pb-$^{206}$Pb ages between 2026 ± 3 and 2163 ± 4 Ma (Figure 4-13). This suggests that the shocked grains experienced extreme Pb-loss at ~2.0 Ga due to new crystal

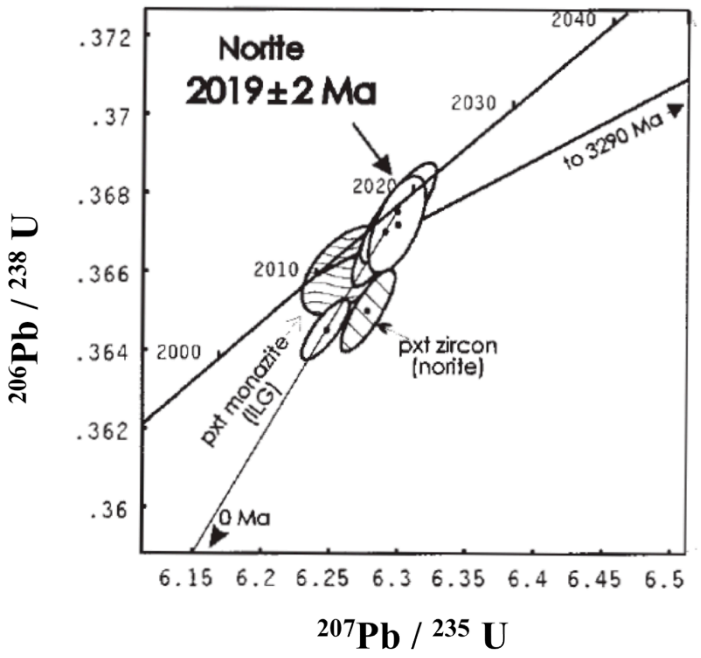


Figure 4-13: Concordia plot for V58-1 zircons, shown in open circles, reproduced from Moser et al. (1997). The zircons Pb-Pb ages are commensurate with the Vredefort impact age suggesting they crystallized in the Norite dyke, which formed soon after the impact event.

growth during post-shock recovery from the 2023 Ma Vredefort impact (Kamo et al., 1996). Moser et al. (2011) characterized the population of unshocked, euhedral grains and report that they have slightly younger, concordant 2019 ± 2 Ma ages suggesting that these zircons crystallized shortly after the impact shock event when the norite dike formed. A bulk analysis of 16 zircons yields a U concentration of 35 ppm, and grains range in size from ~ 100 to 250 μm. For U-Xe measurements, we analyzed grains from the unshocked zircon population. Note that an aliquot from this population yielded a U-Th-He age of 900 Ma, reflecting a time of regional low-temperature heating and Pb-loss associated with Kibaran mafic intrusions (Moser et al., 2011).

*V58-2*

V58-2 is an Inlandsee leucogranofel (felsic orthogneiss) from the same outcrop as V58-1. The zircons from this sample all contain planar shock features and exhibit varying amounts of Pb-loss. Zircon and monazite grains from V58-2 define a discordia line with intercepts of 3292 ± 28 Ma and 2010 ±7 Ma. From this Moser (1997) suggested that the older age is an approximate primary age of the Inlandsee leucogranofels, and the younger age of Pb-loss is due to the Vredefort impact itself or immediate post-impact heating. Unlike V58-1, the shock features of only a subset of V58-2 zircons are partially recrystallized suggesting that post-impact heating of leucogranofels was less, or less pervasive, compared to the post impact temperatures experienced by the norite dike zircons. A bulk analysis of 11 zircons yields a U concentration of 160 ppm, and grains are typically between ~150 and 250 μm (Moser, 1997).

*V49-2*

Sample V49-2 was collected ~15 km from the geographic center of the impact in the transition region between lower and middle crustal rocks, which are characterized by amphibolite and granulite facies metamorphism, respectively. It is a foliated tonalite dyke that crosscuts deformed tonalite gneiss. Individual dissolution analyses of zircons from this sample are up to ~5% discordant and lie on a discordia line between 3092 ± 7 Ma and 2039 ± 49 Ma. Uranium concentrations range from ~150 to 210 ppm and the median grain size is ~100 μm (Moser et al., 2001).

*V62*

Sample V62, located near the collar of the central uplift, is an alkali feldspar granitoid from the Schurwedraai-Baviaanskrantz complex (2050-2060 Ma), which intruded into the Neoarchean Witwatersrand supergroup (Graham et al., 2005). Zircons from this sample tend to be larger and have higher U concentrations (250 ppm from a five grain average) than the other samples we analyzed (Moser et al., 2011). The grains contain planar features and microtwin lamellae indicating that they experienced >40-60 GPa shock pressures from the Vredefort bolide impact. Despite containing shock features, TIMS U-Pb analyses of zircons from V62 do not show evidence of Pb-loss related to the 2020 Ma impact, but instead define a line that intercepts Concordia at 2077 ± 11 Ma and 1016 ± 110 Ma (Moser et al., 2011). The younger age is interpreted to be due to hydrothermal alteration and Pb-loss associated with a regional mafic magmatic intrusive event (Reimold et al., 2000; Moser et al., 2011) and is commonly observed in Vrederfort populations.

*4.5.2. Lunar Samples*

We analyzed zircons from two soil (14163, 14259) and two breccia samples (14305, 14321) collected during the Apollo 14 mission. Detailed information about these samples can be found in Section 2.2. Zircons from these samples were chosen because of their large sizes, and not necessarily due to parent sample characteristics. The average uranium concentration of lunar

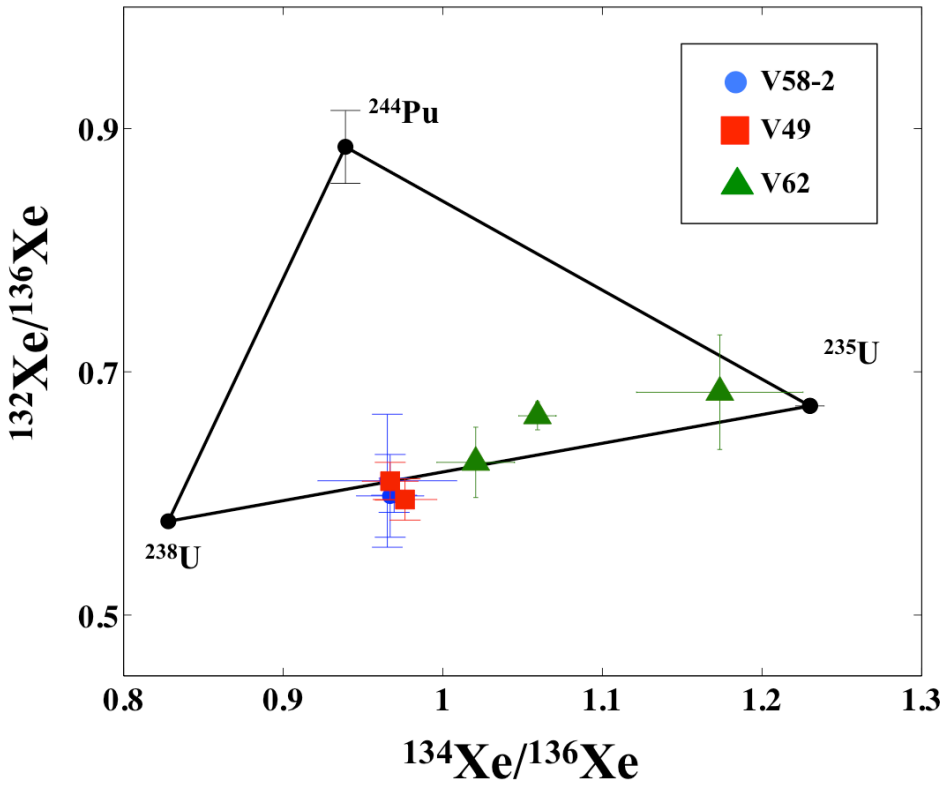


Figure 4-14: Xe ternary diagram for Vrederfort impact zircons, data (shown with 1σ error bars) for these analyses can be found in Table 4-8. All analyses are consistent with a mixture between $^{238}$U and $^{235}$U because these zircons crystallized after $^{244}$Pu became extinct. V58-2 (from the geographic center of the impact) and V49 (from ~15km radially outwards) yield U-Xe ages consistent with their crystallization ages and show no evidence of impact related Xe-loss. Three analyses of V62 (sampled from the crater rim) yield one age that is consistent with the population's crystallization age and two that are distinctly younger. The Xe-loss is most likely due to the local intrusive event, Anna's Rust sheet, which has an estimated emplacement age of 1 Ga. The results from the Vrederfort analyses suggest that exposure to impact shock events alone do not cause appreciable Xe-loss, while exposure to prolonged elevated temperatures could result in open system behavior.

zircons is ~50 ppm, and this low concentration allows for Xe analyses only for zircons with diameters of ~300 μm.

## 4.6 Analyses and Results

### *4.6.1 Vredefort Zircons*

The U-Pb and $^{207}Pb$-$^{206}Pb$ ages for zircons from sample V58-2 were measured with the UCLA Cameca *ims*1270 ion microprobe prior to irradiation (following procedures in Chapter 2.3.2). The Pb-Pb ages of the three additional populations of zircons were characterized by (Moser, 1997; Moser et al., 2001, 2011), and crystallization ages were found to be homogeneous within a population. These ages are listed in the sample descriptions (section 4.5.1) and are presented along with Xe analyses in Table 4-8.

Xenon isotopes were measured in eight of the zircons from V58-2 individually; Z7 and Z8 were grouped together to increase signal intensity and because they have similar U-Pb ages. The samples were measured individually in order to investigate the relationship between U-Pb discordance and Xe age resetting. However, the two discordant zircons (~30%) did not yield enough Xe for accurate ages to be determined. Zircons from the V58-1, V49-2, and V62, which have homogeneous U-Pb ages, were measured in groups of two to three grains in order to increase the Xe signal. In most cases the heating laser coupled well with the zircons, which glowed bright white. The zircons from V58-1 did not couple well with the laser and did not produce large enough Xe releases needed to calculate U-Xe ages. This could be due to either difficulty with laser heating the higher crystallinity samples or possibly due to the low U

concentrations of the samples (Moser, 1997; Moser et al., 2011). The University of Manchester will be installing a new, high power heating laser on RELAX within the next year, and we will attempt to reanalyze the V58-1 zircons using the new instrumental set up.

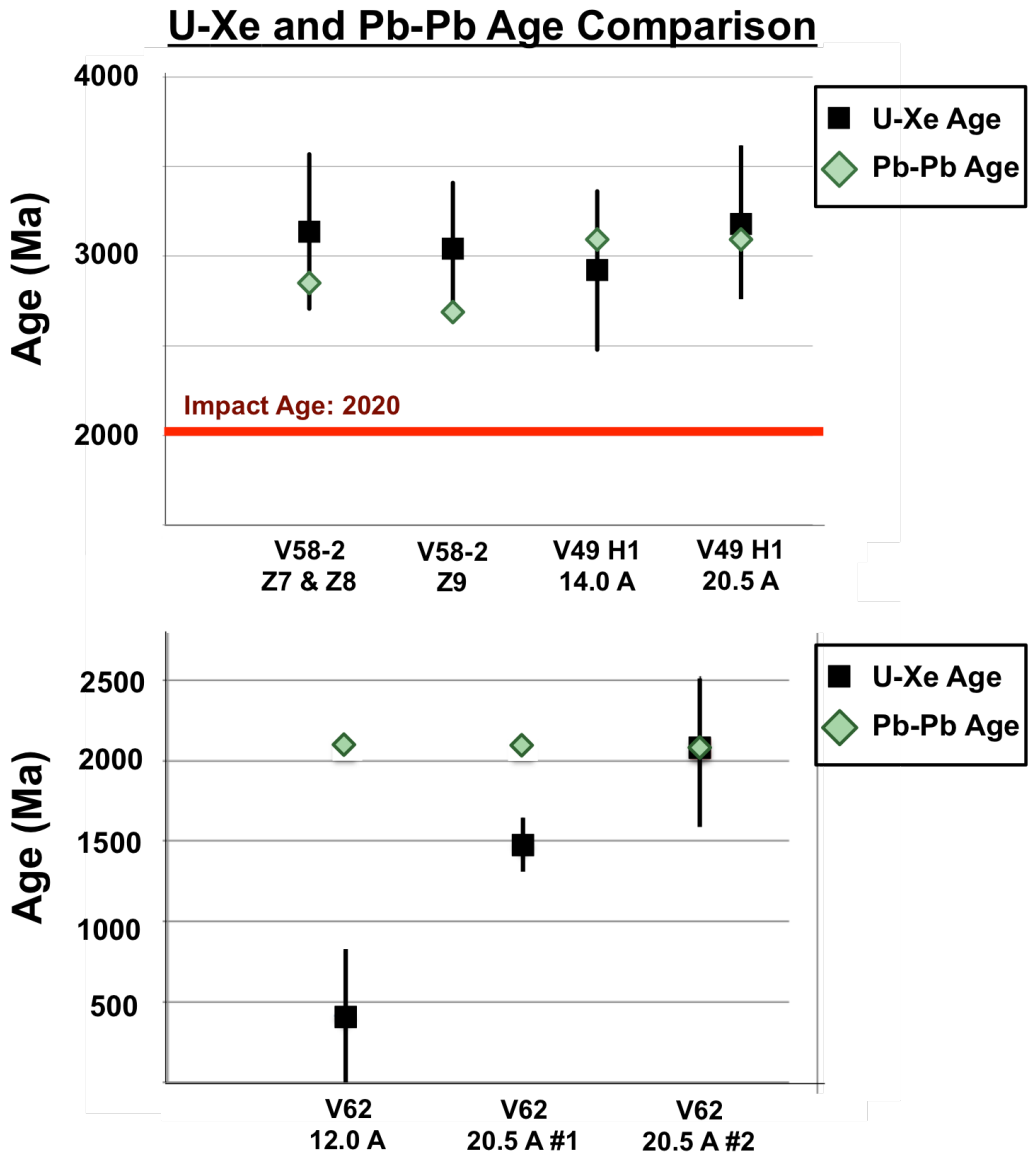


Figure 4-15: Comparison of Pb-Pb and U-Xe ages for (top) V58-2 and V49, and (bottom) V62. Both V58-2 and V29 have U-Xe degassing ages consistent with their Pb-Pb crystallization ages, and show no evidence of impact related Xe-loss. The low laser current (i.e. low temperature) step of V62 yields a U-Xe ages slightly younger than the local igneous event, Anna's Rust Sheet, while the second 20.5A heating step yields a U-Xe age consistent with the Pb-Pb crystallization age.

The V58-2, V49, and V62 samples produced large Xe releases and we were able to calculate U-Xe ages. Figure 4-14 shows the ternary diagram for the largest releases for V58-2, V59, and V62, and Figure 4-15 shows a comparison of the U-Xe and Pb-Pb ages (data for these zircons can be found in Tables 4-6, 4-7, 4-8). All samples are consistent with a mixture of $^{238}U$ and $^{235}U$ fission, and no contribution from $^{244}Pu$. This was an expected result since their crystallization ages are younger than ~3.9 Ga after which the short-lived $^{244}Pu$ is effectively extinct. Both samples V58-2 and V59, which were collected from the geographic center and ~15 km from the center of the Vredefort impact structure, respectively, yield U-Xe ages that are consistent with their Pb-Pb crystallization ages. It appears that despite exposure to high shock pressures during the impact event, they do not show evidence for appreciable amounts of Xe-loss. However, zircons from V62 show evidence for Xe-loss and have U-Xe ages that span from the impact age (~2.0 Ga) down to the later Anna's Rust sheet magmatic event (~1.0 Ga). The U-Pb ages of these grains have also been found to be similarly affected by local intrusive event (Moser et al., 2011).

### *4.6.2 Lunar Zircons*

#### *4.6.2.1 Unirradiated zircons*

We measured the Xe isotopes for three zircons that were not artificially neutron irradiated to test whether the samples would contain measureable amounts of Xe derived from $^{235}U$ fission as a result of the neutron bombardment on the lunar surface. Two of the zircons were from breccias 14305 and a third from soil 14321. Soil grain 14321 BZ2 and breccia zircon 14305 BZ3 produced measurable amounts of Xe, and their isotopes ratios are consistent with $^{238}U$ fission and show no contributions from either $^{235}U$ or $^{244}Pu$ fission (Figure 4-16). This suggests that the

neutron exposure on the lunar surface is not high enough or of the correct energy to produce enough fission Xe from $^{235}U$ so as to interfere with U-Xe age calculations.

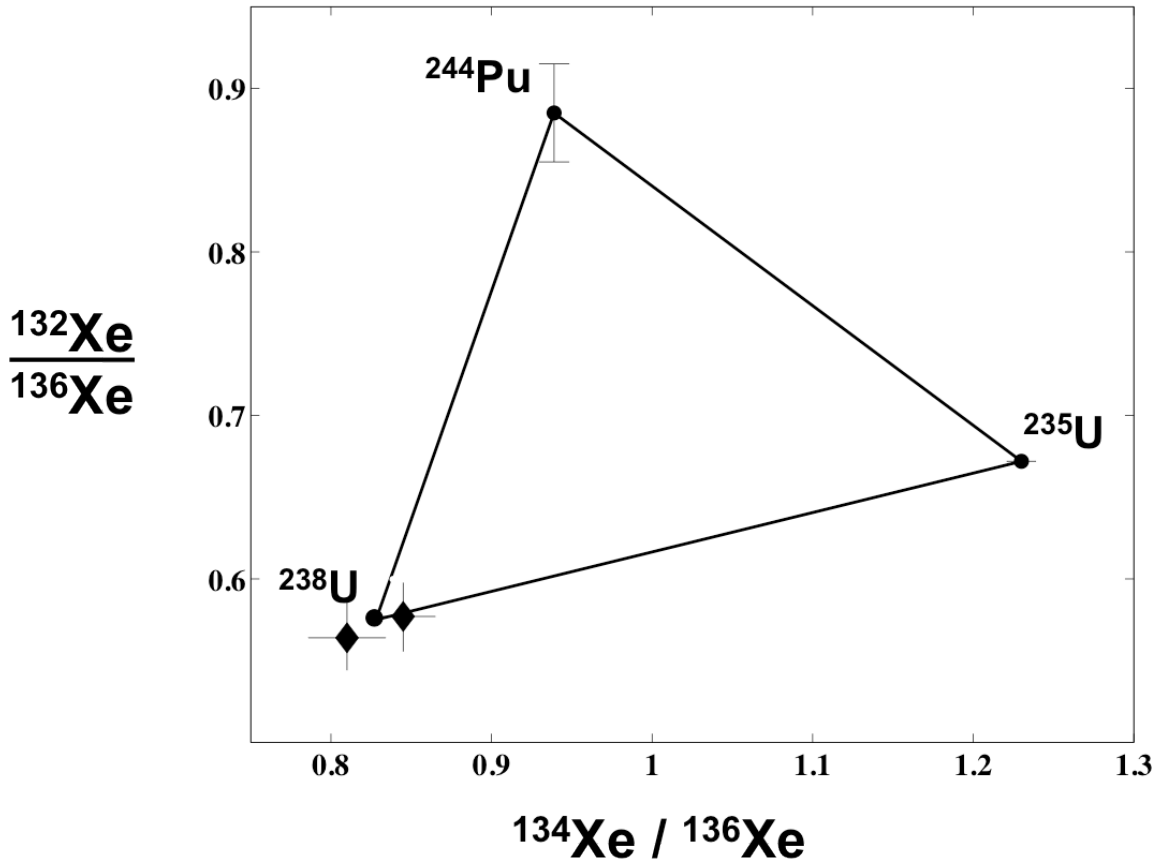


Figure 4-16: Xe ternary diagram for unirradiated lunar zircons 14305 BZ3 and 14321 BZ2. Both samples are consistent with the $^{238}U$ end member with no contributions from either $^{235}U$ or $^{244}Pu$. This suggests that the neutron irradiation on the surface of the Moon was not high enough to induce appreciable amounts of $^{235}U$ fission.

*4.6.2.2 Irradiated Zircons*

We analyzed the Xe isotopes for 13 zircons from Apollo 14 samples. The ternary diagram for the largest gas releases is shown in Figure 4-17 (all errors are 1σ), and the data and U-Xe ages can be found in Tables 4-6, 4-7, and 4-8. Just under half of the grains are consistent with a mixture

between $^{238}$U and $^{235}$U. Two of the grains, 14259,664 Z6 and one analysis from 14259,664 Z1 appear to require some contribution from $^{244}$Pu. Z1 falls on the $^{244}$Pu-$^{235}$U tie line, which is physically impossible because any zircon that incorporates Pu and $^{235}$U would also take in $^{238}$U. This grain, as will be discussed in section 4.7.2, contains a significant spallation component, which may be shifting the datum to an artificially higher $^{134}$Xe/$^{136}$Xe value. A subset of the zircons plot outside of the ternary suggesting mixing with an additional heavy Xe component not

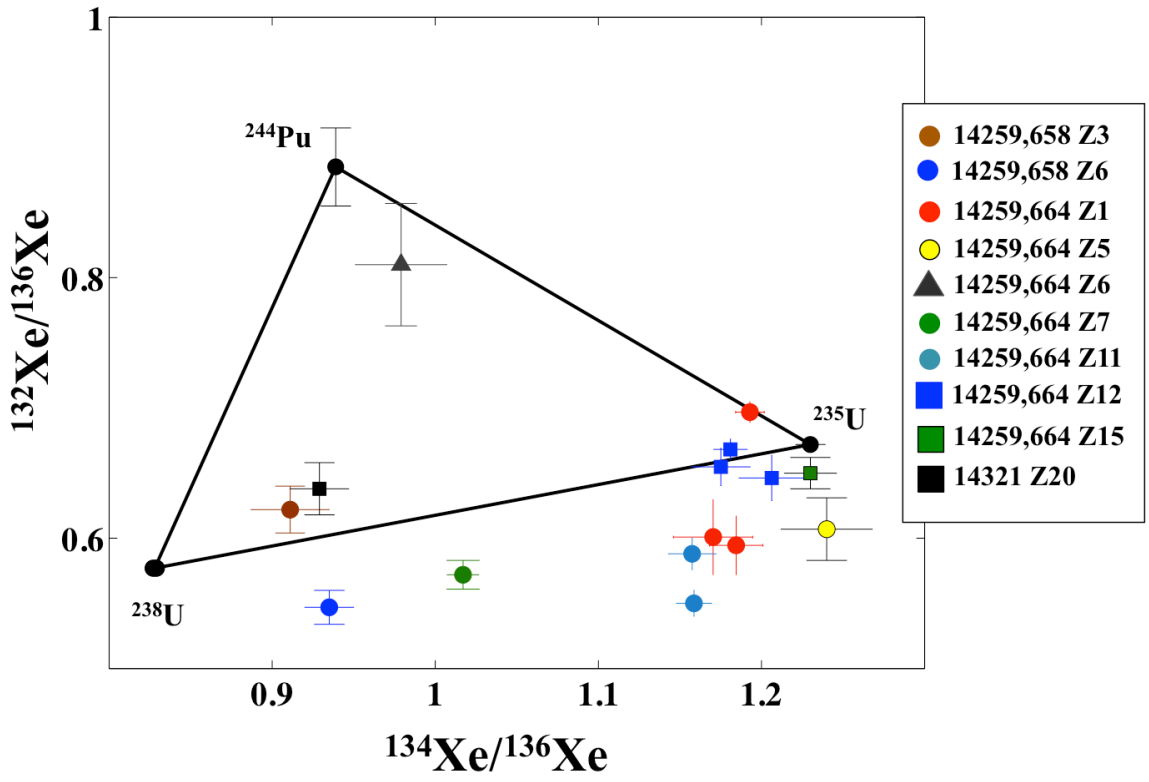


Figure 4-17: Xe ternary diagram showing the final isotope values for the largest lunar zircon gas releases. 14259,658 Z3 and 14321 Z20 are the most robust analyses (see text for explanation) and are consistent with a mixture of $^{238}$U and $^{235}$U fission Xe. Their U-Xe analyses suggest some zircons retain fission Xe for upwards of ~3.8 Ga. A cluster of data near the $^{235}$U end member suggests other grains have experienced extensive Pb-loss within the last 500 Ma. Almost half of the analyses fall outside of the fission parent mixing regime. This may indicate the presence of an additional heavy Xe isotope parent not previous identified. A potential source may be spallation of heavy REEs (see text for more details). The presence of $^{244}$Pu derived Xe cannot be confirmed until the characteristics of this additional component is determined and the extent of its effects on these analyses is assessed.

previously identified. This makes it difficult to confirm or rule out the presence of plutogenic Xe in these samples and calculate meaningful U-Pu-Xe ages. However, there are a few samples that do not appear to have a mixture with this component, and these give the most robust U-Xe ages.

As detailed in section 4.4.3, the lunar zircons were categorized into three groups for data corrections prior to U-Xe age calculations. This was done to prioritize grains with little or no spallation component because the composition of this component has largest uncertainties of all end member compositions. There are no analyses with the absence of both a solar wind and a spallation component that had small enough errors to calculate robust U-Xe ages, but there are zircons that contain only one of these components that produce reasonable results.

Zircon 14259,658 Z3 (brown in Figure 4-17) contained no $^{130}$Xe, so no SW correction was applied. However, it does contain measurable amounts of the light Xe isotopes indicating the presence of a spallation component. The heavy isotopes are consistent with a mixture of $^{238}$U and $^{235}$U with little to (or possibly no) $^{244}$Pu, and it yields an U-Xe age of 3756 Ma (+1376/-875) (see discussion of errors in 4.2.1). Potential mixing with a heavy Xe component would shift the data towards higher $^{134}$Xe/$^{136}$Xe values resulting in age underestimates. This age is therefore potentially the most robust lower limit on a degassing event in this study; however, the degassing age cannot be resolved from the Pb-Pb crystallization age. The $^{207}$Pb-$^{206}$Pb age of this zircon of 4207 ± 19 Ma would suggest the zircon crystallized when $^{244}$Pu was still alive. If this grain does not contain any plutogenic Xe, an upper limit of ~3.9 Ga could be placed on the age of last total degassing. Better characterization of the heavy Xe spallation yields would aid in determining if a plutogenic Xe component is present.

Zircon 14321 Z20 has a similar Xe isotopic composition to that of 14259,658 Z3 analysis and is also consistent, within 2σ, with a mixture of fission gas from only $^{238}$U and $^{235}$U (Figure 4-17). A solar wind correction was applied to this measurement assuming all $^{130}$Xe is from solar wind. After the correction there is still a significant spallation component (similar to Z3), which suggests that the U-Xe age is a lower limit on the degassing age for the same argument as Z3. The U-Xe age calculated from this zircon may also be among the most robust from this data set. The U-Xe age of this zircon is 4569 Ma (+926/-718), which puts a lower limit on the degassing age of 3851 Ma (Note: 14321 Z20 and 14259,658 Z3 received different neutron fluences which explains their dissimilar ages despite similar Xe compositions). However, this lower limit agrees well with the ~3.9 Ga total degassing age based on the absence of plutogenic Xe (here again, characterization of the heavy Xe component would help confirm the absence of plutogenic Xe).

Three analyses of 14259,664 Z12 and one of 14259,664 Z15 cluster close to the $^{235}$U fission end member. This suggests that these grains recently experienced significant, if not total, Xe loss. The U-Xe ages suggest the degassing of Z12 and Z15 occurred within the last 534 Ma and 166 Ma respectively. Zircon 14259,664 Z5 plots just outside of 2σ from the $^{235}$U end member. This grain most likely contains a mixture of fission derived and excess heavy Xe contributions so it's U-Xe age cannot be determined with confidence, but it most likely experienced recent Pb-loss because of its composition near to the $^{235}$U fission end member.

There are two other groupings of analyses: those that fall below the ternary and those that lie above. In principle, these data should all fall within the ternary and thus we conclude that these

zircons must contain an additional Xe component that has not yet been measured in terrestrial samples. Possible sources of this additional Xe component will be discussed in Section 4.7. Until the composition of the additional Xe component is determined and its contribution to the heavy Xe isotope spectrum is removed, the fission Xe ages of these samples cannot be interpreted.

It is interesting to note that one zircon, 14259,664 Z12, contains excess $^{129}$Xe, which is attributed to decay of $^{129}$I. The most likely source so this excess is induced fission of $^{235}$U due to irradiation on the surface of the Moon over 100 Myr ago ($\lambda_{129}$ = 15.7 Myr). This effect is described further in section 4.7.2.

## 4.7 Discussion

The goal of this study was to assess the response of the U-Pu-Xe system to conditions present in impact environments. Our motivating question was whether U-Pu-Xe degassing ages could be used to date impacts on the Moon, possibly during the LHB or even the time period prior to that when the lunar impact flux is not well constrained. We report Xe isotope analyses for a suite of zircons from the Vrederfrot impact structure in addition to the first Xe analyses of lunar zircons extracted from Apollo samples.

### *4.7.1 Overview of Findings*

Three of the four populations of zircons from the Vrederfort impact structure produced measurable fission Xe. Zircons from V58-2, collected near the geographic center of the impact structure, and V49-2, collected ~15 km radially outwards, show no evidence of Xe loss due to

the impact shock event. Their U-Xe ages are consistent with their Pb-Pb and U-Pb ages suggesting that Pb and Xe mobility in zircon are similar and diffusion of either species is not accelerated due to the impact shock event. A third sample, V62, collected near the later Anna's Rust sheet intrusion does show evidence of Xe-loss. Step heating of zircons from this sample yields three U-Xe ages that get progressively older with higher laser current (and thus heating) steps. The progression of ages suggests these zircons experienced partial Xe-loss associated with this 1 Ga event (see Figures 4-14 and 4-15). U-Pb analyses of zircons from this sample also show evidence of significant Pb-loss due to Anna's Rust sheet. Here again, Xe and Pb show similar behavior. The Vrederfort zircons suggest that impact shock alone does not cause appreciable amounts of Xe loss. However, the shock defects produced during the impact event may create pathways for accelerated diffusion during later heating events.

Estimates of the original crater size of the Vredefort structure range from 120 to >300 km (Henkel and Reimold, 1998; Turtle and Pierazzo, 1998). A crater of this diameter on the Moon would be at the transition size between a complex crater and a peak-ring basin (e.g. Baker et al., 2011). The high retentiveness of Xe in zircons from the Vredefort impact structure suggest that it would be difficult to reset lunar zircon U-Xe ages in impacts smaller than basin-forming events. In larger basin-forming impacts, zircons in proximity of long lived melt sheets could be exposed to prolonged elevated temperature, which could result in loss of Xe.

Despite the apparently strong agreement between the behavior of Pb and Xe in the terrestrial grains, the lunar zircon Xe data proved to be more complex and thus more difficult to interpret.

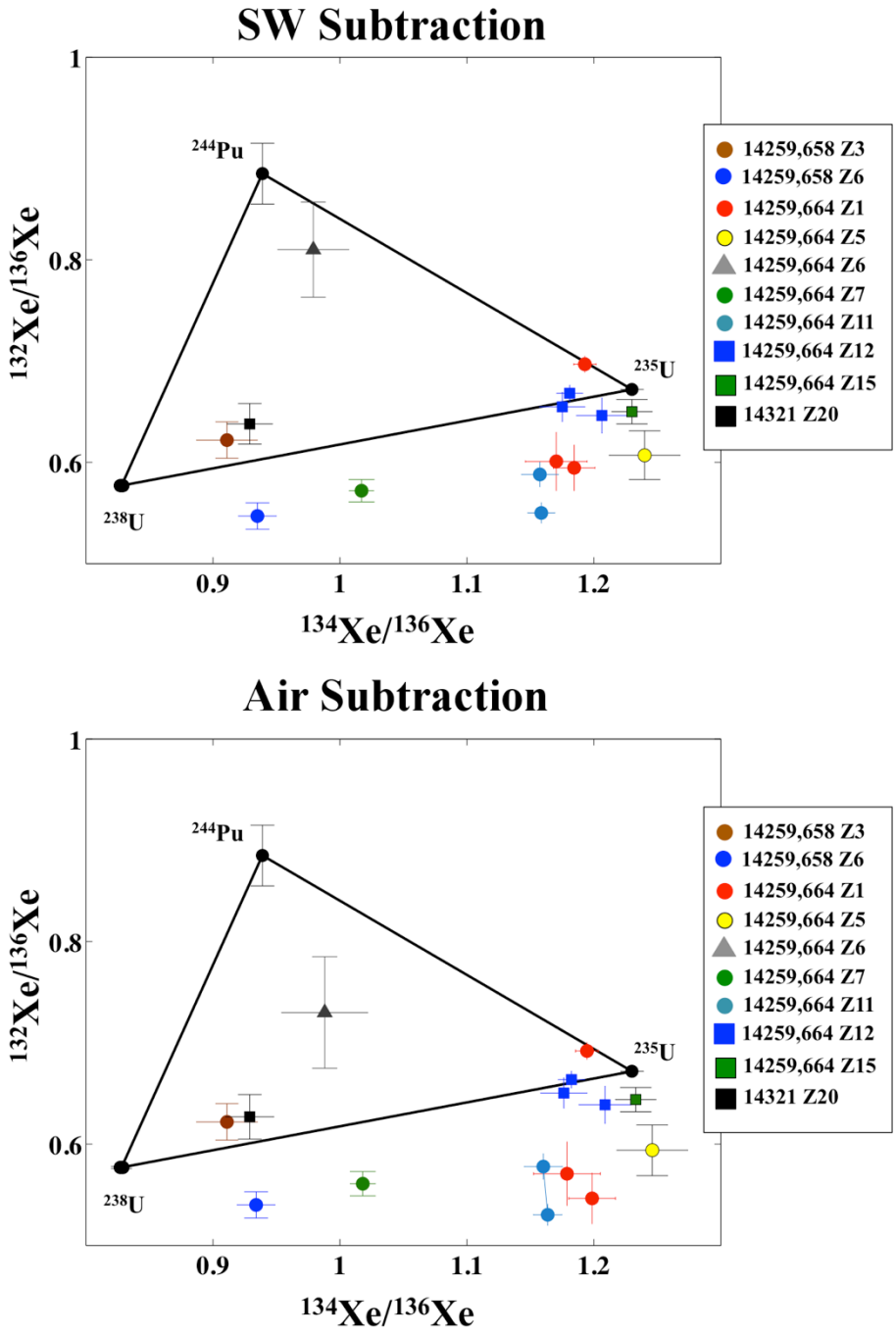


Figure 4-18: Comparison of lunar data corrected using $^{126}Xe/^{130}Xe$ ratio to determine the fraction of trapped component that is spallation derived vs. trapped air/SW. Data are corrected using solar wind subtraction (top) and terrestrial air subtraction (bottom). The choice of trapped component composition makes only slight differences in the final heavy Xe ratios. This is therefore not the source of the excess heavy Xe seen in the lunar data.

The main problem is the apparent presence of an unidentified component, which manifests in the lunar data as an excess of the heavy isotopes of Xe. We investigated multiple possible sources of these excesses including data reduction/correction methods, instrumental errors or artifacts, reactor induced artifacts, and effects of irradiation on the surface of the Moon. I will argue bellow that the most likely source of the heavy Xe excess is from the poorly constrained Xe yields of REE spallation (which occurs due to cosmic ray bombardment on the surface of the Moon).

### *4.7.2 Potential Sources of Heavy Xe Excess in Lunar Zircons*

1. Air vs. Solar Wind Corrections

   The Xe isotope ratios of air and solar wind (SW) are similar but not identical, so the choice of composition used for data corrections will have a small effect on the final Xe isotope ratios. We reduced the lunar data using both compositions to test if the heavy Xe excess is explained if we assume the trapped component is terrestrial air and not implanted SW. The ternary diagrams using both corrections are shown in Figure 4-18 (the SW corrected data is the same as Figure 4-17). If we use air composition for the subtraction, the data fall even further bellow the ternary diagram than do the SW corrected data. Therefore the choice of air vs. SW composition does not explain the heavy Xe excess in the lunar samples.

2. Isotopes Used for Corrections

   We used the $^{130}Xe/^{126}Xe$ and $^{124}Xe/^{126}Xe$ ratios to determine the relative contributions of SW and REE (or Ba in some low temperature steps) spallation in each spectrum. These

values were chosen because spallation is the dominant producer of $^{124}Xe$ and $^{126}Xe$, and SW yields more $^{130}Xe$ than REE spallation. There are two additional isotopes not produced by fission, $^{128}Xe$ and $^{129}Xe$. The latter, $^{129}Xe$, is often avoided when making data corrections due to potential contributions from $^{129}I$, which decays to $^{129}Xe$ ($\lambda$=15.7 My). Although zircons do not incorporate appreciable amounts of I, $^{129}Xe$ is a product of induced fission of $^{235}U$. If the zircons experienced cosmic ray bombardment (including neutron exposure) on the surface of the Moon over tens of millions of years ago, they may contain $^{129}I$-derived Xe. The relatively long exposure age of lunar soil 14259 (450-550 Ma) makes this a concern for the majority of our samples. In fact, zircon 14259,664 Z12 does contain an excess of $^{129}Xe$ that cannot be explained by REE or Ba spallation, and is most likely evidence of neutron bombardment inducing fissionogenic $^{129}I$. We therefore should not use $^{129}Xe$ to correct the lunar zircon data.

The remaining isotope not produced by fission is $^{128}Xe$. RELAX data are not normally corrected using this isotope because of a potential hydrocarbon interference at mass 128. Figure 4-19 shows the data reduced in following the method outlined in section 4.3.3 using the $^{126}Xe/^{128}Xe$ ratio, as opposed to the $^{126}Xe/^{130}Xe$ ratio, to determine the SW correction. The overestimate of the $^{128}Xe$ peak area due to the mass interference, results in an underestimate of the $^{126}Xe/^{128}Xe$ ratio, which results in an underestimate of the SW contribution ($^{126}Xe/^{128}Xe$ (SW) = 0.0389; $^{126}Xe/^{128}Xe$ (REE) = 0.0027). Using $^{128}Xe$ for correcting either the lunar or terrestrial data is therefore not recommended.

3. Ratios Used for Ternary Diagrams

There are four isotopes of Xe that are produced in abundance by fission, $^{131}$Xe, $^{132}$Xe, $^{134}$Xe, $^{136}$Xe. Only three are necessary to produce the ternary, mixing diagrams. If we use different isotopes, is the heavy component still prominent? Figure 4-20 (left) shows the ternary of SW corrected data using $^{132}$Xe/$^{134}$Xe vs $^{131}$Xe/$^{134}$Xe. The data fall to the right of ternary due to an excess of $^{131}$Xe, which is expected since REE spallation is known to produce $^{131}$Xe. Figure 4-20 (right) shows the SW and spallation corrected data using the REE spallation yields from Hohenberg et al. (1981). After the spallation correction the

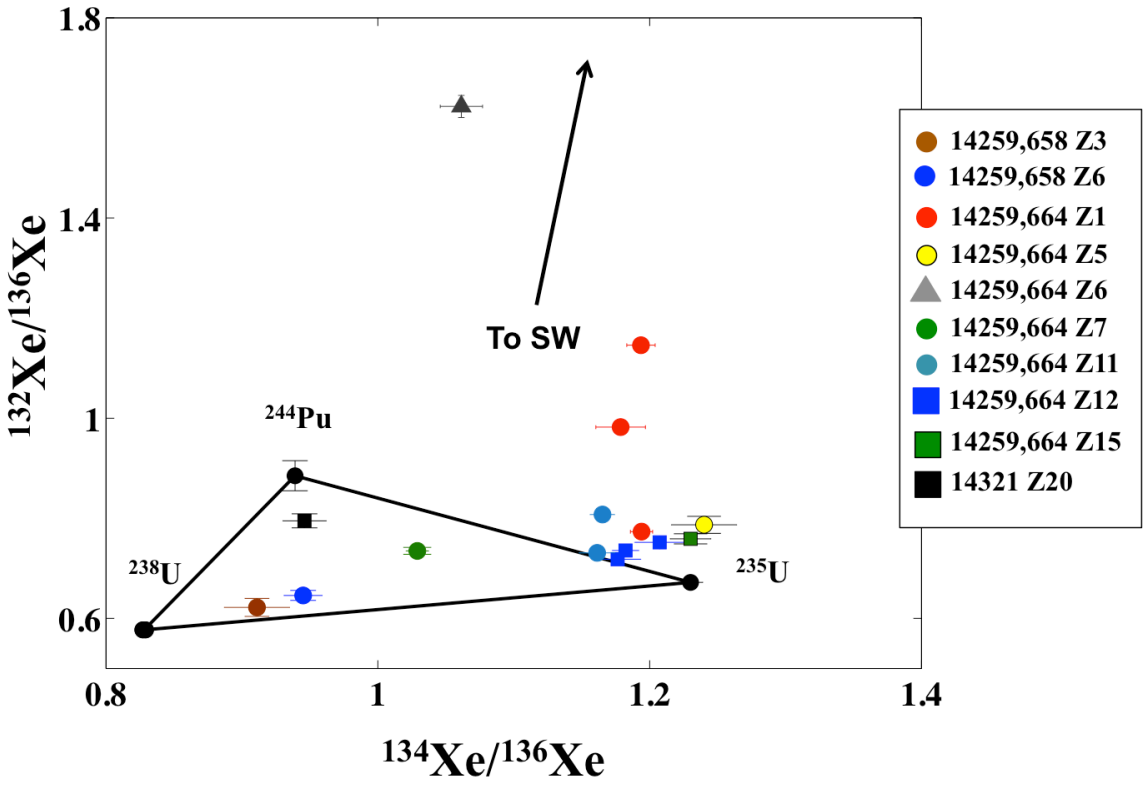


Figure 4-19: Lunar data corrected using the $^{126}$Xe/$^{128}$Xe ratio to determine the fraction of trapped component that is spallation derived vs. trapped SW. The solar wind subtraction is underestimated using the $^{126}$Xe/$^{128}$Xe ratio, most likely due to a hydrocarbon interference at mass 128.

data still fall outside of the ternary diagram, which could be due to the excess heavy Xe component or an incorrect value of $^{131}$Xe spallation yield. Therefore, the data are not consistent with a mixture of end member fission parents regardless of the isotopes used to analyze the data.

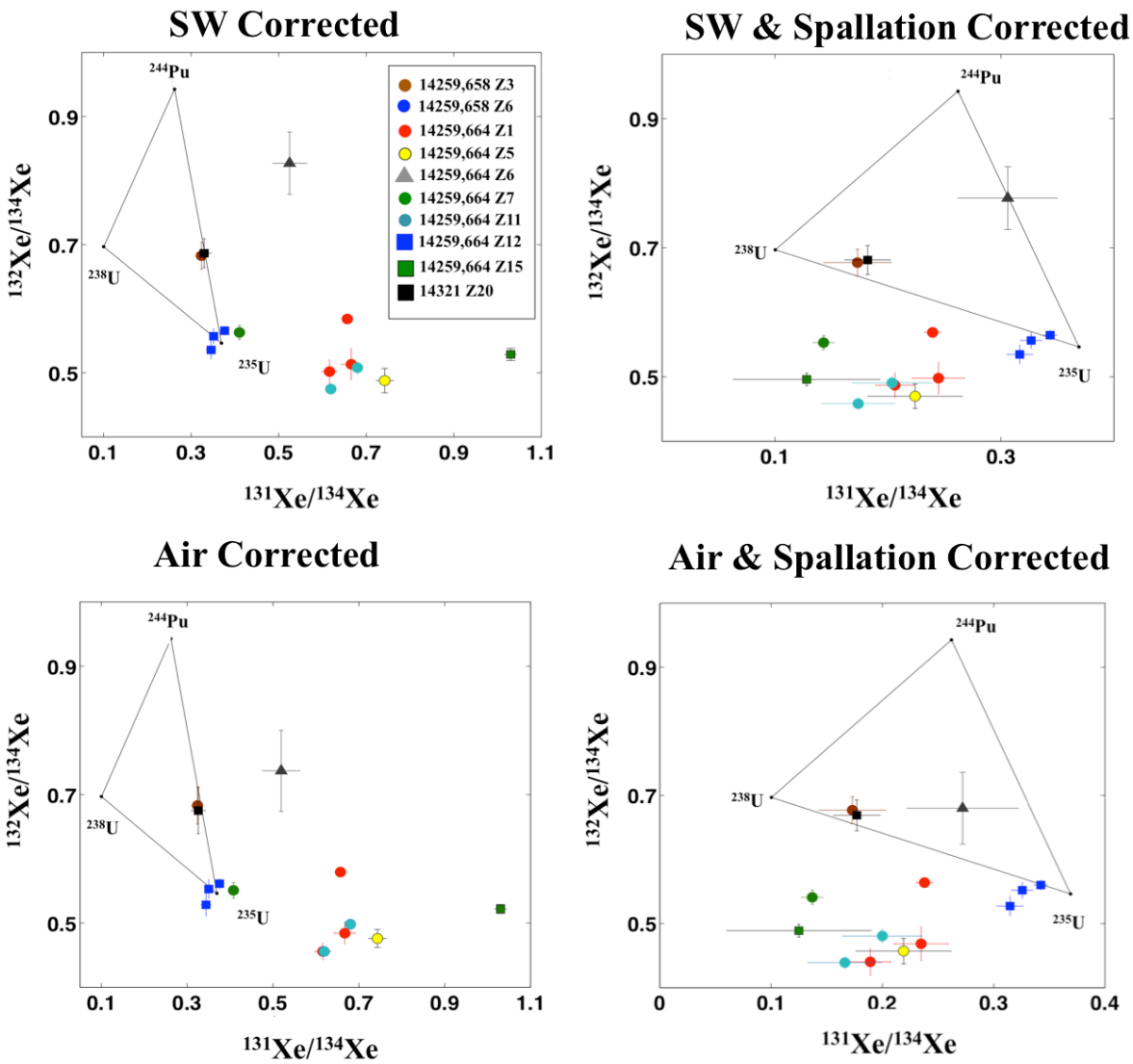


Figure 4-20: Ternary diagrams of air and solar wind corrected lunar data plotted using $^{131}$Xe, $^{132}$Xe, and $^{134}$Xe (left). REE spallation is known to produce appreciable $^{131}$Xe, so a spallation correct was necessary (right). The subtractions were done using the $^{126}$Xe/$^{130}$Xe ratio to determine the fraction of trapped component that is spallation derived vs. trapped SW/air. The excess Xe in the lunar data is visible regardless of which three fission Xe isotopes are used to investigate the data.

4. Instrumental Artifacts and Sample Preparation Methods

The Xe analyses were collected on RELAX during three different sessions, the bulk of which were collected during a month long session in May 2015. There were no significant variations in blank within individual sessions, suggesting blank subtraction cannot explain the excess heavy Xe. Additionally, in the May 2015 session we alternated between analyses of lunar and terrestrial zircons suggesting that if the excess heavy Xe were an instrumental artifact, it should be present in both sets of data. The terrestrial zircons show no evidence of the heavy Xe excess, arguing against instrumental artifacts as being the source of the problem.

We also feel that sample preparation methods are not responsible for the heavy Xe component. The lunar zircons and the V58-2 grains were both mounted in epoxy rounds at UCLA and gold coated for SIMS analyses. Both samples were plucked from the epoxy rounds using the same soldering iron for neutron irradiation. Zircons from V58-2 do not show an excess of heavy Xe suggesting the sample preparation necessary for SIMS analyses is not responsible for this observation. In the May 2015 RELAX session, the lunar zircons and V49-2 and V62 zircons were loaded together in the same sample holder. Contamination from RELAX loading procedures is therefore unlikely.

5. Reactor Induced Artifacts

During neutron irradiation in a nuclear reactor, elements within a sample will capture one or more neutrons resulting in a neutron heavy species. Any radioactive species produced in this manner will either undergo normal β- decay until reaching a stable species, or it

may become unstable and fission. The majority of the zircon samples were irradiated in the second irradiation session (see Table 4- 5), which contained both lunar and terrestrial grains along with the UCLA standard glass. These samples were therefore irradiated under the same conditions. If the heavy Xe excess in the lunar samples is somehow a result of reactor irradiation prior to analyses, it must be due to a compositional difference between the lunar zircons and the terrestrial zircons and the UCLA standard glass on the other because the latter two do contain excess heavy Xe. Compositionally, the terrestrial and lunar zircons are very similar except for their REE concentrations, which is up to an order of magnitude higher in the lunar zircon grains. Both groups of samples contain ~ 1 wt% Hf and have similar U concentrations, with the terrestrial zircons being slightly higher in U (the UCLA glass also has a similar U concentration as the lunar zircons).

In the following paragraphs I will discuss the potential neutron induced reactions and why they are not likely to produce the excess heavy Xe in the lunar samples. Hf is an excellent neutron absorber and is often used in nuclear reactors as thermal neutron shield (e.g. Wallenius and Westlén, 2008; Kamyab, 2014). This behavior along with the similar concentrations in the two zircon populations make Hf an unlikely source of the heavy Xe excess. Neutron induced fission of $^{238}U$ can produce Xe with isotope ratios similar to $^{235}U$, but the cross-section is much smaller than that for $^{235}U$ (e.g. Crouch, 1977; Ragettli et al., 1994). The Xe isotopes measured for the UCLA standard glass, which has a natural $^{238}U/^{235}U$ ratio, are within error of previously reported $^{235}U$ yields suggesting this effect is not significant. Additionally, if induced fission of $^{238}U$ were occurring in the reactor it would affect all zircons and glass samples similarly due to similar U concentrations and

therefore would not produce excess heavy Xe in only the lunar zircons.

The major difference between the two zircon populations is that the lunar samples contain an order of magnitude higher REE concentrations than do the terrestrial samples. Inspection of the chart of nuclides reveals thermal neutron capture of the REEs will produce neutron heavy atoms that do not fission, but instead undergo $\beta^-$ decay or electron capture to produce stable isotopes of other REEs. Xe analyses of a sample of NIST610 glass irradiated by Beth Ann Bell also supports this conclusion. NIST610 glass contains ~500 ppm of all REEs, which is higher than the concentrations of lunar zircons (see Appendix 2-3). The Xe isotopes of NIST610 were measured along with the irradiated UCLA glass at ETH Zurich (see Table 4-4), and the $^{132}$Xe, $^{134}$Xe, and $^{136}$Xe yields of both glasses agree within error of the $^{235}$U fission values reported by Ozima and Podosek. The NIST610 glass has elevated $^{131}$Xe which is an expected result of neutron capture on $^{130}$Ba (NIST610 Ba concentration = 458 ppm, $^{130}$Ba abundance ~0.1%) (Jochum et al., 2011).

All of these points suggest the excess heavy Xe in the lunar zircons is not a product of neutron bombardment in the reactor prior to analyses.

6. Effects From Irradiation on Surface of the Moon

Spallation of REEs and Ba by cosmic rays are known to yield Xe isotopes. Hohenberg and Rowe (1970) conducted spallation experiments in which they irradiated glass samples containing Cs, Ce, Nd, and Dy with 730 Mev protons and measured the resulting Xe yields. The yields of the light isotopes are relatively well constrained; however the

yields of $^{130}$Xe, $^{132}$Xe, $^{134}$Xe, and $^{136}$Xe vary by up to an order of magnitude between analyses. In their later paper Hohenberg et al. (1981) reported a single set of Xe isotope ratios for REE spallation with errors >100% for both $^{130}$Xe and $^{132}$Xe. In addition, they reported no yields of $^{134}$Xe and $^{136}$Xe despite reporting small amounts of both isotopes in their glass experiments. The large variability and uncertainties in the heavy Xe yields of REE spallation make it difficult to accurately correct the lunar data for this component. Additionally, the glasses used by Hohenberg and Rowe (1970) contained relatively equal amounts of light, middle, and heavy REEs. Zircon REE composition is dominated by the heavy REEs (see Figure 4-22), which is not necessarily comparable to the doped glasses

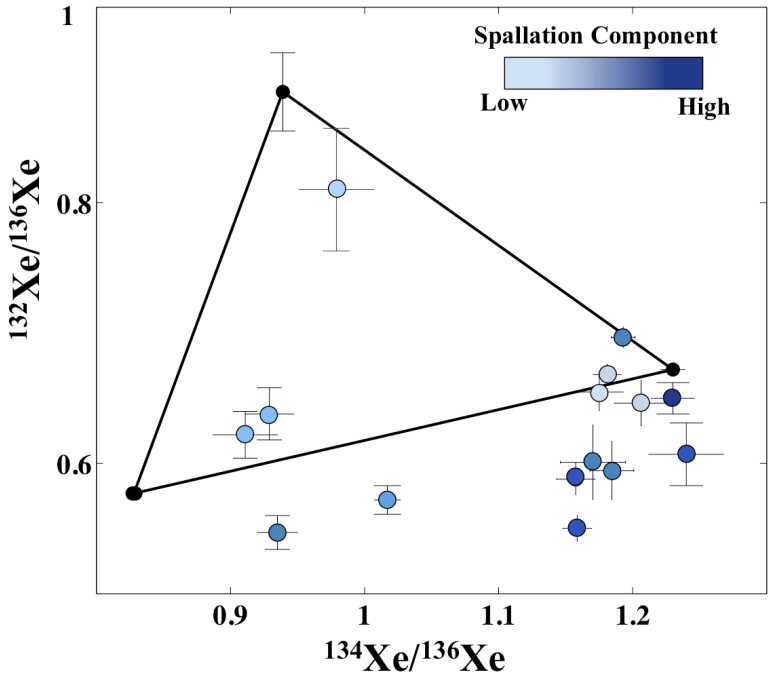


Figure 4-21: Data color coded by amount of spallation component based on the $^{126}$Xe/$^{136}$Xe ratio (ratio ranges from 0.02 to 0.69). The data that fall outside of the ternary diagram have a higher spallation component suggesting the excess heavy Xe is a result of lunar surface reactions. Most likely this is spallation of REEs or other trace elements, for which the Xe yields are not well constrained.

used. Both the compositional differences and the variations in measured spallation yields for the heavy isotopes of Xe make the Hohenberg et al. (1981) not ideal for correcting the lunar zircon data, and yet there are no other experimental results that can be invoked.

The $^{126}Xe/^{136}Xe$ ratio of solar wind corrected data is a proxy for the amount of spallation component in the Xe signal. Figure 4-21 is similar to Figure 4-17, accept that data are color-coded such that light data points have low or negligible spallation components and darkly shaded points have relatively large amounts of spallogenic Xe requiring some correction. It can be seen in that, in general, the data that fall outside of the ternary have larger spallation components than those that can be explained by a mixture of the three fission parents. The correlation of spallation component with excess of heavy Xe suggests that the latter was produced while the samples resided near the surface of the Moon, and the fact that the data fall outside the fission-Xe ternary is therefore likely a result of the poorly known spallation yields of the REEs.

After reviewing potential sources for the excess heavy Xe in the lunar samples, we find that instrument induced artifacts, data correction, and reactor induced artifacts are not likely responsible. The large variability in reported REE spallation yields and the compositional mismatch between our samples and the experimental glasses of Hohenberg and Rowe (1970) suggest that spallation is likely the source of the heavy Xe component. This is also corroborated by the correlation between the apparent magnitude of the spallation component and the plotting of the corrected data outside the fission ternary. This issue can be resolved in future experiments that follow a similar protocol as Hohenberg and Rowe (1970) with more compositionally

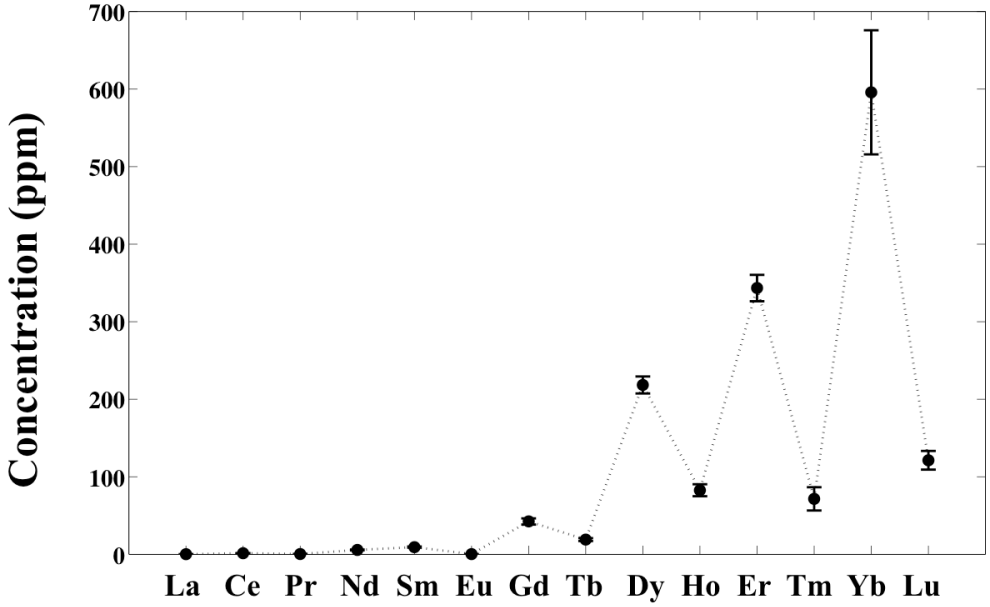


Figure 4-22: Average REE composition (ppm) of lunar zircons reported in Chapter 2. The concentrations of some heavy REEs are orders of magnitude larger than the light REEs.

appropriate samples. I have already begun planning such experiments, which will be conducted during my postdoctoral position at Lawrence Livermore National Lab.

*4.7.2 What can be concluded about U-Pu-Xe ages of lunar zircons?*

In section 4.6.2.2 we discussed criteria for determining the most robust lunar zircon Xe analyses. Seven zircon analyses are consistent with a mixture between $^{235}$U and $^{238}$U fission Xe (see Figure 4-17). The analysis of 14259,664 Z1 that falls on the $^{235}$U-$^{244}$Pu mixing line is impossible to physically explain and contains a significant spallation component. This analysis is therefore not included in the set of most robust analyses discussed bellow. It is possible that the other zircons that fall within the ternary diagram contain a small amount of heavy Xe, so the ages of these six analyses should be interpreted as lower limits on Xe degassing ages. The rest of lunar zircon data

appear to be shifted towards higher $^{134}Xe/^{136}Xe$ ratios, which would result in an apparent increase in the amount of $^{235}U$ in these zircons and an underestimation of their U-Xe ages. Interpretation of these analyses requires results of the spallation experiments proposed in the previous section. We will therefore focus here on the six analyses (of four zircons) with the smallest spallation corrections.

The oldest U-Xe ages are from 14259,658 Z3 (3756 +1372/-875 Ma) and 14321 Z20 (4569 +926/-718 Ma) and are consistent with their associated $^{207}Pb$-$^{206}Pb$ ages (4206 ±19 and 4241 ± 5) However, the large errors on the U-Xe age on Z3 make it difficult to interpret the significance of this age. The lower age limit of 14321 Z20 implies that at least some lunar zircons have retained their fission Xe for the last 3.8 Gyrs. This finding is in agreement with analyses of terrestrial Hadean zircons from Jack Hills, Australia by Turner et al. (2007). Those Jack Hills zircons have $^{207}Pb$-$^{206}Pb$ crystallization ages between 3976 and 4159 Ma and degassing ages between 2510 ± 690 and 4950 ± 540 Ma.

The Jack Hills zircons also contain evidence for plutogenic Xe (Turner et al. 2007), which evident by the significant fraction of the zircons that fall above the $^{238}U$-$^{235}U$ mixing line in Figure 4-23. Lunar zircons 14259,658 Z3 and 14321 Z20 are within 2σ of the $^{238}U$-$^{235}U$ mixing line (the errors in Figure 4-17 are 1σ), so they do not show unequivocal evidence of a plutogenic Xe, although it is possible that after correction for the heavy Xe component these grains will shift away from the mixing line. Zircon 14259,664 Z6 contains the most compelling evidence for Pu-derived Xe. The $^{238}U$-$^{244}Pu$-Xe age of this zircon is 4342 ± 200 Ma (1σ), which is consistent with its $^{207}Pb$-$^{206}Pb$ age of 4338 ± 3 Ma (1σ). However the U-Xe age is 898 (+1400/-898) Ma

(1σ), which places an upper limit on Xe loss of ~3.69 Ga (assuming 2σ errors). The U-Pu-Xe and the U-Xe ages seem to be at odds unless the Xe-loss was relatively recent and not complete, in which case the ratio of $^{238}U/^{244}Pu$ derived Xe would be retained while the ratio of $^{238}U/^{235}U$ would be lowered.

The three analyses of 14259,664 Z12 also show evidence of recent Xe-loss. The data plot within error of the $^{235}U$-$^{238}U$ mixing line cluster near the $^{235}U$ end member. The average U-Xe age of these analyses is 381 ± 101 Ma suggesting that this zircon recently experienced significant, if not close to total, Xe degassing. It is interesting, as noted in Chapter 2, that a subset of zircons from soil 14259 do show evidence of Pb-loss with a lower discord intercept within the last ~ 500 Ma (although U-Pb analyses of Z12 are concordant). Both of these ages are also consistent with the exposure ages for this soil sample, which is placed between 450 and 550 Ma (Burnett et al., 1972; Fields et al., 1973). It must be noted that zircon 14259,664 Z12 has an excess of $^{129}Xe$, which might be due to n-irradiation induced fission of $^{235}U$ (which produced $^{129}I$). Even though the excess is not large, this effect could also result in an over estimate of the $^{235}U$ fission contribution and, hence, an underestimate of U-Xe age. In any case, it is clear that this zircon does not contain any evidence of $^{244}Pu$ fission Xe although, with a Pb-Pb age of ~4240 Ma, it is probable that $^{244}Pu$ existed in the magma from which this zircon crystallized.

The behavior of Xe isotopic in the Vrederfort samples suggests that only large basin-forming impacts have the potential of affecting the U-Xe systems. Schrodinger is thought to be the youngest of the lunar basins with an estimated age of ~3.92 based on crater counting estimates; therefore a basin sized impact could not be responsible for open system behavior observed in

zircons from soil 14259. Although this soil sample has not been recently affected by basin formation, it was collected very near Cone crater (~340 m diameter) and its $^{81}$Kr-K exposure age was used to date the cratering event at 24.4 ± 1.1 Ma (Drozd et al., 1974). The Vrderfort zircons we analyzed were sampled from the crater floor and not impact ejecta material. It is possible that ejection processes could have different effects on the U-Pb and U-Xe systems than processes experienced in the crater floor.

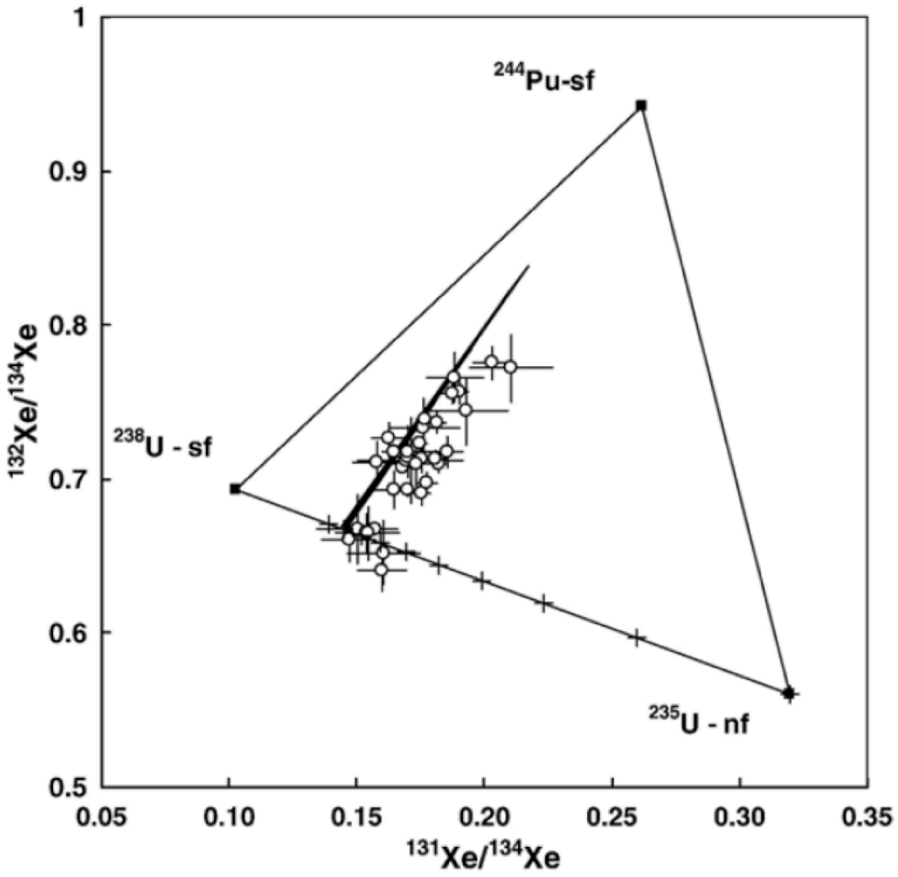


Figure 4-23: Ternary diagram for terrestrial Jack Hills zircons reproduced from Turner et al. (2007). The Jack Hills zircons have $^{207}$Pb-$^{206}$Pb crystallization ages between 3976 and 4159 Ma and U-Xe ages between 2510 ± 690 and 4950 ± 540 Ma. A large fraction of the grains fall above the $^{238}$U-$^{235}$U mixing line showing evidence of plutogenic Xe.

*4.7.3 Future Work*

In order to fully interpret the lunar zircon data, better constraints must be placed on the REE spallation Xe yields. I propose to conduct irradiation experiments similar to those performed by Hohenberg and Rowe (1970) but using targets consisting of glasses and synthetic zircons with REE and trace element compositions similar to those of the lunar zircons. These materials are readily available for purchase or can be synthesized, and the resources to conduct the experiments will be available to me during my postdoctoral position at Lawrence Livermore National Lab.

Experiments to constrain the diffusive properties of Xe in zircon would be desirable, however these experiments are difficult due instrumental requirements such as high sensitivity for Xe and sample requirements such as Xe and/or U homogeneity. More analyses of zircons with a wider range of known thermal histories, including other impact structures and ejecta may help better constrain the diffusive properties of Xe.

The lunar zircons have relatively low concentrations of U, therefore large zircons, >300 μm diameter, are needed for Xe analyses. As we have demonstrated, zircons of this size are present in lunar soil and breccia samples, but their low yields require large amounts of sample (our highest yield was ~ 15 large zircons for ~15g Apollo 14 soil). After samples are crushed and processed through MI, they are deemed unusable by the NASA sample curation team. Allocation of large amounts of pristine samples for continued Xe analyses is therefore unlikely. However, I have begun collaborating with the NASA lunar sample curator to identify previously analyzed, returned samples which would be ideal for zircon separation. The use of returned material

significantly increases the amount of lunar samples available for future Xe analyses. I therefore plan on continuing my investigation of lunar zircons as a probe for the early impact history of the Moon.

## 4.8 Conclusions

1. Xe analyses of zircons sampled near the geologic center of the Vrederfort impact structure suggest that impact shock events alone do not cause measureable amounts of degassing of fission produce xenon. However, zircons sampled further away, near Anna's Rust Sheet, exhibit open system behavior in the both the U-Pb and U-Xe systems due to the later ~1 Ga intrusive event. The difference in Xe behavior is likely due to differences in thermal environments between the samples sites. The analyses of the Vrederfort zircons suggest similar retentiveness of radiogenic Pb and Xe in zircon in an impact environment.
2. Xe analyses of unirradiated lunar soil and breccia zircons show no evidence of Xe from induced fission of $^{235}U$ from exposure to thermal neutron bombardment on the surface of the Moon. Therefore, calculations of U-Xe ages for lunar zircons do not need to account for this potential effect.
3. Most lunar zircon heavy Xe isotopes cannot be explained by mixing of known fission, solar wind, air, and spallation parents. The excess heavy Xe appears to be correlated with the magnitude of the spallation component (as measured on the lighter Xe isotopes), and cannot be explained by data reduction methods or reactor induced effects. The heavy Xe excess is most likely a result of poorly constrained REE spallation yields.

4. The most robust lunar zircon Xe data show a range of results. Six lunar zircon analyses can be explained by a mixture of $^{235}U$ and $^{238}U$ fission Xe only. Two of these zircons have U-Xe ages suggesting retention of fission Xe for the last ~3.8 Ga, and one zircon shows evident of plutogenic Xe and retention of up to ~ 4.1 Ga The other three zircons cluster near the $^{235}U$ end member and their ages suggest extensive Xe-loss within the last ~500 Ma potentially related to the impact that formed Cone Crater (24.4 ± 1.1 Ma).

The analyses in this study suggest that the U-Xe system may be a potential tool for dating impact in lunar samples, however additional experiments and analyses are needed in order to quantify all contributions to the heavy isotope spectrum of Xe and Xe loss kinetics. These include irradiation experiments to better constrain the spallation yields of Xe from heavy rare earth element targets.

**Table 4-1: Constants for U-Xe and Pu-Xe Age Calculations**

| Parameters | Value | |
|---|---|---|
| $^{238}U/^{235}U$ | 138.89 | |
| $\sigma_{235}$ (Cross section) | 5.08 E -22 | mbarns |
| Branching Ratio (nf) | 9.9 E -4 | |
| $Y^{136}$(nf) | 0.0647 | |
| $\lambda$(sf)*$Y^{136}$(sf) | 6.83 ± 0.18 E -18 | $yr^{-1}$ |
| $\lambda$(a) | 1.55 E -10 | $yr^{-1}$ |

**Table 4-2: Xe Composition of Air, Solar Wind, Spallation, and Fission End Members**

| | $^{124}$Xe | $^{126}$Xe | $^{128}$Xe | $^{129}$Xe | $^{130}$Xe | $^{131}$Xe | $^{132}$Xe | $^{134}$Xe | $^{136}$Xe | REF |
|---|---|---|---|---|---|---|---|---|---|---|
| Air | 0.00354 (1) | 0.00330 (2) | 0.07136 (9) | 0.98320 (12) | 0.15136 (12) | 0.7890 (11) | 1 | 0.3879 (6) | 0.3294 (4) | (1) |
| Solar Wind | 0.00449 (150) | 0.00387 (60) | 0.0840 (105) | 1.0450 (50) | 0.1663 (15) | 0.8188 (39) | 1 | 0.3667 (35) | 0.2971 (23) | (2) |
| REE Spal | 0.770 (15) | 1 | 1.22 (03) | 1.6 (4) | 0.04 (9) | 1.64 (24) | 0.06 (7) | | | (3) |
| Ba Spal | 0.5447 (51) | 1 | 1.621 (19) | 1.6 (4) | 1.248 (31) | 4.36 (11) | 1.053 (22) | 0.069 (14) | | (3) |
| $^{235}$U Fiss | | | | | | 0.454 (6) | 0.672 (6) | 1.230 (9) | 1 | (4) |
| $^{238}$U Fiss | | | | 0.0006 | | 0.0830 (6) | 0.577 (1) | 0.828 (1) | 1 | (5) |
| $^{244}$Pu Fiss | | | | 0.048 (55) | | 0.246 (20) | 0.885 (30) | 0.939 (8) | 1 | (6) |

(1) (Basford et al., 1973)

(2) (Crowther et al., 2013)

(3) (Hohenberg et al., 1981)

(4) Values determined from irradiation of UCLA standard glass

(5) (Ragettli et al., 1994)

(6) (Ozima and Podosek, 2002)

**Table 4-3: Major Element Composition of UCLA and NIST Standard Glasses**

| Sample | $TiO_2$ | $SiO_2$ | $Na_2O$ | FeO | $Al_2O_{-3}$ | MgO | CaO | Total |
|---|---|---|---|---|---|---|---|---|
| UCLA Glass | 0.02 ± 0.02 | 71.1 ± 0.18 | 13.74 ± 0.16 | 0.02 ± 0.02 | 2.37 ± 0.08 | 0.01 ± 0.01 | 12.04 ± 0.09 | 99.32 |
| NIST610* | 0.07 ± 0.04 | 69.02 ± 0.11 | 13.55 ± 0.04 | 0.05 ± 0.01 | 1.92 ± 0.03 | 0.07 ± 0.01 | 11.15 ± 0.01 | 96.03 |
| NIST610** | 446 ± 6 ppm | 69.4 ± 0.2 | 13.6 ± 0.1 | 460 ± 7 ppm | 1.98 ± 0.03 | 0.057 ± 0.014 | 11.59 ± 0.06 | 96.72 |

* Composition of NIST610 glass measured at UCLA

** Composition of glass reported by Jochum et al. (2011)

**Table 4-4: Xe Abundance and Isotopic Composition Irradiated UCLA Glass**

| | $^{136}$Xe (atoms/mg) | $\frac{^{131}Xe}{^{136}Xe}$ | $\frac{^{132}Xe}{^{136}Xe}$ | $\frac{^{134}Xe}{^{136}Xe}$ |
|---|---|---|---|---|
| Irradiation 1 | 4.69 E 6 | 0.46 ± 0.004 | 0.68± 0.005 | 1.242 ± 0.003 |
| Irradiation 2 | 7.88 E 6 | 0.454 ± 0.006 | 0.672 ± 0.006 | 1.23 ± 0.009 |
| NIST610 | 5.60 E 6 | 1.581 ± 0.068 | 0.677 ± 0.027 | 1.209 ± 0.045 |
| $^{235}$U Fission* | | 0.453 ± 0.013 | 0.685 ± 0.02 | 1.246 ± 0.036 |

* Values from (Ozima and Podosek, 2002)

**Table 4-5: Irradiation Parameters**

| Irradation # | Date | Flux (n/cm$^2$/s) | $^{136}$Xe ($10^6$ atoms/mg glass) | Fluence* (n/cm$^2$) |
|---|---|---|---|---|
| 1 | 26-Nov-12 | 8 x $10^{11}$ | 4.69 | 3.14 x $10^{16}$ |
| 2 | 11-Aug-14 | 8 x $10^{11}$ | 7.88 | 5.1 x $10^{16}$ |

* Fluence calculated from $^{136}$Xe abundance.

**Table 4-6: Raw Data, Summed First 5 Spectra from RELAX**

| Sample | Laser (Amps) | Air SW Corr | $^{124}$Xe | 1σ | $^{126}$Xe | 1σ | $^{128}$Xe | 1σ | $^{129}$Xe | 1σ | $^{130}$Xe | 1σ |
|---|---|---|---|---|---|---|---|---|---|---|---|---|
| 14259 ,568 | | | | | | | | | | | | |
| Z3 | 20.5 | Y | 48061 | 3500 | 55974 | 3730 | 81164 | 4536 | 122705 | 5462 | 7395 | 1677 |
| Z6 | 20.5 | Y | 390479 | 7885 | 453980 | 8495 | 533399 | 9199 | 714820 | 10644 | 64665 | 3264 |
| | | | | | | | | | | | | |
| 14259 ,664 | | | | | | | | | | | | |
| Z1 | 17.0 | Y | 511914 | 6915 | 608250 | 7482 | 815428 | 8546 | 2557780 | 15048 | 332040 | 5503 |
| Z1 | 18.0 | Y | 492648 | 11784 | 592558 | 12910 | 754157 | 14491 | 1797050 | 22312 | 217740 | 7795 |
| Z1 | 20.5 | Y | 97401 | 4441 | 112916 | 4777 | 137393 | 5265 | 255055 | 7132 | 18735 | 2008 |
| Z5 | 20.5 | Y | 367009 | 8932 | 416499 | 9513 | 487111 | 10285 | 811635 | 13243 | 62355 | 3700 |
| Z6 | 14.0 | Y | 43909 | 2557 | 60935 | 2942 | 254496 | 5875 | 2420380 | 17930 | 390050 | 7214 |
| Z6 | 20.5 | Y | 6266 | 1421 | 9706 | 1674 | 66186 | 3885 | 397630 | 9282 | 66980 | 3866 |
| Z7 | 16.0 | Y | 224789 | 6328 | 279433 | 7097 | 510733 | 9426 | 2305000 | 19855 | 372560 | 8059 |
| Z7 | 18.0 | Y | 493335 | 7387 | 599626 | 8127 | 738762 | 8874 | 1388480 | 12109 | 164650 | 4253 |
| Z11 | 14.0 | Y | 1499353 | 14080 | 1751188 | 15294 | 2109902 | 16620 | 3641390 | 21820 | 384070 | 7170 |
| Z11 | 20.5 | Y | 1953229 | 27979 | 2259630 | 30163 | 2603327 | 32217 | 3957900 | 39668 | 308740 | 11200 |
| Z11 | 20.5 | Y | 132630 | 4131 | 159731 | 4526 | 223147 | 5331 | 915480 | 10710 | 117210 | 3888 |
| Z12 | 14.0 | Y | 307487 | 11480 | 369487 | 12520 | 527893 | 14978 | 2897760 | 34620 | 254140 | 10357 |
| Z12 | 16.0 | Y | 45128 | 3556 | 48090 | 3640 | 81158 | 4734 | 481125 | 11409 | 43200 | 3484 |
| Z12 | 20.5 | Y | 36678 | 2950 | 43667 | 3234 | 94249 | 4704 | 440395 | 10055 | 53150 | 3596 |
| Z15 | 20.5 | Y | 1138474 | 12361 | 1307326 | 13251 | 1432271 | 13820 | 1933890 | 16049 | 100240 | 3749 |
| | | | | | | | | | | | | |
| 14321 | | | | | | | | | | | | |
| Z14 | 20.5 | Y | 42668 | 2764 | 48575 | 2931 | 96036 | 4084 | 633905 | 10314 | 86320 | 3865 |
| Z20 | 20.5 | N | 102841 | 4455 | 119793 | 4792 | 154130 | 5442 | 497805 | 9711 | 57910 | 3427 |
| | | | | | | | | | | | | |
| Vredefort | | | | | | | | | | | | |
| V58-2 Z1 | 20.5 | Y | 1581 | 991 | 14561 | 2792 | 32811 | 4006 | 295150 | 11761 | 45955 | 4681 |
| V58-2 Z5 | 20.5 | Y | 970 | 1009 | 8847 | 2209 | 20045 | 3207 | 148000 | 8533 | 29630 | 3864 |
| V58-2 Z11 | 20.5 | Y | 3504 | 924 | 9587 | 1317 | 155725 | 4904 | 1233665 | 13623 | 212155 | 5657 |
| V58-2 Z7+8 | 20.5 | Y | 10889 | 2178 | 12017 | 2362 | 265158 | 7484 | 3455480 | 25898 | 533140 | 10220 |
| V58-2 Z10 | 20.5 | Y | -102 | 595 | 71 | 783 | 14732 | 1974 | 148490 | 5945 | 16365 | 2017 |
| V58-2 Z9 | 20.5 | Y | -5 | 681 | 147 | 655 | 8999 | 1305 | 89165 | 3764 | 18075 | 1739 |
| V49-2 H1 | 14.0 | Y | -575 | 922 | 1504 | 1006 | 4176 | 1489 | 27125 | 3371 | 8390 | 2022 |
| V49-2 H1 | 20.5 | Y | -207 | 2917 | 10583 | 4103 | 17589 | 5096 | 207840 | 15449 | 37180 | 6852 |
| V62 H4 | 12.0 | Y | -223 | 1348 | 618 | 1304 | 22999 | 3490 | 53585 | 5207 | 10310 | 2354 |
| V62 H4 | 20.5 | Y | 3663 | 1464 | 1018 | 1272 | 115647 | 5376 | 1128750 | 16543 | 176760 | 6741 |
| V62 H4 | 20.5 | Y | 1132 | 908 | 2696 | 1117 | 63959 | 4158 | 617155 | 12652 | 94510 | 4993 |

| Sample | $^{131}Xe$ | 1σ | $^{132}Xe$ | 1σ | $^{134}Xe$ | 1σ | $^{136}Xe$ | 1σ |
|---|---|---|---|---|---|---|---|---|
| 14259 ,568 | | | | | | | | |
| Z3 | 47793 | 20540 | 139322 | 24308 | 223280 | 11271 | 213351 | 9635 |
| Z6 | 851146 | 19920 | 1066094 | 22675 | 1823002 | 23090 | 1950392 | 18471 |
| | | | | | | | | |
| 14259 ,664 | | | | | | | | |
| Z1 | 1481332 | 37773 | 1206569 | 44033 | 2403699 | 24015 | 2029319 | 19401 |
| Z1 | 1524718 | 46998 | 1175603 | 53546 | 2289764 | 33360 | 1956441 | 28933 |
| Z1 | 294249 | 13285 | 266831 | 15099 | 465935 | 11074 | 395616 | 9924 |
| Z5 | 210998 | 13102 | 132111 | 14447 | 277486 | 9959 | 230865 | 8839 |
| Z6 | 515120 | 36997 | 812162 | 44174 | 981923 | 21899 | 1002938 | 18651 |
| Z6 | 114209 | 19137 | 282946 | 23511 | 426900 | 13391 | 325747 | 11399 |
| Z7 | 614862 | 48827 | 553324 | 57883 | 1228198 | 27738 | 1264813 | 24178 |
| Z7 | 1499943 | 30854 | 2058369 | 37121 | 3655967 | 26376 | 3595673 | 22342 |
| Z11 | 3751305 | 69576 | 2876834 | 70136 | 6059218 | 75346 | 5229777 | 31715 |
| Z11 | 4981577 | 86546 | 3722666 | 83254 | 7327782 | 97063 | 6330597 | 54431 |
| Z11 | 371856 | 25336 | 340615 | 29573 | 551881 | 15852 | 483849 | 12119 |
| Z12 | 6445337 | 105919 | 9689786 | 135951 | 17126952 | 196162 | 14502453 | 81539 |
| Z12 | 1038439 | 27509 | 1647433 | 34798 | 2956535 | 42222 | 2516017 | 27216 |
| Z12 | 779022 | 25622 | 1207639 | 31729 | 2254139 | 33899 | 1868633 | 22204 |
| Z15 | 2309020 | 22410 | 1185053 | 18356 | 2240888 | 20590 | 1821024 | 16309 |
| | | | | | | | | |
| 14321 | | | | | | | | |
| Z14 | 112053 | 21833 | 197381 | 26288 | 264272 | 12459 | 267452 | 11025 |
| Z20 | 410428 | 19954 | 855146 | 25073 | 1245292 | 18430 | 1340579 | 17484 |
| | | | | | | | | |
| Vredefort | | | | | | | | |
| V58-2 Z1 | 161320 | 29158 | 447261 | 37681 | 707260 | 23416 | 732733 | 22436 |
| V58-2 Z5 | 56733 | 24510 | 206351 | 31610 | 369158 | 18369 | 394976 | 17616 |
| V58-2 Z11 | 103947 | 33491 | 390590 | 42242 | 803284 | 21002 | 803872 | 18767 |
| V58-2 Z7+8 | 664245 | 75643 | 1727951 | 95915 | 2794376 | 46544 | 2889756 | 40692 |
| V58-2 Z10 | 132387 | 17099 | 292357 | 22016 | 403801 | 12876 | 394552 | 12001 |
| V58-2 Z9 | 381459 | 17074 | 1100638 | 23385 | 1783047 | 19203 | 1839117 | 18222 |
| V49-2 H1 | 430872 | 20721 | 1259283 | 30285 | 2065114 | 30641 | 2115195 | 30142 |
| V49-2 H1 | 1665467 | 74069 | 4781849 | 105821 | 7580146 | 99744 | 7835807 | 97583 |
| V62 H4 | 334189 | 19414 | 377447 | 22956 | 648338 | 19689 | 552471 | 17914 |
| V62 H4 | 1675966 | 45738 | 3855190 | 60962 | 6152237 | 51845 | 5807694 | 41591 |
| V62 H4 | 356821 | 30125 | 899165 | 38926 | 1467106 | 25591 | 1437473 | 23329 |

**Table 4-7: Mass Fractionation and SW Corrected Values**

| Sample | Laser (Amps) | Air SW Corr | $^{124}Xe$ | 1σ | $^{126}Xe$ | 1σ | $^{128}Xe$ | 1σ | $^{129}Xe$ | 1σ | $^{130}Xe$ | 1σ |
|---|---|---|---|---|---|---|---|---|---|---|---|---|
| 14259 ,568 | | | | | | | | | | | | |
| Z3 | 20.5 | Y | 21338 | 4640 | 17976 | 3915 | 12654 | 9461 | 16142 | 24692 | 0 | 5236 |
| Z6 | 20.5 | Y | 506412 | 88712 | 529864 | 88336 | 469171 | 54153 | 415307 | 19440 | 21195 | 4624 |
| | | | | | | | | | | | | |
| 14259 ,664 | | | | | | | | | | | | |
| Z1 | 17.0 | Y | 503721 | 7151 | 601148 | 8908 | 579673 | 18820 | 593840 | 44697 | 24046 | 9463 |
| Z1 | 18.0 | Y | 487587 | 11925 | 588170 | 13785 | 579433 | 20784 | 557623 | 53461 | 23527 | 11500 |
| Z1 | 20.5 | N | 97140 | 4533 | 112690 | 5353 | 114070 | 6178 | 166210 | 14710 | 4508 | 3498 |
| Z5 | 20.5 | Y | 88039 | 9756 | 96339 | 8308 | 102352 | 5572 | 105737 | 14483 | 3854 | 3370 |
| Z6 | 14.0 | Y | 35172 | 5028 | 49435 | 4894 | 78276 | 7521 | 295350 | 44793 | 61695 | 9958 |
| Z6 | 20.5 | Y | 4075 | 1696 | 7588 | 1728 | 32629 | 4195 | 38710 | 23014 | 9469 | 5236 |
| Z7 | 16.0 | Y | 215096 | 6588 | 271029 | 8589 | 279611 | 14873 | 32308 | 59046 | 10841 | 12437 |
| Z7 | 18.0 | Y | 489745 | 7608 | 596514 | 9454 | 591353 | 17569 | 492640 | 35278 | 23861 | 7840 |
| Z11 | 14.0 | Y | 1528442 | 386484 | 1645822 | 303718 | 1831335 | 85178 | 1510795 | 66468 | 65833 | 13437 |
| Z11 | 20.5 | Y | 1995428 | 503630 | 2127948 | 392408 | 2340012 | 107383 | 2413129 | 78015 | 85118 | 16299 |
| Z11 | 20.5 | Y | 132252 | 34246 | 147965 | 27953 | 154180 | 10297 | 194656 | 30141 | 5919 | 6266 |
| Z12 | 14.0 | Y | 305836 | 79310 | 342361 | 64894 | 373099 | 25498 | 1305034 | 84164 | 13694 | 16928 |
| Z12 | 16.0 | Y | 44402 | 11998 | 44222 | 8966 | 54492 | 5724 | 212220 | 25091 | 1769 | 5129 |
| Z12 | 20.5 | Y | 35446 | 9738 | 39798 | 8111 | 61862 | 6026 | 112777 | 25598 | 1592 | 5358 |
| Z15 | 20.5 | Y | 1166301 | 112552 | 1233299 | 87412 | 1324949 | 25386 | 1521190 | 20210 | 49332 | 4337 |
| | | | | | | | | | | | | |
| 14321 | | | | | | | | | | | | |
| Z14 | 20.5 | Y | 40667 | 5039 | 43631 | 4238 | 47341 | 4601 | 93059 | 26789 | 1745 | 5634 |
| Z20 | 20.5 | N | 103300 | 11038 | 111651 | 9116 | 117464 | 5890 | 155581 | 22770 | 4466 | 4890 |
| | | | | | | | | | | | | |
| Vredefort | | | | | | | | | | | | |
| V58-2 Z1 | 20.5 | Y | 666 | 1348 | 13707 | 3693 | 6209 | 5168 | 5970 | 34287 | 0 | 6991 |
| V58-2 Z5 | 20.5 | Y | 416 | 1360 | 8330 | 3274 | 2001 | 4523 | -31934 | 29229 | 0 | 6034 |
| V58-2 Z11 | 20.5 | Y | -1076 | 1301 | 5313 | 2753 | 42706 | 6623 | -132864 | 40539 | 0 | 8268 |
| V58-2 Z7+8 | 20.5 | Y | -473 | 4238 | 1415 | 9947 | -10262 | 15364 | 15555 | 92151 | 0 | 18769 |
| V58-2 Z10 | 20.5 | Y | -364 | 1086 | -173 | 2539 | 3130 | 3619 | 49847 | 20311 | 0 | 4127 |
| V58-2 Z9 | 20.5 | Y | -304 | 1135 | -133 | 2503 | -2783 | 3331 | -16266 | 18831 | 0 | 3896 |
| V49-2 H1 | 14.0 | Y | -661 | 1294 | 1424 | 2617 | -2808 | 3423 | -15067 | 19801 | 0 | 4132 |
| V49-2 H1 | 20.5 | Y | -632 | 4658 | 10187 | 10496 | -12046 | 13270 | 10690 | 75021 | 0 | 15498 |
| V62 H4 | 12.0 | Y | -1245 | 1545 | 158 | 1271 | 15064 | 3583 | 941 | 18097 | 0 | 3789 |
| V62 H4 | 20.5 | Y | -1782 | 2039 | -3162 | 1360 | 25035 | 6416 | -20538 | 49463 | 0 | 10177 |
| V62 H4 | 20.5 | Y | -1746 | 1159 | 356 | 1115 | 15524 | 4712 | 670 | 34985 | 0 | 7148 |

| Sample | $^{131}Xe$ | 1σ | $^{132}Xe$ | 1σ | $^{134}Xe$ | 1σ | $^{136}Xe$ | 1σ |
|---|---|---|---|---|---|---|---|---|
| 14259 ,568 | | | | | | | | |
| Z3 | 47793 | 20540 | 139322 | 24308 | 223280 | 11271 | 213351 | 9635 |
| Z6 | 851146 | 19920 | 1066094 | 22675 | 1823002 | 23090 | 1950392 | 18471 |
| | | | | | | | | |
| 14259 ,664 | | | | | | | | |
| Z1 | 1481332 | 37773 | 1206569 | 44033 | 2403699 | 24015 | 2029319 | 19401 |
| Z1 | 1524718 | 46998 | 1175603 | 53546 | 2289764 | 33360 | 1956441 | 28933 |
| Z1 | 294249 | 13285 | 266831 | 15099 | 465935 | 11074 | 395616 | 9924 |
| Z5 | 210998 | 13102 | 132111 | 14447 | 277486 | 9959 | 230865 | 8839 |
| Z6 | 515120 | 36997 | 812162 | 44174 | 981923 | 21899 | 1002938 | 18651 |
| Z6 | 114209 | 19137 | 282946 | 23511 | 426900 | 13391 | 325747 | 11399 |
| Z7 | 614862 | 48827 | 553324 | 57883 | 1228198 | 27738 | 1264813 | 24178 |
| Z7 | 1499943 | 30854 | 2058369 | 37121 | 3655967 | 26376 | 3595673 | 22342 |
| Z11 | 3751305 | 69576 | 2876834 | 70136 | 6059218 | 75346 | 5229777 | 31715 |
| Z11 | 4981577 | 86546 | 3722666 | 83254 | 7327782 | 97063 | 6330597 | 54431 |
| Z11 | 371856 | 25336 | 340615 | 29573 | 551881 | 15852 | 483849 | 12119 |
| Z12 | 6445337 | 105919 | 9689786 | 135951 | 17126952 | 196162 | 14502453 | 81539 |
| Z12 | 1038439 | 27509 | 1647433 | 34798 | 2956535 | 42222 | 2516017 | 27216 |
| Z12 | 779022 | 25622 | 1207639 | 31729 | 2254139 | 33899 | 1868633 | 22204 |
| Z15 | 2309020 | 22410 | 1185053 | 18356 | 2240888 | 20590 | 1821024 | 16309 |
| | | | | | | | | |
| 14321 | | | | | | | | |
| Z14 | 112053 | 21833 | 197381 | 26288 | 264272 | 12459 | 267452 | 11025 |
| Z20 | 410428 | 19954 | 855146 | 25073 | 1245292 | 18430 | 1340579 | 17484 |
| | | | | | | | | |
| Vredefort | | | | | | | | |
| V58-2 Z1 | 161320 | 29158 | 447261 | 37681 | 707260 | 23416 | 732733 | 22436 |
| V58-2 Z5 | 56733 | 24510 | 206351 | 31610 | 369158 | 18369 | 394976 | 17616 |
| V58-2 Z11 | 103947 | 33491 | 390590 | 42242 | 803284 | 21002 | 803872 | 18767 |
| V58-2 Z7+8 | 664245 | 75643 | 1727951 | 95915 | 2794376 | 46544 | 2889756 | 40692 |
| V58-2 Z10 | 132387 | 17099 | 292357 | 22016 | 403801 | 12876 | 394552 | 12001 |
| V58-2 Z9 | 381459 | 17074 | 1100638 | 23385 | 1783047 | 19203 | 1839117 | 18222 |
| V49-2 H1 | 430872 | 20721 | 1259283 | 30285 | 2065114 | 30641 | 2115195 | 30142 |
| V49-2 H1 | 1665467 | 74069 | 4781849 | 105821 | 7580146 | 99744 | 7835807 | 97583 |
| V62 H4 | 334189 | 19414 | 377447 | 22956 | 648338 | 19689 | 552471 | 17914 |
| V62 H4 | 1675966 | 45738 | 3855190 | 60962 | 6152237 | 51845 | 5807694 | 41591 |
| V62 H4 | 356821 | 30125 | 899165 | 38926 | 1467106 | 25591 | 1437473 | 23329 |

**Table 4-8: U-Xe and Pb-Pb Analyses**

| Sample | Laser Current | U-Xe Age (Ma) | 1σ+ | 1σ– | Pb-Pb Age (Ma) | 1σ |
|---|---|---|---|---|---|---|
| 14259,658 Z3 | 20.5 AF | 3756 | 1372 | 875 | 4207 | 19 |
| 14259,658 Z3 | 20.5 AF | 1037 | 913 | 514 | 4207 | 19 |
| 14259,658 Z6 | 20.5 AF | 2903 | 506 | 403 | 4251 | 4 |
| 14259,664 Z1 | 17.0 A | 345 | 109 | 101 | + | + |
| 14259,664 Z1 | 18.0 A | 439 | 177 | 158 | + | + |
| 14259,664 Z1 | 19.0 A | 556 | 337 | 274 | + | + |
| 14259,664 Z1 | 20.5 A | 0 | 109 | 99 | + | + |
| 14259,664 Z1 | 20.5 A | 292 | 56 | 53 | + | + |
| 14259,664 Z1 | 20.5 A | 389 | 299 | 246 | + | + |
| 14259,664 Z5 | 20.5 A | 2958 | 971 | 703 | 3932 | 9 |
| 14259,664 Z5 | 20.5 AF | 1907 | 169 | 156 | 3932 | 9 |
| 14259,664 Z6 | 14.0A | 2703 | 1987 | 1094 | 4338 | 3 |
| 14259,664 Z6 | 20.5 A | 4569 | 926 | 718 | 4338 | 3 |
| 14259,664 Z7 | 16.0 A | 368 | 102 | 95 | 4128 | 6 |
| 14259,664 Z7 | 18.0 A | 368 | 70 | 66 | 4128 | 6 |
| 14259,664 Z11 | 14.0A | 407 | 127 | 116 | 4126 | 8 |
| 14259,664 Z11 | 20.5 A | 522 | 80 | 76 | 4126 | 8 |
| 14259,664 Z11 | 20.5 AF | 530 | 110 | 102 | 4126 | 8 |
| 14259,664 Z12 | 14.0A | 368 | 102 | 95 | 4241 | 2 |
| 14259,664 Z12 | 16.0 A | 368 | 70 | 66 | 4241 | 2 |
| 14259,664 Z12 | 20.5 A | 407 | 127 | 116 | 4241 | 2 |
| 14259,664 Z15 | 20.5 A | 21 | 146 | 130 | 3922 | 8 |
| 14321 Z14 | 20.5 A | 238 | 436 | 328 | ++ | ++ |
| 14321 Z20 | 20.5 A | 4569 | 926 | 718 | 4241 | 5 |
| | | | | | | |
| V58-2 Z1 | 20.5 A | 3284 | 1620 | 1009 | 2324 | 16 |
| V58-2 Z5 | 20.5 A | 4326 | 4502 | 1819 | 2804 | 8 |
| V58-2 Z11 | 20.5 A | 2462 | 851 | 624 | 2469 | 10 |
| V58-2 Z7+8 | 20.5 A | 3234 | 663 | 531 | 2851 | 9 |
| V58-2 Z10 | 20.5 A | 2013 | 922 | 644 | 2026 | 9 |
| V58-2 Z9 | 20.5 A | 3165 | 417 | 360 | 2689 | 8 |
| V49-2 H1 | 14.0 A | 2986 | 567 | 465 | 3092* | 7 |
| V49-2 H1 | 20.5 A | 3224 | 538 | 447 | 3092* | 7 |
| V62 H4 | 12.0 A | 417 | 403 | 313 | 2077** | 11 |
| V62 H4 | 20.5 A | 1484 | 158 | 146 | 2077** | 11 |
| V62 H4 | 20.5 A | 2061 | 463 | 381 | 2077** | 11 |

+ 14259,664 Z1 Pb-Pb ages range from 4075 ± 8 to 4313 ± 8 Ma.
++ Five age analyses of 14321 Z14 have Pb-Pb ages range between 4134 ± 31 to 4216 ± 27
* (Moser et al., 2001)
** (Moser et al., 2011)

## Chapter 5: Summary, Conclusions, and Recommendations

The research in this thesis addresses two poorly understood components of lunar history: the timing of residual KREEP magmatism and the nature of the pre-3.9 Ga impact flux, in particular the timing of large basin forming events. This is achieved through coordinated isotopic, chemical, and microstructural investigations of zircon grains separated from Apollo samples. Previous analyses of lunar zircons have suggested a picture contradictory to the LMO modal of early lunar evolution, which suggests ~ 500 Myr duration of KREEP magmatism (e.g. Nemchin et al., 2008). The extensive surveys reported herein lead to a better characterization of lunar zircons and thus have change our understanding of the early lunar history they record. The results of our analyses suggest a shorter duration of KREEP magmatism than previously proposed, which agrees well with models of LMO crystallization. Additionally, our investigation of zircon trace elements are consistent with multiple KREEP source regions and do not require the presence of hydrous or oxidizing conditions. Microstructural and $^{207}Pb$-$^{206}Pb$ age analyses, paired with previously reported zircon ages, suggest that large impact events, potentially basin forming, occurred as often as every 100 Myr in the pre-3.9 Ga era. The work herein also suggests the U-Xe system in zircon may be useful in dating impact events, however poorly constrained Xe spallation yields make full interpretation of the data difficult. Future experiments to better measure these yields will be completed during my postdoctoral position at Lawrence Livermore National Lab, and will be informative for not only this work, but also for future analyses of meteoritic and asteroid sample return materials which are subject to spallation effects.

## 5.1 Summary

Zircons were separated from a suite of lunar breccia and soil samples from Apollo 14, 15, and 17. These grains were investigated by using a range of analytical techniques including in situ electron beam imaging and SIMS analyses, and a subset of the zircons was also chosen for destructive Xe analyses. The correlation of these large datasets, in addition to the characterization of Apollo 15 zircons, which had previously only been minimally investigated, can contribute to developing a large scale understanding of zircon forming magmatism (most likely KREEP magmatism) and subsequent impact alteration on the Moon.

The analyses presented in Chapter 2 represent one of the largest collections of lunar zircon ages and the largest survey of lunar zircon trace elements to date. Statistical analyses of the distributions of $^{207}$Pb-$^{206}$Pb crystallization ages reveal variations between landing sites. Most notable is the absence of a post ~4.1 Ga zircon population in the Apollo 15 and 17 samples. Approximately 90% of the zircons reported herein have crystallization ages older than 4.1 Ga, suggesting that the vast majority of KREEP magmatism ceased by this time. We also identified three zircons that contain textural evidence of recrystallization in an impact environment. The ages of these zircons suggest impact events at ~4.33 and 4.20 Ga, which coincide with peaks in the Pb-Pb age histograms of zircons from Apollo 14, 15, and 17 samples.

The trace element survey includes 102 REE and trace element analyses for 90 lunar zircons. We developed new criteria to identify evidence of trace element contributions from micron to sub-

micron impact melt glass inclusions. In about half of the zircons surveyed, an inspection of SIMS analysis spots (using electron imaging) or monitoring Fe concentration, which is usually less than a few hundred ppm in igneous zircons, led to identification of impact-induced contamination. Once the data were filtered to include only pristine zircon analyses, the lunar zircon trace elements could be described by a single REE pattern characterized by a negative Eu anomaly and no Ce anomaly. This finding obviates previous work that had suggested up to four unique trace element groupings in the lunar zircon population. We also calculated Ti-in-zircon temperatures using new best estimates of $TiO_2$ and $SiO_2$ activities determined for likely KREEP parent melt compositions. The temperatures of lunar zircons span from 958 ± 57° to 1321 ± 100°C, which are well bounded by the dry granite solidus and the zircon saturation temperatures for KREEP-rich rocks. There is no need to appeal to especially hydrated melts to account for crystallization temperatures.

In Chapter 3 we presented an extensive microstructural survey conducted at the University of Western Ontario using electron beam imaging techniques, including EBSD crystallographic analyses, for 30 of the zircons reported in Chapter 2. These analyses greatly increase the number of lunar zircons for which coordinated data on isotopic age, chemical compositions, and microstructural information exist. The major findings from this survey are:

1. Igneous zonation and shock microtwins were found only in zircons older that 4.2 Ga.
2. Over two-thirds of the grains examined contained curviplanar features and/or impact melt glass inclusions, suggesting most of the lunar zircons experienced at least 20 GPa shock pressures.

3. Pb-loss in zircons with crystal plastic deformation appears to be associated with degree of crystallinity and not degree of deformation.
4. Recrystallization textures were observed in ~2% of the samples, and no impact growth textures were identified. This may imply that only a small subset of the lunar zircons have been exposed to both high shock pressures and prolonged elevated temperatures.

In addition to the survey results we report the first evidence of the decomposition of zircon to its constituent oxides, baddeleyite and silica, in lunar samples. Future trace element analyses of these grains and their interstitial impact melt may give insight into the impact environment in which these zircons formed. We also report the observation of a set of curved shock microtwins, a previously unidentified shock morphology. The association of the twins with impact melt glass inclusions suggests the twins nucleated on previously existing curviplanar fractures.

In the following chapter, we investigated the U-Xe chronometer in zircon and assessed the usefulness of the system in constraining impact ages. A subset of the largest Apollo zircons and a suite of their terrestrial analogues from the Vrederfort impact structure were chosen for Xe analyses collected using the RELAX instrument at the University of Manchester. The zircons from the geographic center of the Vrederfort structure yield U-Xe ages consistent with their Pb-Pb crystallization ages (that predate the impact) suggesting that impact shock alone does not cause appreciable Xe loss. However, zircons from the crater rim, which have been exposed to prolonged elevated temperatures due to a local intrusive event, do show evidence of Xe loss associated with emplacement of this intrusion. The results of the Vrederfort zircons suggest a

similar retentiveness of Pb and Xe in zircon and a potentially similar response of the U-Pb and U-Xe system to large, basin sized impacts.

Xe analyses of zircons from Apollo 14 samples proved more complex than their terrestrial analogues. Six of the analyses contained little to no trapped solar wind component and only small amounts of spallation due to cosmic ray exposure. For these analyses we were able to determine minimum U-Xe degassing ages. Two of the zircons have relatively old ages suggesting at least some of the lunar zircons have retained their fission Xe for upwards of ~3.8 Ga. The Xe isotopes of a third zircon contain evidence plutogenic Xe, suggesting that it has not experienced total degassing since ~3.9 Ga. Three analyses of a fourth zircon from a soil cluster close to the $^{235}$U end member and suggest significant Xe loss within the last ~500 Myr. The U-Pb systems for some zircons from the same soil sample show evidence of a similarly recent disturbance, however the extent of Pb-loss is notably less than Xe-loss.

For the rest of the lunar zircons, the Xe analyses could not be fully interpreted due to contributions from an unknown heavy Xe component. After reviewing potential sources of the heavy Xe excess, we conclude the most likely source of this contribution is spallation from heavy REEs, the yields of which are not well constrained. Future experiments to constrain these yields will allow for a better interpretation of the lunar Xe data.

## 5.2 Conclusions

Here we revisit the big picture questions outlined in Chapter 1 and discuss how our results have contributed to our understanding of the early lunar magmatic and impact histories. In particular, we have reconciled the zircon ages and chemistry with the results of LMO solidification models and other chemical systems on the Moon, and we contributed to the number of suggested pre-3.9 Ga large impact events.

### *5.2.1 Early Magmatic History of the Moon*

Model ages suggest the Moon forming impact occured between ~4.54 – 4.53 Ga after which the Moon possessed a partial or global magma ocean (Hartmann and Davis, 1975; Canup and Asphaug, 2001; T. Kleine et al., 2005; Touboul et al., 2009). Models for solidification of this LMO suggest time scales ranging up to ~ 200 Myr, which would suggest that only a small fraction of melt remained after ~4.33 Ga (mantle overturn not considered here). The residual KREEP melts, after >99% of LMO crystallization, would have been highly enriched in incompatible elements and are the most likely source of zircons in lunar samples (Warren and Wasson, 1979). The peak in zircon age histograms at ~4.33 Ga identified in all landing sites aligns well with the time of residual melt formation predicted by LMO solidification models. Even though Apollo 14 samples contain zircons with ages ranging from 4.4 to 3.9 Ga, the vast majority of all lunar zircons crystallized before 4.1 Ga (90%), and a significant fraction of Apollo 15 and 17 zircons crystallized before 4.2 Ga (>92%). Only Apollo 14 contains zircon

younger than 4.1 Ga, and samples from this location are thought to contain Imbrium ejecta material. Imbrium-related impact induced Pb-loss is therefore a plausible explanation for the younger population of grains. The distribution of zircon ages suggests that majority of KREEP magmatism ceased around 4.2 or 4.1 Ga, which is contrary to previous studies that only considered the full range of ages (~500 Myr).

Previous analyses of lunar zircon trace elements have required oxidizing or hydrous systems to explain anomalous measurements including positive Ce anomalies and sub-solidus Ti-in-zircon temperatures (Nemchin et al., 2010; Valley et al., 2014). Our rigorous interrogation of the trace element analyses revealed that contributions from micron to sub-micron sized impact melt glass inclusions, which are common in lunar zircons, could drastically influence the measured compositions. After filtering our data to exclude this source of contamination, the lunar zircons are characterized by one REE pattern with no positive Ce anomaly, consistent with formation of the zircons in a reducing environment. Additionally, our new best estimates of $TiO_2$ and $SiO_2$ activities result in calculated Ti-in-zircon temperatures that fall above the dry granite solidus and bellow the zircon saturation temperature for KREEP-rich rocks. This suggests the lunar zircons formed in reducing, anhydrous conditions, which is commensurate with the current understanding of the lunar environment.

### *5.2.2 Early Impact History of the Moon*

Recrystallized domains in shocked zircons have been used to date impacts both terrestrially and on the Moon (Moser et al., 2009; Grange et al., 2013b). In our survey of lunar zircons we

identified three zircons that are characterized by granular texture that is best explained as formed by recrystallization in an impact environment. The ages of these zircons, paired with previously proposed impact ages from lunar zircons and associated phases, suggest large impacts (potentially basin-forming impacts) occurred on the Moon at least as often as every 100 Myr prior to ~3.9 Ga. Additionally, we see no evidence in zircons from the three Apollo landing sites of significant impact bombardment occurring around ~ 3.9 Ga as would be predicted by the late heavy bombardment. If there was a lunar cataclysm, the zircons, which existed on the Moon at the time, failed to record any obvious evidence of this hypothesized event or series of events.

### 5.3 Recommendations for Future Research

The following are recommendations aimed to improve and continue the work reported herein.

1. The nature of the young (<4.1 Ga) zircon population in Apollo 14 still remains poorly constrained. Many of these grains are small and are highly shocked. However, a dedicated investigation of this population of samples to determine the extent of impact alteration would inform our assumption that these grains likely experienced Pb-loss due to the Imbrium basin forming event.
2. Dating of recrystallized regions of shocked zircons remains a useful method for constraining impact ages in lunar samples. Recovering these types of zircons should therefore be a priority for further investigations into the early impact history of the Moon.
3. During my postdoctoral position at Lawrence Livermore National Lab I plan to conduct experiments to more accurately measure Xe spallation yields for samples that have REE concentrations commensurate with the lunar zircons. These analyses will allow for

correction of the lunar Xe data for contributions from this effect, and will allow for full interpretation of the U-Xe ages.

4. Expanding the Xe analyses to a suite of zircons from other terrestrial impact structures would improve our understanding of the behavior of the U-Xe system in these settings. If the method proves useful for constraining impact ages, the study should be expanded to include more lunar zircons as well. However, requirements for large grain size, U concentrations, and crystallization ages warrant more consideration before future Xe analyses are conducted.

**References**

Abramov, O., Mojzsis, S.J., 2009. Microbial habitability of the Hadean Earth during the late heavy bombardment. Nature 459, 419–422. doi:10.1038/nature08015

Ahrens, T.J., 1993. Impact Erosion of Terrestrial Planetary Atmospheres. Annu. Rev. Earth Planet. Sci. 21, 525–555. doi:10.1007/s13398-014-0173-7.2

Alexander, Jr., E.C., Kahl, S.B., 1974. 40Ar-39Ar studies of lunar breccias. Proc. Lunar Sci. Conf. 5th Supplement, 1353–1373.

Arnold, J.R., 1975. Monte Carlo simulation of tunrover processes in the lunar regolith, in: Proc. Lunar Sci. Conf. 6thth. pp. 2375–2395. doi:10.1007/s13398-014-0173-7.2

Asimow, P.D., Ghiorso, M.S., 1998. Algorithmic modifications extending MELTS to calculate subsolidus phase relations. Am. Mineral. 83, 1127–1132.

Baker, D.M.H., Head, J.W., Fassett, C.I., Kadish, S.J., Smith, D.E., Zuber, M.T., Neumann, G.A., 2011. The transition from complex crater to peak-ring basin on the Moon: New observations from the Lunar Orbiter Laser Altimeter (LOLA) instrument. Icarus 214, 377–393. doi:10.1016/j.icarus.2011.05.030

Basford, J.R., Dragon, J.C., Pepin, R.O., Coscio, M.R.J., Murthy, V.R., 1973. Krypton and Xenon in lunar fines, in: Fourth Lunar Science Conference. pp. 1915–1955.

Bell, E. a., Harrison, T.M., 2013. Post-Hadean transitions in Jack Hills zircon provenance: A signal of the Late Heavy Bombardment? Earth Planet. Sci. Lett. 364, 1–11. doi:10.1016/j.epsl.2013.01.001

Bell, E.A., Boehnke, P., Harrison, T.M., n.d. Recovering the primary geochemistry of Jack Hills zircons through quantitative estimates of chemical alteration. GCA.

Belousova, E.A., Griffin, W.L., O'Reilly, S.Y., Fisher, N.I., 2002. Igneous zircon: trace element composition as an indicator of source rock type. Contrib. to Mineral. Petrol. 143, 602–622. doi:10.1007/s00410-002-0364-7

Bernatowicz, T.J., Hohenberg, C.M., Hudson, B., Kennedy, B.M., Podosek, F.A., 1978. Argon ages for lunar breccias 14064 and 15405. Proc. Lunar Sci. Conf. 9th 905–919.

Binder, A.B., 1986. The Initial Thermal State of the Moon, in: Origin of the Moon. pp. 425–433. doi:10.1007/s13398-014-0173-7.2

Blanchard, D.P., Haskin, L.A., Jacobs, J.W., Brannon, J.C., Korotev, R.L., 1975. Major and Trace Element Chemistry of Boulder 1 at Station 2, Apollo 17. Moon 14, 359–371.

Boehnke, P., Watson, E.B., Trail, D., Harrison, T.M., Schmitt, A.K., 2013. Zircon saturation re-

revisited. Chem. Geol. 351, 324–334. doi:10.1016/j.chemgeo.2013.05.028

Bohor, B.F., Betterton, W.J., Krogh, T.E., 1993. Impact-shocked zircons: discovery of shock-induced textures reflecting increasing degrees of shock metamorphism. Earth Planet. Sci. Lett. 119, 419–424. doi:10.1016/0012-821X(93)90149-4

Borg, L.E., Gaffney, A.M., Shearer, C.K., 2015. A review of lunar chronology revealing a preponderance of 4.34-4.37 Ga ages. Meteorit. Planet. Sci. 50, 715–732. doi:10.1111/maps.12373

Boss, A.P., Peale, S.J., 1986. Dynamical Constraints on the Origin of the Moon, in: Origin of the Moon. pp. 59–101. doi:10.1007/s13398-014-0173-7.2

Boyce, J.W., Tomlinson, S.M., McCubbin, F.M., Greenwood, J.P., Treiman, a H., 2014. The lunar apatite paradox. Science (80-. ). 344, 400–2. doi:10.1126/science.1250398

Braddy, D., Hutcheon, I.D., Price, P.B., 1975. Crystal chemistry of Pu and U and concordant fission track ages of lunar zircons and whitlockites. Proc. Lunar Sci. Conf. 6th 3587–3600.

Burnett, D.S., Huneke, J.C., Podosek, F.A., Russ III, G.P., Turner, G., Wasserburg, G.J., 1972. The Irradiation History of Lunar Samples, in: 3rd Lunar and Planetary Science Conference. p. 105.

Burnham, A.D., Berry, A.J., 2012. An experimental study of trace element partitioning between zircon and melt as a function of oxygen fugacity. Geochim. Cosmochim. Acta 95, 196–212. doi:10.1016/j.gca.2012.07.034

Canup, R.M., Asphaug, E., 2001. Origin of the Moon in a giant impact near the end of the Earth's formation. Nature 412, 708–712. doi:10.1038/35089010

Chen, C.H., Hurst, G.S., Payne, M.G., 1980. Direct counting of Xe atoms. Chem. Phys. Lett. 75, 473–477. doi:10.1016/0009-2614(80)80558-6

Cherniak, D.J., Hanchar, J.M., Watson, E.B., 1997. Rare-earth diffusion in zircon. Chem. Geol. 134, 289–301. doi:10.1016/S0009-2541(96)00098-8

Cherniak, D.J., Watson, E.B., 2000. Pb diffusion in zircon. Chem. Geol. 172, 5–24. doi:10.1016/S0009-2541(00)00233-3

Christian, R.P., Berman, S., Dwornik, E.J., Rose Jr., H.J., Schnepfe, M.M., 1976. Composition of some Apollo 14, 15, and 16 Lunar breccias and two Apollo 15 fines, in: Proc. Lunar Sci. Conf. 7th. pp. 138–140.

Church, S.E., Tilton, G.R., Chen, J.H., 1976. Lead isotopic studies of lunar soils: Their bearing on the time scale of agglutinate formation. Proc. Lunar Sci. Conf. 7th 351–371.

Claiborne, L.L., Miller, C.F., Wooden, J.L., 2010. Trace element composition of igneous zircon: A thermal and compositional record of the accumulation and evolution of a large silicic batholith, Spirit Mountain, Nevada. Contrib. to Mineral. Petrol. 160, 511–531. doi:10.1007/s00410-010-0491-5

Cohen, B. a, Swindle, T.D., Kring, D. a, 2000. Support for the lunar cataclysm hypothesis from lunar meteorite impact melt ages. Science (80-. ). 290, 1754–1756. doi:10.1126/science.290.5497.1754

Crouch, E. a. C., 1977. Fission-product yields from neutron-induced fission. At. Data Nucl. Data Tables 19, 417–532. doi:10.1016/0092-640X(77)90023-7

Crowther, S. a, Gilmour, J.D., 2013. The Genesis solar xenon composition and its relationship to planetary xenon signatures. Geochim. Cosmochim. Acta 123, 17–34. doi:10.1016/j.gca.2013.09.007

Crowther, S. a., Mohapatra, R.K., Turner, G., Blagburn, D.J., Kehm, K., Gilmour, J.D., 2008. Characteristics and applications of RELAX, an ultrasensitive resonance ionization mass spectrometer for xenon. J. Anal. At. Spectrom. 23, 921–1044. doi:10.1039/b802899k

Dalrymple, G.B., Ryder, G., 1996. Argon-40/argon-39 age spectra of Apollo 17 highlands breccia samples by laser step heating and the age of the Serenitatis basin. J. Geophys. Res. 101, 26069–26084. doi:10.1029/96JE02806

Dalrymple, G.B., Ryder, G., 1993. Ar-40/Ar-39 age spectra of Apollo 15 impact melt rocks by laser step-heating and their bearing on the history of lunar basin formation. J. Geophys. Res. 98, 13085–13095. doi:10.1029/93JE01222

Dalrymple, G.B., Ryder, G., 1991. 40Ar-39Ar ages of six Apollo 15 impact melt rocks by laser step heating. Geophys. Res. Lett. 18, 1163–1166.

Dasch, E.., Shih, C.-Y., Bansal, B.., Wiesmann, H., Nyquist, L.E., 1987. Isotopic analysis of basaltic fragments from lunar breccia 14321: Chronology and petrogenesis of pre-Imbrium mare volcanism. Geochim. Cosmochim. Acta 51, 3241–3254. doi:10.1016/0016-7037(87)90132-3

Dence, M.R., Plant, A.G., 1972. Analysis of Fra Mauro samples and the origin of the Imbrium Basin, in: Third Lunar Science Conference. pp. 379–399.

Deutsch, A., Schärer, U., 1990. Isotope systematics and shock-wave metamorphism: I. U-Pb in zircon, titanite and monazite, shocked experimentally up to 59 GPa. Geochim. Cosmochim. Acta 54, 3427–3434. doi:10.1016/0016-7037(90)90295-V

Deutsch, A., Stöffler, D., 1987. Rb-Sr-analyses of Apollo 16 melt rocks and a new age estimate

for the Imbrium basin: Lunar basin chronology and the early heavy bombardment of the moon. Geochim. Cosmochim. Acta 51, 1951–1964. doi:10.1016/0016-7037(87)90184-0

Dickinson, T., Taylor, G.J., Keil, K., Schmitt, R.A., Hughes, S.S., Smith, M.R., 1985. Apollo 14 Aluminous Mare Basalts and Their Possible Relationship to KREEP, in: 15th Lunar and Planetary Science Conference. pp. C365–C374.

Drozd, R.., Hohenberg, C.., Morgan, C.., Ralston, C.., 1974. Cosmic-ray exposure history at the Apollo 16 and other lunar sites: lunar surface dynamics. Geochim. Cosmochim. Acta 38, 1625–1642. doi:10.1016/0016-7037(74)90178-1

Eikenberg, J., Signer, P., Wieler, R., 1993. U-Xe, U-Kr, and U-Pb systematics for dating uranium minerals and ivestigations of the production of nucleogenic neon and argon. Geochim. Cosmochim. Acta 57, 1053–1069.

Elkins Tanton, L.T., Van Orman, J. a., Hager, B.H., Grove, T.L., 2002. Re-examination of the lunar magma ocean cumulate overturn hypothesis: Melting or mixing is required. Earth Planet. Sci. Lett. 196, 239–249. doi:10.1016/S0012-821X(01)00613-6

Elkins-Tanton, L.T., Burgess, S., Yin, Q.Z., 2011. The lunar magma ocean: Reconciling the solidification process with lunar petrology and geochronology. Earth Planet. Sci. Lett. 304, 326–336. doi:10.1016/j.epsl.2011.02.004

Erickson, T.M., Cavosie, A.J., Moser, D.E., Barker, I.R., Radovan, H.A., 2013. Correlating planar microstructures in shocked zircon from the Vredefort Dome at multiple scales: Crystallographic modeling, external and internal imaging, and EBSD structural analysis. Am. Mineral. 98, 53–65. doi:10.2138/am.2013.4165

Eugster, O., Eberhardt, P., Geiss, J., Grogler, N., Jungck, M., Meier, F., Morgell, Niederer, F., 1984. Cosmic Ray Exposure Histories of Apollo 14, Apollo 15, and Apollo 16 Rocks, in: Proc. 14th Lunar and Planet. Sci. Conf. pp. B498–B512.

Ferriss, E.D.A., Essene, E.J., Becker, U., 2007. Computational study of the effect of pressure on the Ti-in-zircon thermometer. Eur. J. Mineral. 20, 745–755.

Ferry, J.M., Watson, E.B., 2007. New thermodynamic models and revised calibrations for the Ti-in-zircon and Zr-in-rutile thermometers. Contrib. to Mineral. Petrol. 154, 429–437. doi:10.1007/s00410-007-0201-0

Fields, P.R., Diamond, H., Metta, D.N., Rokop, D.J., 1973. Reaction products of lunar uranium and cosmic rays, in: Fourth Lunar Science Conference. pp. 2123–2130.

Foster, W.R., 1948. Useful aspects of the fluorescence of accessory-mineral-zircon. Am. Mineral. 33, 724–735.

Fu, B., Page, F.Z., Cavosie, A.J., Fournelle, J., Kita, N.T., Lackey, J.S., Wilde, S. a., Valley, J.W., 2008. Ti-in-zircon thermometry: Applications and limitations. Contrib. to Mineral. Petrol. 156, 197–215. doi:10.1007/s00410-008-0281-5

Garver, J.I., Kamp, P.J.J., 2002. Integration of zircon color and zircon fission-track zonation patterns in orogenic belts: application to the Southern Alps, New Zealand. Tectonophysics 349, 203–219. doi:10.1016/S0040-1951(02)00054-9

Gault, E.D., Horz, F., Brownlee, E.D., Hartung, B.J., 1974. Mixing of the lunar regolith, in: Proceedings of the Fifth Lunar Conference. pp. 2365–2386.

Ghiorso, M.S., Sack, R.O., 1995. Chemical Mass Transfer in Magmatic Processes. IV. A Revised and Internally Consistent Thermodynamic Model for the Interpolation and Extrapolation of Liquid-Solid Equilibria in Magmatic Systems at Elevated Temperatures and Pressures. Contrib. to Mineral. Petrol. 119, 197–212.

Gibson, R.L., Armstrong, R. a., Reimold, W.U., 1997a. The age and thermal evolution of the Vredefort impact structure: A single-grain U□Pb zircon study. Geochim. Cosmochim. Acta 61, 1531–1540. doi:10.1016/S0016-7037(97)00013-6

Gibson, R.L., Armstrong, R.A., Reimold, W.U., 1997b. The age and thermal evolution of the Vredefort impact structure: A single-grain U□Pb zircon study. Geochim. Cosmochim. Acta 61, 1531–1540. doi:10.1016/S0016-7037(97)00013-6

Gilmour, J.D., Johnston, W.A., Lyon, I.C., Turner, G., 1992. RELAX-1, a refrigerator enhanced laser analyser for xenon, in: Meteoritical Society Meeting. p. 225.

Glass, B.P., Liu, S., 2001. Discovery of high-pressure ZrSiO4 polymorph in naturally occurring shock-metamorphosed zircons. Geology 29, 371–373. doi:10.1130/0091-7613(2001)?029<0371:DOHPZP>?2.0.CO

Goodrich, C. a., Taylor, G.J., Keil, K., Kallemeyn, G.W., Warren, P.H., 1986. Alkali norite, troctolites, and VHK mare basalts from breccia 14304. Proc. 16th Lunar Plan. Sci. Conf. Journal of, D305–D318. doi:10.1029/JB091iB04p0D305

Graham, I.T., De Waal, S.A., Armstrong, R.A., 2005. New U–Pb SHRIMP zircon age for the Schurwedraai alkali granite: Implications for pre-impact development of the Vredefort Dome and extent of Bushveld magmatism, South Africa. J. African Earth Sci. 43, 537–548. doi:10.1016/j.jafrearsci.2005.09.009

Grange, M.L., Nemchin, a. a., Pidgeon, R.T., Timms, N., Muhling, J.R., Kennedy, a. K., 2009. Thermal history recorded by the Apollo 17 impact melt breccia 73217. Geochim. Cosmochim. Acta 73, 3093–3107. doi:10.1016/j.gca.2009.02.032

Grange, M.L., Nemchin, a. a., Timms, N., Pidgeon, R.T., Meyer, C., 2011. Complex magmatic and impact history prior to 4.1 Ga recorded in zircon from Apollo 17 South Massif aphanitic breccia 73235. Geochim. Cosmochim. Acta 75, 2213–2232. doi:10.1016/j.gca.2011.01.036

Grange, M.L., Nemchin, A.A., Pidgeon, R.T., Merle, R.E., Timms, N.E., 2013a. What Lunar Zircons Ages Can Tell?, in: 44th Lunar and Planetary Science Conference. p. #1884.

Grange, M.L., Pidgeon, R.T., Nemchin, a. a., Timms, N.E., Meyer, C., 2013b. Interpreting U-Pb data from primary and secondary features in lunar zircon. Geochim. Cosmochim. Acta 101, 112–132. doi:10.1016/j.gca.2012.10.013

Grieve, R.A., McKay, G.A., Smith, H.D., Weill, D.F., 1975. Lunar polymict breccia 14321: a petrographic study. Geochim. Cosmochim. Acta 39, 229–245.

Grimes, C.B., John, B.E., Kelemen, P.B., Mazdab, F.K., Wooden, J.L., Cheadle, M.J., Hanghøj, K., Schwartz, J.J., 2007. Trace element chemistry of zircons from oceanic crust: A method for distinguishing detrital zircon provenance. Geology 35, 643–646. doi:10.1130/G23603A.1

Hanchar, J.M., Hoskin, P.W.O. (Eds.), 2003. Reviews in Mineralogy & Geochemistry, Volume 53. The Mineralogical Society of America, Washington, DC.

Harrison, T.M., 2009. The Hadean Crust: Evidence from >4 Ga Zircons. Annu. Rev. Earth Planet. Sci. 37, 479–505. doi:10.1146/annurev.earth.031208.100151

Harrison, T.M., Lovera, O.M., 2013. The Multi-diffusion Domain Model: Past, Present and Future. Gelogical Soc. London, Spec. Publ. 378, 91–106.

Harrison, T.M., Schmitt, A.K., 2007. High sensitivity mapping of Ti distributions in Hadean zircons. Earth Planet. Sci. Lett. 261, 9–19. doi:10.1016/j.epsl.2007.05.016

Hartmann, W.K., 2003. Megaregolith evolution and cratering cataclysm models—Lunar cataclysm as a misconception (28 years later). Meteorit. Planet. Sci. 38, 579–593. doi:10.1111/j.1945-5100.2003.tb00028.x

Hartmann, W.K., 1975. Lunar “cataclysm”: A misconception? Icarus 24, 181–187. doi:10.1016/0019-1035(75)90095-0

Hartmann, W.K., Davis, D.R., 1975. Satellite-sized planetesimals and lunar origin. Icarus 515, 504–515. doi:10.1016/0019-1035(75)90070-6

Head, J.W., 1976. Lunar volcanism in space and time. Rev. Geophys. Sp. Phys. 14, 265–300. doi:10.1029/RG014i002p00265

Hebeda, E.H., Schultz, L., Freundel, M., 1987. Radiogenic, fissiogenic and nucleogenic noble gases in zircons. Earth Planet. Sci. Lett. 85, 79–90. doi:10.1016/0012-821X(87)90023-9

Heiken, G., Vaniman, D., French, B.M., 1991. Lunar Sourcebook: A User's Guide to the Moon. Cambridge University Press.

Henkel, H., Reimold, W., 1998. Integrated geophysical modelling of a giant, complex impact structure: anatomy of the Vredefort Structure, South Africa. Tectonophysics 287, 1–20. doi:10.1016/S0040-1951(98)80058-9

Herpers, U., Herr, W., Kulus, H., Michel, R., Thiel, K., Woelfle, R., 1973. Manganese-53 profile, particle track studies and the rhenium-187 iostopic anomaly of breccia 14305. Proc. 4th Lunar Sci. Conf. Supplement, 2157–2169.

Hinton, R.., Upton, B.G.., 1991. The chemistry of zircon: Variations within and between large crystals from syenite and alkali basalt xenoliths. Geochim. Cosmochim. Acta 55, 3287–3302. doi:10.1016/0016-7037(91)90489-R

Hinton, R.W., Meyer, C., 1991. Ion Probe Analysis of Zircon and Yttrobetafite in a Lunar Granite, in: Lunar Planet. Sci. Conf. pp. 575–576.

Hohenberg, C.M., Hudson, B., Kennedy, B.M., Podosek, F. a., 1981. Xenon spallation systematics in Angra dos Reis. Geochim. Cosmochim. Acta 45, 1909–1915.

Hohenberg, C.M., Rowe, M.W., 1970. Spallation Yields of Xenon from Irradiation of Cs, Ce, Nd, Dy, and a Rare Earth Mixture with 730-Mev Protons. J. Geophys. Res. 75, 4205–4209.

Hoskin, P.W.O., 2005. Trace-element composition of hydrothermal zircon and the alteration of Hadean zircon from the Jack Hills, Australia. Geochim. Cosmochim. Acta 69, 637–648. doi:10.1016/j.gca.2004.07.006

Hoskin, P.W.O., Ireland, T.R., 2000. Rare earth element chemistry of zircon and its use as a provenance indicator. Geology 28, 627–630. doi:10.1130/0091-7613(2000)28<627

Hoskin, P.W.O., Schaltegger, U., 2003. The Composition of Zircon and Igneous and Metamorphic Petrogenesis. Rev. Mineral. Geochemistry 53, 27–62. doi:10.2113/0530027

Hudson, G.B., Kennedy, B.M., Podosek, F.A., Hohenberg, C.M., 1989. The Early Solar System Abundance of 244Pu as Inferred from the St. Severin Chondrite. Proc. 19th Lun. Planet. Sci. Conf. 547–557.

Hurst, G.S., Payne, M.G., Kramer, S.D., Young, J.P., 1979. Resonance ionization spectroscopy and one-atom detection. Rev. Mod. Phys. 51, 767–819. doi:10.1103/RevModPhys.51.767

Jacobsen, S.B., 2005. THE Hf-W ISOTOPIC SYSTEM AND THE ORIGIN OF THE EARTH

AND MOON. Annu. Rev. Earth Planet. Sci. 33, 531–570. doi:10.1146/annurev.earth.33.092203.122614

Jochum, K.P., Weis, U., Stoll, B., Kuzmin, D., Yang, Q., Raczek, I., Jacob, D.E., Stracke, A., Birbaum, K., Frick, D. a., Günther, D., Enzweiler, J., 2011. Determination of reference values for NIST SRM 610-617 glasses following ISO guidelines. Geostand. Geoanalytical Res. 35, 397–429. doi:10.1111/j.1751-908X.2011.00120.x

Kamo, S.L., Reimold, W.U., Krogh, T.E., Colliston, W.P., 1996. A 2.023 Ga age for the Vredefort impact event and a first report of shock metamorphosed zircons in pseudotachylitic breccias and Granophyre. Earth Planet. Sci. Lett. 144, 369–387. doi:10.1016/S0012-821X(96)00180-X

Kamyab, R., 2014. Sensitivity Analyses of the Use of Different Neutron Absorbers on the Main Safetly Core Parameters in MTR Type Research Reactor. Nucl. Eng. Technol. 46, 513–520. doi:10.5516/NET.07.2014.002

Kleine, T., Mezger, K., Palme, H., Scherer, E., Münker, C., 2005. The W isotope composition of eucrite metals: Constraints on the timing and cause of the thermal metamorphism of basaltic eucrites. Earth Planet. Sci. Lett. 231, 41–52. doi:10.1016/j.epsl.2004.12.016

Kleine, T., Palme, H., Mezger, K., Halliday, A.N., 2005. Hf-W chronometry of lunar metals and the age and early differentiation of the Moon. Science (80-. ). 310, 1671–1674. doi:10.1126/science.1118842

Korotev, R.L., 1987. Mixing Levels, the Apennine Front Soil Component, and Compositional Trends in the Apollo 15 Soils, in: Lunar and Planetary Science Conference 7th. pp. E411–E431.

Krogh, T.E., Davis, D.W., Corfu, F., 1984. Precise U-Pb zircon and baddeleyite ages for the Sudbury area, in: Pye, E.G., Naldrett, A.J., Giblin, P.E. (Eds.), The Geology and Ore Deposits of the Sudbury Structure. Ontario Geological Survey, Special Volume 1, pp. 421–446.

Krogh, T.E., Kamo, S.L., Bohor, B.F., 1996. Shock Metamorphosed Zircons with Correlated U-Pb Discordance and Melt Rocks with Concordant Protolith Ages Indicate an Impact Origin for the Sudbury Structure. Earth Process. Read. Isot. Code. Geophys. Monogr. 95 343–353. doi:http://dx.doi.org/10.1029/GM095p0343

Krogh, T.E., Kamo, S.L., Sharpton, V.L., Marin, L.E., Hildebrands, A.R., 1993. U–Pb ages of single shocked zircons linking distal K/T ejecta to the Chicxulub crater. Nature 366, 731–734. doi:10.1038/366731a0

Krylov, D.P., Meshick, A.P., Shukolyukov, Y.A., 1993. The zircon Xe(s)-Xe(n) spectrum dating of primary events in high-grade metamorphic terrains-the examples of Archean Napier Complex (East Antartica. Geochem. J. 27, 91–102.

Labotka, T.C., Kempa, M.J., White, C., Papike, J.J., Laul, J.C., 1980. The lunar regolish: Comparative petrology of the Apollo sites. Proc. Lunar Planet. Sci. Conf. 11th 1285–1305.

Laul, J.C., Schmitt, R.A., 1972. Chemical compositin of Apollo 15, 16, and 17 samples, in: Proc. 4th Lunar Sci. Conf. pp. 1349–1367.

Lawrence, D.J., Feldman, W.C., Barraclough, B.L., Binder, A.B., Elphic, R.C., Maurice, S., Miller, M.C., Prettyman, T.H., 1999. High resolution measurements of absolute thorium abundances on the lunar surface. Geophys. Res. Lett. 26, 2681–2684.

Lee, D.-C., Halliday, A.N., Snyder, G.A., Taylor, L.A., 1997. Age and Origin of the Moon. Science (80-. ). 278, 1098–1103. doi:10.1126/science.278.5340.1098

Leroux, H., Reimold, W.U., Koeberl, C., Hornemann, U., Doukhan, J.C., 1999. Experimental shock deformation in zircon: A transmission electron microscopic study. Earth Planet. Sci. Lett. 169, 291–301. doi:10.1016/S0012-821X(99)00082-5

Lindstrom, M.M., Duncan, R.A., Fruchter, J.S., McKay, S.M., Stoeser, J.W., Goles, G.G., Lindstrom, D.J., 1972. Compositional characteristics of some Apollo 14 clastic materials. Proc. 3rd Lunar Sci. Conf. Supplement, 1201–1214.

Lindstrom, M.M., Marvin, U.B., Vetter, S.K., Shervais, J.W., 1988. Apennine Front Revisited: Diversity of Apollo 15 Highland Rock Types. Proc. 18th Lunar Planet. Sci. Conf. 169–186.

Liu, D., Jolliff, B.L., Zeigler, R. a., Korotev, R.L., Wan, Y., Xie, H., Zhang, Y., Dong, C., Wang, W., 2012. Comparative zircon U-Pb geochronology of impact melt breccias from Apollo 12 and lunar meteorite SaU 169, and implications for the age of the Imbrium impact. Earth Planet. Sci. Lett. 319-320, 277–286. doi:10.1016/j.epsl.2011.12.014

Lovering, J.F., Wark, D.A., Gleadow, A.J.W., Sewell, D.K.B., 1972. Uranium and potassium fractionationin pre-Imbrian lunar crustal rocks, in: Third Lunar Science Conference. pp. 281–294.

LSPET, 1973. Apollo 17 lunar samples: Chemical and petrographic descriptions. Science (80-. ). 182, 659–672.

LSPET, 1971. Preliminary examination of lunar samples from Apollo 14. Science (80-. ). 173, 681–693.

Lugmair, G.W., Marti, K., 1972. Neutron and Spallation Effects in Fra Mauro Regolish, in: Lunar and Planetary Science Conference. p. 495.

Mann, H.B., Whitney, D.R., 1947. On a Test of Whether one of Two Random Variables is Stochastically Larger than the Other. Ann. Math. Stat. 18, 50–60. doi:10.1214/aoms/1177730491

McGee, P.E., Simonds, C.H., Warner, J.L., Phinney, W.C., 1979. Introduction to the Apollo Collection: Part II, Lunar Beccias.

McKay, D.S., Heiken, G.H., Taylor, R.M., Clanton, U.S., Morrison, D.A., Ladle, G.H., 1972. Apollo 14 soils: Size distribution and particle types, in: Third Lunar Science Conference. pp. 983–994.

Merle, R.E., Nemchin, a. a., Grange, M.L., Whitehouse, M.J., Pidgeon, R.T., 2014. High resolution U-Pb ages of Ca-phosphates in Apollo 14 breccias: Implications for the age of the Imbrium impact. Meteorit. Planet. Sci. 49, 2241–2251. doi:10.1111/maps.12395

Meyer, C., 1977. Petrology, mineralogy and chemistry of KREEP basalt. Phys. Chem. Earth 10, 239–260.

Meyer, C., Brett, R., Hubbard, N.J., Morrison, D.A., McKay, D.S., Aitken, F.K., Takeda, H., Schonfeld, E., 1971. Mineralogy, chemistry, and origin of the KREEP component in soil samples from the Ocean of Storms, in: Second Lunar Science Conference. pp. 393–411. doi:10.1007/s13398-014-0173-7.2

Meyer, C., Hubbard, N.J., 1970. High Potassium, high phosphorous glass as an important rock type in Apollo 12 soil samples. Meteoritics 5, 210–211.

Meyer, C., Williams, I.S., Compston, W., 1996a. Uranium-lead ages for lunar zircons: Evidence for a prolonged period of granophyre formation from 4.32 to 3.88 Ga. Meteorit. Planet. Sci. 31, 370–387.

Meyer, C., Williams, I.S., Compston, W., 1996. Uranium-lead ages for lunar zircons: Evidence for a prolonged period of granophyre formation from 4 . 32 to 3 . 88 Ga. Meteorit. Planet. Sci. 387, 370–387.

Meyer, C., Williams, I.S., Compston, W., 1996b. Uranium-lead ages for lunar zircons: Evidence for a prolonged period of granophyre formation from 4.32 to 3.88 Ga. Meteorit. Planet. Sci. 31, 370–387.

Meyer, C., Williams, I.S., Compston, W., 1989. 207Pb-206Pb Ages of zircon-containing rock fragments indicate continuous magmatism in the lunar crust from 4350 to 3900 million years, in: Lunar and Planetary Science Conference. pp. 691–692.

Meyer, J., Elkins-Tanton, L., Wisdom, J., 2010. Coupled thermal-orbital evolution of the early Moon. Icarus 208, 1–10. doi:10.1016/j.icarus.2010.01.029

Mezger, K., Krogstad, E., 1997. Interpretation of discordant U-Pb zircon ages: An evaluation. J. Metamorph. Geol. 15, 127–140. doi:10.1111/j.1525-1314.1997.00008.x

Mojzsis, S.J., Devaraju, T.C., Newton, R.C., 2003. Ion Microprobe U-Pb Age Determinations on Zircon from the Late Archean Granulite Facies Transition Zone of Southern India. J. Geol. 111, 407–425. doi:10.1086/375285

Moore, C.B., Lewis, C.F., Cripe, J., Delles, F.M., Kelly, W.R., 1972. Total carbon, nitrogen, and sulfur in Apollo 14 lunar samples, in: Third Lunar Science Conference. pp. 2051–2058.

Morbidelli, A., 2013. Dynamical evolution of planetary systems, in: Oswalt, T.D., French, L.M., Kalas, P. (Eds.), Planets, Stars and Stellar Systems. Springer Science and Buisness Media Dordrecht, p. 63.

Morbidelli, A., Marchi, S., Bottke, W.F., 2012. The Sawtooth-like Timeline of the First Billion Years of Lunar Bombardment, in: Early Solar System Impact Bombardment II. p. #4014.

Morris, R. V., 1978. The surface exposure (maturity) of lunar soils: Some concepts and Is/FeO compilation. Proc. Lunar Planet. Sci. Conf. 9th 2287–2297.

Morris, R. V., Score, R., Dardano, C., Heiken, G.H., 1983. Handbook of Lunar Soils.

Moser, D.E., 1997. Dating the schock wave and thermal imprint of the giant Vrederfort impact, South Africa. Geology 25, 7–10. doi:10.1130/0091-7613(1997)025<0007:DTSWAT>2.3.CO;2

Moser, D.E., Cupelli, C.L., Barker, I.R., Flowers, R.M., Bowman, J.R., Wooden, J., Hart, J.R., 2011. New zircon shock phenomena and their use for dating and reconstruction of large imact structures revealed by electron nanobeam (EBSD, CL, EDS) and isotopic U-Pb and (U-Th)/He analysis of the Vredefort dome. Can. J. Earth Sci. 48, 117–139. doi:10.1139/E11-011

Moser, D.E., Davis, W.J., Reddy, S.M., Flemming, R.L., Hart, R.J., 2009. Zircon U–Pb strain chronometry reveals deep impact-triggered flow. Earth Planet. Sci. Lett. 277, 73–79. doi:10.1016/j.epsl.2008.09.036

Moser, D.E., Flowers, R.M., Hart, R.J., 2001. Birth of the Kaapvaal tectosphere 3.08 billion years ago. Science 291, 465–468. doi:10.1126/science.291.5503.465

Muehlberger, W.R., Batson, R.M., Cernan, E.A., Freeman, V.L., Hait, M.H., Holt, H.E., Howard, K.A., Jackson, E.D., Larson, K.B., Reed, V.S., Rennilson, J.J., Schmitt, H.H., Scott, D.R., Sutton, R.L., Stuart-Alexander, D., Swann, G.A., Trask, N.J., Ulrich, G.E., Wilshire, H.G., Wolfe, E.W., 1973. Preliminary geologic investigation of the Apollo 17 landing site, in: Apollo 17 Preliminary Science Report. pp. 6–91.

Nemchin, A.A., Grange, M.L., Pidgeon, R.T., 2010. Distribution of rare earth elements in lunar zircon. Am. Mineral. 95, 273–283. doi:10.2138/am.2010.3297

Nemchin, A.A., Pidgeon, R.T., Healy, D., Grange, M.L., Whitehouse, M.J., Vaughan, J., 2009a. The comparative behavior of apatite-zircon U-Pb systems in Apollo 14 breccias: Implications for the thermal history of the Fra Mauro formation. Meteorit. Planet. Sci. 44, 1717–1734. doi:10.1111/j.1945-5100.2009.tb01202.x

Nemchin, A.A., Pidgeon, R.T., Whitehouse, M.J., Vaughan, J.P., Meyer, C., 2008. SIMS U-Pb study of zircon from Apollo 14 and 17 breccias: Implications for the evolution of lunar KREEP. Geochim. Cosmochim. Acta 72, 668–689. doi:10.1016/j.gca.2007.11.009

Nemchin, A.A., Timms, N., Pidgeon, R., Geisler, T., Reddy, S., Meyer, C., 2009b. Timing of crystallization of the lunar magma ocean constrained by the oldest zircon. Nat. Geosci. 2, 133–136. doi:10.1038/ngeo417

Nemchin, A.A., Whitehouse, M.J., Pidgeon, R.T., Meyer, C., 2006. Oxygen isotopic signature of 4.4-3.9 Ga zircons as a monitor of differentiation processes on the Moon. Geochim. Cosmochim. Acta 70, 1864–1872. doi:10.1016/j.gca.2005.12.009

Nemchin, B.A.A., Pidgeon, R.T., Whitehouse, M.J., Vaughan, J.P., Meyer, C., n.d. A zircon U-Pb study of the evolution of lunar KREEP By A.A. Nemchin, R.T. Pidgeon, M.J. Whitehouse, J.P. Vaughan and C. Meyer.

Neumann, G.A., Zuber, M.T., Wieczorek, M.A., Head, J.W., Baker, D.M.H., Solomon, S.C., Smith, D.E., Lemoine, F.G., Mazarico, E., Sabaka, T.J., Goossens, S.J., Melosh, H.J., Phillips, R.J., Asmar, S.W., Konopliv, A.S., Williams, J.G., Sori, M.M., Soderblom, J.M., Miljkovi, K., Andrews-hanna, J.C., Nimmo, F., Kiefer, W.S., 2015. Lunar impact basins revealed by Gravity Recovery and Interior Laboratory measurements. Sci. Adv. 1, 1–11.

Norman, M.D., Nemchin, A.A., 2014. A 4.2 billion year old impact basin on the Moon: U–Pb dating of zirconolite and apatite in lunar melt rock 67955. Earth Planet. Sci. Lett. 388, 387–398. doi:10.1016/j.epsl.2013.11.040

Nyquist, L.E., Bansal, B.M., Wiesmann, H., 1975. Rb-Sr ages and initial 87Sr/86Sr for Apollo 17 basalts and KREEP basalt 15386, in: Proc. Lunar Sci. Conf. 6th. pp. 1445–1465.

Nyquist, L.E., Hubbard, N.J., Gast, P.W., 1973. Rb-Sr systematics for chemically defined Apollo 15 and 16 materials, in: Proc. 4th Lunar Sci. Conf. pp. 1823–1846.

Ozima, M., Podosek, F.A., 2002. Noble Gas Geochemistry, Second Edi. ed. Cambridge University Press.

Ozima, M., Podosek, F.A., 1983. Noble Gas Geochemistry. Cambridge University Press,

Cambridge.

Paces, J.B., Miller, J.D., 1993. Precise U-Pb Ages of Duluth Complex and Related Mafic Instrusions, Northeastern Minnesota: Geochronological Insights to Physical, Petrogenetic, Paleomagnetic, and Tectonomagmatic Processes Associated with the 1.1 Ga Midcontinent Rift System. System 98.

Palme, H., Baddenhausen, H., Blum, K., Cendales, M., Dreibus, G., Hofmeister, H., Kruse, H., Palme, C., Spettel, B., Vilcsek, E., Wanke, H., 1978. New data on lunar samples and achondrites and a comparison of the least fractionated samples from the earth, the moon and the eucrite parent body, in: Lunar and Planetary Science Conference 9th. pp. 25–57.

Papanastassiou, D.A., Wasserburg, G.J., 1971. RbSr ages of igneous rocks from the Apollo 14 mission and the age of the Fra Mauro formation. Earth Planet. Sci. Lett. 12, 36–48. doi:10.1016/0012-821X(71)90052-5

Payne, M.G., Chen, C.H., Hurst, G.S., Foltz, G.W., 1981. Applications of Resonance Ionization Spectroscopy in Atomic and Molecular Physics. Adv. At. Molectular Phys. 17, 229–274.

Pepin, R.O., Becker, R.H., Rider, P.E., 1995. Xenon and krypton isotopes in extraterrestrial regolith soils and in the solar wind. Geochim. Cosmochim. Acta 59, 4997–5022. doi:10.1016/0016-7037(96)80916-1

Pidgeon, R.T., Nemchin, a. a., van Bronswijk, W., Geisler, T., Meyer, C., Compston, W., Williams, I.S., 2007. Complex history of a zircon aggregate from lunar breccia 73235. Geochim. Cosmochim. Acta 71, 1370–1381. doi:10.1016/j.gca.2006.11.021

Pritchard, M.E., Stevenson, D.J., 2000. Thermal Aspects of a Lunar Origin by Giant Impact, in: Canup, R.M., Righter, K. (Eds.), Origin of the Earth and Moon. University of Arizona Press, pp. 179–196.

Ragettli, R.A., Hebeda, E.H., Singer, P., Wieler, R., 1994. Uranium-Xenon chronology: precise determination of lsf* 136Ysf for spontaneous fission of 238U. Earth Planet. Sci. Lett. 128, 653–670.

Reimold, W.U., Pybus, G.Q.J., Kruger, F.J., Layer, P.W., Koeberl, C., 2000. The Anna's rust sheet and related gabbroic intrusions in the Vredefort dome-kibaran magmatic event on the Kaapvaal craton and beyond? J. African Earth Sci. 31, 499–521. doi:10.1016/S0899-5362(00)80004-4

Rice, W.R., 1989. Analyzing Tables of Statistical Tests. Evolution (N. Y). 43, 223–225.

Robertson, J.K., Wyllie, P.J., 1971. Rock-Water Systems, with Special Reference to the Water-Deficient Region. Am. J. Sci. 271, 252–277.

Ryder, G., 1976. Lunar Sample 15405: Remnant of a KREEP basalt-granite diferentiated pluton. EPSL 29, 255–268.

Schmitt, A.K., Zack, T., 2012. High-sensitivity U-Pb rutile dating by secondary ion mass spectrometry (SIMS) with an O 2 + primary beam. Chem. Geol. 332-333, 65–73. doi:10.1016/j.chemgeo.2012.09.023

Shearer, C.K., Hess, P.C., Wieczorek, M.A., Pritchard, M.E., Parmentier, E.M., Borg, L.E., Longhi, J., Elkins-Tanton, L.T., Neal, C.R., Antonenko, I., Canup, R.M., Halliday, A.N., Grove, T.L., Hager, B.H., Lee, D.-C., Wiechert, U., 2006. Thermal and Magmatic Evolution of the Moon. Rev. Mineral. Geochemistry 60, 365–518. doi:10.2138/rmg.2006.60.4

Shervais, J.W., Lawrence, A., Lindstrom, M.M., 1985. Apollo 14 Mare Basalts: Petrology and Geochemistry of Clasts from Consortium Breccia 14321, in: Lunar and Planetary Science Conference 5th. pp. C375–C395.

Shervais, J.W., Taylor, L.A., Laul, J.C., Smith, M.R., 1984. Pristine Highland Clasts in Consortium Breccia 14305: Petrology and Geochemistry. Proc. 15th Lunar Plan. Sci. Conf. Journal of, C24–C40.

Shih, C.-Y., Bansal, B.M., Wiesmann, H., Nyquist, L.E., Bogard, D.D., 1986. Geochronology and petrogenesis of Apollo 14 very high potassium mare basalts 91. doi:10.1029/JB091iB04p0D214

Shih, C.-Y., Nyquist, L.., Bogard, D.., Dasch, E.., Bansal, B.., Wiesmann, H., 1987. Geochronology of high-K aluminous mare basalt clasts from Apollo 14 breccia 14304. Geochim. Cosmochim. Acta 51, 3255–3271. doi:10.1016/0016-7037(87)90133-5

Shih, C.-Y., Nyquist, L.., Dasch, E.., Bogard, D.., Bansal, B.., Wiesmann, H., 1993. Ages of pristine noritic clasts from lunar breccias 15445 and 15455. Geochim. Cosmochim. Acta 57, 915–931. doi:10.1016/0016-7037(93)90178-Y

Shih, C.-Y., Nyquist, L.E., Bansal, B.M., Wiesmann, H., 1992. Rb-Sr and Sm-Nd chronology of an Apollo 17 KREEP basalt. Earth Planet. Sci. Lett. 108, 203–215. doi:10.1016/0012-821X(92)90023-O

Shukoljukov, J., Kirsten, T., Jessberger, E.K., 1974. The Xe-Xe spectrum technique, a new dating method. Earth Planet. Sci. Lett. 24, 271–281. doi:10.1016/0012-821X(74)90105-8

Shukolyukov, Y. a., Fugzan, M.M., Paderin, I.P., Sergeev, S. a., Krylov, D.P., 2009. Unusually high thermal stability of the Uranium-Xenon isotopic system in nonmetamict zircons. Dokl. Earth Sci. 425, 287–290. doi:10.1134/S1028334X09020251

Simon, S.B., Papike, J.J., 1981. The Lunar regolith: Comparative petrology of the Apollo and

Luna soils, in: Lunar and Planetary Science Conference 12B. pp. 984–986.

Simonds, C.H., Phinney, W.C., Warner, J.L., McGee, P.E., Geelsin, J., Brown, R.W., Rhodes, J.M., 1977. Apollo 14 revisited, or breccias aren't so bad after all, in: 8th Lunar Science Converence. pp. 1869–1893.

Snyder, G.A., Taylor, L.A., Crozaz, G., 1993. Rare earth element selenochemistry of immiscible liquids and zircon at Apollo 14: An ion probe study of evolved rocks on the Moon. Geochim. Cosmochim. Acta 57, 1143–1149. doi:10.1016/0016-7037(93)90046-Y

Snyder, G.A., Taylor, L.A., Halliday, A.N., 1995. Chronology and petrogenesis of the lunar highlands alkali suite: Cumulates from KREEP basalt crystallization. Geochim. Cosmochim. Acta 59, 1185–1203. doi:10.1016/0016-7037(95)00034-W

Solomon, S.C., 1986. On the early thermal state of the Moon. Orig. Moon 435–452.

Stadermann, F.J., Heusser, E., Jessberger, E.K., Lingner, S., Stöffler, D., 1991. The case for a younger Imbrium basin: New 40Ar-39Ar ages of Apollo 14 rocks. Geochim. Cosmochim. Acta 55, 2339–2349. doi:10.1016/0016-7037(91)90108-h

Swann, G.A., Bailey, N.G., Batson, R.M., Eggelton, R.E., Hait, M.H., Holt, H.E., Larson, K., McEwen, M.C., Mitchell, E.D., Schaber, G.G., Schafer, J.P., Shepard, A.B., Sutton, R.L., Trask, N.J., Ulrich, G.E., Wilshire, H.G., Wolfe, E.W., 1971a. Preliminary Geologic Investigation of the Apollo 14 landing site, in: Apollo 14 Preliminary Science Report Nasa Sp-272. pp. 39–85.

Swann, G.A., Bailey, N.G., Batson, R.M., Eggelton, R.E., Hait, M.H., Holt, H.E., Larson, K.B., McEwen, M.C., Mitchell, E.D., Schaber, G.G., Schafer, J.P., Shepard, A.B., Sutton, R.L., Trask, N.J., Ulrich, G.E., Wilshire, H.G., Wolfe, E.W., 1971b. Preliminary Geologic Investigation of the Apollo 14 landing site. In Apollo 14 Preliminary Science Report. NASA SP-272.

Swann, G.A., Bailey, N.G., Batson, R.M., Eggelton, R.E., Hait, M.H., Holt, H.E., Larson, K.B., Reed, V.S., Schaber, G.G., Sutton, R.L., Trask, N.J., Ulrich, G.E., Wilshire, H.G., 1977. Geology of the Apollo 14 landing site in the Fra Mauro Highlands.

Swann, G.A., Bailey, N.G., Batson, R.M., Freeman, V.L., Hait, M.H., Head, J.W., Holt, H.E., Howard, K.A., Irwin, J.B., Larson, K.B., Muehlberger, W.R., Reed, V.S., Rennilson, J.J., Schaber, G.G., Scott, D.R., Silver, L.T., Sutton, R.L., Ulrich, G.E., Wilshire, H.G., Wolfe, E.W., 1972. Preliminary geologic investigation of the Apollo 15 landing site, in: Apollo 15 Preliminary Science Report NASA SP-289.

Tatsumoto, M., Hedge, C.E., Doe, B.R., Unruh, D.M., 1972. U-Th-Pb and Rb-Sr measurements

on some Apollo 14 lunar samples. Proc. 3rd Lunar Sci. Conf. Supplement, 1531–1555.

Taylor, D.J., McKeegan, K.D., Harrison, T.M., 2009a. Lu-Hf zircon evidence for rapid lunar differentiation. Earth Planet. Sci. Lett. 279, 157–164. doi:10.1016/j.epsl.2008.12.030

Taylor, D.J., McKeegan, K.D., Harrison, T.M., Young, E.D., 2009b. Early differentiation of the lunar magma ocean – new Lu-Hf isotope results from Apollo 17. Geochim. Cosmochim. Acta Suppl. 73, A1317.

Taylor, G.J., Warner, R.D., Keil, K., Ma, M.-S., Schmitt, R.A., 1980. Siliate liquid immiscibility, evolved lunar rocks and the formation of KREEP, in: Proc. Conf. Lunar Highlands Crust. pp. 339–352. doi:10.1007/s13398-014-0173-7.2

Taylor, L.A., Shervais, J.W., Hunter, R.H., Shih, C.-Y., Bansal, B.M., Wooden, J., Nyquist, L.E., Laul, L.C., 1983. Pre-4.2 AE mare-basalt volcanism in the lunar highlands. Earth Planet. Sci. Lett. 66, 33–47. doi:10.1016/0012-821X(83)90124-3

Taylor, S.R., Kaye, M., Muir, P., Nance, W., Rudowski, R., Ware, N., 1972. Composition of the lunar uplands: Chemistry of Apollo 14 samples from Fra Mauro. Proc. 3rd Lunar Sci. Conf. Supplement, 1231–1249.

Teitsma, A., Clarke, W.B., 1978. Fission Xenon Isotope Dating. J. Geophys. Res. 83, 5443–5453.

Teitsma, A., Clarke, W.B., Allègre, C.J., 1975. Spontaneous Fission-Neutron Fission Xenon: A New Technique for Dating Geological Events. Scien 189, 878–800.

Tera, F., Papanastassiou, D.A., Wasserburg, G.J., 1974. Isotopic evidence for a terminal lunar cataclysm. Earth Planet. Sci. Lett. 22, 1–21. doi:10.1016/0012-821X(74)90059-4

Tera, F., Papanastassiou, D.A., Wasserburg, G.J., 1973. A Lunar Cataclysm at ~3.95 AE and the Structure of the Lunar Crust. Lunar Planet. Sci. Conf. 4, 723–725.

Terada, K., Anand, M., Sokol, A.K., Bischoff, A., Sano, Y., 2007. Cryptomare magmatism 4.35 Gyr ago recorded in lunar meteorite Kalahari 009. Nature 450, 849–852. doi:10.1038/nature06356

Timms, N.E., Reddy, S.M., Healy, D., Nemchin, A. a., Grange, M.L., Pidgeon, R.T., Hart, R., 2012. Resolution of impact-related microstructures in lunar zircon: A shock-deformation mechanism map. Meteorit. Planet. Sci. 47, 120–141. doi:10.1111/j.1945-5100.2011.01316.x

Touboul, M., Kleine, T., Bourdon, B., Palme, H., Wieler, R., 2009. Tungsten isotopes in ferroan anorthosites: Implications for the age of the Moon and lifetime of its magma ocean. Icarus 199, 245–249. doi:10.1016/j.icarus.2008.11.018

Trail, D., Bruce Watson, E., Tailby, N.D., 2012. Ce and Eu anomalies in zircon as proxies for the

oxidation state of magmas. Geochim. Cosmochim. Acta 97, 70–87. doi:10.1016/j.gca.2012.08.032

Turner, G., Busfield, A., Crowther, S. a., Harrison, M., Mojzsis, S.J., Gilmour, J., 2007. Pu-Xe, U-Xe, U-Pb chronology and isotope systematics of ancient zircons from Western Australia. Earth Planet. Sci. Lett. 261, 491–499. doi:10.1016/j.epsl.2007.07.014

Turner, G., Cadogan, P.H., Yonge, C.J., 1973. Argon selenochronology, in: Proc. 4th Lunar Sci. Conf. pp. 1889–1914.

Turner, G., Harrison, T.M., Holland, G., Mojzsis, S.J., Gilmour, J., 2004. Extinct 244Pu in Ancient Zircons. Science (80-. ). 306, 89–91.

Turtle, E.P., Pierazzo, E., 1998. Constraints on the size of the Vredefort impact crater from numerical modeling. Meteorit. Planet. Sci. 33, 483–490. doi:10.1111/j.1945-5100.1998.tb01652.x

Valley, J.W., Spicuzza, M.J., Ushikubo, T., 2014. Correlated δ18O and [Ti] in lunar zircons: a terrestrial perspective for magma temperatures and water content on the Moon. Contrib. to Mineral. Petrol. 167, 956. doi:10.1007/s00410-013-0956-4

Von Engelhardt, W., Arndt, J., Stoffler, D., Schneider, H., 1972. Apollo 14 regolith and fragmental rocks, their compositions and origin by impacts, in: Third Lunar Science Conference. pp. 753–770.

Wadhwa, M., 2008. Redox Conditions on Small Bodies, the Moon and Mars. Rev. Mineral. Geochemistry 68, 493–510.

Wallenius, J., Westlén, D., 2008. Hafnium clad fuels for fast spectrum BWRs. Ann. Nucl. Energy 35, 60–67. doi:10.1016/j.anucene.2007.05.006

Wanke, H., Baddenhausen, H., Balacesu, A., Teschke, F., Spettel, B., Dreibus, G., Palme, H., Quijano-Rico, M., Kruse, H., Wlotzka, F., Begemann, F., 1972. Multielement analyses of lunar samples and some implications of the results. Proc. 3rd Lunar Sci. Conf. Supplement, 1251–1268.

Warren, P.H., Taylor, G.J., Keil, K., Marshall, C., Wasson, J.T., 1981. Foraging westward for pristine nonmare rocks: Complications from petrogenetic models, in: Lunar and Planetary Science Conference 12B. pp. 21–40.

Warren, P.H., Wasson, J.T., 1979. The origin of KREEP. Rev. Geophys. Sp. Phys. 17, 73–88. doi:10.1029/RG017i001p00073

Watson, E.B., Green, T.H., 1981. Apatite/liquid partition coefficients for the rare earth elements and strontium. Earth Planet. Sci. Lett. 56, 405–421. doi:10.1016/0012-821X(81)90144-8

Watson, E.B., Harrison, T.M., 2005. Zircon thermometer reveals minimum melting conditions on earliest Earth. Science (80-. ). 308, 841–844.

Wetherill, G.W., 1953. Spontaneous fission yields from uranium and thorium. Phys. Rev. 92, 907–912.

Wieczorek, M.A., Philips, R.J., 2000. The "Procellarum KREEP Terrane": Implications for mare volcanism and lunar evolution. J. Geophys. Res. 105, 20417–20430.

Wiedenbeck, M., Hanchar, J.M., Peck, W.H., Sylvester, P., Valley, J., Whitehouse, M., Kronz, A., Morishita, Y., Nasdala, L., Fiebig, J., Franchi, I., Girard, J.-. P., Greenwood, R.C., Hinton, R., Kita, N., Mason, P.R.D., Norman, M., Ogasawara, M., Piccoli, R., Rhede, D., Satoh, H., Schulz-Dobrick, B., Skar, O., Spicuzza, M.J., Terada, K., Tindle, A., Togashi, S., Vennemann, T., Xie, Q., Zheng, Y.-. F., 2004. Further characterisation of the 91500 Zircon Crystal. Geostand. Geoanalytical Res. 28, 9–39. doi:DOI 10.1111/j.1751-908X.2004.tb01041.x

Wielicki, M.M., Harrison, T.M., Schmitt, A.K., 2012. Geochemical signatures and magmatic stability of terrestrial impact produced zircon. Earth Planet. Sci. Lett. 321-322, 20–31. doi:10.1016/j.epsl.2012.01.009

Wiik, H.B., Maxwell, J.A., Bouvier, J.-L., 1973. Chemical composition of some Apollo 14 lunar samples. EARTH Planet. Sci. Lett. 17, 365–368.

Willis, J.P., Erland, A.J., Gurney, R.H., Theil, R.H., Ahrens, L.H., 1972. Major, minor, and trace element data for some Apollo 11, 12, 14, and 15 samples. Proc. 3rd Lunar Sci. Conf. Supplement, 1269–1273.

Wilshire, H.G., Jackson, E.D., 1972. Petrology and Stratigraphy of the Fra Mauro Formation at the Apollo 14 Site. Geol. Surv. Prof. Pap. 785.

Wittmann, A., Kenkmann, T., Schmitt, R.T., Stoffler, D., 2006. Shock-metamorphosed zircon in terrestrial impact craters. Meteorit. Planet. Sci. 41, 433–454. doi:10.1111/j.1945-5100.2006.tb00472.x

Wopenka, B., Jolliff, B.L., Zinner, E., Kremser, D.T., 1996. Trace element zoning and incipient metamictization in a lunar zircon: Application of three microprobe techniques. Am. Mineral. 81, 902–912.

Yin, Q., Jacobsen, S.B., Yamashita, K., Blichert-Toft, J., Télouk, P., Albarède, F., 2002. A short timescale for terrestrial planet formation from Hf-W chronometry of meteorites. Nature 418, 949–952. doi:10.1038/nature00995

York, D., Kenyon, W.J., Doyle, R.J., 1972. 40Ar-39Ar ages of Apollo 14 and 15 samples, in:

Third Lunar Science Conference. pp. 1613–1622.

Young, B.G., Thode, H.G., 1960. Absolute yield of the xenon and krypton isotopes in 238U spontaneous fission. Can. J. Phys. 38, 1–9.

Zahnle, K., Arndt, N., Cockell, C., Halliday, A., Nisbet, E., Selsis, F., Sleep, N.H., 2007. Emergence of a habitable planet. Space Sci. Rev. 129, 35–78. doi:10.1007/s11214-007-9225-z

Zhang, A.C., Taylor, L. a., Wang, R.C., Li, Q.L., Li, X.H., Patchen, A.D., Liu, Y., 2012. Thermal history of Apollo 12 granite and KREEP-rich rock: Clues from Pb/Pb ages of zircon in lunar breccia 12013. Geochim. Cosmochim. Acta 95, 1–14. doi:10.1016/j.gca.2012.07.023

Zuber, M.T., Smith, D.E., Watkins, M.M., Asmar, S.W., Konopliv, A.S., Lemoine, F.G., Melosh, H.J., Neumann, G.A., Phillips, R.J., Solomon, S.C., Wieczorek, M.A., Williams, J.G., Goossens, S.J., Kruizinga, G., Mazarico, E., Park, R.S., Yuan, D., 2013. Gravity Field of the Moon from the Gravity Recovery and Interior Laboratory (GRAIL) Mission. Science (80-. ). 339, 668–671.